**Navigation system based in motion tracking sensor for percutaneous renal access**

Pedro Miguel Loureiro Rodrigues

UMinho|2016

---

**Universidade do Minho**
Escola de Engenharia

Pedro Miguel Loureiro Rodrigues

# Navigation system based in motion tracking sensor for percutaneous renal access

junho de 2016

**Universidade do Minho**
Escola de Engenharia

Pedro Miguel Loureiro Rodrigues

# Navigation system based in motion tracking sensor for percutaneous renal access

Tese de Doutoramento em Engenharia Biomédica

Trabalho efetuado sob a orientação do
**Professor Doutor Jaime Francisco Cruz Fonseca**
e do
**Professor Doutor João Luís Araújo Martins Vilaça**

junho de 2016

# STATEMENT OF INTEGRITY

I hereby declare having conducted my thesis with integrity. I confirm that I have not used plagiarism or any form of falsification of results in the process of the thesis elaboration. I further declare that I have fully acknowledged the Code of Ethical Conduct of the University of Minho.

University of Minho, June 27, 2016

Full name: Pedro Miguel Loureiro Rodrigues

Signature:

Pedro Miguel Loureiro Rodrigues

# Acknowledgements

This doctoral thesis, besides a result of extensive hours of work and dedication over the past years, represents also a truly life-changing experience. It ends now as an important phase of my life. Last years were so full of good moments, that all of them contribute to this work, influence my personal growth and have created unforgettable experiences. None of this would have been possible without the contribution of a considerable number of people that I am grateful.

First of all, I would like to thank my supervisor Professor Jaime Fonseca for all the scientific orientation, suggestions, advice, support and final revision of the thesis. I am also grateful for the opportunity he gave me to be part of this fantastic and energetic research group, yet during my master thesis. Thank you for your support and friendship along my academic journey.

A very special thanks to my co-supervisor Professor João Vilaça for his scientific orientation, know-how, daily supervision, availability, sympathy, final revision of the thesis and support over all these years. It was a real enriching experience to work with you. Thank you also for the opportunity of working with this group from its beginning. I am very grateful for the opportunity that I had in participating in all the conferences, "mini" projects and being part of IPCA. Although all this work is synonym of sleepless nights and tired days, they also helped moments of friendship, new experiences and ideas, personal growth and strengthen our team relationship. Thank you for your continuous friendship.

I would like to thank to Nuno Rodrigues for all the support, advice, paper revisions and friendship over these years.

To my PhD partner António Moreira who had time during his PhD to got married ☺ Thank you for all the discussions, shared moments, suggestions, stressful deadlines and for being part of the *estouro* methodology.

This thesis was also part of a fruitful collaboration with IPCA. Thank you for all support and receptiveness.

I would like to thank to my fellow Besurg friends, who in one way or another, contributed in a significantly way to this thesis. A special thanks to Fonseca, Sandro, Morais, Fernando and Bruno.

To Professor Estêvão and Paulo Mota for all the medical opinions, support and guidance.

I would like to thank to Professor Wagner and Professor Markao for the opportunity of working at the Federal University of Rio de Janeiro during 6 months and for all the advice during the development stages.

To all my friends that continue to create special moments every day. Special thanks to Helena, Rui, Rita, Moras, Gui, Getta, Marri, Pires, Capitão, Clara, Sara, Gonçalo, Martirinho, Isabel, Tatiana and Sonia. Without you all, these past years would not have the same magic.

Special thanks to Helena for the immeasurable love, friendship, companionship, support, understanding, constant positivism and patience over the past years. Thanks for everything.

Last but not the least, to my parents, brother and godmother for all the love, unconditional support and opportunities in all moments, that made me everything I am today.

The present work was only possible thanks to the support by the Portuguese Science and Technology Foundation through the PhD grant with reference SFRH/BD/74276/2010 funded by FCT/MEC (PIDDAC) and by Fundo Europeu de Desenvolvimento Regional (FEDER), Programa COMPETE - Programa Operacional Factores de Competitividade (POFC) do QREN.

# Abstract

Minimally-invasive kidney interventions are daily performed to diagnose and treat several renal diseases. Percutaneous renal access (PRA) is an essential but challenging stage for most of these procedures, since its outcome is directly linked to the physician's ability to precisely visualize and reach the anatomical target.

Nowadays, PRA is always guided with medical imaging assistance, most frequently using X-ray based imaging (e.g. fluoroscopy). Thus, radiation on the surgical theater represents a major risk to the medical team, where its exclusion from PRA has a direct impact diminishing the dose exposure on both patients and physicians.

To solve the referred problems this thesis aims to develop a new hardware/software framework to intuitively and safely guide the surgeon during PRA planning and puncturing.

In terms of surgical planning, a set of methodologies were developed to increase the certainty of reaching a specific target inside the kidney. The most relevant abdominal structures for PRA were automatically clustered into different 3D volumes. For that, primitive volumes were merged as a local optimization problem using the minimum description length principle and image statistical properties. A multi-volume Ray Cast method was then used to highlight each segmented volume. Results show that it is possible to detect all abdominal structures surrounding the kidney, with the ability to correctly estimate a virtual trajectory.

Concerning the percutaneous puncturing stage, either an electromagnetic or optical solution were developed and tested in multiple *in vitro*, *in vivo* and *ex vivo* trials. The optical tracking solution aids in establishing the desired puncture site and choosing the best virtual puncture trajectory. However, this system required a line of sight to different optical markers placed at the needle base, limiting the accuracy when tracking inside the human body. Results show that the needle tip can deflect from its initial straight line trajectory with an error higher than 3 mm. Moreover, a complex registration procedure and initial setup is needed.

On the other hand, a real-time electromagnetic tracking was developed. Hereto, a catheter was inserted trans-urethrally towards the renal target. This catheter has a position and orientation electromagnetic sensor on its tip that function as a real-time target locator. Then, a needle integrating a similar sensor is used. From the data provided by both sensors, one computes a virtual puncture trajectory, which is displayed in a 3D visualization software. *In vivo* tests showed a median renal and ureteral puncture times of 19 and 51 seconds, respectively (range 14 to 45 and 45 to 67 seconds). Such results represent a puncture time improvement between 75% and 85% when comparing to state of the art methods.

3D sound and vibrotactile feedback were also developed to provide additional information about the needle orientation. By using these kind of feedback, it was verified that the surgeon tends to follow a virtual puncture trajectory with a reduced amount of deviations from the ideal trajectory, being able to anticipate any movement even without looking to a monitor. Best results show that 3D sound sources were correctly identified 79.2 ± 8.1% of times with an average angulation error of 10.4° degrees. Vibration sources were accurately identified 91.1 ± 3.6% of times with an average angulation error of 8.0° degrees.

Additionally to the EMT framework, three circular ultrasound transducers were built with a needle working channel. One explored different manufacture fabrication setups in terms of the piezoelectric materials, transducer construction, single *vs.* multi array configurations, backing and matching material design. The A-scan signals retrieved from each transducer were filtered and processed to automatically detect reflected echoes and to alert the surgeon when undesirable anatomical structures are in between the puncture path. The transducers were mapped in a water tank and tested in a study involving 45 phantoms. Results showed that the beam cross-sectional area oscillates around the ceramics radius and it was possible to automatically detect echo signals in phantoms with length higher than 80 mm.

Hereupon, it is expected that the introduction of the proposed system on the PRA procedure, will allow to guide the surgeon through the optimal path towards the precise kidney target, increasing surgeon's confidence and reducing complications (e.g. organ perforation) during PRA. Moreover, the developed framework has the potential to make the PRA free of radiation for both patient and surgeon and to broad the use of PRA to less specialized surgeons.

**Keywords:** percutaneous renal access; image processing; surgery navigation; motion tracking systems.

# Sumário

Intervenções renais minimamente invasivas são realizadas diariamente para o tratamento e diagnóstico de várias doenças renais. O acesso renal percutâneo (ARP) é uma etapa essencial e desafiante na maior parte destes procedimentos. O seu resultado encontra-se diretamente relacionado com a capacidade do cirurgião visualizar e atingir com precisão o alvo anatómico.

Hoje em dia, o ARP é sempre guiado com recurso a sistemas imagiológicos, na maior parte das vezes baseados em raios-X (p.e. a fluoroscopia). A radiação destes sistemas nas salas cirúrgicas representa um grande risco para a equipa médica, aonde a sua remoção levará a um impacto direto na diminuição da dose exposta aos pacientes e cirurgiões.

De modo a resolver os problemas existentes, esta tese tem como objetivo o desenvolvimento de uma *framework* de hardware/software que permita, de forma intuitiva e segura, guiar o cirurgião durante o planeamento e punção do ARP.

Em termos de planeamento, foi desenvolvido um conjunto de metodologias de modo a aumentar a eficácia com que o alvo anatómico é alcançado. As estruturas abdominais mais relevantes para o procedimento de ARP, foram automaticamente agrupadas em volumes 3D, através de um problema de optimização global com base no princípio de “minimum description length” e propriedades estatísticas da imagem. Por fim, um procedimento de Ray Cast, com múltiplas funções de transferência, foi utilizado para enfatizar as estruturas segmentadas. Os resultados mostram que é possível detetar todas as estruturas abdominais envolventes ao rim, com a capacidade para estimar corretamente uma trajetória virtual.

No que diz respeito à fase de punção percutânea, foram testadas duas soluções de deteção de movimento (ótica e eletromagnética) em múltiplos ensaios *in vitro*, *in vivo* e *ex vivo*. A solução baseada em sensores óticos ajudou no cálculo do melhor ponto de punção e na definição da melhor trajetória a seguir. Contudo, este sistema necessita de uma linha de visão com diferentes marcadores óticos acoplados à base da agulha, limitando a precisão com que a agulha é detetada no interior do corpo humano. Os resultados indicam que a agulha pode sofrer deflexões à medida que vai sendo inserida, com erros superiores a 3 mm.

Por outro lado, foi desenvolvida e testada uma solução com base em sensores eletromagnéticos. Para tal, um cateter que integra um sensor de posição e orientação na sua ponta, foi colocado por via trans-uretral junto do alvo renal. De seguida, uma agulha, integrando um sensor semelhante, é utilizada para a punção percutânea. A partir da diferença espacial de ambos os sensores, é possível gerar uma trajetória de punção virtual. A mediana do tempo necessário para puncionar o rim e ureter, segundo esta trajetória, foi de 19 e 51 segundos, respetivamente (variações de 14 a 45 e 45 a 67 segundos). Estes resultados representam uma melhoria do tempo de punção entre 75% e 85%, quando comparados com o estado da arte dos métodos atuais.

Além do feedback visual, som 3D e feedback vibratório foram explorados de modo a fornecer informações complementares da posição da agulha. Verificou-se que com este tipo de feedback, o cirurgião tende a seguir uma trajetória de punção com desvios mínimos, sendo igualmente capaz de antecipar qualquer movimento, mesmo sem olhar para o monitor. Fontes de som e vibração podem ser corretamente detetadas em 79,2 ± 8,1% e 91,1 ± 3,6%, com erros médios de angulação de 10.4° e 8.0 graus, respetivamente.

Adicionalmente ao sistema de navegação, foram também produzidos três transdutores de ultrassom circulares com um canal de trabalho para a agulha. Para tal, foram exploradas diferentes configurações de fabricação em termos de materiais piezoelétricos, transdutores multi-array ou singulares e espessura/material de layers de suporte. Os sinais originados em cada transdutor foram filtrados e processados de modo a detetar de forma automática os ecos refletidos, e assim, alertar o cirurgião quando existem variações anatómicas ao longo do caminho de punção. Os transdutores foram mapeados num tanque de água e testados em 45 phantoms. Os resultados mostraram que o feixe de área em corte transversal oscila em torno do raio de cerâmica, e que os ecos refletidos são detetados em phantoms com comprimentos superiores a 80 mm.

Desta forma, é expectável que a introdução deste novo sistema a nível do ARP permitirá conduzir o cirurgião ao longo do caminho de punção ideal, aumentado a confiança do cirurgião e reduzindo possíveis complicações (p.e. a perfuração dos órgãos). Além disso, de realçar que este sistema apresenta o potencial de tornar o ARP livre de radiação e alarga-lo a cirurgiões menos especializados.

**Palavras-chave:** acesso renal percutâneo; processamento de imagem; navegação cirúrgica; sistemas de deteção de movimento.

# Table of Contents

# List of Figures

# List of Tables

# List of Abbreviation

| | |
|---|---|
| **2D** | Two-dimensional |
| **3D** | Three-dimensional |
| **BNC** | Bayonet Neill–Concelman |
| **ESWL** | Extracorporeal Shockwave Lithotripsy |
| **CT** | Computed Tomography |
| **CWT** | Continuous Wavelet Transform |
| **Dicom** | Digital Imaging and Communications in Medicine |
| **DOF** | Degrees of Freedom |
| **DSC** | Dice Similarity Coefficient |
| **EAX** | Environmental Audio Extensions |
| **EMT** | Electromagnetic Motion Tracking |
| **FPS** | Frames per Second |
| **GPS** | Global Position System |
| **GUI** | Graphical User Interface |
| **ICP** | Interactive Closest Points |
| **IMT** | impedance Matching Transformer |
| **ITK** | Insight Toolkit |
| **IVU** | Intravenous Urography |
| **MISs** | Minimal Invasive Surgeries |
| **MIS** | Minimal Invasive Surgery |
| **MR** | Magnetic Resonance |
| **NDI** | Northern Digital Inc |
| **OMT** | Optic Motion Tracking |
| **PCNL** | Percutaneous Nephrolithotomy |
| **PPT** | Percutaneous Puncture Trajectory |
| **PRA** | Percutaneous Renal Access |
| **PVC** | Polyvinyl Chloride |

| | |
|---|---|
| **PVCP** | Plastic Polyvinyl Chloride |
| **PVDF** | Polyvinylidene Fluoride |
| **PZT** | Lead Zirconate Titanate |
| **ROM** | Read Only Memory |
| **SCU** | System Control Unity |
| **SIU** | Sensor Interface Units |
| **SS1** | First Sound Strategy |
| **SS2** | Second Sound Strategy |
| **SS3** | Third Sound Strategy |
| **SS4** | Forth Sound Strategy |
| **ST** | Soft Tissue |
| **US** | Ultrasound |
| **UT** | Ultrasonic Transducer |
| **VOI** | Volume of Interest |
| **VTK** | Visualization Toolkit |

# 1

# Introduction

This chapter provides an initial background about the work developed during this doctoral thesis in Biomedical Engineering. The main applications, features and challenges of percutaneous procedures are initially described. Nephrolithiasis is then addressed, in more detail, since it will be used as the case study to develop, test and validate new technological solutions that may overcome current challenges within percutaneous procedures. Finally, it presents the thesis motivation, followed by the main research goals, contributions and remaining thesis organization.

## Contents

## 1.1 Minimal Invasive Surgeries

Minimally invasive surgeries (MISs) have gained considerable attention in the past decade and have been changing the way people think about surgery. The early and immediate success of MISs led to unrealistic expectations, revolutionizing and converting many surgical procedures to less invasive approaches [1, 2].

In contrast to open surgeries (skin incision is sufficiently large to allow the intervention under direct vision), MISs involve the insertion and manipulation of different surgical instruments (e.g. catheters, needles, smaller probes), inside the human body through small orifices. Although MISs are performed without direct access to the organ or tissue, the spatial information (position and orientation) inside the human body is usually accessed using endoscope video or medical imaging. The image information are displayed in monitors allowing surgeons to get indirect view of the surgical field.

The development of MISs techniques has been an important advance for the benefit of patients, being useful for the treatment of many conditions. With shorter hospital stays and recovery times, less scarring and pain than conventional surgery, MISs are currently performed in different medical specialties as first-line procedure, such as general surgery (e.g. colon resection, hernia repair, appendectomy), gynecology (e.g. pelvic floor reconstruction, removal of adnexal structures), urology (e.g. nephrectomy, percutaneous nephrolithotomy (PCNL), adrenalectomy), plastic surgery (e.g. breast reconstruction, face lifts), thoracic surgery (e.g. lung biopsy, bronchoscopy) and cardiothoracic surgery (e.g. coronary artery bypass surgery, heart valve replacement, congenital defect surgery) [1-4].

MISs can be used from simple diagnosis, to specialized and complex forms of surgery, such as excisional, ablative or reconstructive.

### 1.1.1 Percutaneous Surgery

Percutaneous surgeries are one of the most common MISs employed in clinical practice. These procedures are commonly used to gain access to an anatomical target such as a blood vessel or a vital organ (e.g. liver, kidney, lung, stomach) though a needle puncturing stage.

Considering the future trends towards minimal incisions, percutaneous access may be one of the few ways to quickly create a path between skin surface and any anatomical organ, in order to diagnose, treat and manipulate it through millimetric incisions (Figure 1.1) [5].

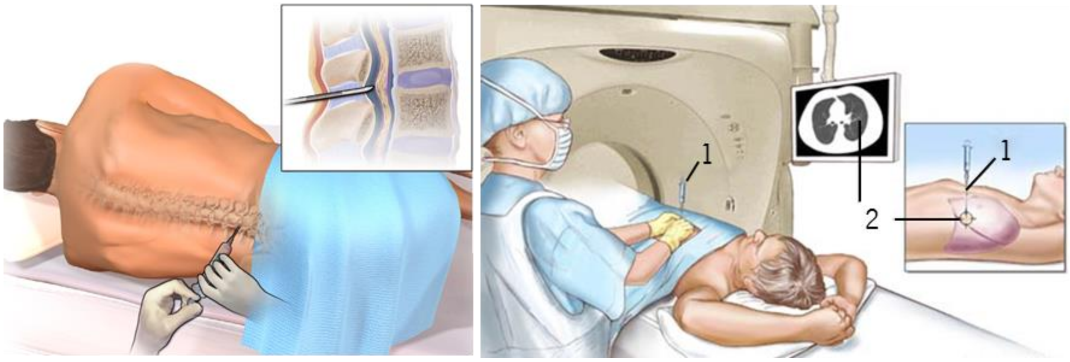

Figure 1.1. Examples of percutaneous procedures: (left) percutaneous puncture for epidural anesthesia; (right) percutaneous puncture of a long tumor (2) using a biopsy needle (1) [6].

When inserting the needle, the target might be in a millimeter neighborhood of another vital organ or nerve. Extra caution is necessary to avoid any damage or disease spread, which can compromise the surgical outcome. Some of the key and well known issues that contribute for needle misplacement are related to human errors (related to poor techniques and insufficient physician skills), target visibility, target access, tool maneuverability, needle deflections and target or tissues movements [7-11].

The main challenge during percutaneous access is to select and plan the appropriate puncture site and needle orientation so that, upon insertion, the needle tip follows the desired trajectory and hits the target. Although there is not a defined tolerance for the desired accuracy in clinical practice, in general, insertions with lesser needle misplacements result in more effective treatment or better diagnosis.

The desired performance depends on the anatomical organ to be treated, anatomic target location, shape and size [8, 12-14]. It can ranges from micro-millimeters accuracy (e.g. brain, fetus, eye and ear procedures) to some millimeters (e.g. kidney, liver and lung biopsies) [15].

Although most of percutaneous approaches share common features, due to the wide range of applications, they differ in the surgical workflow and technological requirements, influencing the needle length and diameter, medical imaging armamentarium, surgical tools instrumentation, patient position, among others [16-18].

Therefore, the development of new technological surgical systems must be specified, developed and tested for each case, existing the need of focusing in one surgical procedure. Consequently, this thesis uses the percutaneous renal access (PRA) as the chosen one, because (1) it is daily performed to treat and diagnose several renal diseases; (2) shares common problems with other percutaneous procedures; (3) is performed near several vital organs; (4) plays a key role in the surgical outcome; and finally (5) remains the most challenging task for surgeons in different minimally-invasive kidney interventions. Nephrolithiasis was selected as the targeted kidney disorder where PRA is used due to its significant worldwide source of morbidity [19-21].

## 1.2 Nephrolithiasis

Nephrolithiasis or kidney stone disease is a common urological disease that affects 10-15% of the developed world population [19-21]. The worldwide prevalence of kidney stones has increased last years as a result of bad eating habits, having a male predominance (80%) and a subsequent clinical relapse rate of approximately 50% over a 10-year and 75% over 20-year period [22, 23]. The number of deaths due to kidney stones is estimated at 19,000 per year being fairly consistent between 1990 and 2010 [23].

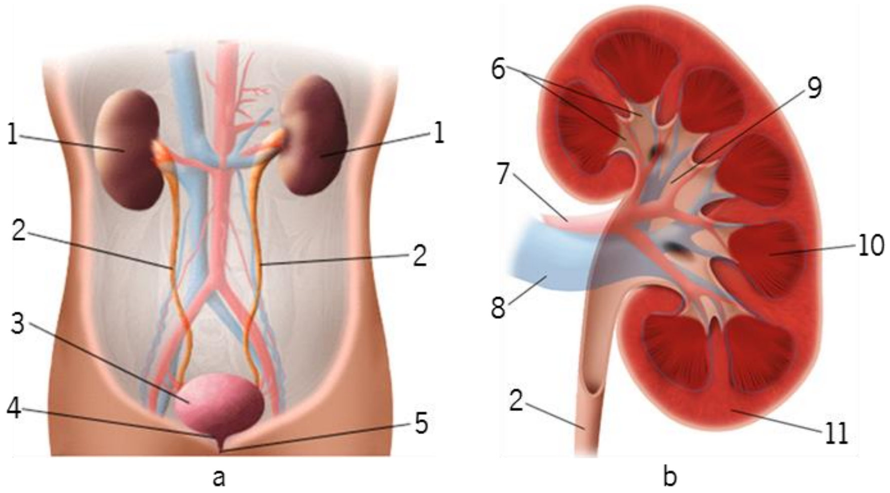

Figure 1.2. (a) Front view of the urinary tract [24]: 1 – kidney, 2 – ureter, 3 – bladder, 4 – sphincter, 5 – urethra. (b) Anatomy of the kidney [25]: 6 – kidney calyces, 7 – renal artery, 8 – renal vein, 9 – renal pelvis, 10 – medulla, 11 – cortex.

### 1.2.1 Urinary Kidney Stones

The urinary tract is the body's drainage system and it is responsible for removing wastes and extra water from the blood (Figure 1.2). The urinary tract (Figure 1.2-a), composed by two kidneys, two ureters, a bladder and a urethra, plays one important function in maintaining the electrolyte balance of the human body. The urine flows from the kidneys to the bladder through tubes called ureters. The bladder stores the urine until releasing it by the urethra through urination.

In some cases, some substances and minerals may stay behind and joins with other waste products, causing kidney stones in unhealthy people.

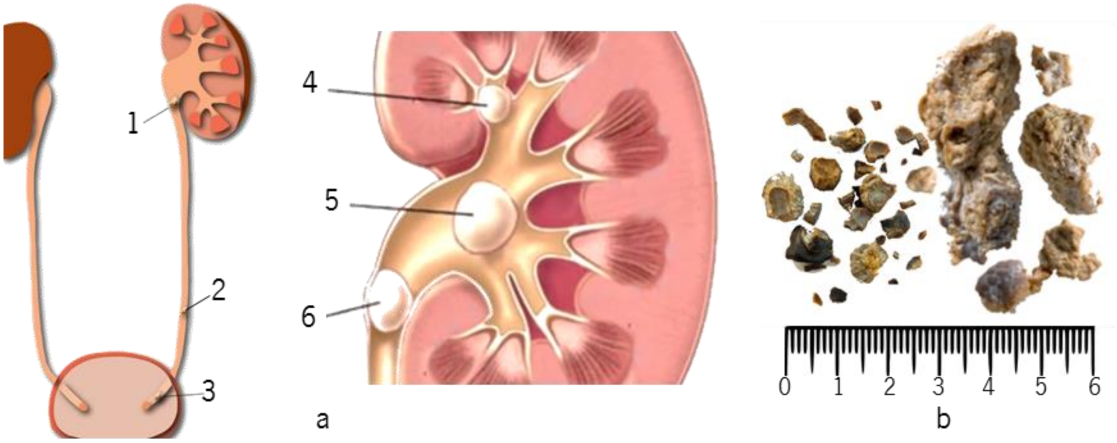

Figure 1.3. (a) Kidney stones ledged at different places: (1) junction between renal pelvis and ureter, (2) crossing of ureter over iliac blood vessels, (3) entrance of ureter into bladder, (4) kidney calyx, (5) renal pelvic and (6) upper ureter. (b) Example of different sizes of kidney stones (adapted from [26]).

Kidney stones can form anywhere in the urinary tract from the kidneys down to the ureters and bladder (Figure 1.3). The stone location is commonly used to classify the disease as Nephrolithiasis, Ureterolithiasis, Cystolithiasis when placed inside the kidney, ureter and bladder, respectively.

### 1.2.2 Surgical Treatments

Although up to 98% of small stones (less than 5 mm) may pass spontaneously through urination, for larger stones (5 to 10 mm) the rate of spontaneous passage decreases to less than 53% [27]. Initial stone location also influences the likelihood of spontaneous stone passage. Rates increase from 48% for stones located in the proximal ureter to 79% for stones located at the vesicoureteric junction, regardless of stone size [27]. For moderate symptoms with no high-grade obstruction or associated urinary tract infection, non-surgical procedures are usually performed for pain control [28, 29].

More severe cases require surgical intervention. The choice of the surgical treatment generally depends on the stone size, composition and location, presence of distal urinary obstruction and anatomic variations of the urinary system.

### A. Open Surgery

Open surgery involves the creation of an incision to gain direct access to the ureter and the kidney. This kind of surgery is very invasive, produces large scars with bad aesthetic results and increases hospitalization and recovery time.

With the advent of new technologies, the demand for open surgery to remove kidney stones has been drastically reduced, being only recommended for extremely large stones or an abnormal anatomy. Hereupon, this kind of procedure has been replaced by non-invasive or MIS, such as extracorporeal shock wave lithotripsy (ESWL), ureterenoscopy and PCNL.

### B. Extracorporeal Shock Wave Lithotripsy

As an alternative to open surgery, ESWL is a non-invasive strategy to fragment kidney stones. After localizing the stones through medical imaging, a lithotripter machine creates high-intensity pulses of ultrasonic energy to fragment all the stones with the patient under local or general anesthesia. The idea is to break down the stones into small particles, allowing its elimination through urination [30, 31] (Figure 1.4).

The performance of the ESWL procedure is influenced, at least, from the stone chemical composition, presence of anomalous renal anatomy, stone distance from the skin surface, stone location inside the kidney, presence of hydronephrosis and body mass index [32, 33].

Common adverse effects of ESWL include trauma, kidney or ureter obstruction, damage to blood vessels of the kidney, acute kidney injury, internal bleeding and subcapsular hematomas, pain and discomfort [34].

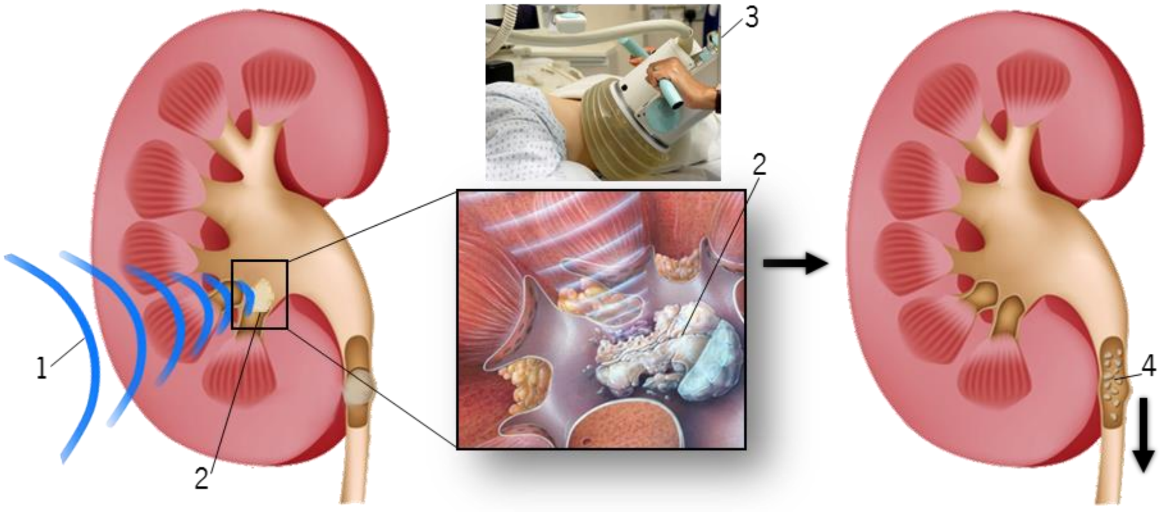

Figure 1.4. Representation of some stages of the ESWL procedure: (1) shock waves moving towards a (2) kidney stone. These waves are produced by an extracorporeal wave generator (3). After fragmented, the stones are eliminated from the kidney through urination (adapted from [35]).

### C. Ureteroscopy

With the development of flexible and rigid fiberoptic ureteroscopes, ureteroscopies have become increasingly popular in the diagnosis and treatment of disorders such as kidney stones [17].

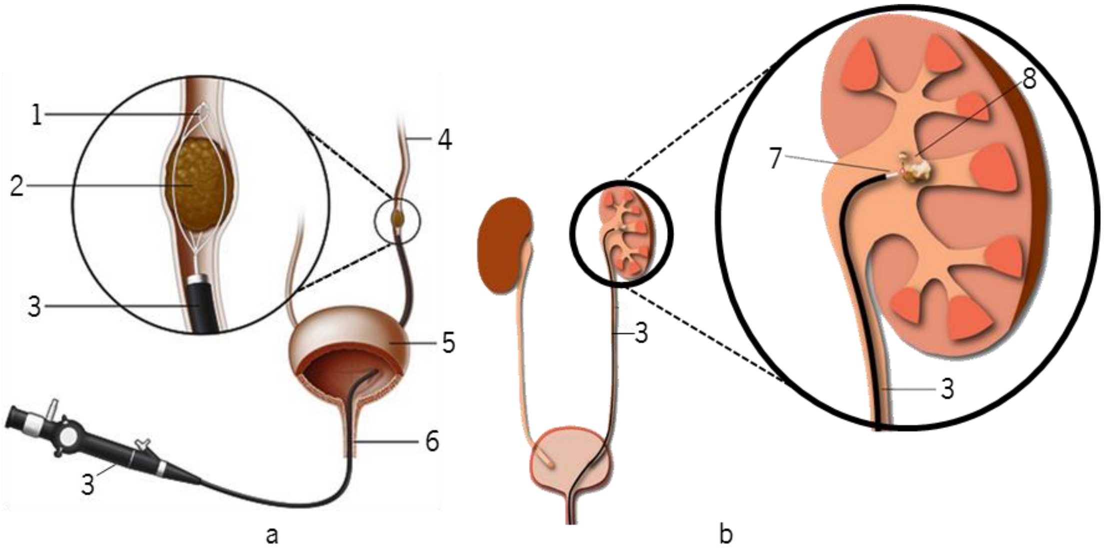

Figure 1.5. (a) Ureter ureteroscopy: 1 – basket removing ureteral stone (2); 3 – ureteroscope 4 – ureter; 5 – bladder; 6 – urethra; (b) Kidney ureteroscopy: 7 – laser fiber; 8 – stone being fragmented by laser lithotripsy (adapted from [36]).

Flexible ureteroscopes are employed in treatment of stones localized in the upper ureter (Figure 1.5-a), renal pelvis and calyces (Figure 1.5-b). Smaller stones, in the bladder or lower ureter, can be removed in one piece, while the bigger ones are usually broken before removal [37]. This procedure involves passing an ureteroscope (2.5 - 3 mm diameter) through the urethra into the bladder and finally moved up into the ureter where the stone is located (Figure 1.5).

The ureteroscope enables the urologist to directly visualize the stone (Figure 1.6-a) and to remove it using a specialized stone basket (see 3 in Figure 1.6-c). Larger stones are firstly fragmented into smaller pieces (~1 mm) using a laser, a US device or a pneumatic lithotripter (Figure 1.6-b).

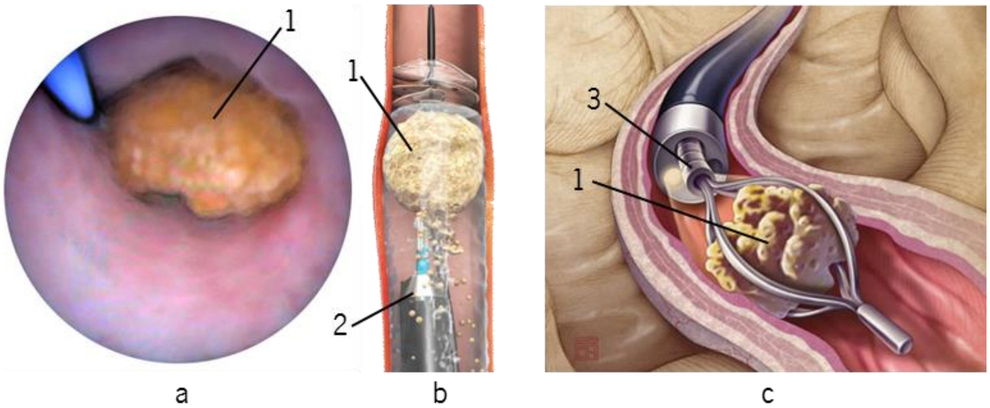

Figure 1.6. (a) Ureteroscope video image displaying a stone (1); (b) Stone being fragmented using a pneumatic lithotripter (2); (c) Stone being pushed out using a stone basket (3) (adapted from [38]).

A ureteral stent may be placed in the ureter to provide immediate relief of an obstructed kidney, allowing the urine to flow past an obstruction in the ureter. Stent placement can be useful to avoid acute renal failure, due to the increased hydrostatic pressure and infection caused by an obstructing stone. The presence of indwelling ureteral stents may cause minimal to moderate discomfort, incontinence and infection, which are general resolved on cystoscopically removal [37].

Ureteroscopic techniques are generally more effective than ESWL for treating stones located in the lower ureter, with higher success and clearance rates (between 93 and 100%) [39].

### D. Percutaneous Nephrolithotomy

PCNL is another surgical procedure to remove stones from the urinary tract. It comprises three main surgical stages [40, 41]. With the patient under general anesthesia and supine position, in the first stage, a catheter is inserted through the urethra towards the renal stone. This step is used to perform a retrograde pyelogram study (Figure 1.7-a). At this point, a radiopaque contrast dye is injected through the catheter, improving and facilitating the visualization (e.g. using a real-time fluoroscope C-Arm) of the kidney stone location, shape and size. Usually the catheter is guided using pre-operative image data from CT (Computed Tomography) and direct video from an ureterorenoscope.

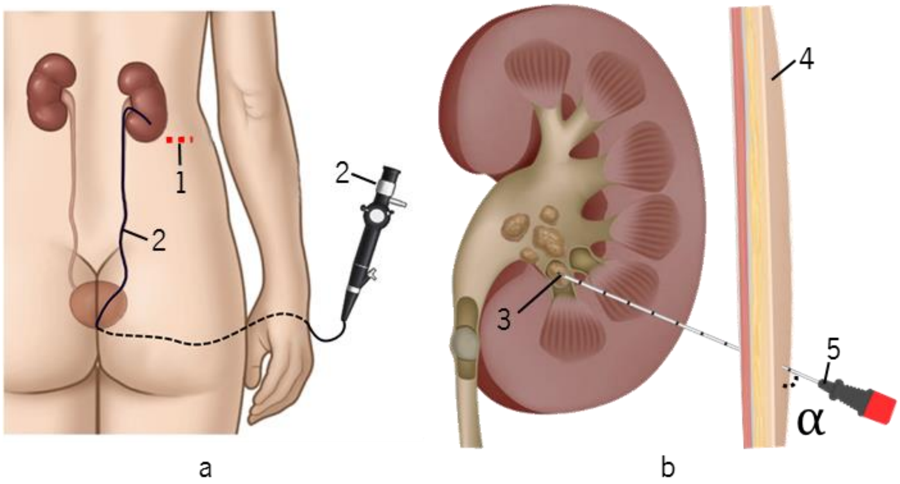

Figure 1.7. Representation of the first two surgical stages of PCNL: (a) Insertion of a ureteral catheter: 1 – skin puncture site, 2 – ureterenoscope; (b) Puncture of the kidney: 3 – kidney stone, 4 – skin, 5 – surgical needle, and α is the angle between the needle and skin (adapted from [35]).

According to the stone location, the patient is usually re-placed in prone position to perform the second surgical stage, which consists in the PRA. At this point, a surgical needle with about 150 mm length and 18 G of diameter is inserted from the skin surface (puncture site) towards the renal calyx where the stone is located (Figure 1.7-b). Nowadays, this stage is only performed by specialized urologists, because the surgery efficacy and success are highly dependent on the precision and accuracy that the needle reaches the stone. The position of the needle, that defines a percutaneous route from where the stones will be removed, is normally confirmed by fluoroscopy imaging at the end of the second surgical stage.

Finally, at the third surgical stage (Figure 1.8), a guide wire is passed through the needle into the kidney pelvis. Once the guide wire is in position, the needle is withdrawn and a 1 – 2 cm skin incision is made to insert a dilator over the guide wire down to the stone. Different surgical dilators are then used to create a tunnel (~ 1 cm diameter) directly into the kidney (see 4 in Figure 1.8-b). An operating nephroscope (1 in Figure 1.8-a) and forceps are then passed through the tube into the kidney. Small stones can be removed with a grasper, while larger ones need to be broken up using ultrasound (US) waves, laser or electrohydraulic probes before they can be removed [20, 42]. Once the stone removal is complete, a small tube may be left in the kidney for a few days, through the accessible tract, to allow the drain of urine.

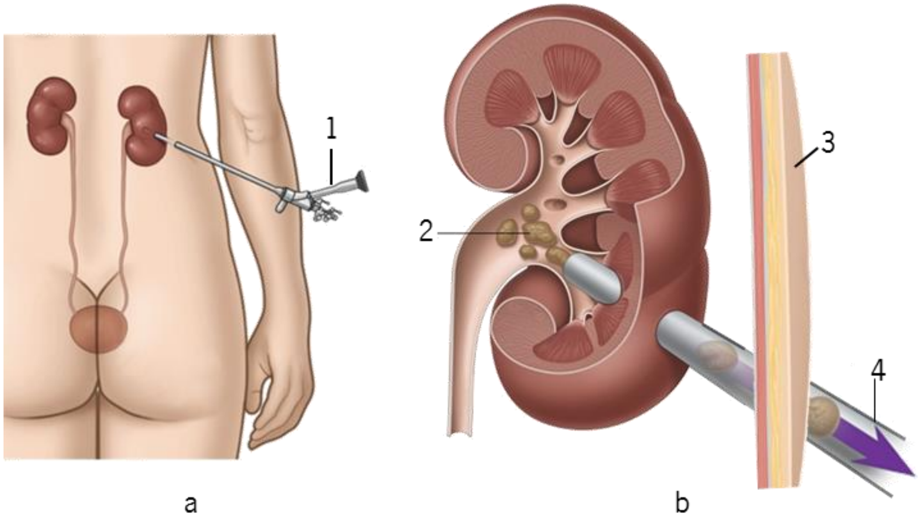

Figure 1.8. Disintegration and removal of renal calculi: 1 – nephroscope, 2 – kidney stone, 3 – skin, 4 – stones being removed by the PRA path created between the skin surface and the kidney calyx (adapted from [36]).

This technique has higher success rates, for clearing all stones in one setting, than other techniques such as ESWL. Depending on the location and number of stones, surgery can take from 1 to 4 hours and 3 – 4 hospitalization days of recovery. Common complications include tissue or organ injury (bowel, vascular structures, spleen, liver, lung, pancreas and gallbladder), loss of kidney function, bleeding, infection, conversion to open surgery due to difficulties encountered during the procedure and death in very rare cases [43-47].

## 1.3 Motivation

Due to their non-invasiveness, ESWL and ureteroscopy were rapidly and widely accepted as treatment alternatives for renal and ureteral stones when the stone diameter is less than 10 mm. Although 80% of small renal stones can be effectively treated with these two surgical procedures, they sometimes fail and are also not recommended for larger ones [21, 48].

In fact, ESWL does not always promote the total stone fragmentation, is not recommended for pregnant women, elderly people, patients with urinary tract infections and anatomic variations. When compared to ESWL, ureteroscopy has lower treatment costs and is the first choice in pregnant and morbidly obese people as well as those with bleeding disorders. However, it is a cumbersome and time consuming task for large stones [21, 49-51].

Considering the disadvantages of the two previous methods, PCNL is the first-line and established surgical procedure to treat kidney stones regardless the calculi location, size, shape, for staghorn calculi, large lower pole stones and also in cases of ectopic or malformed kidneys. PCNL also complements ESWL or ureteroscopy procedures when the kidney stones are not completely fragmented or removed [20, 42, 52].

As a MIS, PCNL presents some limitations and surgical complications that are primarily connected with the second surgical stage. In fact, PRA remains the most challenging task for surgeons, being difficult to plan and to perform.

The ideal PRA is one that allows a precise assessment for the kidney target site while minimizing bleeding. Although the risks for this percutaneous step are less than with open surgery, inaccurate and multiple needle punctures often cause complications, such as injuries in the kidney or contiguous organs, and eventually decreases the overall surgical success.

Due to its difficulties, PRA procedures are always guided with medical imaging (commonly fluoroscopy). Despite its advantages, this technique is intrinsically 2D (two-dimensional), presents little soft tissue contrasts and requires continuous radiation exposure. The radiation on the surgical theater is a major risk to the medical team, as they are continually exposed over their daily activities. Thus, removing radiation-based imaging techniques will have a direct impact in dose exposure on both patients and physicians.

In addition, known limits are related to MISs such as the restricted vision of the anatomical target; the difficulty in handling and moving the surgical instruments inside the human body; the need of dexterity to hand-eye coordination; highly dependent on the surgeon expertise; target movements due to tissue deformation and some deflections on the surgical instruments; and inadequate surgical instruments. Other problems, include the localization of the needle tip, resulting in a long procedure and increasing the risk of complications.

Considering that each year, millions of PRA interventions are performed worldwide, the development of an innovative solution to reduce current limitations can lead to a significant improvement in patient care and simplification of the surgical procedure. In addition, the development of such solution may be explored in the future for other medical interventions with similar surgical workflow.

## 1.4 Goals

The overall goal of this thesis is to develop a new hardware/software framework to aid the percutaneous kidney puncture. This system should be able to easily and safely guide the PRA, guaranteeing that any organ is accidentally perforated and responding to current surgeon's demands. This new framework should also optimize the puncture planning increasing the certainty of reaching a specific target inside the kidney.

This main goal can be refined into a set of three specific phases:

**Phase 1:** Motion tracking of the surgical tools – Intends to assess the applicability of real-time motion tracking sensors (electromagnetic motion tracking (EMT) or optic motion tracking (OMT) technology) to monitoring the position and orientation of the needle and catheter during PRA. This phase aims to create a virtual environment where the information retrieved by motion tracking sensors is used to guide the surgeon during whole puncture stage. To this extent, a software framework, that automatically performs multi abdominal organ segmentation from CT data sets, was tested for surgical puncture planning (Chapter 3) and guidance when combined with an OMT system (Chapter 4). Additionally, an EMT imageless framework was tested for puncture planning and guidance itself (Chapter 4 and 5). This second test aimed to eliminate the need of X-Ray based imaging and other imaging modalities. For both tracking methodologies, one study the compatibility with current surgical setups, instruments and imaging systems.

**Phase 2:** User guide interface – Investigates different ways to provide user feedback about the spatial relationship between the surgical tools. The outcome is a simple and intuitive interface, capable of guiding the surgeon throughout the entire renal access stage, namely puncture planning and needle insertion (Chapter 5).

**Phase 3:** Security assessment – Aims to study, identify and develop a framework to alert the surgeon when exists the risk of organ perforation (Chapter 6).

Since the need of PRA has increased in recent years, the improvement in patient care and simplification of this surgical step, through the proposed phases, may lead to several advantages:

- Broad the PRA procedure to surgeons less specialized and familiarized with MISs due to an intuitive and efficient platform. Today, due to its high learning curve, only 10% of specialized urologist perform this procedure;
- Eliminate X-ray imaging during PRA, which significantly decreases patient radiation exposure, especially for the surgeon who performs this intervention more than once a day;
- Improve preoperative planning through the availability of accurate and complete tracking of the surgical tools;
- Reduce surgery time, because one of the most time-consuming steps may be shortened through an easier puncture
- Minimize potential surgical complications caused by human errors, image misinterpretation and hand/eye coordination limitations;
- Decrease errors related to target movements and tissue deformations, by permanently monitored them during PRA;
- Reduce surgery costs.

## 1.5 Contributions

An overview of the particular ways in which the state of the art regarding PRA is improved by this thesis can be summarized according to the following points (with respect to all phases described above (Sub-Chapter 1.4):

a) A critical review that addresses the methodologies and techniques for conducting kidney targeting and the puncture step during PCNL;

b) A real-time navigation system to plan and guide PRA based on an OMT technology. It allows the surgeon to establish the desired puncture site by superimposing a needle virtual tool and a virtual puncture trajectory in a preoperative 3D (three-dimensional) image data (**Phase 1**);

c) A new real-time navigation system, based in EMT, to plan and guide PRA. It shows virtual surgical tools (needle and catheter) in 3D or 2D, according to the 3D spatial information provided by EMT sensors coupled in their tips. This framework aids the surgeon to navigate a tracked needle towards a catheter placed near the anatomical target (**Phase 1**);

d) 3D sound interface capable of providing spatialized sounds from different point sources surrounding the user. These sounds are defined and positioned in a 3D space according to the current orientation error, that is calculated as the spatial difference between the needle tip and the puncture trajectory that the surgeon must follow (**Phase 2**);

e) Vibration device capable of providing spatialized vibration feedback using different vibration motors. These motors positioned and coupled to an elastic headband according to the eight cardinal points. Each motor generates a vibration pattern that depends on the spatial difference between the needle tip and the puncture trajectory that the surgeon must follow (**Phase 2**);

f) A new image based methodology that reconstructs a 3D US volume around the puncture trajectory path, for security assessment before the needle insertion (**Phase 3** – see attachment 2);

g) Two new US probes with a needle working channel: one based on a single and circular piezoelectric ceramic; another based on an array of piezoelectric ceramics around the working channel. The signals provided by each transducer are processed in order to generate alerts when some changes occur during needle insertion, in terms of anatomical structures in between the puncture path (**Phase 3**);

In regard to publications, this work has generated 5 papers (2 journal papers, 3 conference papers and 2 awards in medical conferences) and 1 provisional patent.

- [53] – Rodrigues, Pedro L., Et al. "*Kidney targeting and puncturing during percutaneous nephrolithotomy: recent advances and future perspectives*". Journal of Endourology 27.7 (2013): 826-834.
- [54] – Rodrigues, Pedro L., Et al. "*Collecting system percutaneous access using real-time tracking sensors: first pig model in vivo experience*". The Journal of urology 190.5 (2013): 1932-1937.

- [55] – Rodrigues, Pedro L., Et al. "*Preliminary clinical trial in percutaneous nephrolithotomy using a real-time navigation system for percutaneous kidney access.*" SPIE Medical Imaging. International Society for Optics and Photonics, pp. 903606-903606-7, 2014.
- [56] – Rodrigues, Pedro L., Et al. "*Validation of percutaneous puncture trajectory during renal access using 4D ultrasound reconstruction*". SPIE Medical Imaging. International Society for Optics and Photonics, pp. 94152D-94152D, 2015.
- [57] – Rodrigues, Pedro L., Et al. "*A-scan ultrasound system for real-time puncture safety assessment during percutaneous nephrolithotomy.*" SPIE Medical Imaging. International Society for Optics and Photonics, pp. 94190T-94190T, 2015.
- [58] – Rodrigues, Pedro L., Et al. "*Confirmação da eficácia da punção renal e ureteral em modelo experimental com a utilização de um sistema de localização eletromagnética*", Portuguese Symposium of Urology, 2013 (1st price award).
- [59] – Rodrigues, Pedro L., Et al. "*Experiência inicial em humanos de um novo aparelho para ajuda na punção de um cálice renal na Nefrolitotomia percutânea*". Portuguese Symposium of Urology, 2012 (1st price award).
- Rodrigues, Pedro L., Et al. *"A radiation free guidance system for percutaneous renal access in minimally invasive interventions"*. Provisional Patent.

We are currently compiling two new papers entitled:

- Rodrigues, Pedro L., Et al. *"Ultrasound probe with a needle working channel for safe guidance of percutaneous procedures"*.
- Rodrigues, Pedro L., Et al. *"How to turn the kidney access in the percutaneous surgery the easiest step: novel 3D audiovisual assisted navigation"*.

## 1.6 Structure and Methodology

This thesis is organized into the following chapters:

**Chapter I:** Introduction: This chapter provides an overall outline of this thesis describing the surgical treatment of kidney stones, as well as the motivation behind this thesis, main research objectives, work contributions and remaining thesis organization.

**Chapter II:** Percutaneous Renal Access: This chapter reviews the most relevant contributions in the field of urology and minimally invasive surgery to improve the PRA stage. It focus on the following topics: medical imaging guidance, new surgical tools, motion tracking systems, robotics, image processing and computer graphics.

**Chapter III:** KidneyNav framework: This chapter investigates a software application based in image processing techniques to facilitate planning and puncture in a pre-operative stage.

**Chapter IV:** Motion Tracking Systems: This chapter explores, tests and evaluates EMT and OMT technologies to plan and guide PRA in several tests performed *in vitro*, *in vivo* and in a clinical trial.

**Chapter V:** Multi-Sensorial Interface: This chapter presents an intuitive puncture guidance interface based in a sight view, 3D audio and vibrotactile feedback.

**Chapter VI:** PRA Security assessment: This chapter tests and validates a new design of US probes with a needle working channel.

**Chapter VII:** Conclusions and future work: This chapter provides final thesis remarks in regards with the main objectives. Different research paths are also suggested so that the developed methods can be improved in the future.

# 2

# Percutaneous Renal Access

The main objective of this chapter is twofold: first, present the state of the art in terms of methodologies and techniques for conducting PRA during PCNL; second, provide future research paths for the PCNL procedure improvement. This chapter is based on the work published by the authors in the Journal of Endourology [53].

## Contents

## 2.1 Introduction

Recent technological advances have replaced the need for open surgery with less invasive procedures, such as PCNL, ESWL and ureterenoscopies [21, 60]. The surgical approach to be performed usually depends on the size, composition and location of the renal calculi, the presence of distal urinary obstructions and anatomic variations of the urinary system.

Being very well known the limitations of the ESWL with respect to large and complex stones, PCNL became accepted as the treatment of choice for large and staghorn renal stones [20, 42, 52].

When compared to open surgeries, PCNL is a MIS with many associated benefits, such as producing small patient incisions in the abdominal area, reducing hospitalization time and improving postoperative recovery [1]. Though complications may still exist [42].

The success and treatment outcomes are highly dependent on the precision and accuracy of the puncture stage (since the needle must precisely reach the stone with a direct path), making this step the most challenging task for surgeons [14, 44, 52, 61]. The ideal renal access is one that allows a complete removal of the calculi while minimizing bleeding. Inaccurate needle punctures often cause complications, such as injuries in the kidney and contiguous organs, and eventually prejudice the overall surgical success [14].

Since PCNL first description, nearly four decades ago, remarkable advances have been proposed in the field of urology, engineering and MISs in what concerns of all surgical stages. Multiple research paths have been followed to try to minimize some limitations such as anatomic target restricted vision, difficulty in handling the surgical instruments, restrictive mobility inside the human body, high dexterity levels of surgeon's hand-eye coordination, needle deflections, moving anatomic target, and anatomical structures deformations and movements [9, 52].

In what concerns to PRA in particular, various techniques have been used to perform a secure and accurate puncture. The most relevant contributions have been provided by the application of medical imaging techniques [1, 10, 14, 62]. Aside from medical imaging, robotic systems and medical instrumentation [1, 18, 63], navigation systems [64], finite element models [8, 65], computer graphics and image processing [1], have been proposed in recent years. However, its current clinical practice is still very limited [66].

## 2.2 Methods

Every year, several scientific papers reporting new advances for PRA are published in the literature. This state of the art was performed by analyzing all articles written in English and published in peer-reviewed journals or conference proceedings reporting qualitative data concerning kidney targeting and puncturing from 2007 to December 2015. No further constraints were considered. A systematic literature search was performed considering available reports at Medline/PubMed, ISI Web of Science and Scopus databases.

Searches were performed using the combination of one or more of the following keywords: *percutaneous nephrolithotomy*, *puncture*, *navigation systems*, *robotic surgery*, *medical imaging*, *percutaneous* and *renal access*. Manual search on the reference lists of the included papers were also considered.

3352 titles were analyzed whether the paper was potentially relevant to the review topic. 825 abstracts and 641 full-text articles were assessed and discussed. 65 final papers were included in this thesis as the main contributions to kidney targeting and puncturing during PCNL.

For the purpose of this state of the art, one discusses the main benefits and limitations for kidney targeting and PCNL conduction for the following research paths: medical imaging, surgical procedural modifications, medical instrumentation, robotics and computer aided surgery.

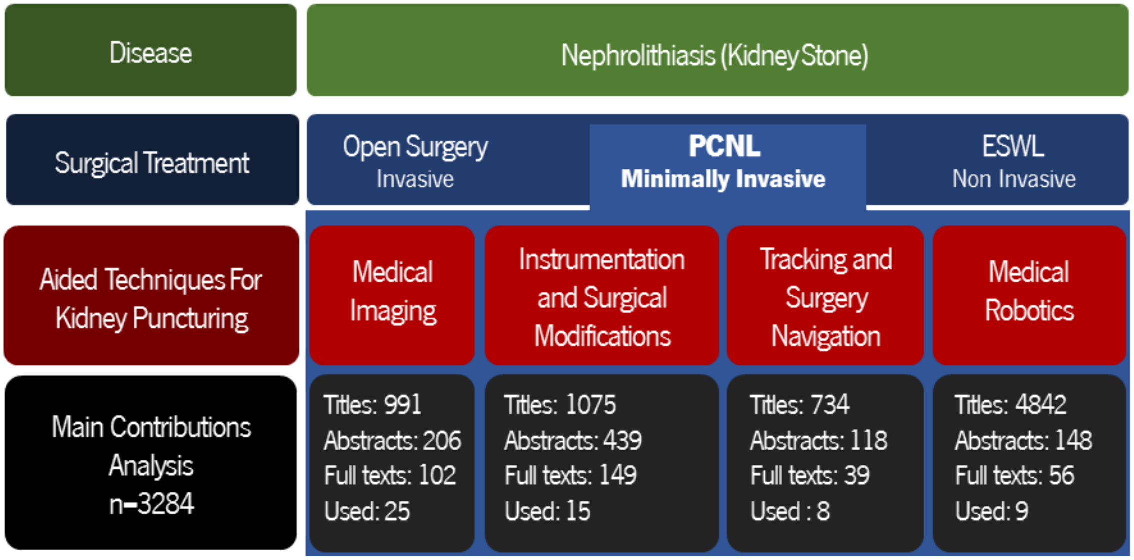

Figure 2.1. Study selection process for the main contribution for PCNL puncture, showing the number of titles, abstracts, and full texts analyzed for each technique for kidney puncture.

## 2.3 State of the Art

Inaccurate punctures during PCNL can cause damage in the kidneys and their surrounding tissues and organs [14, 42]. The learning curve for PRA is estimated to be around 60 cases, a situation that increases the complication rates during the long surgeons training period [44, 47].

Although the kidney is normally at a depth of 5-10 cm, the needle trajectory cannot be changed once the needle is inserted to a depth greater than 2 cm [9, 67]. If the needle does not hit the target, it has to be removed from the human body and reinserted again, because the final needle position influences the efficiency with which the kidney stones are fragmented and removed, providing the path from the skin periphery to the renal calyx [44, 50, 66, 68]. So, several attempts may be needed to accomplish a correct needle insertion, causing an increase in postoperative complications, poorer surgical outcomes and increased likelihood of surrounding structures perforation.

### 2.3.1 Surgical Complications

Although PCNL is widely performed and has proven to be safe, there are risks and potential complications. Complications during renal access may occur in as many as 4% of procedures [69].

Some studies have been made to classify the PCNL complications with the Clavien classification system (five grade system that provides a straightforward and validated method to classify surgical postoperative complications) [69]. This classification system is defined according to Table 2.1 [69].

A worldwide study with 5803 patients was performed by De la Rosette et al. [70] to assess the PCNL indications, complications and outcomes. The study reports a high success rate and a low major complication rate, showing the effectiveness and safety of the minimally invasive removal of kidney stones. The most frequent complications were bleeding (7.8%), renal pelvis perforation (3.4%), and hydrothorax (1.8%), fever >38.5°C (10.5%) and blood transfusion (5.7%).

In 79.5% of cases there were no complication and in the remaining cases the study presents Clavien grade I (11.1%), II (5.3%), IIIa (2.3%), IIIb (1.3%), IVa (0.3%), IVb (0.2%), or V (0.03%).

Minor complications (Clavien grade I) include urinary tract infections, catheter displacement/occlusion or urinary leakage. In contrast major complications may occur, even when the procedure is performed by experience surgeons or radiologists, including bleeding, infection,

Table 2.1. Definition of the different grades of the Clavien classification system.

| **Grades** | | **Clavien classification system** |
|---|---|---|
| | | **Definition** |
| **Grade I** | | Any deviation from the ideal postoperative course, non-life-threatening and no lasting disability. Does not need any further surgical, endoscopic or radiological intervention. Require only simple therapeutic drugs and do not significantly extend hospital stay. |
| **Grade II** | | Complication potentially life-threatening but without residual disability. Requires complex therapeutic treatment or blood transfusions. |
| **Grade III** | **III-a** | Complications with residual disability, requiring surgical, endoscopic or radiological intervention without the patient being submitted to general anesthesia. |
| | **III-b** | Complications with residual disability, requiring surgical, endoscopic or radiological intervention under general anesthesia. |
| **Grade IV** | **IV-a** | Life-threatening complication with single organ dysfunction |
| | **IV-b** | Life-threatening complication with multi organ dysfunction |
| **Grade V** | | Death of the patient |

tissue and organ injury. In such cases, the conversion to open surgery to remove the stones may be needed [71].

Kidney adjacent organ injuries to the lung, liver, spleen, biliary system, colon, or small bowel have been described. The most common of these complications are pulmonary and colonic, which have been reported to occur in 2.3-3.1% and 0.2-0.8% of the percutaneous procedures, respectively [68].

PCNL has also been safely applied in children with a Clavien classification comparable to those seen in adults [72]. Guven et al. [72] and Ozden et al. [73] evaluated the safety of PCNL in 130 children with mean age of 10.17 years and 94 children with mean age of 9.5 years. They reported the following Clavien classification scores: Clavien grade I (12% versus 7.4%), II (2.8% versus 2%), IIIa (6.4% versus 4.3%) (no grade IV or V were reported in both studies).

### 2.3.2 Optimal Puncture Orientation

The optimal access route always depends on the stone shape and location inside the kidney. To avoid puncture complications, the kidney lower pole and distal part are the most secure and common access route since they decrease the risk of arterial or organ injury [42]. However, a supracostal puncture (above the 12th rib) may be necessary to obtain better access to the lower kidney pole and ureter.

A supracostal puncture increases the probability of thoracic complications to 3-15% (e.g. hydro/pneumothorax), due to the anatomic proximity between the upper pole of the kidney and the pleura and lung [74]. On the other hand, punctures below the 12th rib are linked with hydro/pneumothorax in <0.5% of cases and 10-100% above the 11th rib. Likewise, injuries to the spleen and liver occur more rarely. The probability increases in the presence of abnormal organs or with punctures above the 11th or 10th rib [71].

### 2.3.3 Patient Position

The optimal patient position and the puncture site for accessing the collecting system remains a controversial issue. The safety and efficacy of different surgical positions, mainly prone and supine ones, have lately been compared in several studies [75-80]. Usually, the patient starts the surgery in supine position to perform a retrograde study and is subsequently repositioned in a prone position for the remaining phases. However, since patient reposition increases surgery time in about 30-40 minutes, some practitioners opt to perform the entire surgery with the patient in supine position [80, 81].

Prone position in PCNL is frequently associated with patient discomfort, especially for those with severe musculoskeletal deformities, cardiovascular and respiratory problems [44]. Despite its shortcomings, prone position facilitates the puncture stage by avoiding abdominal visceral injuries and allowing posterior access to the collecting system, with no limits for instrumental excursion and multiple accesses.

Although the supine position has been described as more attractive, and associated with improved levels of comfort for both patient and surgeon, it is limited for upper-pole calyceal puncture, due to its medial, posterior and concealed position in the rib cage. It is also commonly associated to technical difficulties related to the surgeon's manipulations, which are related to the longer access tract and more limited access field. The use of a virtual trajectory to guide the surgeon in a 3D environment throughout the puncture path, may increase the viability of carrying out the whole surgery with the patient in supine position.

### 2.3.4 Surgical Tools Instrumentation

New surgical needles have been reported in order to facilitate PRA procedures. Yan *et al.* [82] developed a needle with piezoelectric crystals, allowing needle bending along particular orientations for compensation of needle deflections. This study evaluated different factors such as the input tension and piezoelectric crystals length and thickness to produce particular deflections.

Hernandez [83] modified a PRA surgical needle to integrate a bio-impedance sensor at its tip to continuously measures electrical impedance. This needle was tested 16 times in 4 *ex vivo* porcine kidneys to confirm when the collecting system is reached. A characteristic sharp drop in resistivity was noted from 1.9 to 1.1 ohms when the needle tip entered a kidney calyx. However, this *ex vivo* porcine model is limited in different ways, namely by the absence of blood flow, respiratory motion, physiological processes (e.g. higher distension pressures) and the urine was substituted by a normal saline solution which presents different mineral concentration that may vary the measured impedance values. Therefore, although these impedance needles may provide great assistance in MISs, they still require further *in vivo* testing.

Other needles integrate EMT sensors that provide real-time information of position and orientation of 5 degrees of freedom (DOF) with millimetric precision [64]. These are related to navigation systems, e.g. the EMT Aurora system [84], and are capable of being sterilized and used at medical level.

### 2.3.5 Needle Insertion Simulation

Besides the instrumentation of surgical needles with different miniaturized sensors and actuators, mathematical models have also been reported to aid the puncture stage [15]. Commonly, these require prior quantification of different elements such as biomechanical properties of tissues, material and geometry of the needle and insertion properties such as speed, strength and orientation [8, 85].

Studies have shown that the needle diameter, perforation depth, frictional forces between the needle and tissue, needle tip shape, mechanical properties of the tissue, insertion force and insertion speed are the most leading causes of needle deflections [8, 65, 86]. Consequently, the needle insertion point and orientation in the skin periphery are crucial to successfully intercept the puncture target.

Additionally, different physical phenomena occur during puncture, such as cutting/fracture, sliding, friction, stick-slip friction, tissue deformation, tissue displacement and peeling. These may influence the penetration forces and needle bending [86, 87].

Abolhassani [88] tests the influence of needle rotation during puncture in two-layer phantoms of turkey tissue with its skin intact. The needle was inserted in the following cases: no rotational motion; continuous rotation (motion in one direction); rotation with force control in the X and Y direction (keeping them as close to zero as possible); and partial rotation (90°, 30° and 10° rotational motion in each direction about its nominal (zero) position). The author concluded that inserting the needle with partial axial rotations can reduce frictional forces as well as tissue damage and indentation. In contrast, continuous rotation can make the needle insertion easier, but it causes more tissue damage and deformation when the needle is not perfectly straight.

Modelling the interaction between surgical tools and deformable tissues has been a topic of significant interest in recent years. Hing *et al.* [65] described a finite element model to simulate needle insertion and removal in soft tissues, at speeds of 1.016 mm/s, 12.7 mms/s and 24.4 mm/s. He found that the smaller the insertion speed, the smaller was the force exerted on the needle tip and the deformation of soft tissues. Okamura [86] characterized the effects of needle diameter and tip type to the insertion force, when inserting the needle in a silicone rubber phantom. The authors concluded that a bevel tip causes more needle bending and is more easily affected by tissue density variations when compared to a triangle and diamond tips. Likewise, other study reported that the cutting and friction forces increases with an increase of the needle diameter [65].

### 2.3.6 Image Guidance Puncture

In order to continuously track the needle tip inside the human body and to avoid targeting errors and damage of vital structures, through imprecise planning or puncture, imageless techniques are never used. Although medical imaging can provide further information for diagnostic and pre-operative planning, it may also presents some limitations.

Table 2.2. Summary of image-guided puncture characteristics for PCNL puncture guidance.

| **Imagiology Technique** | | **PCNL Image-Guided Puncture** | | |
|---|---|---|---|---|
| | | Advantages | Disadvantages | Main Usage |
| **X-Ray Based Imaging** (uses radiation exposure for real-time image acquisition) | CT | - 3D reconstruction<br>- Real time | - High cost<br>- Needs large spaces to be used intraoperatively that may restrict surgeon's movements | Preoperative planning |
| | C-Arm | - Most common technique for puncture conduction<br>- Real-time images<br>- Compact and portable | - 2D images only | Intra-operative |
| | IVU | - Clear visualization of anomalies<br>- Low cost | - Needs a radiopaque dye<br>- 2D images only | Preoperative planning |
| **Without X-Ray** | Magnetic Resonance (MR) | - High contrast and resolution images in orthogonal and non-orthogonal planes | - High cost<br>- Needs large spaces to be used intraoperatively that may restrict surgeon's movements<br>- Needs non-ferromagnetic surgical instruments | Preoperative planning |
| | US 2D | - Versatile method of conducting surgical needles in percutaneous procedures<br>- Real-time images<br>- Reduced cost | - Low quality images<br>- 2D images only<br>- Image artifacts<br>-User dependence<br>- Difficulties in the identification of small calculus | Intra-operative |
| | US 3D | - 3D images<br>- No real-time | - Needs experienced technicians<br>- Difficulties in the identification of small calculus | Preoperative planning |
| | Endoscopic Imaging | - Visualization in real time of adjacent structures | - Only information about the surface of organs | Intra-operative |
| **Multi-modal Imaging** | US & CT<br>US & MR | - Combines the advantages from different imaging modalities | - Needs non-rigid registration to align anatomical structures | Preoperative Planning |

Table 2.2 gives an overview of possible advantages and disadvantages of different imaging modalities for usage in PRA during PCNL.

### A. X-Ray based imaging

Fluoroscopic radiograph is the most common technique for conducting the PRA, allowing the acquisition of real-time 2D images inside the human body, which provides information about the whole anatomy of the urinary system, including kidney stones [20]. Fluoroscopic methods are also often combined with direct endoscopic visualization for the analysis of anatomical structures [14].

The C rotational fluoroscopy (C-Arm) consists of a compact arc-shaped (180°) system, which is inserted under the patient stretcher [14, 61]. This allows the acquisition of real-time images, reporting the location of kidney stones in relation to the whole surrounding anatomy. As a result of the reduced space that this equipment occupies in the surgery room, percutaneous interventions have benefited from this method [14].

Apart from fluoroscopy, CT and IVU (Intravenous Urography) appear as other imaging possibilities [89, 90]. However, both techniques are mainly used as a means of diagnosis and surgical planning, and not PRA guidance itself.

When using a radiopaque dye, IVU imaging provides a clear visualization of anomalies in 2D images of the urinary system. As a result of its low cost and high level definition of the urinary system and kidney stones, this method has even replaced CT for puncture planning [1, 14].

CT still is the method of choice for the diagnosis and preoperative planning of PRA, since it involves a number of advantages over the IVU, namely the detection of renal calculi with a sensitivity and specificity of 97 % and 100%, respectively, identification of renal lesions and blood vessels and 3D visualization of the urinary system [1, 14, 45, 81, 91]. On the other hand CT can also be used with radiopaque contrast dye (angiographic CT) to produce detailed images of blood vessels, ureters, kidney calyces and surrounding tissues [14].

### B. X-Ray free imaging

To reduce X-Ray usage in PCNL, techniques based on US, MR and endoscopic imaging have been successfully reported in several studies [1, 14, 62].

The use of US is being recognized as a safe and effective method of conducting surgical needles in percutaneous procedures, since it enables real-time image acquisition, is versatile and has a reduced cost when compared to other imaging options [92]. As a result of the absence of X-ray exposure, this is often the method of choice in pregnant, children and patients with transplanted organs [1, 14, 40]. However, it is not a substitute for CT since it often fails to detect small anatomical targets, due to the noise available on the image (e.g. ureteral stones). Moreover, the poor image quality, shadow and speckle artifacts and user dependence are some problems that limit US usage for PRA guidance.

In order to reduce some of these US shortcomings, the SonixGPS system [66] has been tested for PRA. This system overlaps the current and predicted needle tip position over the US stream. To this extent, the needle tip integrates an EMT sensor at its tip that retrieves the 3D spatial information. Although this methodology can help the physician to choose a correct puncture path, it remains very limited since it only provides 2D US images, requires much practice and experience, does not identify or tracks the anatomical target and surrounding structures and, finally, the needle tip is not always displayed in the US stream due to limited information about the 3D space in 2D images.

At the level of percutaneous puncture, MR has become clinically important, since it provides 2D or 3D visualization of high resolution and multiplanar images. Furthermore, the MR allows high contrast and construction of images in non-orthogonal oblique planes, which provides a complete view of the total needle length and its spatial relationship relative to the puncture target [14, 62].

Apart from US an MR, that enable surgeons to noninvasively visualize and collect information about internal organs and its associated phenomena, endoscope methods have also gained importance in recent years for establishing a percutaneous path [1, 61].

Recently, Bader *et al.* [10] reported a modified needle with 1.6 mm that integrates a micro-optics of 0.9 and 0.6 mm diameter. This micro-optics integrates light and can be inserted either in the stylet or in the working sheath of the puncture needle. This system was tested for creating a PRA in 15 patients. The authors reported a decrease in tract size, need of medical imaging and morbidity. This optical needle helps the surgeon to avoid adjacent organs during needle insertion and to decrease the time needed to puncture. Desai *et al.* [93] used the above needle to define *microperc* as a modified PCNL procedure. Under US and/or fluoroscopic guidance a selective calyceal puncture is made with the optical needle guidance. The authors reported that the main disadvantage was the long duration time for stone fragmentation, recommending it for small stones with diameters less than 20mm.

The new *microperc* procedure may be compared in terms of clinical outcome with flexible ureteroscopy, which has been recommended as a second-line treatment for calculi with <1 cm, or as the third choice for stones with 1–2 cm [17, 42]. Modern endoscopes with smaller diameters can be easily maneuvered into the intra-renal space from upper to lower kidney poles [21].

### C. Multimodal imaging

Several authors have explored multimodal imaging for PRA, combining the accurate anatomical information of pre-operative images (CT/MR) with the real-time capabilities of interventional imaging (US/fluoroscopy).

In this sense, the rigid registration of intra-operative US images with high-resolution pre-operative CT volumes has been explored. Leroy [94] presented an automatic rigid registration method based on cross-correlation of the image intensity of US and CT images. In order to improve cross-correlation, the CT and US image contours were highlighted using image processing algorithms. Results present a total registration time of 80s and a mean squared error of 5.1mm. More recently, Li [62] has explored the Iterative Closest Points (ICP) registry algorithm to align intraoperative US images and preoperative MR images. Manual selection of pairs of points in both images from the cranial pole, caudal pole and kidney hilum were used, as well as a respiratory gating method to minimize the impact of kidney deformation. US images were only acquired at the same stages of the respiration cycles. The authors reported a mean squared error of 3.53 mm.

Often, the use of statistical metrics, such as mutual information and correlation ratio, allows the estimation of the correspondence of original CT and US intensities. Registry errors of 1.2mm and target distances of 4,7mm have been obtained by Mozer [95]. In this work, the authors use a 3D/3D surface matching rigid registration between CT segmented structures and the 3D US images. Wein [89] presented a fully automatic image-based algorithm for registering 3D freehand US sweeps with CT. They applied a linear correlation non-rigid registration technique to achieve a processing time of 28s and target distance error of 8.1mm.

Nonetheless, all these approaches formalize such fusion as a rigid problem, disregarding deformation of the kidney and its surrounding structures [96-99].

### 2.3.7 Medical Robotics

Over the last decade robotic-assisted surgery has become an increasingly popular approach for treatment of a variety of urologic disorders. Several robots with different levels of specialization, precision and automation have emerged with high potential to improve surgical performance, by providing precise and stable movements and decreasing surgeon dependence [18, 63, 100]. Currently, most of these systems are based on medical imaging information since it is decisive for all PCNL stages.

Only a few of robotic devices may be specialized to a level that allows the improvement of the puncturing step in PCNL.

PAKY-RCM [18], reported by the Johns Hopkins University group (Baltimore, USA), was developed to aid the PCNL puncture step. This robotic arm have 7 DOF that allows the needle positioning in the skin puncturing site and execution of its insertion. Moreover it also quantifies the strength exercised at any time of puncture. The robot acts as a slave since it is fully controlled by the surgeon via a joystick. Experimental tests in humans reported errors of 2 mm and a nonsignificant difference between the procedure performed by PAKY-RCM and the manual procedure (10.4 ± 6.5 *vs*. 15.1 ± 8.8, p = 0.06). Similar to PAKY-RCM, the AcuBot robot adds a bridge support over the table of the imager and a linear pre-positioning stage with 3 DOF [18].

Given the MR advantages over fluoroscopy, especially the absence of ionizing radiation, the same group reported the Johns Hopkin MrBot [18]. It employs a new generation of pneumatic stepper motors using nonmagnetic and dielectric materials. This system, with 6 DOF, has a great potential for PCNL, given its demonstrated precision of 0.72 ± 0.36 mm in *in vitro* assays.

Lately, dozens of research works have been reported concerning the development and testing of US-guided robotic systems [100]. The typical approach resorts to a surgical needle attached to a robotic arm which is driven – automatically or controlled by the surgeon – in a 3D or 2D imaging volume. In the 3D case, the imaging volume results from the acquisition of a 3D US or by overlapping and combining multiple 2D US images. The robotic arms, whose control is automatic, are also represented in the volume imaging using similar navigation systems. Although recent studies do not aim at conducting a surgical needle for PRA, live biopsy procedures have been reported with an accuracy ranging from 2 to 6 mm. Recent studies also present the use of robotic arms to support and compensate gravity during needle insertion. A locator apparatus that stabilizes the needle during the puncture was tested in [9], where the authors achieved a mean puncture time of 225 s for kidney access, which is quite inferior to the average puncture time reported in literature (approx. 12 min) [44, 101]. The robotic arm DLR MIRO with 7 DOF, 10 Kg and 30 N of strength has been introduced by Hagn [102]. Laboratory tests, exploring its surgical suitability, demonstrated its ability for aligning endoscopes, biopsy needles, electrodes and brain stimulation catheters, with millimetric precision.

### 2.3.8 Computer Aided Surgery

The combination of medical imagiology and tracking systems have recently been used for computer-assisted navigation systems. Different works have been proposed in literature, regarding navigation and augmented reality software. Most of them start by emphasizing the target structures of surgery and surrounding tissues in preoperative data, using image segmentation algorithms or computer graphics (direct volume or surface rendering). Then, the image processed data is superimposed and registered onto real time intraoperative video (augmented reality) or static preoperative volume data (navigation software) [103]. The surgical tools are commonly updated using OMT and EMT systems.

Most augmented reality systems are tested in neurosurgery, otolaryngology and orthopedics. In these cases, the target organs are assumed to be rigid [103]. Only a few trials have been applied to urology [104], since the use of augmented reality in abdominal surgery is more challenging due to tissue deformation and respiratory movements.

Mozer [67] described an optical guided system to superimpose US nephrostomy tract onto fluoroscopic images during PRA. Recently, Rassweiler [52] reported an augmented iPad-Assisted PRA, where before the surgical procedure, all relevant anatomic structures are identified and marked in CT preoperative images. During surgery, the iPad camera is used to obtain intraoperative real-time images and, simultaneously, the monitor shows an enhanced virtual reality of the patient's anatomy. For this purpose, four optical markers, which must always be visible on the iPad screen, were rigidly registered. This system helps the surgeon obtain kidney access by showing the relationships between the surgical structures and surgical instruments.

Besides PCNL, the number of authors reporting augmented reality systems has increased considerably in the last decade [62, 103-105]. Considering the Teber [104] and Su [105] contributions for PRA, using image navigation systems for nephrectomy laparoscopic surgery, it is expected that the use of this approach – and similar ones – provide good opportunities for PCNL improvement.

Li et al. [101] designed a modified “stereotactic localization” system for PCNL, inspired by the locating principle of extracorporeal shock-wave lithotripsy and by stereotactic techniques. Although they decreased the puncture time from 17 to 7 min, they still continue using X-Ray imaging with an exposure time higher than 2 min and success rates lower than 90%.

In addition to augmented reality, Huber [106] reported an EMT system for navigated renal access in an *ex vivo* model. The surgical needle is guided from the skin puncture site towards the renal calix, according to information retrieved by a catheter that integrates EMT sensors. The researchers accomplished shorter puncture times of 17 s and with a higher precision of 1.7 mm. EMT navigation has also been successful described to guide percutaneous puncture in liver and lungs [90].

## 2.4 Discussion

The number of PCNL procedures is steadily increasing, despite the number of trained urologists mastering this technique has not kept up to this growth factor [44]. This chapter specifically focused on methodological and technological advances that may leverage better and easier PRA during PCNL.

Several surgical and technological paths have been explored to facilitate and improve the different surgical stages. New surgical positions, simulation systems for puncture training, instrumented needles and biomechanical models can contribute to puncture effectiveness, decrease the number of attempts and procedure time. Consequently, the development of new surgical instruments, biocompatible with imaging systems, easy to use, durable and capable of transmitting force and movement haptic feedback (with tremor compensation), may greatly facilitate many of the

PCNL steps as well as other MISs. Moreover, needles allowing the spatial monitoring tips can be used to reduce respiratory movements and tissues deformations influences.

Several shortcomings related to image guided techniques were investigated, showing that real-time tracking and registration of organ motion and deformation remains the biggest challenges to achieve robust navigation. Although breath hold, respiratory gating and biomechanical models have been employed, no widely acceptable solution has yet been reached due to the lack of robustness, precision and real-time algorithms.

The medical benefits of the various imaging techniques are unquestionable for PCNL and other MISs. Despite its advantages on diagnosis, surgical planning and guidance, there are some factors that limit the use of imaging techniques in renal puncture.

Although fluoroscopy and US are the most popular approaches, providing real-time image stream, they also present some limitations. Fluoroscopy is intrinsically 2D (a series of "overlapping shadows"), presenting little soft tissues contrast (which decreases target and surrounding structure definition) and exposes the patient, as well as the physician, to a significant amount of radiation [106]. Mancini [107] reported higher body mass index, greater stone burden, nonbranched stones and multiple nephrostomy access tracts as the main aspects for increased radiation exposure during PCNL.

On its turn, the low image quality of 2D US still remains one of the most limitations. Although the use of 3D US is a promising method for mitigating the disadvantages of 2D US, providing volumetric measurements and 360° analyses of anatomical structures, at the moment it demands experienced technicians in handling the US probe during volume reconstruction.

Finally, both 2D and 3D US present difficulties at the identification and visualization of the urinary system anatomy and small kidney stones, particularly in obese patients [42, 60, 62].

Many of the current imaging methods only allow the acquisition of 2D images (fluoroscopy, IVU and US) and therefore do not take into account the 3D structure of the urinary system anatomy. Human error may stem from the misinterpretation of images during puncture and fluoroscopic methods [1, 45, 62].

Despite IVU and angiographic CT have potential to improve the image quality for PRA planning and guidance, when compared to CT itself, they require the injection of a radiopaque dye, which can cause allergic reactions in some patients and potentially further damage to kidney function, blood vessels and nerves [14].

Other imaging modalities, such as CT or MR, offer high quality images, but are only used for diagnosis and surgical planning, since their acquisition is not in real-time or require large spaces that can obstruct the surgeon's actions.

The use of MR image acquisition in real-time is also limited by the large magnetic field generated, which disables the examination of patients with electronic devices (e.g. pacemakers and defibrillators), and imply the use of non-ferromagnetic surgical instruments, increasing the procedure costs. Since MR produces high quality images and eliminates radiation exposure, new ergonomically designs of MR systems will certainly constitute an important research path on medical imaging.

Although multimodal imaging systems can reduce many of the problems mentioned above, the lack of algorithms for preforming a robust real-time non-rigid registration continues to limit its use in clinical routine [108, 109].

Finally, endoscopic methods present high spatial resolutions and provide real-time image acquisition, allowing direct visualization of the structures manipulated in surgery. The use of flexible ureteroscopy in pediatric patients has been debatable, due to small caliber of urethra and ureter. Consequently, *micorperc* may be more valuable technique, with no morbidity associated with tract size [10]. However, these methods only provide information about the surface of organs and cavities, therefore preventing its use in surgery planning and limiting its capability for puncture guidance [1, 103, 106, 109]. Future developments of endoscopic surgery may focus on camera resolution, field of view and depth perception, tactile feedback and improvements on mobility and handling of instruments.

Obtaining clinical relevance in the field of image recording remains a challenge and a large active research area, mainly as a result of the difficulties imposed by breathing movements and deformation of tissues during surgical manipulation [103].

Computer aided surgeries and tracking devices are subject of ongoing research since they may play an important role in the future of PRA. These techniques have the potential to provide valuable interfaces between anatomical structures and surgical tools, medical robots, organ deformation and movements. Therefore, navigation systems could represent a step forward to reduce the medical imaging dependence and associated shortcomings in puncture conduction. Although computer aided surgery may improve surgeon skills, it remains a challenging issue. The lack of non-rigid registration methods that estimate soft organ movements and interaction between surgeon instruments and organs, limits its use in medical robotics and multimodal imaging. Many improvements are still needed for both mathematical algorithms and equipment to reach widespread computer aided surgery in the operating room. Moreover, the registration process, between image data and surgical tools, also needs additional medical experts, being a constraint in today's clinical environment.

OMT has been very helpful intraoperatively when combined with pre-operatory CT imaging. However, it demands a line of view to the optical references and the image acquisition should be with the patient lying in the same position of the surgical procedure.

In contrast, EMT do not depend on a clear line of sight. Therefore, surgical tools with small coils may be placed near the renal stone, acting as a real-time anatomic target locator. Although Yaniv et al. [64] concluded that it is difficult to generalize working conditions for each EMT system, he achieved average errors under 3 mm in different operating rooms.

Considering the state of the art of medical robots, one may conclude that surgeons are still in the early stages of understanding and taking advantage of the full potential of robots in medical practice. However, one should note that the robot introduction in surgery procedures is increasing steadily, mainly due to the potential of these systems to increase surgeon movement accuracy, and the overall quality of surgeries. Consequently, one has assisted to an increased number of urologists with training to conduct robotic assisted surgeries [1].

Medical robotics also constitute an essential component in the path for achieving full functional telesurgery, a concept that has been widely debated in the literature [18, 63, 100].

Despite its unquestionable advantages, medical robotics are still struggling to overcome some important problems to its widespread use, in particular the difficult initial setups, expensive costs, mechanical problems, absence of tactile feedback and steep learning curves associated with the acquisition of proficiency. New developments of medical robotics should focus on overcoming these disadvantages as well as on improving the easy attachment of surgical instruments, sterilization and installation facilitation, security and more independence to imaging systems.

Hereupon, it is expected that future improvements on the PRA will comprise the elimination of radiation, reduction of surgical costs and time. Finally, although the development and improvement of autonomous robots may broad the use of PRA of surgeons less familiarized with MISs, it also raises challenging robustness and safety issues that have to be tackled in the future.

# 3

# KidneyNav – Framework for PRA Planning

The chapter describes the development of a software application entitled KidneyNav. It integrates a set of image processing and computer graphics algorithms that allow an intuitive visualization of multiple organs surrounding the kidney for aiding of the PRA planning.

Additionally, KidneyNav was further combined and tested with OMT technology for PRA guidance (Chapter 4) [55].

## Contents

## 3.1 Introduction

During PRA, the surgeon must assure that the needle reaches the desired target without damaging any other organ during needle insertion. A pre-operative study followed by an accurate puncture planning is often performed using CT data sets [14, 44, 110].

Image processing based methodologies have been suggested over the years to facilitate, automatize and improve surgical planning [109]. Many existing ones focus on the segmentation of individual organs [111-113], where the liver have been the most preferred organ, where kidneys, spleen, pancreas were analyzed less frequently [96].

Robust segmentation of abdominal organs remains a challenging task because of the variability of the shape, sizes and locations can vary significantly in different subjects [114-116]. The fusion between 3D segmented organs and virtual surgical tools may leverage the surgeon to achieve high surgical success rates, benefiting needle-based interventions such as laparoscopic biopsies, radio-frequency and cryo ablations [117, 118].

Some researchers have already been focus on abdominal multi-organ segmentation with increasingly promising results in recent years. Despite of the high variability between patients, authors use frequently some basic rules of anatomy and physiology, combining statistical models into developed methodologies [96, 113, 119-121].

Zhou et al. [121] combine a pre-segmented atlas into a fuzzy connectedness framework. Several parameters, such as organ intensity features, seeds, and threshold values were combined to achieve automatic segmentation of abdominal organs. The overlap between neighboring organs was solved based on Euclidean distance and watershed methodology. The authors segmented the liver, right kidney, left kidney and spleen with false positive rates of 6.6%, 8.5%, 7.6% and 6.4%, respectively.

Shimizu et al. [122] propose a method for the extraction of 12 organs from non-contrast 3D abdominal CT data. An atlas guided segmentation with an expectation maximization was used to deal with large fluctuations in the feature distribution parameters between subjects. The final segmentation was obtained using multiple level sets. The average performance of the liver, spleen, left and right kidneys, heart, gallbladder and abdominal aorta was 78.8%.

Another fully-automated method was presented by Wolz et al. [98]. Hierarchical atlas registration and weighting scheme was used to generate specific priors from an atlas database by combining aspects from multi-atlas registration and patch-based segmentation. When testing the methodology in 100 CT datasets, the authors reported a DSC (dice similarity coefficient) score of 94%, 91%, 66% and 94% for liver, spleen, pancreas and kidney respectively.

Linguraru et al. [96] described a new formulation of 4D directional graph based methods in integrated statistical location priors. Training data from a patient population were used to automatically initialize the graph by an adaptive 4D convolution. Liver, spleen and kidneys were robustly and accurately segmented with volume overlaps over 93.6%. However, the algorithm takes 9 h 25 min on a typical dataset. Employing multiscale optimization the computation was reduced to an average of 3 h.

Kobashi et al. [116] uses dynamic thresholds under a priori shape information constraints. They showed fragmented results disturbed by intensity inhomogeneity. On the other hand, Lee et al. [120] created several spatial fuzzy rules to identify abdominal organs. Such method is not generalized for a full range of individuals and uses a complex set of fuzzy rules.

Although multi-organ segmentation algorithms in CT/MR volumes and non-rigid real-time CT/US registration methods [105, 108, 123] have been proposed in literature, they have not yet been applied for PRA to automatically segment and enhance the pre-operative data or to estimate the best trajectory for PRA. Therefore, this chapter aims to develop and test a new framework (hereinafter referred as KidneyNav) to automatically segment the kidney and surrounding structures, helping the surgeon to easily and intuitively plan the PRA. From a PRA point of view, it should segment and represent in a 3D space the kidney and its surrounding structures allowing the surgeon to rapidly identify all the anatomical structures, stone shape, size and location, define a skin site to insert the needle and evaluate a virtual path between the between the anatomical target and the skin puncture site.

Being an application for surgical guidance, KidneyNav framework follows the common and necessary steps in which the user imports a volumetric image data, defines the anatomical target, plans the needle insertion trajectory, registers the image data to the patient, and navigates to the target using tracked tools that are overlaid onto the image data.

# 3.2 Methods

## 3.2.1 Framework Overview

Since real-time execution (> 25 frames per second (FPS)) is a critical situation for these kind of applications, C++ was used as the main programming language. KidneyNav was created and compiled using the Microsoft's Visual C++ 2010.

For the graphical display and user interface control, one used Qt 4.8.5. It is a C++ cross-platform application framework that can be easily integrated in the Visual Studio suite, improving and faster the implementation workflow.

Finally, KidneyNav is fully integrated with open source libraries such VTK (Visualization Toolkit) and ITK (Insight Toolkit). These libraries provide advanced functions for computer guided surgery segmentation and image registration as well as many 3D visualization and rendering capabilities.

The KidneyNav graphical user interface (GUI) was optimized for kidney based interventions, integrating many functionalities that can be used pre- or intra-operatively. The development of such framework comprises the following steps:

I. Development of a GUI that guides users throughout whole functionalities for surgical navigation:
    a. 3D Visualization: draws virtual tools in a 3D world, imported by a STL file (tool in red, Figure 3.1-f). The user can use different camera views: front view (represents Ox vs Oy), side (represents Oz vs Ox), top (represents Oy vs Oz) and needle view (3D camera placed at the needle tip);
    b. 2D Visualization (Figure 3.1-g): draws a circle and a ring. The ring is always drawn in the view. In contrast, the circle moves according to the Euclidean distance between the needle tip and anatomic target. Likewise, the user can be guided through different views: front view (positional differences between Ox and Oy), side (positional differences between Oz and Ox), top (positional differences between Oy and Oz) and orientation view (positional differences between the needle tip and target orientation).

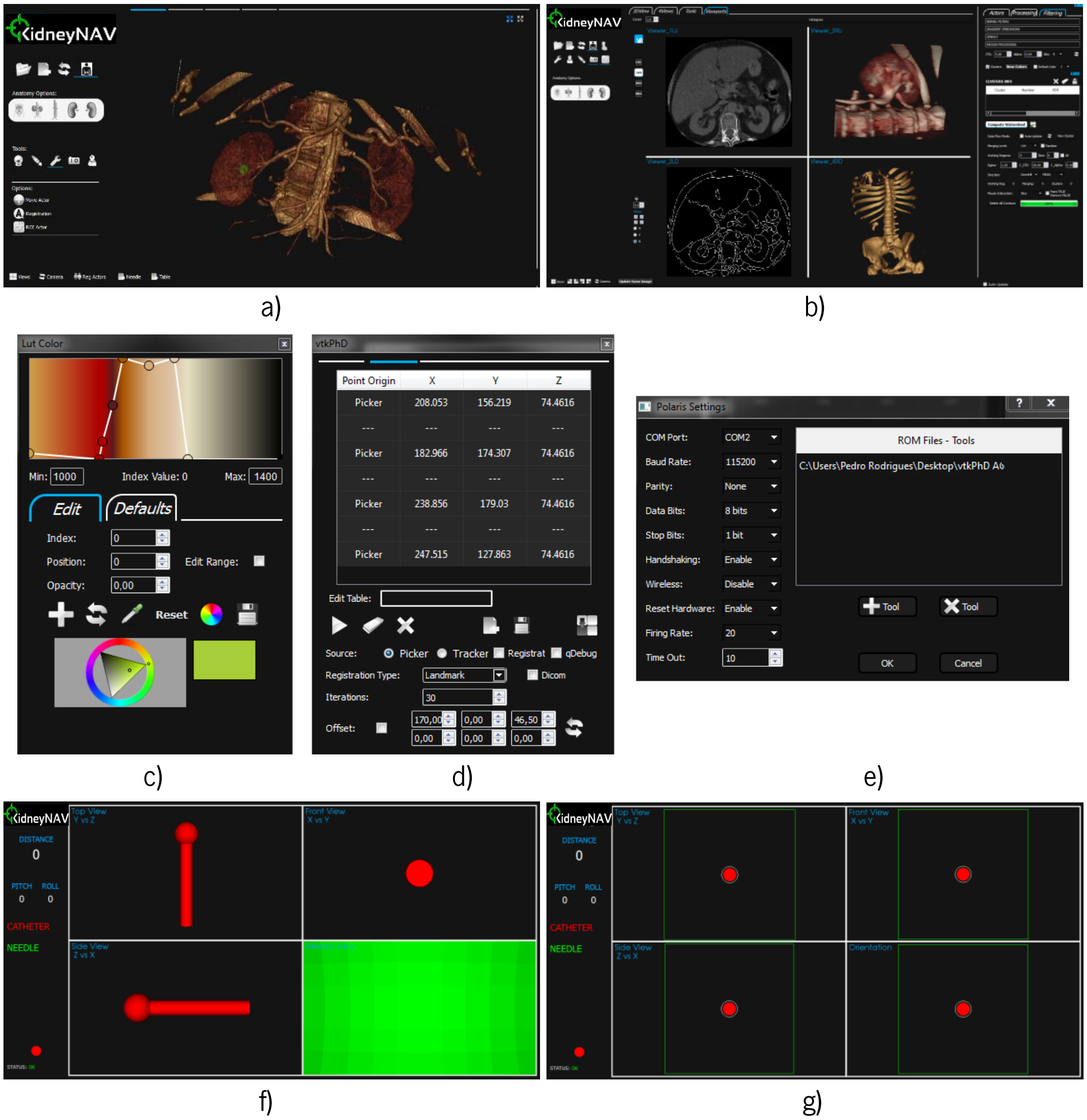

Min: 1000
Index Value: 0
Max: 1400
Index: 0
Position: 0
Edit Range: ☐
Opacity: 0,00

| Point Origin | X | Y | Z |
|---|---|---|---|
| Picker | 208.053 | 156.219 | 74.4616 |
| --- | --- | --- | --- |
| Picker | 182.966 | 174.307 | 74.4616 |
| --- | --- | --- | --- |
| Picker | 238.856 | 179.03 | 74.4616 |
| --- | --- | --- | --- |
| Picker | 247.515 | 127.863 | 74.4616 |

Edit Table:
Source: ● Picker ○ Tracker ☐ Registrat ☐ qDebug
Registration Type: Landmark ☐ Dicom
Iterations: 30
Offset: ☐ 170,00 0,00 46,50 / 0,00 0,00 0,00

COM Port: COM2
Baud Rate: 115200
Parity: None
Data Bits: 8 bits
Stop Bits: 1 bit
Handshaking: Enable
Wireless: Disable
Reset Hardware: Enable
Firing Rate: 20
Time Out: 10
C:\Users\Pedro Rodrigues\Desktop\vtkPhD A6

Figure 3.1. Representation of different KidneyNav windows: a) volume rendering widget; b) processing widget with different windows and configurable settings; c) widget to define and change transfer functions for volume rendering; d) 3D registration control widget; e) OMT/EMT interface; f) and g) show 2D or 3D guidance interfaces.

II. OMT/EMT interface allowing:

   a. Communication with the OMT Polaris Optical System and EMT Aurora Electromagnetic System (both from NDI (Northern Digital Inc.), Waterloo, Canada);
   b. Configuration and initialization of the tracking tools;
   c. Gathering and processing of the transformation matrixes for each tracking tool.

III. Pre-operative image segmentation highlighting through volume rendering techniques different anatomical structures used during the surgical procedure (e.g. left kidney, right kidney, ureters). The data is loaded by TIFF or DICOM (Digital Imaging and Communications in Medicine) datasets.

### 3.2.2 Abdominal Multi-Organ Segmentation for PRA Planning

KidneyNav integrates an image processing methodology that allows 3D automatic labelling of relevant anatomical structures such as colon, spleen, kidney, kidney calyces and stones. Such methodology was tested in CT images since it is method of choice for the preoperative planning of PRA [1, 14, 45, 81, 91].

#### A. Volume of Interest

The methodology starts by automatically define a volume of interest (VOI) where the kidney and their neighborhood structures, with relevance for PRA planning, are placed. Such volume will be calculated according to the inner volume of the rib cage.

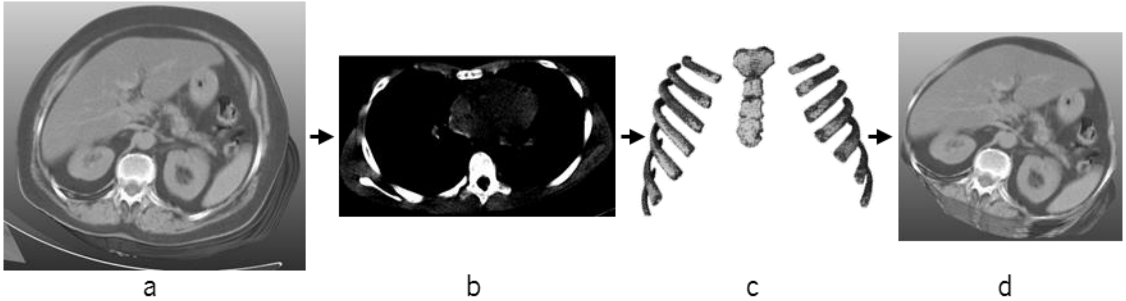

Figure 3.2. Representation of the different steps to calculate the VOI for PRA planning: a) shows the input Dicom volume; b) shows the output of the pre-processing stage using a sigmoid non-linear filter; c) shows the rib cage by applying an iso threshold; and d) show the VOI within the rib cage.

To this extent, the input slices are firstly smoothed using an anisotropic diffusion algorithm which reduce the noise spots corrupting the image [124]. It depends on three parameters: number of iterations, edge parameter (σ) and an edge-stopping diffusivity function $g(x, \sigma)$ that evaluates the Tukey's function with the edge parameter $\sigma$ at the pixel $x$ (Equation 3-1):

$$g(x,\sigma) = \begin{cases} \frac{1}{2}\left[1-\left(\frac{x}{\sigma}\right)^2\right]^2, & |x| \le \sigma \\ 0, & |x| > \sigma \end{cases}$$ Equation 3-1

The filtering outcome was input to a sigmoid non-linear function that maps the image intensities into a new range (Figure 3.2-b). The output pixel intensity $I'$ was determined according to Equation 3-2:

$$I' = (I_{MAX} - I_{MIN}) \cdot ({}^{1}\Big/_{1+e^{-(I-\beta)/\alpha}})$$ Equation 3-2

where $I$ represents the intensity of the input pixel, $I_{MAX}$ and $I_{MIN}$ the maximum and minimum values of the output image, $\alpha$ the width of the input intensity range and $\beta$ the intensity around which the range is centered.

The bone segmentation (Figure 3.2-c) was accomplished using an iso-surface threshold $T$, whose level was automatically calculated based in a entropy maximization criterion. Ranging from a minimum pixel intensity $I_{MIN}$ to maximum one $I_{MAX}$, the $T$ value was determined as the one that maximizes the total entropy $E_T$ (Equation 3-3):

$$E_T = EB_i + E0_i$$ Equation 3-3

where $E0_i$ is the entropy of the segmented objects as the result of the threshold algorithm at level $T$ and $EB_i$ is the entropy of the background objects.

Regarding the Hounsfield scale, bone structures intensities varies between $I_{MIN}$ = 900 and $I_{MAX}$ = 1400 for all the used CT data.

The segmented rib cage defines the targeted VOI, where relevant structures for image navigation should be segmented and highlighted (Figure 3.2-d).

### B. Volume Course Partitioning

This section describes the processes to partition the image volume into small primitive volumes. However, the probability that a single primitive will suitably associate to each object of interest is small. Knowing this limitation, a good design goal is to create a high number of primitives and try to semantically link them into a hierarchy.

Since image intensity is characterized by a significant change across boundaries between different objects (image edge), the partitioning procedure starts by computing the gradient of magnitude $mag(\nabla f)$ of the smoothed image (Equation 3-1). The $mag(\nabla f)$ is determined using the Sobel operator that computes the partial derivative in all axis (Equation 3-4):

$$mag(\nabla f) = \sqrt{\left(\frac{df^2}{dx}, \frac{df^2}{dy}, \frac{df^2}{dz}\right)} \quad \text{Equation 3-4}$$

All primitive volumes were created by recursively tracking all pixels between a starting pixel (red, Figure 3.3-c) and a local minimum of the image gradient magnitude (green, Figure 3.3-c), i.e. for each starting pixel $p$ of the input image, a pixel $q$ in the 26-connected neighborhood (yellow in Figure 3.3-c, showing 8-connected 2D neighborhood) was selected.

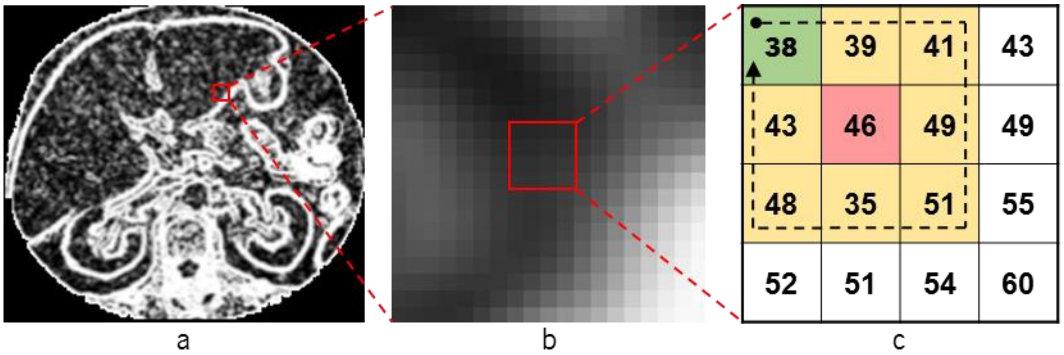

Figure 3.3. Schematic for the partitioning process: a) image gradient magnitude; b) zooming area of the gradient magnitude; c) pixel intensities of the zooming area in b) where the arrow is the searching direction.

If more than one pixel $q$ exists, the last pixel found was taken, considering $p$ as a reference pixel. Every pixel $q$ along the path is marked as a local minimum of the gradient magnitude and assigned a distinct label.

Each created region shares the same statistical properties and the boundaries coincide with the ridges of the gradient magnitude surface.

### C. Volume Merging

Although the probability of having region boundaries corresponding to boundaries of important objects increases with over-segmentation, it can also create many insignificant boundaries. Since all pixels within the same image object are homogeneous and considerably different from other objects, there are neighboring primitive volumes that can be merged, yielding a meaningful segmentation. This stage describes how one dealt with this problem in order to segment and select relevant anatomical structures for PRA planning.

Briefly, primitive volumes were clustered in different groups as a local optimization problem, considering that all pixels within the same image object are homogeneous and considerably different from other objects.

### *I. Minimum Description Length*

The large quantity of primitive volumes $V_i$ $(i = 1,2, \dots, k$, with $k$ being the total number of primitive volumes) was reduced using a merging procedure, based on the pixels entropy distribution between neighboring regions. All pixels in $V_i$ were treated as a stochastic variable with distribution $P_{V_i}(I_i)$, where $I_i$ $(i = 1,2, \dots, k)$ is the original image intensity in the $i$th primitive volume.

Apart from pixels distributions, small primitive volumes that had large common boundaries compared to their size were firstly merged.

These criteria were formulated mathematically as a global optimization problem using the minimum description length principle [125]. Formally, it is determined from the total number of bits necessary to encode the volume $V(B_V)$ inside the rib cage given by the Equation 3-5:

$$V(B_V) = \sum_i B_i(V_i) - B_B(V) \quad \text{Equation 3-5}$$

where:

1. $B_i(V_i)$ is the total number of bits needed to describe the image intensity for each primitive volume given by $B_i(V_i) = nV_i \cdot H(V_i)$; with $nV_i$ being the number of voxels and $H(V_i)$ the entropy of the volume $V_i$. The entropy $H(V_i)$ of a discrete random variable $V_i$ is defined as: $H(V_i) = -\sum_{\mu_i \in V_i} P_{V_i(I_i)} \cdot log_2(P_{V_i(I_i)})$;
2. $B_B(V)$ is the number of bits needed to code the volume boundary information given by $B_B(V) = N_r(V) \cdot b_1 + N_b(V) \cdot b_2$; with $N_r(V)$ being the number of primitive volumes in $V$; $N_b(V)$ the total boundary length of the volume partitioning; $b_1$ the number of bits required to code the starting point; and $b_2$ the number of bits required to code each element of the boundary chain code.

The advantage of applying the minimum description length principle to merge regions is that decisions were made adaptively, taking into account local region statistics. As a result, salient boundaries are preserved while others are deleted by region merging.

### *II. Merging Cost*

According to the above information, the total number of primitive volumes was reduced by merging, at each step, the pair of volumes that provided the largest positive description gain $G$ among all possible merges.

The value of description length gain $G$ associated with this merging is given by Equation 3-6:

$$G = nV_aH(V_a) + nV_bH(V_b) - nV_{new}H(V_{new}) + b_1 + nb(V_a, V_b) \cdot b_2 \qquad \text{Equation 3-6}$$

Where $nb(V_a, V_b)$ is the number of common boundary elements between a primitive volume $V_a$ and $V_b$; $V_{new}$ is a volume resulting after merging $V_a$ with $V_b$; $b_1$ is the number of bits required to encode the starting point; and $b_2$ the number of bits required to encode each element of the boundary chain code.

### *III. Hierarchy Tree*

These two neighboring primitive volumes were chosen in a greedy way (meaning that the problem is solved by making a locally optimal choice at each stage trying to find a global optimum), as long as regions can be merged towards a minimum value of $G$ (the increase of the entropy value is compensated by the elimination of the common boundary).

Primitive volumes were merged in a deterministic order, so that computation time was reduced. Firstly, a histogram was created for each primitive volume $V_i$ and subsequently neighbor volume relations were extracted from the original image partitioning. Finally, the common boundary line length and the description length reduction are computed for every pair of neighboring regions. The merging procedure inherently builds a hierarchy tree of different levels, nodes and leaves. The number of leaves is equal to the number of primitive regions in the volume. The links in the tree are created based on how primitive regions at one level are joined into new single regions at the next level.

The greedy procedure is stopped when only K main volumes exists, corresponding to K volumes to display inside the rib cage. This number K must be specified by the user as the number of anatomical structures to highlight and display during volume rendering. Figure 3.4 show different merging levels.

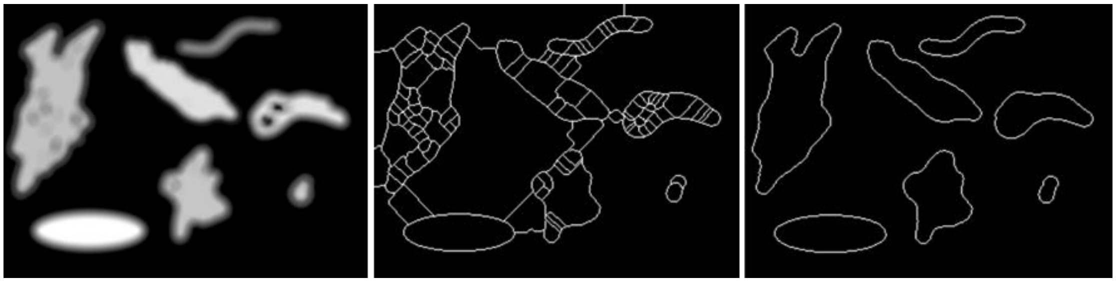

Figure 3.4. Representation of different merging levels: (left) input image; (center) set of 96 regions; (right) set of 7 regions.

### D. Volume Rendering

Since the definition of a rendering transfer function may a time-consuming and a challenging task, KidneyNav provides different functions that can be automatically loaded by the user (Figure 3.1-c). Each function is applied to map the voxels of each segmented volume through a multi-volume Ray Cast method [126]. The user can build and load pre-defined transfer functions, highlighting areas of interest in the volume mesh, while disregarding the rest by making them transparent.

Ray casting, like other volume rendering methods, is based on the rendering equation [127]:

$$I(x_1,x_2) = v(x_1,x_2)\left[\epsilon(x_1,x_2) + \int_S \rho(x_1,x_2,y)I(x_2,y)dy\right]$$ Equation 3-7

Equation 3-7 models the physical phenomenon of light emission and scattering in computer graphics, showing that the transported intensity of light $I$ from a point $x_1$ to $x_2$ can be determined by summing the emitted light $\epsilon$ at the same path and the total light intensity $\rho$ that is scattered from all other surfaces $y$ reflected at $x_2$. $v(x_1,x_2)$ is a geometry term which giving the mutual visibility between $x_1$ and $x_2$.

A volume rendering integral can be derived to Equation 3-8 [127]:

$$I = \int_{t1}^{t2} C(t)e^{-\int_{t1}^{t}\alpha(s)ds}dt$$ Equation 3-8

Within Equation 3-8, the image intensity $I$ is dependent on the relation between the volume intensities at point $t$ along the ray, the color $C$ (light information, including emitted, scattered, and reflected light) and an opacity value $\alpha$. Considering the computational limitations, a good discrete approximation of Equation 3-8 is shown in Equation 3-9:

$$I = \sum_{k=1}^{M} C_k \alpha_k \prod_{i=1}^{k-1} (1 - \alpha_i) \qquad \text{Equation 3-9}$$

where $C_k$ and $\alpha_k$ are the color and opacity samples collected along the ray.

For each pixel in the image plan, an imaginary ray is casted in the view direction. The intensity values along the ray (at small and equivalent intervals) are converted into color and opacity using RGBA transfer functions. Since multi dependent volumes may be intersected by a single ray, different transfer function were defined and used for each segmented volume. The final pixel intensity is based on the composition function that gathers information about all volumes.

The following algorithm was used to implement the above methodology under VTK (Table 3.1).

Table 3.1 Algorithm for multi-volume rendering.

```
Input: Clustered volume - $C_v$
Output: Rendered image - $Re_I$
%Processing
CreateVTKRenderer() % Initialization of the volume object, environment lights, and a camera view
CreateVTKVolume() % Volume data to render
CreateVTKVolumeMapper() % Delegates to a specific volume mapper based on rendering parameters and available hardware. When supported, GPU ray casting was used for volume rendering.
CreateVTKOpacityColorFunction () % Creates a supported transfer function based on the function defined by the user using the KidneyNav interactive tool.
CreateVTKVolumeProperty () % Determines the type of interpolation to use when sampling the $C_v$, and receives the information stated by the CreateVTKOpacityColorFunction().
for each Volume $i$ in $C_v$
    Mask ← CreateMaskFromInput($C_v[i]$); % gets the original pixel intensities where
    $C_v[i]$.SetColor(GetVTKOpacityColorFunction()$[i]$);
    $C_v[i]$.SetOpacity(GetVTKOpacityColorFunction()$[i]$) ;
    GetVTKVolume()$[i]$.Set($C_v[i]$);
    GetVTKRenderer.Add(GetVTKVolume()$[i]$); % Adds each Cluster $i$ to the window
end for
UpdateWindow() % Updates the visualization and camera
```

### E. Volume Editing

After the merging and rendering procedure, different anatomical structures may be visualized as one single volume. In these cases manual editing might be needed to correct segmentation errors. KidneyNav interface provides two ways to facilitate this manual editing.

#### *I. Direct Manipulation of the Merging Tree*

Since the merging procedure automatically builds a hierarchy tree, the user can easily modify an interface slide bar value, allowing to choose the tree level output, i.e., the number of output volumes.

Figure 3.5 shows a short example of hierarchy tree constructed after the merging procedure. Each number from 0 to 9 represents a primitive volume in the image. The -1 labels indicate that these volumes are not merged together with any other region at the current level. Suppose that region 6 is an unwanted result of a volume of interest being a merging result of leaf regions 1 and 2 (each leaf corresponding to different anatomic object). In this cases, the user can move down in the tree, increasing the probability that leafs from different object are not merged in a single output volume.

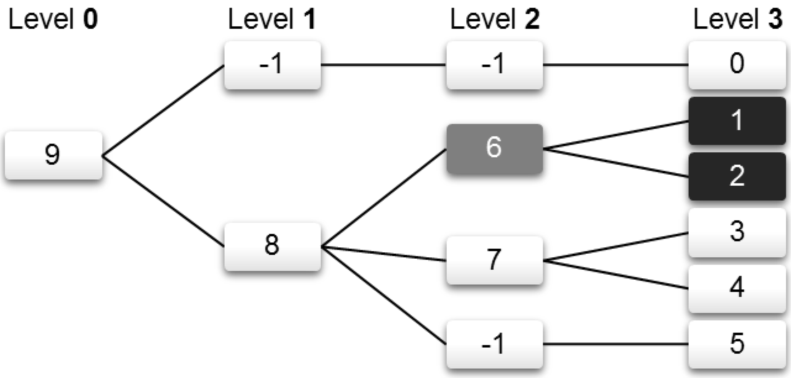

Figure 3.5. Tree hierarchy example.

#### *II. Shape Separation*

By clicking at any voxel inside a specific volume, it will be re-structured and divided into new sub-volumes according to the volume shape. The idea is to use local minimum spots in the center of each structure that should be separated.

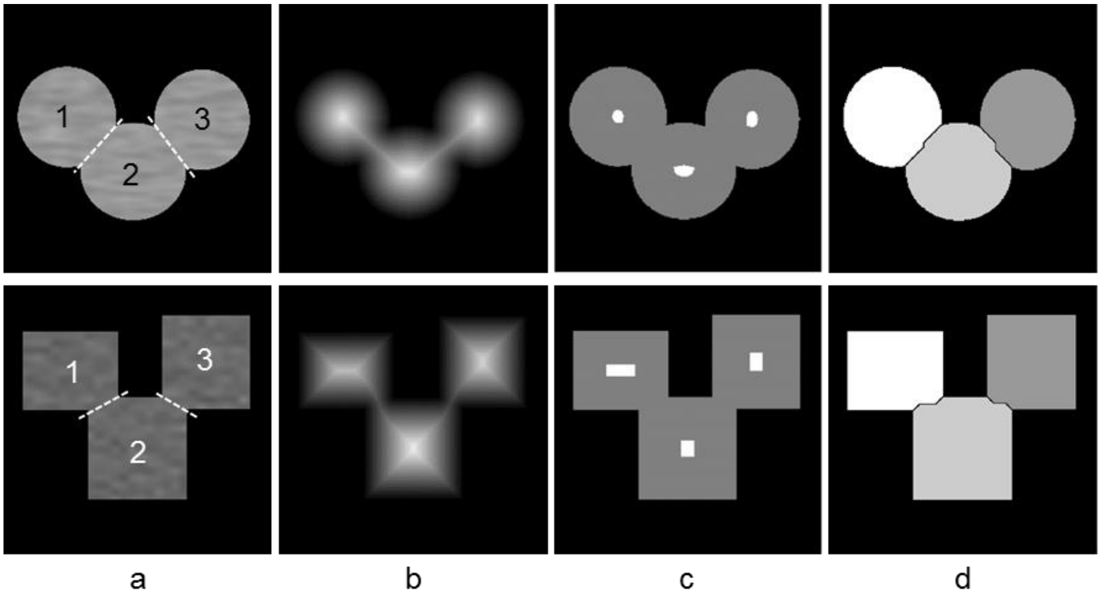

Figure 3.6. Overview of the shape separation methodology: a) input image representing three different objects with similar image intensity and labelled as the same object; b) distance transform; c) local minima to distinguish each object; d) new labelling output.

Since volumes from different anatomical structures and similar intensities are connected by small bindings when compared their total volume (three objects separated by a dashed line, Figure 3.6-a), the distance transform method was useful to create fiducials inside each object (Figure 3.6-b) [128].

A Otsu threshold [129] method is used to automatically create a binary image $I_B$ that classifies the object of interest and image background. The Euclidean distance between the white pixels in $I_B$ and its nearest nonzero pixel was used to define the pixel intensity of a new image $I_D$ (Figure 3.6-b).

The local minima from $I_D$, whose external boundary pixels have a higher value, were tracked and used to define fiducials points (Figure 3.6-c shows the overlap between $I_B$ and local minima). Noise spots were reduced by only considering minima regions with area higher than 5 pixels. Finally, primitive volumes are created by tracking all image local minima. In the end, each minima correspond to a segmented volume and a distinguishable anatomical structure (Figure 3.6-d).

## 3.3 Experiments

### 3.3.1 Segmentation and Rendering

Different experiments were carried out to provide specific information regarding the parameters which work more effectively, namely the merging stage and the best number of primitive volumes for volume rendering.

The methods were evaluated using a Dicom dataset of the human abdomen from 16 different patients acquired at Hospital of Braga (10 male and 6 female patients). The input dataset have $512 \times 512 \times \sim 174$ (width × height × depth) pixels of size with a slice thickness of 1-5 mm and a pixel resolution between 0.680 and 0.816 mm. Synthetic images were equally used.

All of the experiments were conducted on a PC equipped with a NVIDIA® GeForce® GT 330M, 8 GB of RAM and an Intel® Core™ i7-740QM CPU. The rendering widow size was about 650x650 pixels.

In order to evaluate the segmentation procedure, anatomical relevant structures were manually segmented (by expert surgeons) and marked with different labels. Each model was then used as reference for the evaluation study. The performance of segmentation method was accessed by quantifying the spatial overlap between both manual and semi-automatic segmentations. If more than 1 primitive volume exists inside the manual segmentation, only the primitive with higher volume (total number of voxels) was considered.

The spatial overlap was calculated using the DSC, i.e, a statistic used for comparing the similarity of two samples (Equation 3-10).

$$DSC(A,B) = \frac{2|A \cap B|}{|A| + |B|} = \frac{2TP}{2TP + FP + FN} \qquad \text{Equation 3-10}$$

Where $TP$ is the number of true positives, $FP$ the false positives and $FN$ the false negatives between two data set $A$ and $B$. The DSC score ranges from 0%, indicating no spatial overlap between sets of binary segmentation results, to 100%, indicating complete overlap.

Considering the hierarchy tree of the merging procedure, DSC scores were accessed when keeping 7, 10 and 15 final volumes inside the rib cage. Volume editing methods were evaluated by calculating DSC score improvements.

The sigmoid non-linear filter (Equation 3-2) was configured with $I_{MAX} = 3000$, $I_{MIN} = 1$, $\alpha = 400$ and $\beta = 1500$ for all the experiments to enhance the bones structures as the lightest areas. On the other hand, the images were diffused according to the Tukey's function Equation 3-1 using 80 iterations and an edge parameter of $\sigma = 4.5$ (values determined experimentally).

Concerning the rendering process, one evaluates the following outputs:

- Time needed to load and render a Dicom volume;
- Refresh rate while updating a virtual needle;
- Refresh rate while volume manipulating: translate, rotate and zoom.

## 3.4 Results

### 3.4.1 Segmentation

Figure 3.7-a3, -b3, -c3 and –d3 shows segmentation results with DSC=98.86%, DSC=96.19%, DSC=86.44% and 95.04%, respectively. These results were achieved after keeping only a specific number of $k$ regions: $k$=2, $k$=1, $k$=3 and $k$=1 for images in Figure 3.7-a2, -b2, -c2 and –d2, respectively.

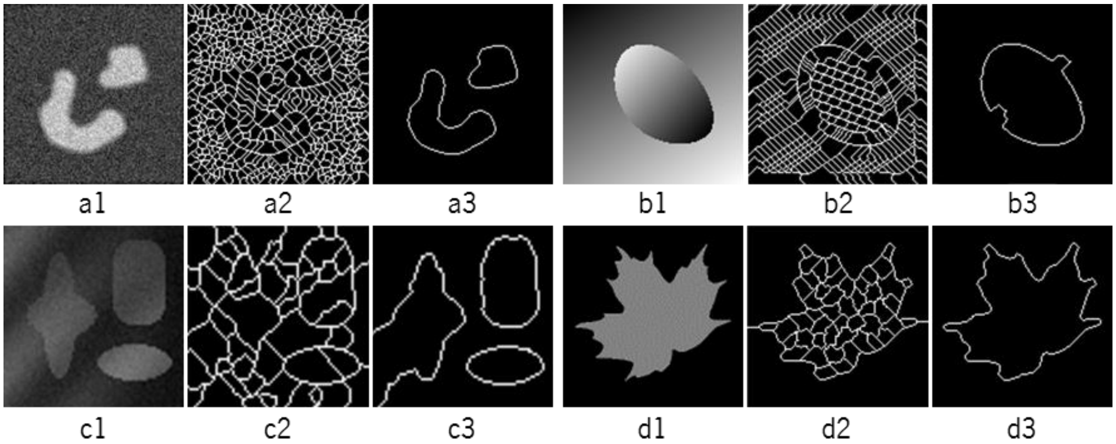

Figure 3.7. Segmentation results for synthetic images: a1, b1, c1 and d1 show the input images; a2, b2, c2, and d2 show over-segmented partitioning results; and a3, b3, c3, and d3 show the final segmentation.

Figure 3.8 shows over-segmented regions of axial CT slices. Visually, whole pixels within one primitive volume belong to the same anatomical object and their edges coincide with the structure boundaries. However, this result is not reliable to achieve high DSC scores, since a large amounts of volumes exists.

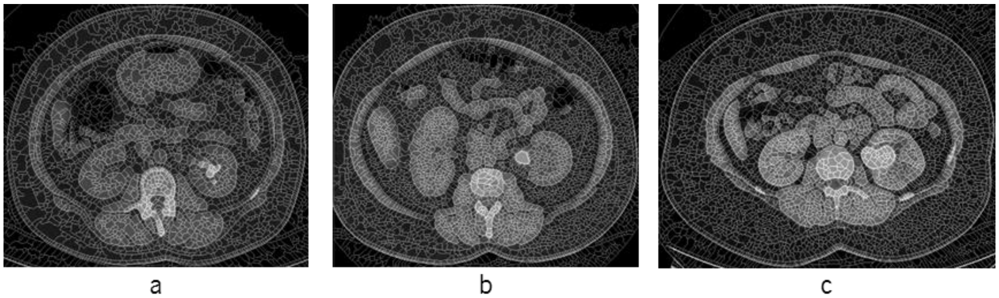

Figure 3.8. Axial slices showing over-segmented results: a) 3039 regions; b) 3570 regions; and c) 4372 regions.

Table 3.2 presents DSC scores for different organs when the segmentation was performed in two modes: Auto (without manual editing) or Interactive (with manual editing). As expected, best results were obtained when interactive editing was used. Best automatic results were obtained by keeping 10 output volumes, while for the interactive interaction 25 outputs volumes were used.

Table 3.2. DSC scores for different organs. *indicates statistically significance (Auto *vs*. Interactive) according t-test Welch (see attachment 1 for more detail).

| **Segmented Organ** | **Intestine** | | **Spleen** | | **Liver** | | **Kidneys** | |
|---|---|---|---|---|---|---|---|---|
| **Segmentatio n Mode** | Auto | Interactive* | Auto | Interactive | Auto | Interactive | Auto | Interactive |
| **DSC (%)** | 51.8 ±10.6 | 80.7 ±3.2 | 86.4 ±6.9 | 90.5 ±4.6 | 72.3 ±6.6 | 95.6 ±1.6 | 88.1 ±3.1 | 94.3 ±1.1 |

High DSC scores were harder to get for the intestine because of its irregular shape and high variations of intensity. By manually editing all primitive volumes belonging to the intestine, the DSC scores can be increased from 51.8% to 80.7%.

After the merging procedure, both kidney and spleen could be segmented by one single primitive volume. In 4 cases, manual editing was necessary to separate the kidney from other neighborhood structures such the liver, intestine or spleen (Figure 3.9).

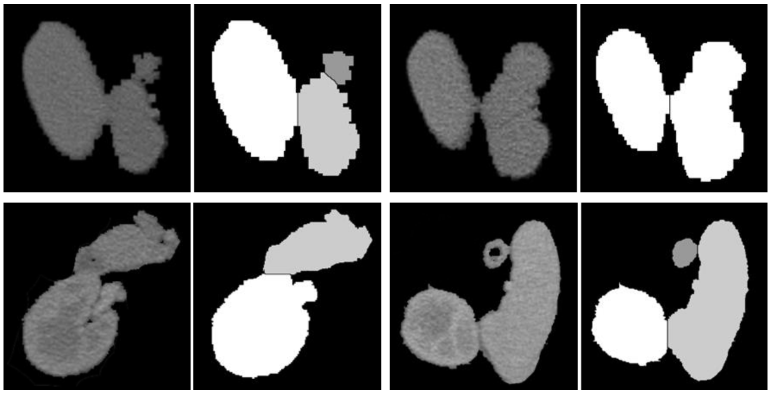

Figure 3.9. Representation of different cases where kidneys was connected to neighbor structures.

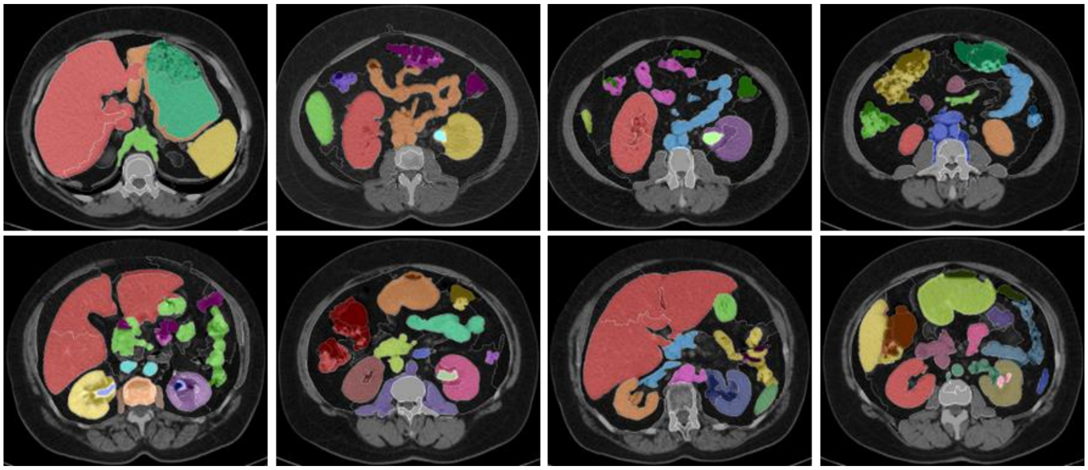

Figure 3.10. Examples of segmentation results in 2D axial slices. Different final primitive volumes are labeled with different colors.

Generally, best results were obtained for the liver. Due to its high volume, DSC scores were not influenced by a small variation of false positives or negatives. Figure 3.10 show some final segmentation results.

When using the interactive mode, 2 to 6 mouse clicks per organ were enough to get the final segmentation. Therefore, the segmentation procedure remains fast and easy to perform, taking less than 1 minutes to segment all anatomic structures.

The average estimated time to create the volume partitioning was 0,03±0,02 seconds/per slice and the time needed for region merging and hierarchy segmentation tree was 0,21±0,06 seconds/per slice. A total of about 12 seconds were necessary for a 50 slices volume.

## 3.4.2 Rendering

Figure 3.11 shows direct volume rendering results of a Dicom dataset. As illustrated in Figure 3.11-a, a global transfer function is usually not able to provide a distinguishable visibility of all anatomical organs.

Figure 3.11-b, -c, -d and –e show results when using multi-volume ray casting to render volumes selected by the user. Interactive manipulation was used to obtain Figure 3.11-f showing the kidney and liver fully distinguishable, when compared to Figure 3.11-e.

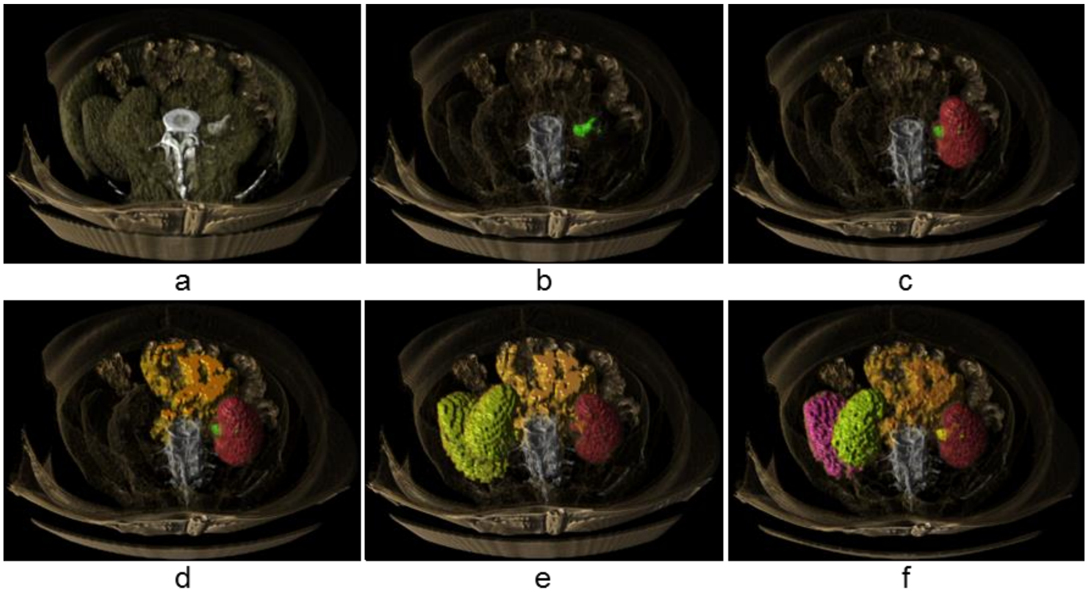

Figure 3.11. Volume rendering enhancing different anatomical structures.

Figure 3.12-a shows the time needed to load and render Dicom volumes with different sizes. The loading and initial rendering takes more when the dataset has a higher number of slices. When rendering small and medium sized dataset, the time needed remained almost similar. Figure 3.12-b shows the refresh rate to manipulate different rendered volumes with particular sizes. Results indicate that volumes can be rendered with an interactive frame rate higher than 19 Hz.

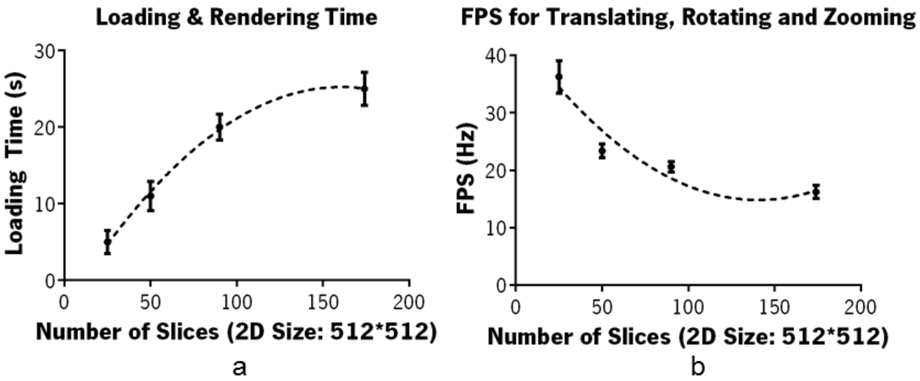

Figure 3.12. a) Time needed to load and apply a rendering transfer function. b) Refresh rate when manipulating a rendered volume (translate, rotate, zoom and moving a virtual tool).

## 3.5 Discussion

Considering the state of the art for multi-organ segmentation, the goal of this chapter was to combine the advantages of region-based algorithms, to create an automatic system to extract the kidney and surrounding structures, while generalizing and improving its visualization. The developed methodology does not need any initialization [111], training data set [111, 112] and is not depended on the variation between atlas and subjects [121, 130].

The total number of decisions to segment all relevant organs was reduced to the selection of the number of output volumes to be rendered. Time-consumption for rendering anatomical structures of interest, user dependence and subjectivity were reduced.

The global threshold, based in the entropy maximization criterion, was efficient to automatically segment the rib cage and surround all the anatomical structures that can be perforated during PRA. The total volume to be processed and rendered was reduced, leading to a decrease of the time needed to create and merge primitive volumes and an increase of the frame rate.

The merging procedure was essential to achieve high DSC scores. The significant amount of primitive regions was reduced using the minimum description length criterion. By knowing the number of anatomical structures to be segmented, primitive volumes were selectively clustered, based on their image intensity distribution, until a suitable number of output volumes exists.

The main difficulties found in the segmentation procedure were the contrast ambiguity and variances between neighbor anatomical structures and complexity of the shape. As a result of poor contrast boundaries between different structures, clustered volumes may leap outside its contours to the background or surrounding tissue. Therefore, it is also difficult to distinguish these structures using only one single transfer function or by selecting different tree levels. In these cases, the user may select a particular function that allows volume separation by shape. It was adequately to divide and separate, e.g. the kidney from the liver or spleen.

Even with manual intervention, the number of mouse click to segment one fully volume was reduced to 2-6 mouse clicks. A small number of output volumes can be used for fast and rough segmentations, while a higher number of volume can be used for erasing and detailed editing, existing a trade-off between the number of output volumes and high DSC scores. Commonly, a number of volumes, equal to thrice the number of anatomical structures to be segmented, was enough to get high DSC scores.

Worst results were obtained for the intestine, which present a wide range of intensities: the intestine lumen presents dark pixels, while the intestine mucosa and muscles presents gray levels with low perceptibility from the background tissue. Often the intestine was segmented with different and individual volumes due to the complexity of its branched shape.

Despite all problems, automatic segmentations (without manual editing) achieved DSC scores of 73.9±15.8% (range from 37.8% to 93.2%). By adding interactive editing scores raised to 90.0±6.2% (range from 76.7% to 97.4%). With a simple an intuitive setup, it was enough to evaluate all structure that might compromise the PRA access.

When comparing to literature outcomes, our method performs as well as state of the art when comparing to works described in [96, 98, 121, 122]. However, the methods were not evaluated with the same CT data sets. Additional work is required to validate this approach on a larger and more varied dataset.

Since our aim was not to effectively quantify the organs geometry properties (e.g. area, perimeter, eccentricity), such scores are well suitable to acknowledge the presence and distribution of anatomical structures inside the rib cage. The user interface provided by KidneyNav allows one to quickly identify segmented structures and to select or divide sub-volumes that belong to them. The mouse pointer behaves like an intelligent paintbrush that selects or erases merged volumes, while the partitioning remains hidden.

Finally, the selected volumes were rendered with a multi-volume ray-casting methodology (Table 3.1). The strategy of using multiple rendering function improve the visibility of structures with similar intensity. One detected problem during the rendering procedure, is that anatomical structures of interest can become obscured by regions of less interest. The user may overcome this problem by defining new transfer function with different opacity values, or by defining clipping planes though the selection of two points.

The main advantage of using rendering techniques is that the object continues being displayed to the user even it was not fully segmented. This methodology fully integrated with VTK pipeline allowed an assertive surgical planning by the visualization of the anatomical structures surrounding the kidney and the puncture target.

# 4

# Motion Tracking for Surgical Navigation

The chapter describes and evaluates an EMT and OTM system for kidney puncture guidance and planning. It is based on the work published by the authors in The Journal of Urology, SPIE Medical Imaging and Portuguese Symposium of Urology [54, 55, 58, 59].

## Contents

## 4.1 Introduction

One way to track the position and orientation of the catheter and needle relies on OMT or EMT systems. As already stated in State of the Art (Section 2.3), the reliability and performance of OMT and EMT technologies have made them the trackers of choice to develop advanced surgical navigation systems.

Both technologies present specific and particular advantages, but also some shortcomings. As well known, the great advantage of EMT is the ability to perform motion tracking of small and flexible instruments without the need of a line-of-sight. Yet EMT is liable to ferromagnetic interferences due to surgical equipment and operating environment itself that degrade its accuracy and precision. Moreover, additional interferences may be originated due to the risk of sensor–sensor interaction when two or more sensors are in the immediate vicinity of each other.

Ideally, when choosing a tracking system, it is desirable that it will work with the same characteristics regardless the operating environment. From the PRA standpoint, this chapter tests the Polaris and Aurora system to provide spatial information regarding the needle and catheter tip. The following motion tracking requirements were considered:

### A. Refresh Rate

During PRA, as the physician inserts the needle towards the kidney stone, the needle spatial position and depth should be monitored at a rate that does not limit the physician's actions. Regardless of the number of sensors, the position and orientation of the sensors should be updated with a refresh rate of approximately 25 Hz. Both manufacturer specifications from Polaris and Aurora systems states refresh rates higher than 40 Hz.

### B. Concurrency

The motion tracking system must be able to track all the tools used during the surgical procedure. At the PRA, the system should be able to monitor the catheter located near the kidney stone and the puncture needle. Since any commercial system is able to track more than 8 sensors, they do not stand as an obstacle for this type of procedure.

### C. Working volume

The working volume defines a 3D space where the surgical tools can be detected by an electromagnetic field generator (Aurora system) or an infrared camera (Polaris system). For both tracking technologies, the signal/noise ratio decreases as the sensors are away from the camera or signal generator.

Electromagnetic sensors located within this volume respond with an induced voltage across the sensor that is proportional to the field strength self-excitation at that location. The power drop-off is inversely proportional to the fourth power of the distance from the field generator [131]. On the other hand, optical markers must be place in a line-of-sight with the tracking cameras, where the system performance may be influenced by ambient light.

Manufactures specifications for each tracking device define operating sub-volumes where it is possible to get the highest tracking precision and accuracy, while minimizing environmental interferences. During a surgical procedure, the overlap between the optimal working volume and the anatomical structures of interest should be maximized. Since the working volume is invisible, the camera or field generator positioning are usually a trial and error process. Both Polaris and Aurora systems states manufacturer working volumes higher than 500 $mm^3$. In the Polaris case, the working volume starts 1000 mm away from the camera sensor.

### D. Intrusiveness

Navigation frameworks that use optic markers or electromagnetic sensors intra-operatively may be obtrusive, because new hardware is inserted into a clinical environment. Its physical presence may affect the performance of other medical devices, such as imaging modalities, due to electrical interferences.

### E. Sensor Dimension and DOFs

Sensors should be small enough to be integrated or easily coupled to the catheter and needle used for PRA. The working channel of traditional needles for percutaneous punctures are less than 1.2 mm. For the Aurora system, this is not a problem since the smallest sensor have 0.5 mm of diameter. On the other hand, the optic markers must be visible from the camera and cannot be placed inside the patient or in the needle working channel. Both the Aurora and Polaris support 5DOF or 6DOF sensors.

### F. Accuracy

The sensors accuracy should be sufficient to effectively puncture the kidney stone vicinity and to obtain direct vision and manipulation of the stones using endoscope cameras or surgical tools. Therefore an accuracy of ∼3 mm will be enough for this kind of procedure. In ideal conditions, working specifications for Polaris and Aurora states accuracies less than 0.35 mm and 1 mm, respectively.

### G. Robustness

A motion tracking system is robust when it is able to tolerate perturbations that might affect the system's functionality. Such perturbations arise when tools or surgical equipment are introduced and removed from the working volume. Therefore, besides being accurate, the system should be robust to distortions and environment changes. For robust systems, accuracy errors can be corrected using static or dynamic methodologies [132].

The next sub-chapters describe the principle of operation of each tracking system, as well as the corresponding tests to validate the proposed solution at the level of the PRA. Since, the accuracy and precision of any OMT or EMT system may diverge greatly from manufacturer stated guidelines, which error sources depend on the operating environment, both devices were tested *in vitro*, *ex vivo* and *in vivo* conditions.

## 4.2 Optical Tracking for Puncture Guidance

### 4.2.1 Polaris System

Optical devices have been used in a variety of surgical applications, providing accurate, reliable and flexible surgical navigation systems [64, 90, 109, 133]. The Polaris is an optical measurement system that calculates the 3D position and orientation of tools within a specific measurement volume. This system includes a power supply unit, passive markers that should be coupled to application specific tools and a position camera sensor.

The camera sensor contains two arrays of infrared light emitting diodes which radiates and receives infrared waves through and from the Polaris working volume, respectively (Figure 4.1-1). These infrared waves floods the surrounding area of the passive markers coupled to the tool to be tracked (Figure 4.1-5). Since markers are coated with retro-reflective surfaces, the light is reflected back to its source instead of being scattered.

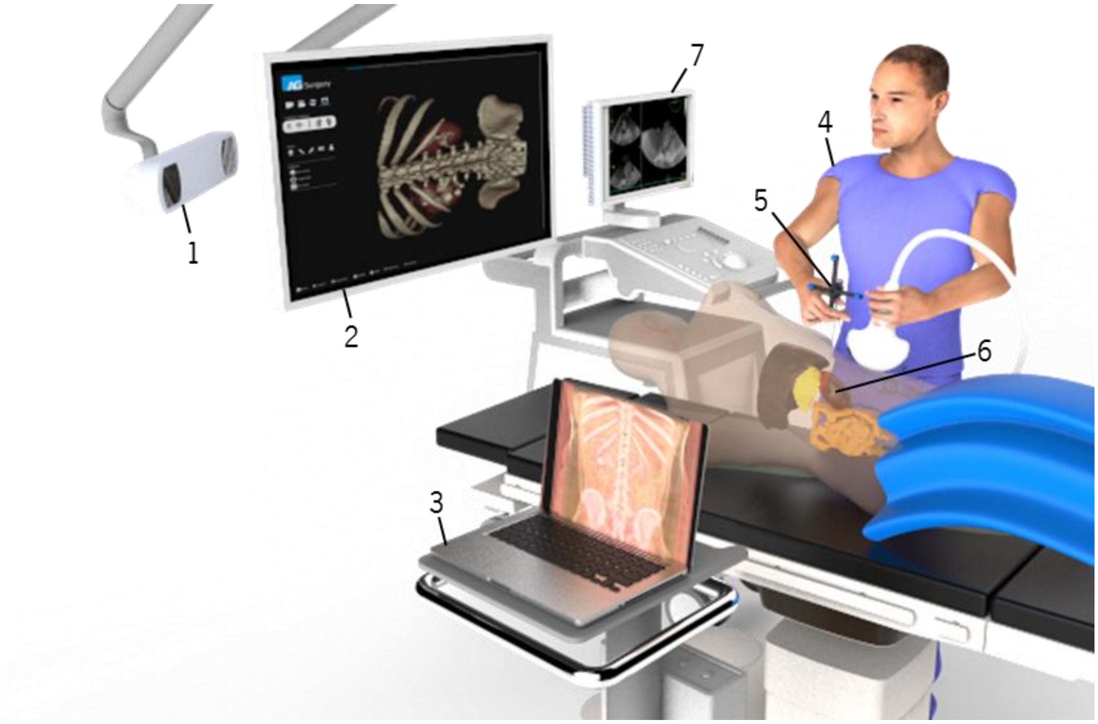

Figure 4.1. Representation of the surgical setup when using the Polaris system. The Polaris camera sensor (1) radiates infrared light that is reflected by the markers with reflective spheres coupled to the needle base (5). The surgeon (4) can be guided towards the anatomical target (6) using an OMT navigation interface (2) and ultrasound imaging modalities (7). The information retrieved by the OMT system is processed in a host computer.

The Polaris camera sensor can receive and measure the center position of passive marker, so that it can calculate in real-time, using triangulation technique, the position and orientation (6 DOF) of each tool that incorporate them [134].

### 4.2.2 Methods

The KidneyNav framework working together with the Polaris system was used to create a PRA virtual environment to guide the surgeons during planning and puncture.

Figure 4.1 shows a possible surgical setup highlighting different important elements, such as Polaris camera sensor, optical markers coupled to a surgical needle base, patient lying in the surgical stretcher, patient collecting system, monitor displaying the KidneyNav software, PC for processing and US system.

Given the optical nature of this methodology, it is not possible to track the catheter position and orientation near the anatomical target. Therefore, this target position was set manually by the user by picking a 3D region visualized in a pre-operative CT volume. Then, the surgical needle, coupling optical markers at its base, can be tracked in a 3D environment. Its positional data is transferred and processed by KidneyNav in a host PC and a virtual needle model is updated over an image volume acquired pre-operatively.

Intraoperatively, once the patient is registered with the image data and OMT system, the target point inside or near a kidney calix can be easily identified in the image data as well as the entry point on the skin surface. The vector defined by these two points defines the desired path for PRA.

Standard axial, sagittal, coronal views but also a 3D reconstructed volume can be used for guidance, by displaying the skin entry point, the alignment and depth of the needle relative to the selected trajectory and target point and a 3D representation of the needle (loaded by STL or PLY files) on the preoperative planning image data. All relevant anatomical structures are segmented and highlighted providing an enhanced environment to the user (already described in Chapter 3).

The development of this methodology include the following development steps:

A. KidneyNav interface for OMT and EMT technologies;

B. Polaris fiducials support: coupling tool that attaches the Polaris sphere markers to the needle base (Section 4.2.2-A);

C. Tool tip calibration: method to calculate the offset between the geometrical centre of the Polaris support tool and the needle tip (Section 4.2.2-C);

D. Paired-point registration based on the *Iterative Closest Point* [135] algorithm. It allows to select registration fiducial and target locations which are saved and used as input to the registration process (Section 4.2.2-D).

### A. KidneyNav | OMT/EMT Interface

KidneyNav modifications for tracking communication was driven by different high-level functions available in the NDI Combined API Sample (developed by NDI, Waterloo, Canada).

After connecting a tracking device (Polaris or Aurora system) via USB to a host computer, RS-232 communications are used to send and receive commands. Ideal configurations use 115200 baudrate, 8 data bits, 1 stop bit, 60 Hz of acquisition rate, with hardware handshaking and 0 parity bit.

The application will timeout when the connection to the system is lost, or if the amount of time the program polls the COM port for a reply before assuming communication has been lost. Here, the user can retry to resend the command, restart the COM port communication and close the application.

After stablishing successfully the communication between the host computer and the tracking device, the user must specify the tool definition files to be loaded to the system. By pressing a play button, KidneyNav initializes and enables all code variables needed to update the user interface.

During tracking, KidneyNav displays several status information including the frame rate; if the tool is partially out of volume, but can still be tracked by the system; if the tool is out of volume, but can still be reported by the system; if the tool is within the characterized measurement volume and is being tracked; if the tool cannot be tracked; if the markers are off angle; and maximum 3D error was exceeded.

### B. Polaris Fiducials Support

In order to use the Polaris system for PRA guidance, one start by defining and choosing a support tool to attach optical markers to the needle base, in order to report the 3D position and orientation of the needle for surgical guidance.

Although tools with a high number and spread out markers increase the tools visibility and accuracy, it may decrease the needle usability when manipulated by the surgeon. Therefore, a trade-off between ergonomics and accuracy was considered. Moreover, since the needle is not a rigid structure and tip deflections may occur while puncturing, the needle tip should be close as possible to the markers.

Different Polaris supported tools were studied and tested according to the following requirements:

1. Ergonomics: weight, size and coupling facilities so that it does not hampers how the needle is being handled;
2. Rigid material capable of holding all the fiducials markers throughout the entire procedure. Likely, it should be capable of being sterilized, without compromising the spheres reflectivity.

Since NDI Digital already commercializes supported tools assuring the second point, the efforts were directed to the study of the first point. To this extent, a qualitative study was performed to evaluate the ergonomic of different coupling tools (Figure 4.2).

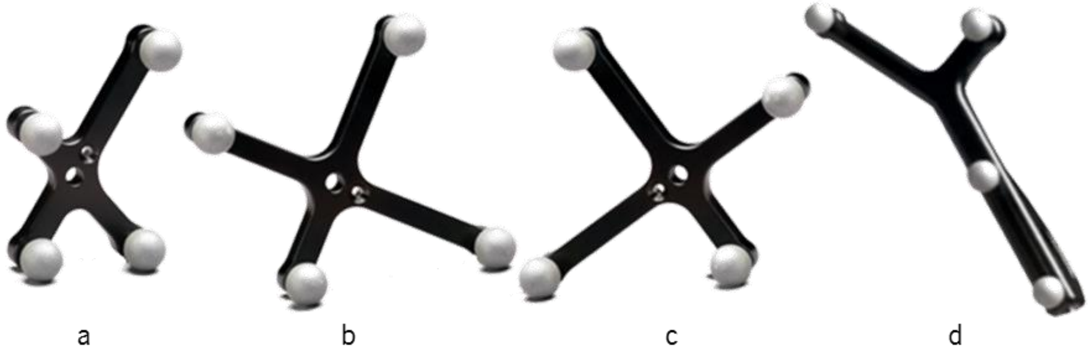

Figure 4.2. Representation of different Polaris supported tools: a) single-faced tool with a minimum marker spacing of 30 mm; b), c) and d) different geometries for a single-faced tool with a minimum marker spacing of 50 mm.

This support structure should:

- Maximize the line-of-sight with the Polaris camera to avoid marker occlusions;
- Avoid sphere markers with collinear positions to reduce situations where the marker becomes partially occluded by another that increases the overall tracking error.

Each structure was attached to the needle base through a tool clamp. This tool clamp allow a single and secure connection by means of hinged jaws, ensuring that the support tool does not move during the entire procedure.

## C. Tool Tip Calibration

### *I. ROM (Read Only Memory) File*

The Polaris sensor reports the 3D transformations of the passive support tool, from the Polaris coordinate system, according a tool definition file (ROM file) that states the following information for each tool (Figure 4.2):

- Geometry and manufacturing information;
- Tool origin;
- Maximum 3D error (maximum allowable difference between the measured and expected location of each marker on the tool);
- Maximum marker angle (maximum allowable angle between a marker and each Polaris sensor; for greater angles, the system will not use the data from that marker to determine the tool transformation);
- Minimum number of markers (minimum number of markers that the system must use in the calculation of a tool transformation).

However one is interested in receiving the tracked information regarding the needle tip. Therefore, a new customized ROM file was created using a proprietary software called *NDI 6D Architect* (from NDI). This file takes into account the offset between the needle tip and the support tool origin, avoiding future mathematical transformations between these two spatial coordinate systems. Such offset was measured by a tool calibration procedure based on pivoting algorithm.

### *II. Pivoting Algorithm*

With the pivoting method, a geometrical constraint is defined by rotating the needle while keeping its tip in a fixed location (Figure 4.3). For this purpose, the needle tip was fixed in a small hole drilled in an acrylic base. Then, in order to determine a translation vector $p_{tip}$, between the needle tip and the marker coordinate system, the following 3D vectors were considered:

a) $\vec{p}_{tip}$ - defined by one point at the marker coordinate system and another at the pivot point. This vector is a constant in the marker coordinate system and independent of the needle orientation;

b) $\vec{p}_{piv}$ - defined by one point at Polaris sensor coordinate system and another at the pivot point. This vector is a constant in the marker coordinate system and independent of the needle orientation;

c) $\vec{p}_{base}$ - defined by one point at Polaris sensor coordinate system and another at the marker coordinate system. This vector depends on the frame transformation between the marker and tracker frames, while the needle is rotated around the pivot point: $F_i = (R_i t_i)$, where $R_i$ is the current 3D rotation and $t_i$ the correspondence translation.

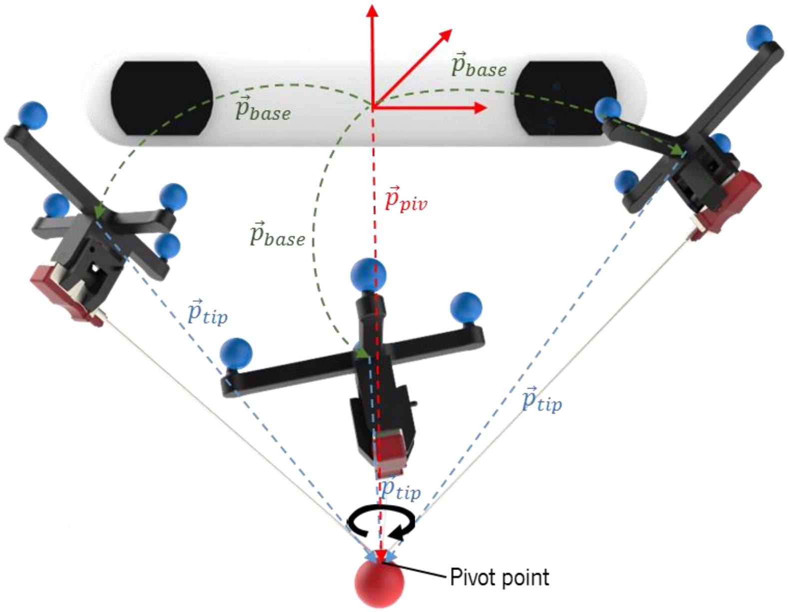

Figure 4.3. Schematic of the pivot method.

From the tracker coordinate system it is possible to reach the pivot position according to the following relation:

$$F_i * \vec{p}_{tip} = \vec{p}_{piv} \qquad \text{Equation 4-1}$$

First rotating $\vec{p}_{tip}$ by $R_i$ and then translation by $t_i$:

$$R_i * \vec{p}_{tip} + t_i = \vec{p}_{piv} \qquad \text{Equation 4-2}$$

Considering $p_{tip}$ and $p_{piv}$ as the 2 unknowns for Equation 4-2, the optimal solution of such linear relationship can be computed using the Moore–Penrose pseudoinverse mathematical method [136], providing the best fit and minimizing the sum of the squares of the errors:

$$Ax = b$$

$$\begin{bmatrix} R_0 | -I \\ \vdots \\ R_n | -I \end{bmatrix} \begin{bmatrix} \vec{p}_{tip} \\ \vec{p}_{piv} \end{bmatrix} = \begin{bmatrix} -t_0 \\ \vdots \\ -t_n \end{bmatrix}$$

The developed add-on for the KidneyNav framework provides a user guide interface that guides the user during all calibration steps.

### D. Paired-Point Registration

For surgical guidance purposes, a virtual tool should be draw and updated within the 3D image volume. Using the above methodology to create a custom ROM file, now the Polaris sensor reports the needle tip position and orientation in the Polaris world through the 3D transformation $\mathrm{M}_{NB,NT}$ (Figure 4.4). The next step is to perform a registration procedure to get the coordinate frame transformation between the Polaris world and the object study represented on the computer screen. The preoperative image data is aligned with the object study using the ICP algorithm ($\mathrm{M}_{ICP}$, Figure 4.4) [137]. Using the mouse pointer, the user must select at least four fiducial points $O\{i\}, i = 1,2 \dots n$ (with $n$ being the total number of fiducials points) using 2D slices or 3D volume showed in the screen (green points at Figure 4.4). Then, the user should touches the needle tip to the corresponding target points $T\{i\}, i = 1,2 \dots n$ (with $n$ being the total number of target points) on the object study body. Although four point are necessary for registration, the user may use as many as he wants.

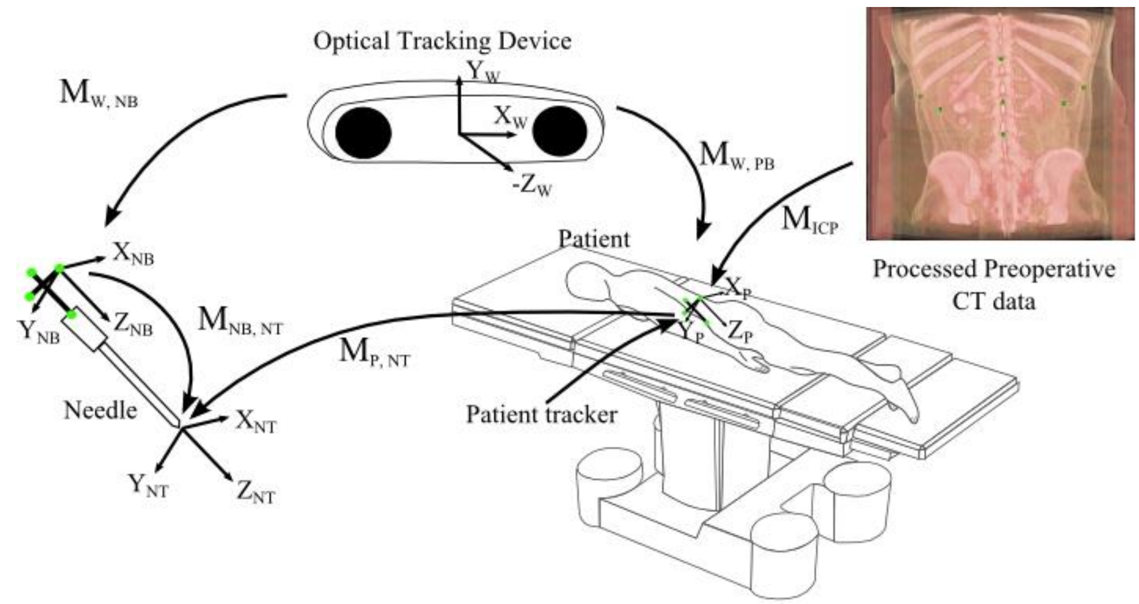

Figure 4.4. Registration overview.

The ICP algorithm estimated the optimum alignment vector between the two sets of points: $O\{i\}$ and $T\{i\}$. For all points in $O\{i\}$ it is calculated the minimum Euclidean distance sum, so that it is found the closest configuration points in $T\{i\}$.

### 4.2.3 Experiments

Different experiments were performed to quantify possible sources of errors that may compromise the accuracy of the PRA when using this OMT approach.

Such studies include laboratory *in vitro* tests, by using a calibrated acrylic plate and abdominal phantom, and also an in vivo clinical trial.

#### A. Laboratory Tests

##### *I. Polaris System Accuracy*

The Polaris accuracy was characterized using a six DOFs robot that worked as a precision positioning device. Since the Polaris system states a manufacturer accuracy of 0.35 mm, tests were performed with an ABB IRB140 (from ASEA Brown Boveri) which have a repeatability accuracy of 0.03 mm. The robotic arm was programmed to place the needle at different locations over a 500 × 500 × 500 in a total of 5000 points equally spaced.

The Polaris tracking tool was attached to the robot end-effector (Figure 4.5-a) assuring that the markers are directly facing the center of the Position Sensor (Figure 4.5-b) and there is a clear line-of-sight between them.

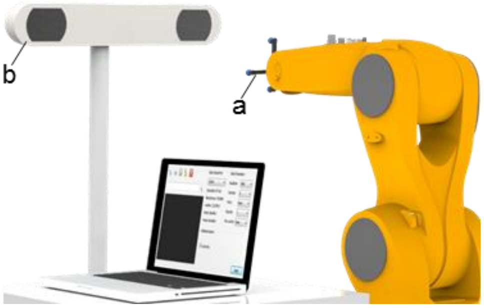

Figure 4.5. Setup for assessing the Polaris accuracy.

At each point, for each system (both Polaris and ABB) 200 samples were acquired, averaged and stored in different data files. Since both systems have different coordinate system, both data sets were rigidly registered though the ICP algorithm.

### *II. Polaris Tool Support*

15 users rated, from 0 to 5 - with 5 being the most favored tool and 0 being the least favored, each supported tool in order to select the best support tool (Figure 4.2) in terms of ergonomic aspects when handling the surgical needle.

### *III. Pivot Calibration*

The pivot calibration was performed by taking eight readings with the needle tip touching a single point at different orientations. The angle of the needle relative to the base was defined as high than 45° and not exceeding 120°. At each position, 100 Polaris readings were stored and its average value was used to calculate the distance between the supported tool center and the needle tip. The data from the pivot calibration was then saved and reused for the remaining tests.

### *IV. Registration Procedure*

The evaluation of the registration accuracy was two-fold: first the procedure was performed using a calibrated acrylic plate with different holes equally spaced by 25 mm; second, one used an abdomen phantom (US Examination Training Model "ABDFAN" - Kyoto Kagaku Co., Ltd). Virtual models of the acrylic plate and the abdominal phantom were loaded into KidneyNav by a STL and Dicom file, respectively (Figure 4.6).

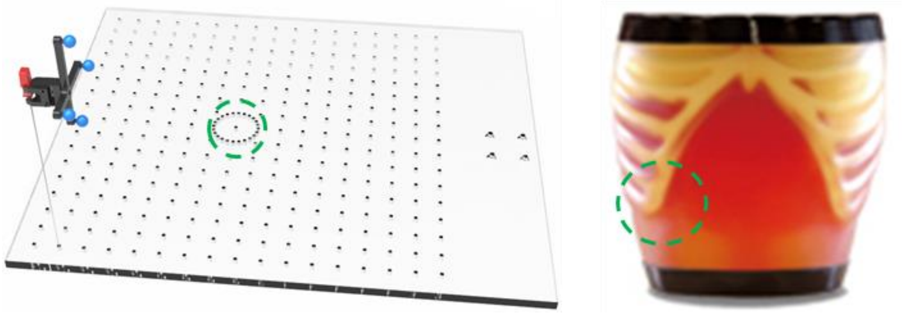

Figure 4.6. Representation of the acrylic plate (left) and abdominal phantom (right).

When using the acrylic plate, the user selected different plate holes by touching each hole with the tracked needle and recording its position. Corresponding virtual holes were selected using the KidneyNav interface. On the other hand, the registration between the abdominal phantom and the Dicom volume was achieved by selecting different points in the abdominal area in both models. Here the user can pick points using a 3D volume or different CT slices in axial, sagittal or coronal views.

The registration error was assessed by the Euclidean distance between the position where the needle tip is displayed on the screen and on it should actually be displayed.

Different users ($n = 22$) performed the registration procedure in triplicate to evaluate the system variability. First they were asked to perform the alignment by choosing 6 points in the object; second, they were asked to choose 6 points near a region of interest (kidney area when using the abdominal phantom or circular region at the acrylic plate center) (dashed circles in Figure 4.6).

### V. *Needle Deflections and Velocity Insertion*

Once the Polaris system tracks the needle tip, based on a ROM file that offsets the Polaris tool origin from the needle base, different tests were carried out to evaluate the best needle orientation, velocity and needle rotation along its main axis, so that the deflections are minimal.

These factors were tested in a gelatin phantom model and *ex vivo* porcine tissue. The gelatin phantom model was created with a gelatin concentration of 50% (m/v) [138]. Although the gelatin phantom cannot replicate identically the abdominal structure between the skin surface and the kidney, nor exhibiting the same tissue interfaces, it has mechanical resistance similar to the human flesh. A more realistic setup was achieved when using *ex vivo* porcine tissue of the abdominal area.

Both the gelatin phantom and *ex vivo* porcine were placed in a plastic box with different input and output points regularly spaced and perfectly aligned (Figure 4.7).

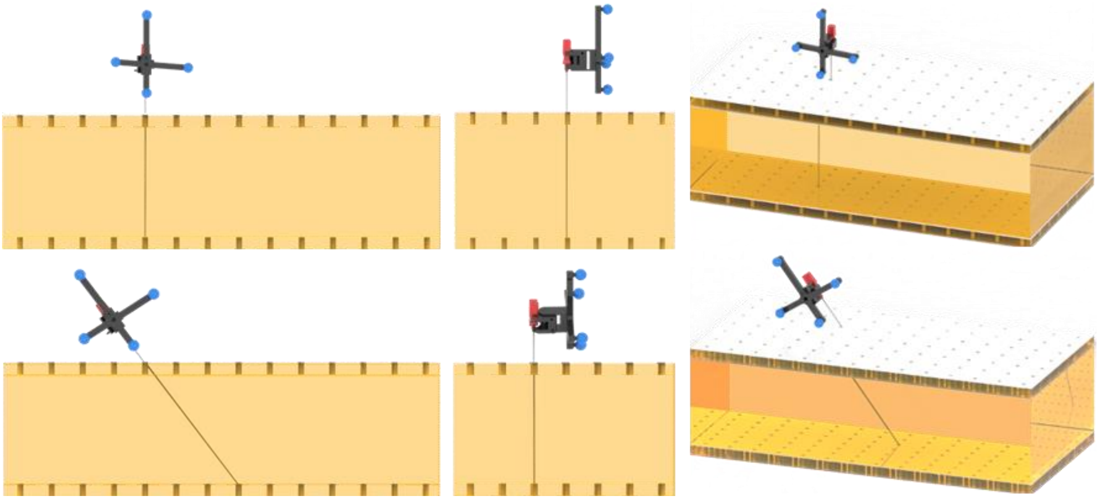

Figure 4.7. Representation of different setups used to study needle deflections and insertion velocity: angles $\alpha = 90°$, $\alpha' = 67°$ and $\alpha'' = 43°$ corresponding to distances $d\alpha = 120\,mm$, $d\alpha' = 141\,mm$ and $d\alpha'' = 173\,mm$, respectively.

Likewise with the registration experimenting tests, this setup was modeled and loaded into the framework and the virtual and real models were also registered through the ICP method. The phantom model was fixed to a table during all experiments in order to avoid slight motions between each experiment.

Three different angles, corresponding to different distances between the input point and the target one were tested (Figure 4.7). For each angle, two different velocities (with qualitative assessment - slow and fast) and needle insertion modes (with or without roll axis rotation) were executed by each user ($n = 14$) in triplicate. The experiments were randomized, so that a possible experience bias is reduced, whereby the last procedure may be facilitated over the first one due to an experience with the device. The needle deflection was calculated as the positional difference between the needle tip estimated by the Polaris system and the target hole from the initial straight line trajectory.

### B. Clinical Trial

Despite of the laboratory trials, the entire KidneyNav framework was tested in a clinical trial. The study was carried out at Hospital of Braga, Braga (Portugal) according to the internal ethical board. A female patient with staghorn calculi and requiring PCNL was informed about the planned procedure. The patient underwent multi-slice angio-CT in prone position (same position as during PCNL) a week before surgery.

Before surgery, all 3D relevant structures were segmented and manually edited. Specific transfer functions were chosen to highlight the kidney stone, kidney calix and bone structures. This segmentation procedure was performed pre-operatively. While the patient was being anesthetized, the Polaris support and sterilized tools were coupled and calibrated with the surgical needle.

Intraoperatively, the surgeon performed the registration procedure by placing the needle in rigid bone structures and near the kidney area. US checking was used to assure that the needle was placed correctly.

After the registration procedure and with the patient fixed on the operating table, the surgeon placed the needle near the skin puncture site and perform needle orientation based on the visual feedback. This trajectory was followed and monitored using US real-time image. Due to ethical constraints and lack of system certification, this framework worked as an additional feedback tool for the routinely guidance strategies (US and fluoroscopic imaging), not interfering with the current adopted clinical workflow.

## 4.2.4 Results

### A. Laboratory Trials

#### *I. Polaris Accuracy*

The color range in Figure 4.8 gives the difference in millimeters between the points acquired with the Polaris system and the robotic arm. Within the 500 × 500 × 500 mm volume, the Polaris system was accurate to better than 0.5 mm. These results shows a greater error in the volume periphery and minor error near the Polaris sensor. Both results are in accordance with the system manufacturer specifications.

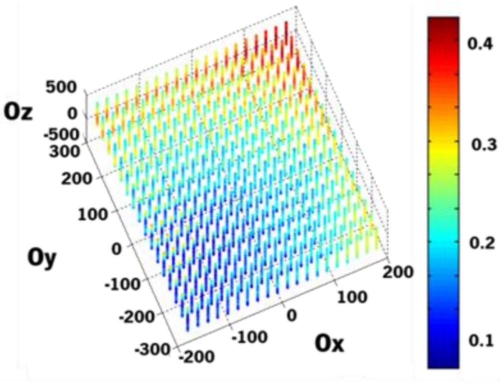

a

Figure 4.8. Positional difference (mm) between the points acquired by the robotic arm and the Polaris system.

### I. *Polaris Tool Support*

Figure 4.9 shows the rating results about the Polaris supported tool preferences (Figure 4.2). The tool Figure 4.2-b was the favorite one (average score of 3.93±0.79) with significant differences when comparing to the other tools ($p < 0.05$, t-test Welch).

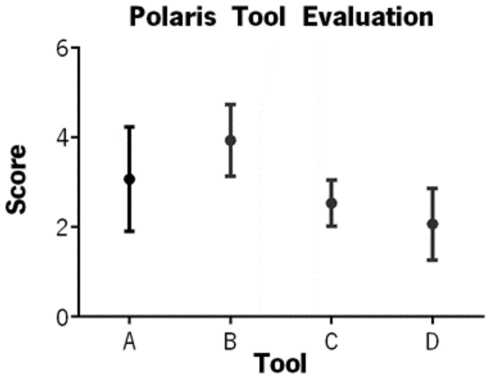

Figure 4.9. Rating scores for different Polaris support tool: A, B, C and D to Figure 4.2-a, -b, -c and –d, respectively.

### I. *Pivot Calibration*

The pivot calibration was performed in total 10 times. The offset, between the needle tip and the Polaris tool center, was successfully calculated with negligible difference (< 0.5 mm). The offset values for $Ox$, $Oy$ and $Oz$ axis were 199.35±0.18 mm, 5.97±0.06 mm and 37.28±0.23 mm, respectively.

### *II. Registration Procedure*

The alignment error was 0.39±0.07 mm if the acrylic plate and virtual holes were visually aligned. During all test, the main source of error was the incorrect selection of the matching pairs of points.

Table 4.1 shows the system variability when the points were determined randomly or centered near a region of interest for both the acrylic plate and abdominal phantom.

Table 4.1. Registration accuracy errors (n=22).

| **Registration** | **Fiducials Markers** | |
|---|---|---|
| | Random (mm) | Centered (mm) |
| **Acrylic Plate** | 1.23±0.43 (0.85 – 3.00) | 1.14±0.36 (0.42 – 1.72) |
| **Abdominal Phantom** | 2.11±1.03 (0.78 – 3.41)* | 1.46±0.53 (0.64 – 2.47) |

* t-test Welch (see attachment 1 for more detail): statistical difference against the acrylic plate setup with centered points

The minimum errors were obtained using the acrylic plate with centered points ($1.14 \pm 0.36$ mm) without significant differences ($p > 0.05$).

Although no significant statistical differences were found within the same test setup (Acrylic Plate or Abdominal Phantom), the registration accuracy was dependent on the spatial position where the targets and source points were chosen. The accuracy was better near the selected points and degraded to locations near the periphery.

### *III. Needle Deflections and Velocity*

At the beginning of the test, the needle tip and shaft were perfectly aligned with the puncture trajectory towards a specific target. Table 4.2 and Figure 4.10 shows the needle deflections and insertion velocities when using the gelatin phantom and *ex vivo* porcine tissue. Whole experiments result in a trade-off between the speed of needle insertion and its deflection to keep a straightness of the insertion trajectory. As shown in Figure 4.10, the needle deflection was higher when the tests were performed in *ex vivo* porcine tissue.

**Phantom Model**

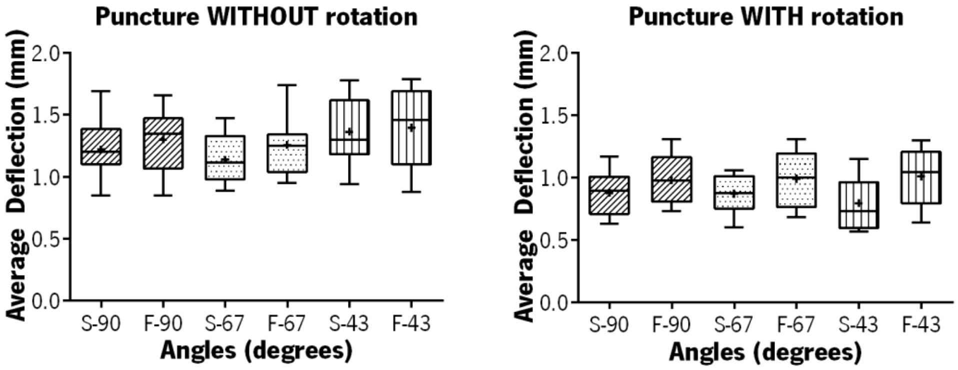

**Ex Vivo Porcine Model**

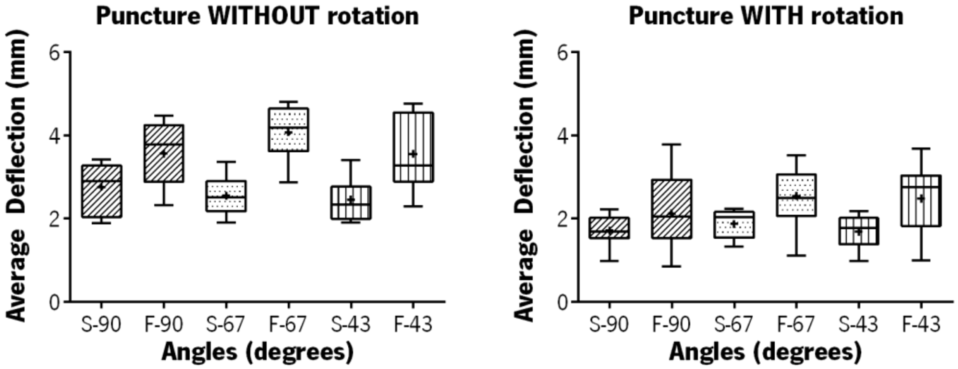

Figure 4.10. Boxplots (see attachment 1 for more detail) of the needle deflection results when puncturing the gelatin phantom or *ex vivo* tissue. The angle prefix S- and F- gives velocity information, e.g. S-90 is a slow insertion at 90 degrees (see Table 4.2 for velocity information). [a] t-test Welch: statistical difference against the same angle (WITH rotation); [b] t-test Welch: statistical difference against the same angle (same mode of insertion).

Table 4.2. Average and standard deviation of the needle insertion velocities.

| **Insertion Mode**<br>S- "Slow"<br>F- "Fast" | **Velocity** | | | |
|---|---|---|---|---|
| | **Without** Needle Rotation | | **With** Needle Rotation | |
| | Phantom Model | *Ex Vivo* Porcine | Phantom Model | *Ex Vivo* Porcine |
| S-90 | 1.49±0.28 | 1.07±0.21[a] | 0.98±0.26 | 0.82±0.19 |
| F-90 | 3.01±0.93 | 2.79±0.52[a] | 2.59±0.46 | 1.87±0.47 |
| S-67 | 1.25±0.24[a] | 1.55±0.37[a] | 1.04±0.23 | 0.70±0.15 |
| F-67 | 2.90±0.75[a] | 2.95±0.68[a] | 2.46±0.53 | 1.84±0.22 |
| S-43 | 1.41±0.23 | 1.19±0.18[a] | 1.02±0.15 | 0.80±0.22 |
| F-43 | 2.81±0.71[a] | 2.79±0.68[a] | 2.29±0.39 | 2.1±0.51 |

[a] t-test Welch: statistical difference against the same angle and setup but WITH rotation.

The maximum needle deflection was found when experimenting with the *ex vivo* porcine model and insertion with needle rotation (4.8 mm). The minimum value was 0.57 mm when inserting the needle also with rotation but in the phantom model.

Results show that the needle tip can be deflected from its initial straight line trajectory (Figure 4.11) in different ways. As represented in Figure 4.11–c and –d, the Polaris system was not sufficient to predict the tip actual position. Such situations were reduced when inserting the needle at slower velocities and by rotating its axis. For both experiments, needle deflections can be minimized by 0.36 ± 0.11 and 1.09 ± 0.34, respectively, if rotating the needle axis during insertion. Finally, the average time for path planning was 33.52 ± 7.33 seconds and 35.21 ± 9.85 seconds for the phantom model and *ex vivo* porcine, respectively ($p > 0.05$).

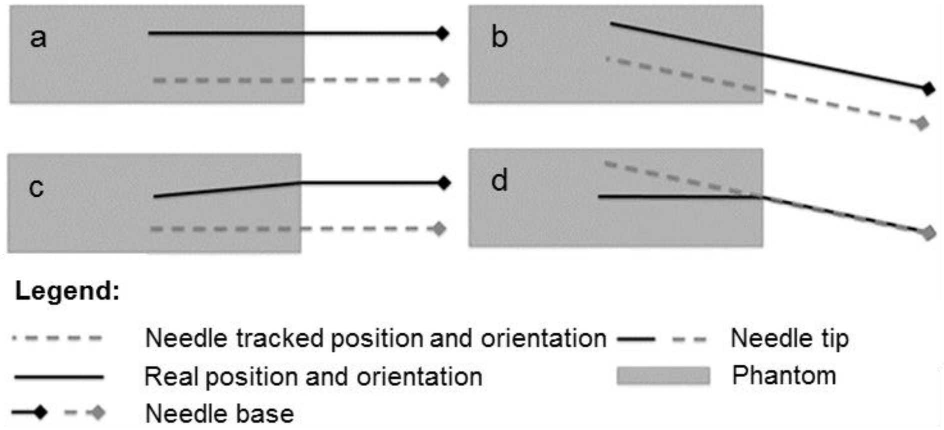

Figure 4.11. Illustration of the main deflection ways.

### B. Clinical Trial

The results obtained in the laboratory experiments were transmitted to the surgeon to perform this preliminary clinical trial. Before surgery, all 3D anatomical structures were segmented and highlighted using rendering transfer functions. This process take about 4 minutes.

The surgeon advanced the needle with intermittent C-Arm imaging or US to evaluate the virtual path and to make corrections in the needle path (Figure 4.12). If necessary, the needle was partially withdrawn and redirected to achieve the path to the target. A single attempt was sufficient to achieve a successful kidney puncture without any complications. The time needed by the surgeon to evaluate the virtual trajectory displayed by the KidneyNav software and to orientate the needle at skin surface was 32 seconds. On the other hand, 265 seconds were needed to perform a successful renal puncture from the skin surface to the puncture target.

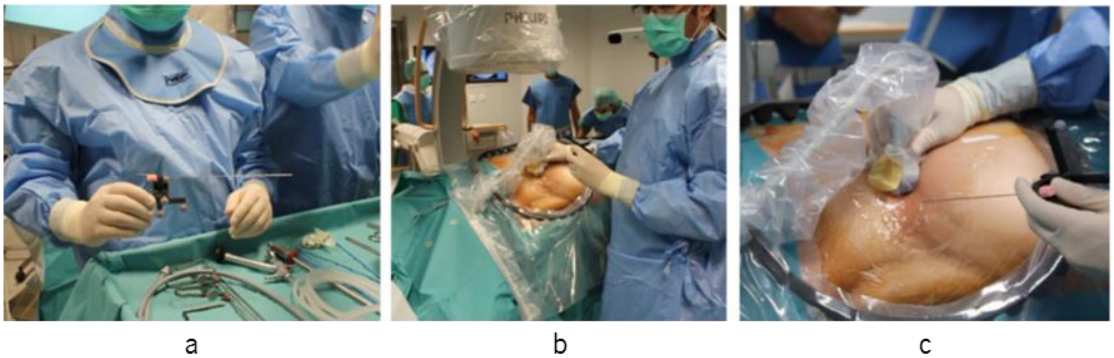

a b c

Figure 4.12. Clinical experience with *KidneyNav framework*: a) Polaris passive markers attached to the needle base; b and c) percutaneous puncture using US, C-Arm fluoroscopy and tracked needle.

## 4.3 Electromagnetic Tracking for Puncture Guidance

### 4.3.1 Aurora System

EMT potentially may be used to guide PRA interventional procedures, since it can provide accurate tracking without the line-of sight requirements of OMT systems. In order to track medical devices such as needles and catheters this system comprises the following hardware devices: field generator, sensor interface units (SIU), system control unit (SCU) and electromagnetic sensors.

The planar field generator emits a low-intensity and varying electromagnetic field that establishes a working volume. When the electromagnetic sensors are placed inside this working volume, small currents are induced in the sensors. These induced voltages are measured by the SCU that calculate the sensors position and orientation. The SCU also transmits the positional data to a host computer using a serial port connector, for subsequent processing and navigation.

The electromagnetic sensors are connected via a SIU to the SCU. This SIU works as an analog-to-digital converter and amplifier of the electrical signals from the sensors to an SCU, decreasing the possibility of electromagnetic interferences in the operating room.

The low electromagnetic field strength can safely pass through human tissue, making it an ideal system to track surgical instruments inserted inside the human body through natural orifices or small incisions.

Finally, the electromagnetic sensors can be embedded into the working surgical tools. For this work, one acquire two modified surgical instruments: one 18G/180 mm Chiba needle; and one ureteral catheter with 1.1 mm diameter and 2 m length. Both incorporate an electromagnetic sensor with 5 DOF at its tip, not being able to infer the orientation about their long axis (roll axis).

### 4.3.2 Methods

#### A. EMT Navigation

The introduction of the Aurora system in the PRA workflow will modify the first two PCNL surgical stages: (a) the trans-urethral catheter placement and (b) the percutaneous puncture.

### *I. Trans-Urethral Catheter Placement*

On the first surgical step, an Uretero-Reno-Fiberscope Flex-X™ from Karl Storz is trans-urethrally placed from the urethra towards the desired renal calyx.

In contrast to the currently used methodology, the catheter will be guided towards the anatomic target using the Flex-X™ camera without requiring other medical imaging modalities. Furthermore, since Flex-X has a working channel of 1.2 mm, it will allow the integration of a positioning and orientation electromagnetic sensor with six DOFs at its tip from Aurora motion tracking system (NDI, Waterloo, Canada). Here the electromagnetic sensor, located at the Flex-X™ tip, will act as an anatomic target locator, operating as a GPS (global position system) for the puncture site.

According to Flex-X™ tip orientation it will be possible to place the sensor in the desired calyx, where the calculi target is located, allowing the surgeon to choose the best virtual trajectory for the percutaneous puncture.

### *II. Puncture Stage*

On the second surgical step, a virtual trajectory will be determined by the relative orientation and position differences retrieved in real-time by both needle and catheter EMT sensors.

This virtual trajectory displayed will be used to confirm that the catheter and needle are parallel aligned. If necessary, the surgeon can redefine the catheter orientation, and the virtual trajectory will be real-time updated. This procedure provides constant real-time positioning feedback (beep sound and 3D representation) to the surgeon, allowing him to accomplish a perfect orientation of the needle at all times, even in the presence of anatomical changes, such as tract dilatation, respiratory movements and needle deflections, among others.

The beep sound was generated by asynchronously and repetitively playing a MP3 file with 0.15 seconds of duration. This sound was played with a frequency calculated with the common linear equation: $y = mx + b$. The slope $m$ of such equation was given by the distance between the catheter and needle EMT sensors. The idea is that the frequency should increase when the needle tip is close to the catheter tip. The $x$ and $b$ were experimentally calculated ($x$=17 and $b$=60), by moving one sensor towards and away from another and by qualitatively evaluate the sound feedback.

Figure 4.13. Representation of the surgical setup when using the Aurora system. The Aurora field generator (3) creates an electromagnetic working space where the needle (5) and catheter (6) can be manipulated. Both tool are wired (4 and 7) connected through the SCU to the KidneyNav software (2). The surgeon can be guided towards the anatomical target (6) using a navigation interface (1).

Concerning this new tracking methodology, Figure 4.13 shows a new surgical setup. When comparing to Figure 4.1, the Polaris sensor is substituted by the Aurora field generator (3 in Figure 4.13). Now it is possible to track accurately the needle tip with an electromagnetic sensor (5) and the anatomical target using a tracked catheter (6). In contrast with the Polaris system, the Aurora tool must be wired connected to the SCU (4 and 7) that communicates with the KidneyNav software (1 and 2).

### B. Animal Preparation

This EMT approach was tested using different female pigs (Sus scrofus domesticus) with various weights (25-35 Kg). Before surgery, the animals were fed with liquids for 3 days and then restrained from food (24 hours) and water (6 hours) before the surgical tests.

All procedures were carried out with the pigs under general anesthesia, with 5.0 mm endotracheal intubation and mechanical ventilation. Pre-anesthesia medication consisted of an intramuscular injection of 32 mg/mL azaperone, reconstituted with 1 mg/mL midazolam with a dose range of 0.15-0.20 mL/kg.

The venous access was obtained through an intravenous line placed at the marginal ear vein. The anesthesia was induced with 3 μg/kg fentanyl, 10 mg/kg thiopental sodium, and 1 mg/kg vecuronium. It was maintained with 1.5% to 2.0% of sevoflurane and a perfusion of 1 mg/kg per hour of vecuronium. All pigs received an intramuscular injection of 1 g ceftriaxone before the tests beginning.

### 4.3.3 Experiments

Likewise with the Polaris system, *in vitro* and *in vivo* experiments were performed to evaluate the accuracy and performance of the EMT framework for PRA.

*Ex vivo* tests aimed to understand and quantify the Aurora system technical characteristics, such as precision, accuracy and critical system problems e.g. electromagnetic interferences. On the other hand, *in vivo* animal trials, with more dynamic characteristics, aimed to define and evaluate the surgical setup, planning and puncture time, system reliability and efficiency for PRA.

#### A. Laboratory Trials

##### *I. Electromagnetic Interferences*

The purpose of this test was to investigate error sources that might compromise the EMT accuracy during surgical navigation.

This experience starts by putting the field generator on a position arm which offers flexibles setup options around an object of interest, e.g. abdominal phantom placed in an electromagnetic free environment. Then, both the needle and catheter sensors, adjacently fixed to each other, were moved randomly along the working volume. The positional difference between both sensors was transmitted and stored to a host computer. In absence of electromagnetic interferences the difference between both sensors should be a constant with negligible variances.

Because one aims to quantify the mean accuracy within this navigation volume, different surgical tools made with different material were placed inside the navigation volume and in the vicinity of the electromagnetic sensors. For each material, one compared the sensors positional difference with the values acquired when any electromagnetic interference exist. The following materials were evaluated due to its usage during PCNL:

- Stainless steel: the majority of medical instruments are manufactured with stainless steel due to its strength and durability. One evaluates electromagnetic interferences of this material by using different surgical instruments such as ureterorenoscope, cytoscope, telescopes, scalpes and forceps.
- Tungsten Carbide: is used in the manufacture of such instruments as needle holders, scissors, pin cutters and pliers;
- Mild steel: this metal is almost obsolete because its tendency to chip and contaminate other instruments. Only scissors were used to test this material.
- Aluminium: only certain instrument parts and cases are manufactured from aluminum due to its lightweight, e.g. handle and or body of the instrument and not the tool itself (scissors and forceps)
- Titanium: The high cost of using titanium for instrument manufacture is often prohibitive. Due to its lightweight, it is commonly used for microsurgery tools, e.g. forceps, laparoscopic tools.

#### *II. Ex Vivo Trial*

*Ex vivo* tests were performed with static characteristics. The model was built with a flap of full thickness (∼8 cm) porcine skin, with subcutaneous fascia and muscle (from a commercial butcher market).

The catheter integrating an Aurora sensor at its tip was randomly placed ∼8 cm away from the skin surface. With different positions and orientations the catheter tip was hidden from the user throughout whole procedure. Then, the user must orientate the needle at the skin surface and finally drive the needle through the selected path, until it reaches a 3 mm neighborhood of the anatomic target.

These tests were performed by 2 different groups: naive ($n$=16 with no experience with PRA) and expert ($n$=5 with more than 2 years performing minimally invasive surgeries). For both groups, each individual performed 3 punctures. Before the tests, each user could practice and become familiar with the software interfaces (up to 5 minutes). The catheter position was always changed in order to avoid the memorization of the puncture trajectory.

### B. Animal Trials

The animal experimental studies were approved by the ethical review boards of Minho University, Braga (Portugal). The animal was monitored by a veterinary anesthesiologists throughout the study.

This experiment starts by placing the pig in supine position. This first stage is used to identify the ureteral orifices of both kidneys using a rigid cystoscope. Then, ureterorenoscopies were performed bilaterally. An ureterorenoscope with 1.2 mm working channel allowed to put the ureteral catheter into the desired puncture site. Figure 4.14 represents the experiment setup.

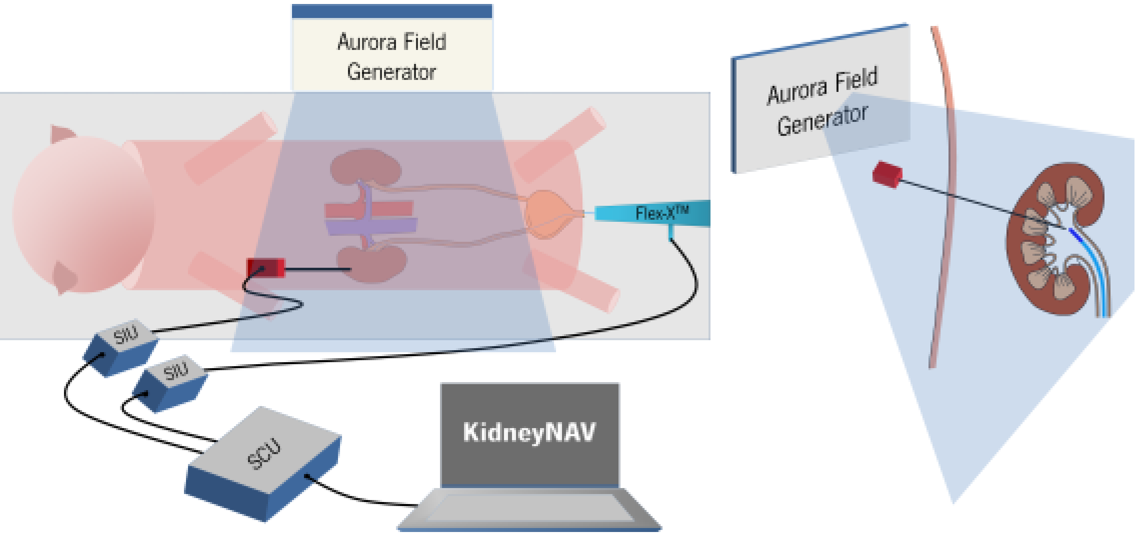

Figure 4.14. Overview of the animal trial for percutaneous collecting system access.

After positioning the ureterorenoscope at the puncture site, resorting to a direct video view, the surgeon inserted the needle into the calyceal fornix by the following actions:

1. Orientate the needle through a virtual direct path, aligning the needle tip with the target position;
2. Puncture the first skin layer and repeat step 1);
3. Drive the needle through the selected path, until it reaches the anatomic target (confirmed by the ureterorenoscope video camera).

The percutaneous punctures were performed for each pig at the ureter half-way between the kidney and the urinary bladder and in renal calyces in order to evaluate the puncture location influence.

### C. Outcome Measurements

The following surgical parameters were evaluated in order to ascertain if the proposed tracking solution confers any advantage to the surgeon performing PCNL:

a. Planning time: time needed by the surgeon to evaluate the virtual trajectory displayed at the software and orient the needle at skin surface;
b. Number of attempts: number of tries to reach the puncture site;
c. Puncture time: time needed to perform a successful renal puncture from the skin surface to the puncture target. When the needle tip was visible by the ureteroscope camera, the needle pass was considered complete.

The experiments were performed by an expert surgeon and a resident in order to avoid a supposed bias related to surgeon ability. Furthermore the puncture location was also analyzed as a variable influencing the above outcomes.

## 4.3.4 Results

### A. Laboratory Trials

#### *I. Electromagnetic Interferences*

The needle and catheter were adjacently placed with 10 millimeters distance between them. No relevant interferences were found when using stainless steel, titanium or tungsten carbide. In these cases the maximum error was not significant (<0.2 mm). The catheter can be placed inside the ureterenoscope or cytoscope working channel without losing tracking accuracy.

When using mild steel or aluminum instruments one found that the error increase proportionally with the distance between the sensors and the ferromagnetic material. Maximum errors of 8 and 15 mm were found when maneuvering EMT sensors in the working volume periphery and a mild metal or aluminum, respectively, were placed in the middle of the working volume. When aluminum tools, e.g. forceps or scissors were manipulated ~7 cm away from the electromagnetic sensors, the maximum error was less than 1 mm.

#### *II. Ex Vivo Trial*

Table 4.3 summarizes measured outcomes (median and range values) for *ex vivo* experiments performed by naive and expert subjects. As shown the median is less for the expert group than the naive one. However, lower values were always obtained by the naive group. Significant differences exists only during puncture ($p < 0.05$).

Table 4.3. Measured outcomes related to surgeon skill and puncture location.

| **Measures**<br>Median (min – max) | ***Ex Vivo* Testing**<br>Naive | Expert | p* |
|---|---|---|---|
| Planning Time (s) | 16 (11 – 56) | 14 (11 – 29) | 0.30 |
| Puncture Time (s) | 33 (12 – 128) | 25 (15 – 54) | 0.026 |
| Number of Attempts | 1 (1 – 2) | 1 (1 – 2) | 0.88 |

* Mann-Whitney test (see attachment 1 for more detail)

### B. Animal Trial

Overall 24 punctures were successfully performed without any complications: 12 in middle ureter and 12 in the kidney calyx (lower, middle or upper kidney calix).

Table 4.4 summarizes measured outcomes for whole procedures. Planning time was longer for the ureter case than the kidney (median 15 versus 13 seconds, range 14–18 versus 11–16; $p$ = 0.1).

Likewise, time to achieve ureteral puncture was significantly longer than kidney puncture, requiring 51 (range 45–67) and 19 (range 14–45) seconds ($p < 0.01$), respectively. Two attempts were needed to carry out the ureteral puncture, contrasting with a single attempt for the kidney ($p < 0.05$). When comparing the puncture time, planning time, number of attempts and final distance (Table 4.5), regarding the percutaneous renal access for the upper, middle and lower calyx, one achieved non-significant differences ($p > 0.05$).

Table 4.4. Surgical outcomes according to puncture location.

| **Measures**<br>Median (min – max) | **Puncture Site** | | |
|---|---|---|---|
| | Kidney calyx | Ureter | p* |
| **Planning Time (s)** | 13 (11 – 16) | 15 (14 – 18) | 0.1 |
| **Puncture Time (s)** | 19 (14 – 48) | 51 (45 – 67) | 0.003 |
| **Number of Attempts** | 1 (1 – 2) | 2 (2 – 4) | 0.01 |
| **Final Distance** | 2.1 (1.5 – 2.7) | 1.9 (1.4 – 2.7) | 0.79 |

* Mann-Whitney test between kidney calyx and ureter

Table 4.5. Surgical outcomes according to the kidney calyx.

| **Measures** | **Kidney Calyx** | | | |
|---|---|---|---|---|
| Median (min – max) | Upper | Middle | Lower | p* |
| **Planning Time (s)** | 15 (12 – 17) | 14 (12 – 16) | 13 (10 – 15) | 0.51 |
| **Puncture Time (s)** | 25 (14 – 48) | 19 (14 – 48) | 20 (14 – 40) | 0.9 |
| **Number of Attempts** | 1 (1 – 2) | 1 (1 – 2) | 1 (1 – 2) | 0.62 |
| **Final Distance** | 2.0 (1.8 – 2.2) | 2.1 (1.5 – 2.5) | 2.1 (1.9 – 2.7) | 0.79 |

* Mann-Whitney test

When results from experts and residents are analyzed independently (Table 4.6), one verifies that, despite of non-significant statistical differences (*p* > 0.05), there was a slight tendency of higher puncture and planning times, as well as, a great number of attempts for residents.

Table 4.6. Surgical outcomes according to the kidney calyx and ureter punctures.

| **Measures** | **Kidney Calyx** | | | **Ureter** | | |
|---|---|---|---|---|---|---|
| Median (min – max) | Resident | Expert | p* | Resident | Expert | p* |
| **Planning Time (s)** | 15 (13 – 17) | 13 (10 – 16) | 0.06 | 17 (17 – 19) | 15 (15 – 16) | 0.08 |
| **Puncture Time (s)** | 29 (14 – 48) | 19 (14 – 34) | 0.38 | 66 (64 – 68) | 48 (46 – 50) | 0.06 |
| **Number of Attempts** | 1 (1 – 2) | 1 (1 – 2) | 0.98 | 4 (3 – 4) | 2 (2 – 3) | 0.99 |
| **Final Distance** | 2.1 (1.5 – 2.2) | 2.0 (1.8 – 2.7) | 0.72 | 1.8 (1.6 –1.9) | 1.6 (1.4 – 2.0) | 0.12 |

* Mann-Whitney Test

Figure 4.15 shows different stages of this animal experiments.

Figure 4.15. Representation of the animal trial: a) and b) shows the surgeon performing the puncture stage; d) and e) shows 2D or 3D views as well as the ureteroscope video; c) animal punctured; f) shows the resident performing the retrograde study.

## 4.4 Discussion

Computer navigation systems, based in OMT or EMT technologies, are an attractive research area and have been suggested for different surgical procedures [52, 133, 139-141]. From the PRA point of view, this chapter performed several *in vitro*, *ex vivo* and *in vivo* experiments to evaluate the efficiency of the KidneyNav framework, working together with OMT Polaris and EMT Aurora systems.

### 4.4.1 Polaris System

The Polaris systems provides a solution to track surgical instruments with high accuracy, large working volume, portable and lack of environment interferences. Although it made possible to track tools without wires and mechanical parts, it required a line of view to the optical sphere markers. Therefore, it was not possible to accurately detect the needle tip positon inside the human body.

Different experiments were performed to assess and quantify the effect of possible sources of errors, namely (1) Polaris accuracy, (2) registration error, (3) needle deflections and (4) image resolution.

Firstly, the most clear error source was the inherent accuracy of the Polaris system. When the spheres were a partially occluded, the overall error increased because one sphere marker position can be calculated as being offset from its actual position. The main causes for optical occlusions, during the clinical trial, were movements of medical staff, medical devices and maneuvering of surgical instruments. One obtained an error below 0.5 mm which is similar to some works reported in literature [142, 143].

Another possible error of this approach is the rigid assumption to align the patient, Polaris world and image data. As well known, the kidney may exhibits complex respiratory-related motion. Nagel et al. [144] reported that the respiration curve in the abdominal region ranged from 2.9 to 16.9 mm with an average of 7.6 mm. One expects that the error might also increases towards the end, because of patient movements and organ manipulation. Hence, real-time registrations based in tracked organs may result in an improved efficacy but also more complex setups. Results show that using fiducials markers centered in a region of interest improves the system accuracy. Even though, an average error of $1.46 \pm 0.53$ mm (maximum error of 2.47 mm) was measured, because of human errors when selecting fiducials points at the optical and image space. By using motion compensation algorithms [145, 146] to reduce the respiratory curve, this interface may be sufficient for an assertive planning, with potential to reduce the number of puncture attempts and surgical complications [9, 47, 66].

Third, pre-operative image resolution may influence how the fiducials markers are chosen, influencing the final registration error. Moreover, the pre-operatory data should be acquired with the patient lying in the same position of the surgical procedure to avoid additional deformations.

Finally, since only the needle base is being tracked, additional errors may be caused due to needle deflections. Results show that deflections can be influenced by insertion velocities, angulation and rotation of the needle around its main axis, but also patient and respiratory movements. Likewise some literature reports [147, 148], results show that an increase in the insertion velocity lead to an increase in the needle deflection. As suggested by Meltsner et al. [148], this increase may be related to higher cutting and unbalanced resistance forces at the needle tip. At slow velocities and with needle rotations, results show errors up to 2 mm.

Although errors from individual sources are fairly small, the cumulative error may exceed the minima requirements to accurately puncture a kidney calyx. The final test was a preliminary clinical trial with much more realistic conditions because of blood irrigation, mechanical tissue properties, breathing. Moreover, it was a non-controlled environment with different elements of the surgical stuff moving around the patient.

Once pre-operative images are loaded and processed, the surgeon performed the registration between the virtual data and the patient. During navigation, a single view informed about the needle spatial position and orientation with respect to a rendered volume. Guided by this visual information and traditional imaging methods (C-Arm fluoroscopy), the surgeon selected an appropriate skin entry point, best needle orientation and trajectory to be followed, considering the anatomic kidney surrounding structures. Update rates around 22 Hz were sufficient for displaying without compromising the surgical navigation.

Even OMT is not the ideal tracking methodology for PRA, it can aid the surgeon by defining an initial orientation, with potential to reduce the number of control scans and thereby the radiation exposure. By displaying and updating in real-time the location of the surgical tools, this framework has the potential to increase the speed and safety of the procedure and at the same time gives confidence to the surgeon. Furthermore, this methodology can also be used for staghorn calculi or obstructive uropathy, where a physical obstruction may hinder the positioning of the desired calyx.

### 4.4.2 Aurora System

All the problems encountered with the OMT Polaris, prompt us to test the EMT Aurora system. The great advantage of Aurora over Polaris was the ability to track small EMT sensors inside the human body without any line-of-sight requirements [64].

The proposed methodology demands endoscopic imaging for real-time monitoring of the puncture target and two EMT sensors. The ureteral catheter and needle, both integrating an Aurora EMT sensor at its tip, are able to retrieve in real-time the position and orientation. The catheter remained associated to the puncture target (worked as a 3D real-time locator) and was permanently monitored by the EMT sensor and the ureterorenoscope video camera. Therefore it followed in real-time all the anatomic tissues deformations and movements – originated by the respiratory cycle and also by those induced to the patient. The surgeon inserted the needle guided by the virtual puncture path displayed in the KidneyNav interface.

An important proof-of-concept step was also achieved by succeeding in performing a direct ureteral puncture, even though the procedure took significantly more time, due to the ureteral movements, ureter small diameter and soft consistence, which made the needle glide on its surface. Even though this preliminary results provide prospective paths for other applications (e.g. Percutaneous Ureteral Lithotripsy), the main objective was to further corroborate the efficiency of the purposed puncture method in a small target cavity.

Interesting of note, no difference in operator skill was found in performing the puncture. Whereby, it is reasonable to speculate that this tracking solution may reduce the number of cases needed to perform an appropriate collecting system access and make it easier. Specific literature reports that the learning curve completion for PCNL surgical competence around 60 cases [44]. Considering the kidney access one of the most challenges phases, in this study a resident achieved the same skill level of an expert surgeon with only twelve cases.

The safety efficacy of different surgical positions for accessing the collecting system has been a controversial issue, with currently no established best practice consensus. The use of a real-time 3D trajectory proposed in this work may broad the use of supine position for the whole PCNL procedure. In this case, the surgeon does not need to reposition the patient (decreasing surgery time in about

30-40 minutes) and may improve levels of comfort for both patient and surgeon as described in literature[77]. On the other hand, when the patient is repositioned, there is a reduced risk of access dislodging, since the catheter remains permanently monitored by the EMT sensor and the ureterorenoscope camera.

Medical imaging assistance to puncture commonly requires approximately 10 min [9, 44, 78, 91, 101], often guided by X-Ray based imaging and *in vitro* conditions. Comparing the related results, one has achieved a puncture time improvements between 75 and 85% without any X-Ray need.

Due to its advantages, the Aurora system has been extensively tested last years in different clinical and nonclinical environments [64, 149]. Different works have reported errors of 0.71±0.43, with a maximum 3D root mean square positional accuracy of 2.96 mm. Although this values are higher than the Polaris accuracy, it remains highly suitable for PRA purposes [143].

Although Yaniv et al. [64] reported that electromagnetic systems may be susceptible to environment interferences in the operating room, we did not experience any kind of interferences that could tamper the tracking information. By evaluating the impact of the surgical instruments, composed by different metals (aluminum, stainless steel, titanium, tungsten carbide and mild steel), one create a more comprehensive list of requirements when using an EMT system in the operating room. Results show that only mild steel or aluminum can influence the error-proneness of EMT sensors. However, this may not represent a problem since mild steel or aluminum instruments have been replaced by stainless steel ones [64]. But, in order to guarantee that the system accuracy is not degraded, aluminum or mild metal should not be used during the surgical procedure. At least, they should not be placed inside the working volume while the puncture is being performed.

Other important evaluation was the intrusiveness of such modality. In contrast to other navigation frameworks, it will not increase the procedural time because the proposed system do not have a large setups and do not require additional steps like immobilization of the patient, preparation of the hardware, registration setup, or initializing of navigation components [1, 52, 64, 150].

The motion tracking field generator must be placed on the surgical stretcher as near as possible to the kidney abdominal area and with an appropriately orientation to minimize the probability of interference distortions. All other possible electromagnetic disturbance sources, such as, cellphones and usual operating room equipment's should kept at least 1.5 meters away from the working volume. The KidneyNav interface will advise when some possible interference exists or if the instruments are being maneuvered at the limits of the working volume.

When compared to the Polaris, the Aurora needs wires to transmit the information between the EMT sensors and control unit and a field generator positioned close to the interventional area. However, it did not restrict the access to the abdominal area, not being a limiting factor in any of the experiments. Since sensors are placed inside the human body during all operation, there was no need for a registration and calibration procedure.

Hereupon, the proposed solution may be the simple and easy way to select and follow the correct puncture path, as well as acquire the required skill to perform PCNL regardless of calculus site, large or multiple renal calculi, or an ectopic or malformed kidney.

# 5

# Multi-Sensorial Guidance Interface

The works assess the value adding multi-sensorial feedback for PRA guidance. It investigates the ability of using audio or vibrotactile sensations to localize, orient and guide the needle along a pre-planned puncture trajectory.

## Contents

## 5.1 Introduction

Visual interfaces have been proposed over the years for biomedical applications covering the diagnostic, planning and guidance of several surgical procedures [1-3, 81]. Currently available visual interfaces, aid surgeons throughout the entire surgical procedure, reducing the risks and possible unknowns [151].

Although new algorithms and registration techniques have been explored to link virtual and real worlds [108, 152-154], the interpretation of 2D images or 3D reconstructions are still a challenging task. For intraoperative complex procedures, visual interfaces may only provide good guidance capabilities for specific points of view. Often, surgeon's skills and expertise strongly affects the surgical outcome [153, 155-157].

In addition to the information received through our sight, audio and tactile information are nowadays becoming commonplace ways of transmitting information [158-161]. Hearing and touch are the second and third major human senses, respectively, being two promising and unique alternatives or complementary modalities for visual systems. Consequently, it allow the development of innovative hand- and eyes-free interfaces [162].

The idea of using new ways of feedback for puncture guidance during PRA, concerns the ability to create accurate and precise localization of the needle tip with respect to the anatomical target.

### 5.1.1 Audio Feedback Systems

First audio feedback methodologies have been explored due to their ability to create, process and localize sounds from complex data in a 3D space. Since computational requirements to generate audio are much smaller than for 3D graphics, this auditory interfaces were created in order to overcome technological limitations, such as limited real-time refresh rates, image poor resolution and rendering capabilities [163].

Nowadays, audio feedback is an attractive area of exploration for a wide range of medical or nonmedical applications [159, 164-166]. Due to the ability of surrounding the listener with sounds at specific locations, sound applications have emerged to create an immersive environments for computer games [164], warning systems for civil aircraft [163, 164], flight and military simulations

[159], guidance interfaces to blind people [159], night vision systems [159], airplane cockpit [158], guidance to athletes [167], augmented reality systems [158, 168], perceptual representation of biomedical data [163] and heart rate monitors [151].

To the best of our knowledge, audio feedback for computer aided surgery have only been only explored by four groups [151, 153, 169, 170]. Preliminary works were reported by Weber et al. [151], describing an audio system to guide a biopsy needle when perforating a gelatin phantom. Although they describe an application with great potential, quantitative or qualitative results are not reported.

Another audio feedback system, presented by Cho et al. [169], guides the surgeon to a cochleostomy location. The authors generate warning tones when an optical tracked drill is closer to the target (tones of 300 Hz) or reaching the target (tones of 900 Hz).

Hansen et al. [153] presents an audio display system to guide tracked instruments in open liver surgery. Audio tones with different frequencies are produced based in three margin areas (safe, warning and outside) defined according a predefined resection line. They report that a combined audio-visual feedback lead to a decrease of time looking to the screen (10% *vs.* 96%) and increase of time for the resection task (47 *vs.* 24 s). From the same research group, Black et al. [171] presents a new method to align and insert an ablation needle. They present two audio approaches. One is based into sequential x-axis, and then y-axis audio feedback. Another uses two repeated pulses played alternatively to align the surgical instrument. Within this second approach, y-axis errors are mapped with differences at the speed between pulses and x-axis errors are mapped with changes in the audio pitch. The authors reports that subjects were comfortable with both the visual and the auditory modalities.

Finally, Woerdeman et al. [170] evaluate the effect of audio feedback on instrument handling for image-guided neurosurgery. Sound feedback did not negatively influence the instrument handling, and surgeons felt that they had performed better (however without any statistical significant improvement).

From the analyzed literature, audio feedback advantages include faster processing data, high temporal resolution, parallel data streams and improves the degree of focus on the task at hand

[168]. Moreover, it creates an effective way to overcome the visual overload from complex data and due to its omnidirectionality, i.e. allows perceptions from any point in space without occlusions.

Low spatial resolution and perception, sound interferences, dependence of user are the main shortcomings [151, 163, 168].

### 5.1.2 Vibration Feedback Systems

Likewise audio feedback system, the usage of vibrotactile feedback has also been described in literature. For instance, vibrotactile has been reported as useful in improving awareness of critical events such driver responses [172], spatial guidance in pedestrian navigation [173, 174], alert system for blind or visually impaired persons [175, 176], gesture guidance [157], human-computer interaction improving realism with tactile display interfaces [177-179], immersive sensations in computer games [180, 181], body posture improvements (Janssen et al., 2010), and assistance in rehabilitation [182, 183].

Bach-y-Rita et al. [184] were pioneered to transform visual stimuli to haptic information. Images captured by a video-camera were transmitted to the skin assisting blind people with environment information. From then on, several authors investigate the best designs for fitting the body, the ideal configuration and number of actuators, minimum threshold for haptic detection, localization accuracy and precision and vibration patterns [153, 185, 186].

Hardly, a larger number of actuators is synonymous of a higher location accuracy [185, 187]. Gilliland et al. [187] tested the feasibility of a vibration helmet, with a variable number of vibration motors, to transmit information in a flight environment. The authors reported an accuracy of 93%, 76% and 47% when 6, 8 and 12 motors were used. Although they only test the system with a minor group, they suggest that an 8-site configuration provides a compromise between speed and accuracy. Thullier et al. [188] presented an compact matrix, composed by seven-by-seven array of electromechanical vibrators used to represent tactile patterns applied to a 16 $cm^2$ skin area. The authors indicate that, after familiarization, 80% of the subjects can recognize tactile patters for gesture guidance or instructional commands.

This work intends to study its ability to drive the surgeon though a virtual trajectory. The idea of using vibrotactile feedback to assist and drive trajectories have already been explored by some authors in different applications [189]. Weber et al. [190] explored the VibroTac device which integrates six cylindrical actuators, equally distributed on the arm's perimeter, with adjustable frequencies from 0 Hz to 190 Hz. When compared to verbal feedback, VibroTac was useful to guide the human operators towards a specific target, showing higher times to complete a translation (7.9 ± 3.5 s *vs*. 6.2 ± 1.3 s) but less times for rotations (5.9 ± 1.2 s *vs*. 7.1 ± 0.8 s).

Howard et al. [191] tested nine different combinations of visual and haptic guidance feedback. Vibrotactile feedback was provided using an eccentric rotating mass motor attached to the inner side of the finger holding instrument. The quality and speed task were evaluated when subjects followed a random and straight virtual trajectory using an optical tracked tool. Authors report that the addition of visual or vibration feedback show greater improvements, reducing error deviations from the ideal path.

Bluteau et al. [192] used a vibrating belt as a guidance system. Two belts were manufactured with a vibration intensity around 5000 rpm: one with 6 vibrators and other with 8 vibrators. Each vibration actuator was manually arranged around the abdomen of 9 tested subjects. Authors reported that vibration feedback introduced a decrease of spatial errors and need for visual feedback.

Hence, various innovative and disruptive devices were proposed for being attached for different human parts, e.g. head [185, 186], fingers [188, 191], forearm [189, 190], hand [179, 180, 193], upper body [174], tongue [161, 162] and foot [160].

Head has been the most preferable site for vibration wearables (e.g. headbands [185], headphones and glasses [175]). They have been studied in various environments, because they do not restrict the users maneuver ability (e.g. devices used in fingers, forearm, and hand), verbal communication (e.g. devices used in the tongue) or touch sensation (e.g. gloves).

Even being an ideal place for receiving feedback, some authors warned that the head sensitivity is not the same throughout whole area. Myles et al. and Weber et al. [194, 195] study and evaluate the sensibility of head surface. Both studies stated that vibration sensitivity is different for different head locations, where the crown of the scalp was reported as the least sensitive to vibration stimuli relative to areas close to the temples, forehead, and back of the head (most sensitive area).

Even ergonomics, positional efficiency and accuracy of a vibrotactile headband has already been studied [185], pattern codification for guidance, the ideal number of actuators and testing in real situations are still needed.

### 5.1.3 Audio and Vibration Feedback for PRA

From the reported applications, it is clearly seen that audio or vibrotactile feedback can considerably highlight 3D orientation and guidance, decreasing the dependence of visual faculties and improving insight into virtual data [159, 196]. They often improve perception capabilities, which may be altered due to continued procedures, fatigue, inaccurate insight and decrease of attention [165, 168].

When compared to other medical technologies routinely used for guidance (e.g. motion tracking systems, robotic devices, improved surgical tools, imaging systems), audio or vibrotactile feedback are relatively unexplored. The wider acceptance of such modalities will mostly depend on the quality and quantity of transmitted information, but also if the user can effectively learn how to use it [168].

In addition to the 3D feedback provided from the KidneyNav interface, this work explores the potentiality of new guidance interfaces including an improved 2D visual interface (from now on referred as NeedleView), a vibrotactile headband and 7.1 headphones able of generating 3D directional sounds.

## 5.2 Methods

### 5.2.1 Overview

In this section, we propose the application of a multisensorial feedback platform combined with the previous described 3D view of the KidneyNav to develop a more intuitive guidance system. At each time, the needle tip deviates from the path to reach the target, a set of audio and vibration signals will be generated and transmitted to the surgeon.

Such information will be perceived from a vibrotactile headband, 7.1 headphones and the NeedleView, that will aware and guide the surgeons towards the ideal path (Figure 5.1).

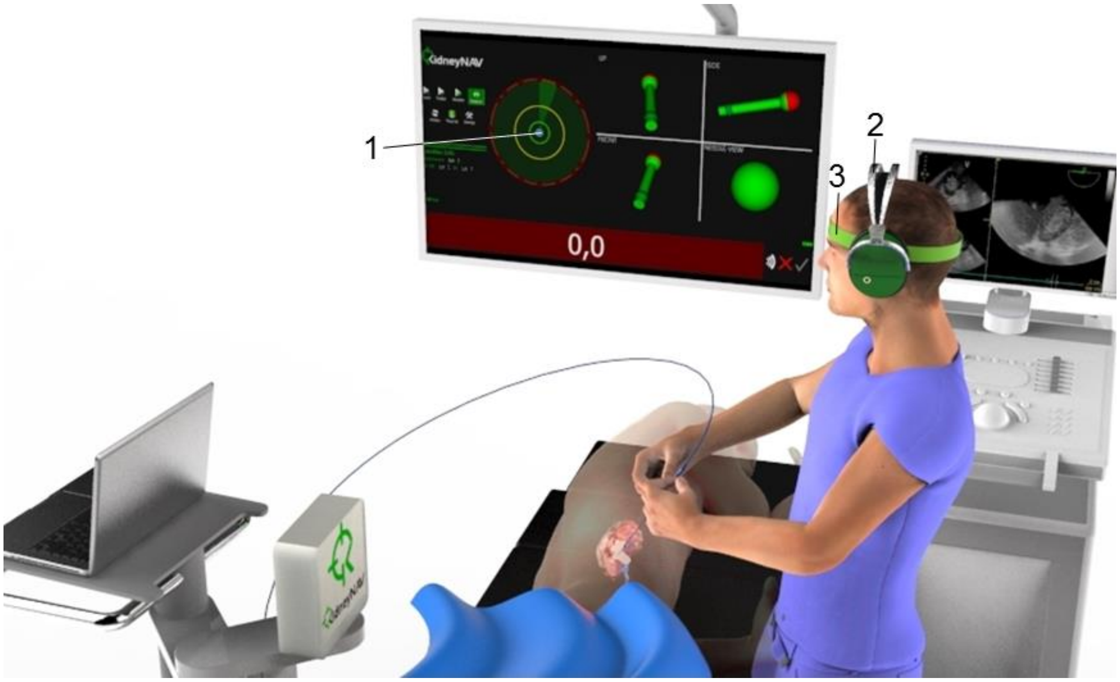

Figure 5.1. Representation of the new surgical setup considering the multi-sensorial interface: 1) NeedleView, 2) 7.1 headphones and 3) vibrotactile headband.

## 5.2.2 NeedleView

Sight devices used to support instruments aligning (e.g. weapons, airplanes, telescopes, etc.) were behind the idea of the NeedleView. Figure 5.2 shows the developed target sight. Vertically and horizontally alignments for the perfect needle orientation is achieved when a blue sphere is placed inside a white disk.

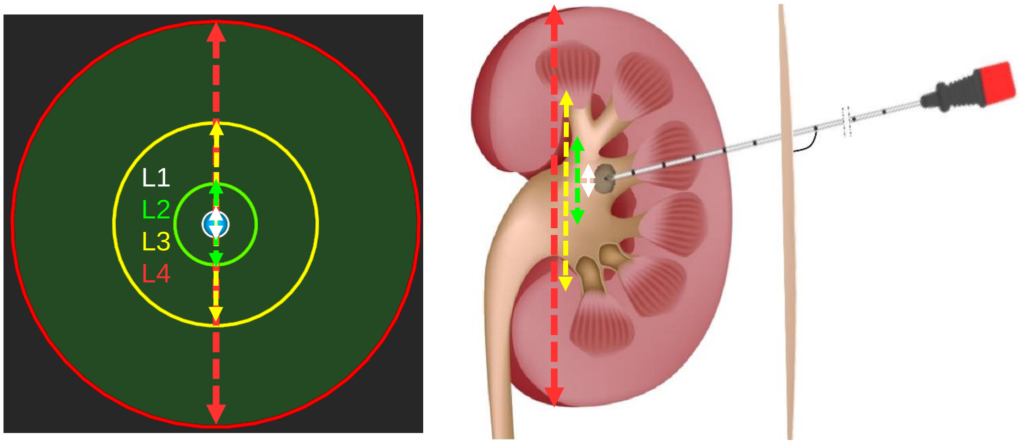

Figure 5.2. Representation of the NeedleView interface (right). The vertical arrows (white, green, yellow and red) show the size correspondence between the circles diameter and the kidney anatomy.

Once the needle is aligned in the right position, a green label showing the distance to the target will be displayed to the user. If any deviation occurs, a red label will be shown. Likewise any sight, the needle tip will reach accurately the anatomical target if the needle is inserted along the path without any deviation. Different color disks (white, green, yellow and red in Figure 5.2) were used to implement a score system that gives information about the current error with respect to the target:

1. White region informs the user that the needle will reach the target within a 2 mm error (approximately the size of a minor kidney calyx);
2. Green region informs the user that the needle will reach the target with a maximum error of 10 mm (proximately the side of a kidney medulla);
3. Yellow region informs the user that the needle will reach the target with a maximum error of 25 mm (proximately the side of a kidney pelvis);
4. Yellow region informs the user that the needle will reach the target with a maximum error of 50 mm (proximately the side of a kidney size);

The blue sphere will be drawn according a method that projects a ray in a 3D plane (Figure 5.3). Let $p_N(x, y, z)$ be the current needle positon and $\vec{v}_N(x, y, z)$ a 3D vector defined at $p_N(x, y, z)$ and the orientation of the needle tip. Let $P$ be a plane defined by the target position $p_T(x, y, z)$ and a normal $\vec{v}_T(x, y, z)$. The needle will accurately reach the target ($p_T(x, y, z)$) if a ray $\overrightarrow{R_N}$ starting at its tip position at $p_N(x, y, z)$ follows a direction $\vec{v}_N(x, y, z)$.

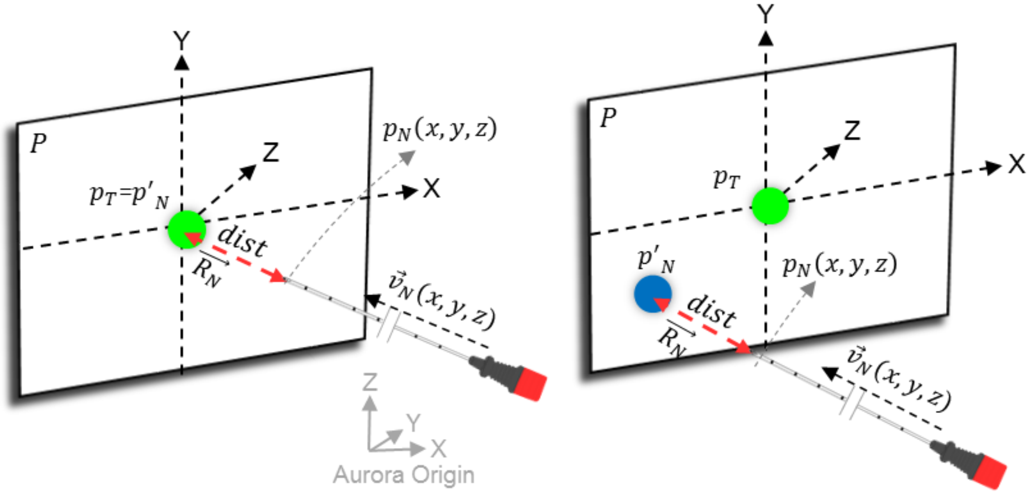

Figure 5.3. Representation of the ray-plane projection method to create the NeedleView visual interface.

The NeedleView represents graphically the intersection of the ray $\overrightarrow{R_N}$ with $P$ at a projection point ${p'}_N(x,y,z)$. When $p_T(x,y,z) = {p'}_N(x,y,z)$ the user is following the correct trajectory.

Any point $p_{Ray}(x,y,z)$ along $\overrightarrow{R_N}$ can be calculated according to (Equation 5-1):

$$p_{Ray}(x,y,z) = p_N(x,y,z) + t \times \vec{v}_N(x,y,z) \qquad \text{Equation 5-1}$$

where $t$ is a free constant that gives different points away from $p_N(x,y,z)$. ${p'}_N(x,y,z)$ is calculated by solving this $t$ parameter (Equation 5-2).

$$\begin{aligned} t &= -\frac{\vec{p}_N(x,y,z) \cdot \vec{v}_T(x,y,z)}{\vec{v}_N(x,y,z) \cdot \vec{v}_T(x,y,z)} \\ &= -\frac{|\vec{p}_N(x,y,z)| \times |\vec{v}_T(x,y,z)| \times \cos(\theta)}{|\vec{v}_N(x,y,z)| \times |\vec{v}_T(x,y,z)| \times \cos(\alpha)} \end{aligned} \qquad \text{Equation 5-2}$$

$\vec{p}_N(x,y,z)$ is a vector defined between $p_N(x,y,z)$ and $p_T(x,y,z)$; $\theta$ is the angle between $\vec{p}_N(x,y,z)$ and $\vec{v}_T(x,y,z)$; and $\alpha$ is the angle between $\vec{v}_N(x,y,z)$ and $\vec{v}_T(x,y,z)$. Finally, by solving Equation 5-2 in Equation 5-1, ${p'}_N(x,y,z)$ is given by Equation 5-3:

$$\begin{aligned} {p'}_N(x,y,z) = {} & p_N(x,y,z) \\ & + \left(-\frac{|\vec{p}_N(x,y,z)| \times |\vec{v}_T(x,y,z)| \times \cos(\theta)}{|\vec{v}_N(x,y,z)| \times |\vec{v}_T(x,y,z)| \times \cos(\alpha)}\right) \\ & \times \vec{v}_N(x,y,z) \end{aligned} \qquad \text{Equation 5-3}$$

Note that if $dot\big(\vec{v}_N(x,y,z),\ \vec{v}_T(x,y,z)\big) = 0$, the needle orientation and target plane are perpendicular. To avoid such cases, at the beginning of the puncture and after performing an initial orientation, $\vec{v}_T(x,y,z)$ is automatically set as $\vec{v}_N(x,y,z)$.

### 5.2.3 Audio Feedback

3D audio feedback was obtained by creating positional sounds varying one or more of the following characteristics: pitch (sound frequency), loudness (sound intensity) and playing location (sound source with a particular 3D location).

#### A. Audio Channels

According to the number of source sounds it is possible to classify sound systems as mono (1 discrete audio channel), stereo (2 discrete audio channels) and surround (N audio channels).

A mono system only produce sounds from a single source, being not able to transmit surround information. On its turn, stereo systems are able to reproduce sound from two independent sound sources, placed at the left and right of the listener. By changing the gain of each channel, it is possible to notice sound in the line between the left and right channel. Commons methods to produce 3D sounds based on stereo systems are based on modifications of audio amplitude or on the delaying the arrival of the sound into the listener [197]. Lastly, true surround sound are created by placing sound sources anywhere in 3D space. The spatial sound resolution is dependent in the number of sound sources surrounding the listener.

This work makes use of 7.1 headphones for producing surrounding audio: 7 directional channels left, center, right, left surround, right surround, left rear surround and right rear surround and 1 subwoofer that enhances low frequencies. This headphones are able to produce spatialized sound in the horizontal listener plane. Still, the reproduction of elevation sounds is still limited.

### B. Audio APIs

A 3D audio space can be created using an audio API. The most known are OpenAL and EAX (Environmental Audio Extensions) from Creative Technology, Ltd. and DirectSound3D produced by Microsoft. All of them provided high-level C++ classes and are available as open source projects in public domain (GNU Public License).

EAX works as an audio extension for OpenAL and DirectSound3D and implements different audio effects (e.g. echo, reverberation, distortion, occlusions, exclusions, obstructions). Therefore, it cannot be used, by itself, to create a 3D sound world. On the other hand, DirectSound3D and OpenAL includes common functionalities [164, 198]:

- Audio Contexts: an audio environment can be described as consisting of a listener and source sounds. One single context is created for each sound card;
- Spatialized Audio: a listener is created per context and is positioned in a 3D world. Then, different audio sources are also defined and placed in the same world. The spatialization is accomplished by attaching a specific buffer to each audio source. A buffer consists in the audio data originated from loading a sound file (e.g. MPR, PCW) or by creating configurable sound functions such as sinusoids with different frequencies.

- High level functions to play, restart, rewind or loop each audio source under the sound card or CPU;
- Audio Attenuation functions: the audio is attenuated as function (linear or exponential) of the distance between the listener and audio source;
- Static and Streaming Audio: can play data completely stored in memory and stream buffers while continually read new portion of data at specific time intervals;
- Pitch and frequency manipulation;
- Doppler effect: automatically modifies the audio source frequencies giving an effect of different moving velocities of an audio source.

DirectSound3D presents some additional capabilities over OpenAL, since it supports audio effects and live voice. However it is limited to wave files data, is more difficult to implement and only works under windows. In contrast, OpenAL supports the most used operating systems such Windows, Android, Linux and Apple [199]. Consequently, OpenAL was chosen as the most suitable API platform concerning the trade-off between potentialities and facility of implementation. By combining all the above characteristics in a single framework, it is possible to create a fully immersive sound environment, with audio sources placed at strategic positions, to precisely and accurately aid the needle tip orientation with respect to the target position.

### C. 3D Audio World

The audio feedback follows the same strategy as the NeedleView. The idea of using audio to correct needle orientation is based on creating and positioning different audio sources in a 3D space around a centered listener (Figure 5.4).

Sound from different positions will reach the listener with different directions. By internally analyzing this direction, the listener will be able to ascertain the corrections to be made. The error at the horizontal plane $P$ of the NeedleView are used to activate or deactivate the playing sources.

Since the reliability of audio spatialization is dependent on the number of sources, three different configurations were tested (Figure 5.4): 8, 16 and 12 source configurations (8SC, 16SC, and 12SC in Figure 5.4-a, -b and -c, respectively).

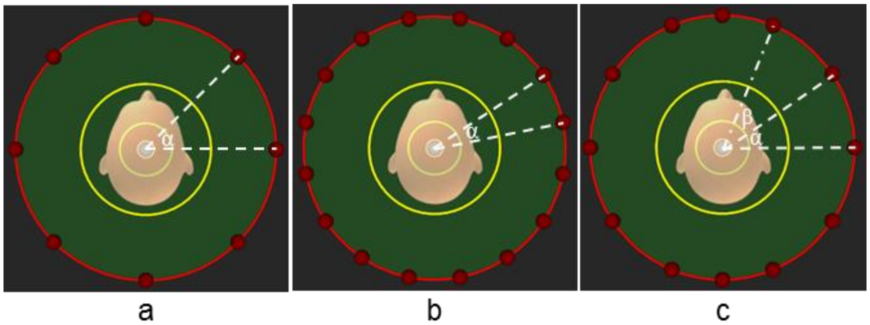

Figure 5.4. Representation of 3D sound configurations around the listener via a direct path. Each sound source is represented by a red circle. a) 8 sources equally spaced by α=45 degrees; b) 16 sources equally spaced by α=22.5 degrees; c)12 sources with two different angles: α=22.5 and β=56.25 degrees.

### D. Positional Feedback

Errors from the ideal trajectory are used to set different audio buffers and to activate/deactivate audio sources from where the sound will be emanated.

Since changes in the needle orientation are correlated with changes in the listened sound, three different strategies were implemented to accurately alert and guide the listener during needle insertion. All of sound strategies are based on the variation of the sound pitch, loudness and source location.

*First sound strategy – SS1*

The audio loudness is calculated according an error function, with respect to the ideal trajectory. When the needle is following the correct path, i.e. the target can be reached with an accuracy less $T_{err}$ mm, no sound will be produced (loudness is 0). As shown in Figure 5.5, f*or errors higher than* $T_{err}$ *, i.e.* the needle starts moving away from the correct path, the sound source with opposite direction to the error will start playing.

$D_{err}$ is calculated through the Euclidean distance from the vertical and horizontal errors and is used to control the source loudness gain from 0 (no sound is listened) to 1 (maximum sound output). The loudness was controlled using a step function (Figure 5.6) that highlights when the error increases from a specific error region (white, green, green and red) to another.

Each sound source played a sinusoid signal with frequency $Sf$, phase $Sp$, duration $Sd$ and a sleep interval between each tone $Ssleep$.

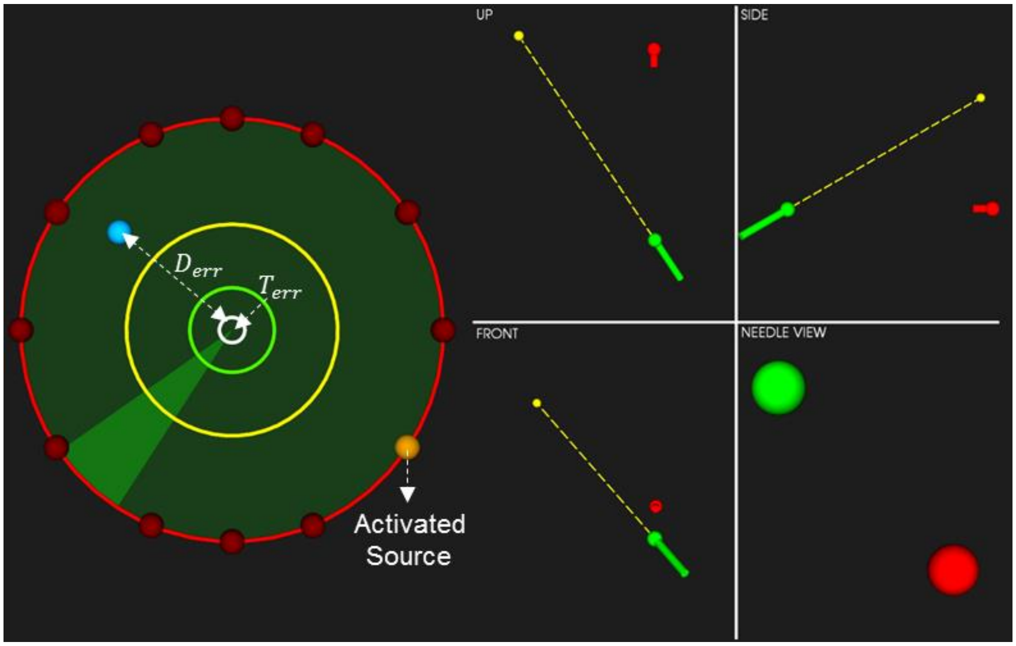

Figure 5.5. Representation of the visual guidance interface while playing a sound source.

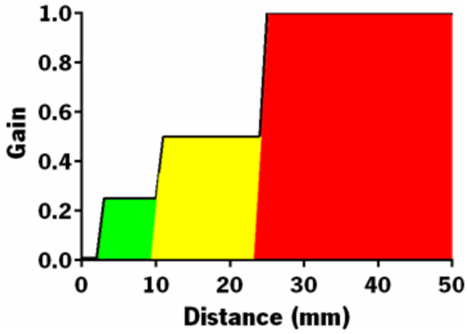

Figure 5.6. Step function that gives the sound loudness gain according to the error region.

$Ssleep$ was proportionally to the distance to reach the target. Being $maxSleep$ and $minSleep$ the maximum and minimum allowable sleep intervals, respectively, and $max_{dist}$ and $min_{dist}$ the maximum and minimum affecting distances, respectively, $Ssleep$ was calculated according to Equation 5-4.

$$Ssleep = m * dist2target + minSleep \qquad \text{Equation 5-4}$$

Where $m = \frac{\text{maxSleep}-\text{minSleep}}{\text{max\_dist}-\text{min\_dist}}$.

*Second sound strategy – SS2*

Same strategy as SS1, but now instead of not playing any sound when the needle is following the correct path (with an accuracy less $T_{err}$ mm), a sound with distinct frequency $S_2f$ is playing by all sound sources.

*Third sound strategy – SS3*

From literature, it is known that horizontal and vertical sounds are well discriminated, but it is more difficult to differentiate between front and back sounds. Efficiencies of about 50% are commonly reported [164, 170, 200].

Due to this shortcomings, this third strategy tries to improve front-back resolution by adding distinguish frequency tones, where front or back sources are playing. Two frequencies were used: frequencies $Sf_{front}$ for sources placed from 0° to 180° degrees; and $Sf_{back}$ for sources placed from 181° to 359° degrees. The frequency gap is used to rapidly ascertain if the needle tip should be moved to the front or back for orientation correction. With such differences, one expect to increase the localization performance, relative to the first strategy (SS1 and SS2).

*Forth sound strategy – SS4*

In order to improve and enhance the spatial sound resolution, *SS3 was further modified by introducing an* intermittent sound at the four cardinal sources. These sound sources will be playing in an alternate mode two sinusoid waves: one with the parameters discussed at SS1 ($Sf$, $Sp$, $Ssleep$ and $Sd$) and another with distinct frequency $S_4f$ and duration $S_4d$.

For all strategies, when the needle tip reaches the target, a message sound is generated ("Target Achieved"). Here, the surgeon must analyze the ureterenoscope video to inspect if the needle is near the target.

### 5.2.4 3D Vibrotactile Feedback

In addition to the NeedleView and 3D sound, this work also explored vibrotactile sensation for needle guidance. Due to desirable site of the head for providing feedback [185, 194], one chose to manufacture a headband with multiple actuators that vibrate according to the needle spatial errors with regards to the punctured target.

Different actuators are commercially available with particular technical specifications, mainly in terms of vibration intensity and size [179]. Miniature loudspeakers, electromagnetic alarm buzzers and coin motors are routinely used [179].

When compared to other solutions, coin motors offers low cost, small size, low voltage and reduced noise devices, being used in routinely devices, e.g. mobile phones. Therefore, coin vibration actuators 308-100 Pico Vibe [201] were used to deliver this kind of feedback. Table 5.1 show important actuator manufacturer specifications.

Table 5.1. 308-100 Pico Vibe operation characteristics.

| Characteristic | Value |
|---|---|
| Diameter | 8 mm |
| Height | 3.4 mm |
| Typical Normalized Amplitude | 0.7 G |
| Rated Operating Voltage | 3V DC |
| Rated Vibration Speed | 12000 |
| Operating Current | 70 mA |
| Vibration efficiency | 3.2 g/W |
| Noise output | 50 dB |
| Typical Lag Time | 51 ms |
| Typical Rise Time | 77 ms |
| Typical Stop Time | 65 ms |

Based on a literature research [185, 187, 192], 8 motors were chosen and placed at the 8 cardinal points (equally placed around the head) (Figure 5.7).

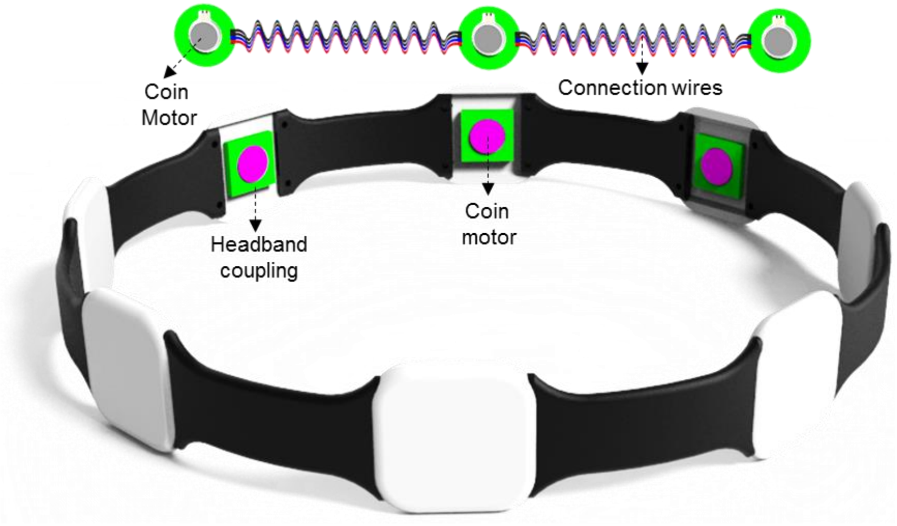

Figure 5.7. Representation of the developed headband device.

Four control strategies were implemented and tested. Each strategy is similar to the ones already described for the 3D sound interface (SS1, SS2, SS3 and SS4), but now a coin motor will vibrate instead of playing a sound source.

The sound loudness, $Ssleep$ and distance to the target are now transmitted from the KidneyNav to the Arduino Uno platform wireless via a Bluetooth connection. The Arduino, based on the Atmega328P microcontroller, is responsible for interpreting and processing the received information and active/deactivate the respective actuators.

The sound loudness (values from 0 to 1) is used to control the vibration intensity $Vi$, as a percentage of the maximum possible vibration. The vibration sensation is achieved by individually controlling the supply voltage using a square wave signal generated by pulse width modulation (PWM).

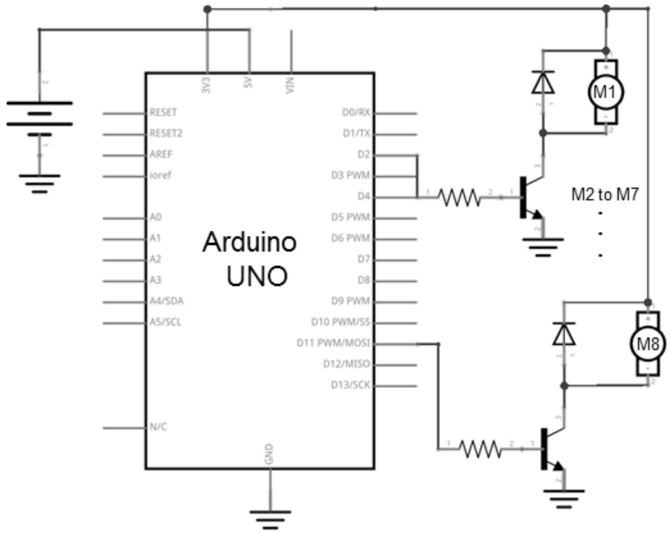

Figure 5.8. Schematic diagram for linking two motors to the Arduino Uno.

Each motor was further connected to a 3.3 V pin at the Arduino board (Figure 5.8). A diode was reversely connected to the motor to protect the microcontroller against voltage spikes. 8 transistors 2N2222 were used to assure high/low current outputs, to activate/deactivate each motor.

## 5.3 Experiments

Different experiments were performed in order to evaluate the accuracy and acuity of each interface in an individual or combined way.

### 5.3.1 Sound Parameter Settings

The sound parameters, such as frequency and duration were found empirically by individually playing and adjusting each source parameters with manual control. To this extent 16 participants listened sounds that were created with sinusoids which frequency vary from 300 Hz to 1200 Hz. In the end, they indicate the frequency that they were most comfortable with. Based on such results, one found that the ideal values for the first and second sound strategies (SS1 and SS2) were:

- $Sf$ = 700Hz;
- $Sp$ = 0;
- $Sd$ = 50 ms;
- $S_2f$ = 950 Hz or 400 Hz;
- $maxSleep$ = 800 ms;
- $minSleep$ = 50 ms;
- $max_{dist}$ = 150;
- $min_{dist}$ = 0;

When evaluating the SS3 strategy, one found that front and back sounds can be well discriminated when $Sf_{front}$ = 690 Hz while $Sf_{back}$ = 490 Hz.

Finally, a sinusoidal sound, with $S_4f$ = 1200 Hz and $S_4d$ = 25 ms, was introduced when testing the SS4. Moreover, the frequency of the sources with positions at the most left, right, up and down were changed to 650 Hz, 650Hz, 730 Hz and 460 Hz, respectively. The other sources remained the same $Sf_{front}$ and $Sf_{back}$ frequencies.

One found that the target can be reached accurately when $T_{err}$ = 2mm. SS2 was discarded for testing because all users prefer the SS1 approach.

It should be highlighted that the user can manually control the headphones volume.

### 5.3.2 Localization Accuracy Test

A set of localization experiments were firstly performed to determine whether a person is able to perceive the direction of random sources or vibration stimulus.

An audio stimuli was presented to the listener with Razer Tiamat 7.1 headphones [202]. This headphones have 10 discrete drivers (5 for each ear) composed by neodymium magnets with 30 mm of diameter and a frequency response between 20 Hz and 20.000 Hz. They were connected to a PC via a 7.1 Surround Sound-enabled Sound Card.

On the other hand, the developed headband was used to create a vibrotactile feedback.

Before any experiment, a brief demonstration was given to each participants and they were allowed to test any sensorial feedback up to 2 minutes, so that they become comfortable and familiarized with the system.

During either audio or vibration experiments, each time the user was ready, a sound or a vibration actuator was activated randomly from a set of possible locations at the same distance from the listener (Figure 5.9).

The chosen strategy for starting the experiment was also determined randomly.

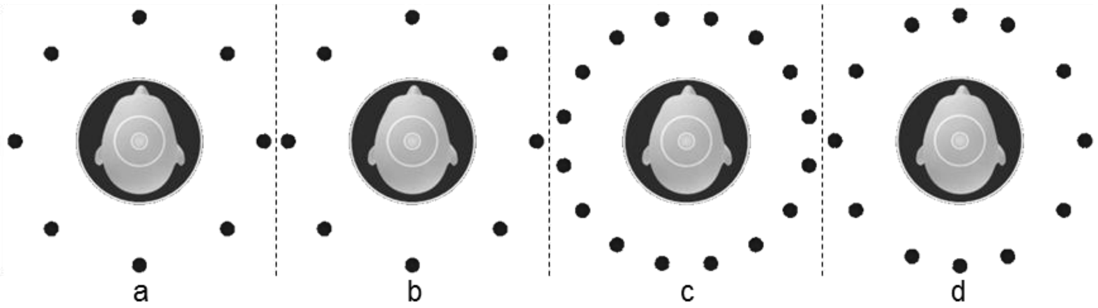

Figure 5.9. Representation of the target location for all experiments: a) shows target locations for the vibrotactile test; b), c) and d) show target locations for the sound sources according to Figure 5.4.

Each sound strategy (SS1, SS3 and SS4) was tested for all the three spatial configurations (Figure 5.9 -b, -c and -d). In contrast, the vibrotactile feedback was tested in a unique distribution (Figure 5.9–a). Each exercise was repeated 16 times.

The users had up to 2 seconds to report the location of the perceived sound or vibration, by marking the perceived location in a printed sheet (showing the Figure 5.9).

In total 31 volunteers participated: 26 medical students and 5 surgeon doctors. During experiments, they had no feedback about the correctness of their answers.

The aim of this test was to select the best audio spatial configuration, sound strategy and finally compare audio against vibration as possible feedback systems.

### 5.3.3 Phantom Test

Despite of the accuracy of detecting single vibration or audio sources it is important to test the efficiency of all interfaces for needle guidance. To this extent, a phantom study was performed to test and evaluate the most valuable feedback interface. The following configurations were tested in a phantom box (Figure 5.10):

- 3D view
- NeedleView
- Audio
- Vibration
- 3D view + NeedleView
- Audio + NeedleView + 3D view
- Vibration + NeedleView + 3D view

The phantom box was made of wooden without any ferromagnetic material to avoid interferences that might reduce the precision of the tracking device. A sponge material with 8 cm of thickness was used to simulate the skin, offering some resistance, low deformability and opaque texture when inserting the needle.

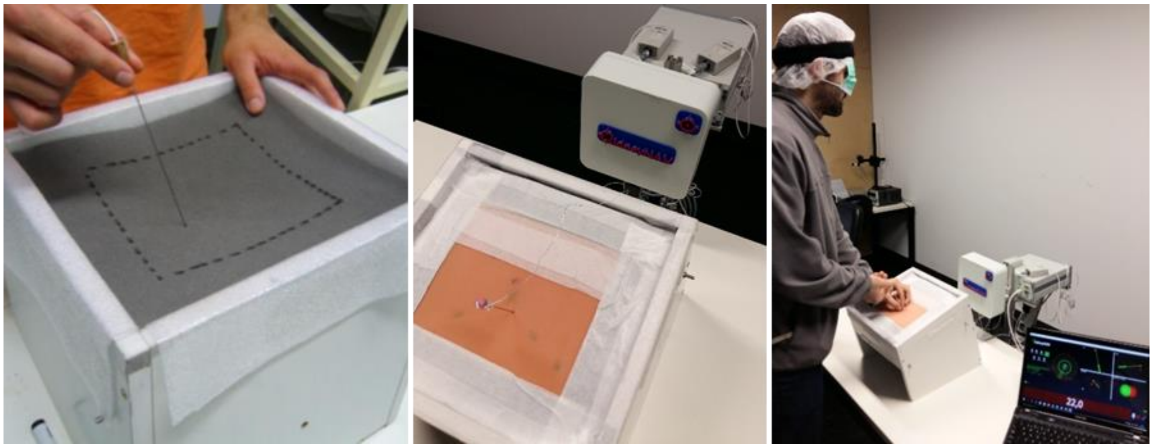

Figure 5.10. Wooden phantom showing the puncture area (about 250 $cm^2$) where the needle should be inserted.

A small plastic arm was attached to one side of the phantom with a 10-15 cm distance from the superficial sponge material. It was used to hold the catheter sensor at different locations inside the phantom box.

When using only vibration or audio, the participants were blinded throughout all planning and puncture procedure. An audio message “target achieved” and a vibration pattern (all motors vibrate at the same time) were used to aware the participants when they reach the target (puncture success).

Puncture success was accomplished when the root mean square distance was less than 3 mm. The planning and puncture time were recorded. Needle position was then verified using a webcam showing the phantom interior. The degree of the needle tip divergence was calculated, during whole insertion procedure, by storing the root mean square distance between the real and virtual path.

The main objective was to assess whether the guidance approach increases the procedure efficiency, in terms of the duration, mean velocity, mean and maximum error.

The testing order was randomized to reduce target position-related familiarization and learning issues. Otherwise, the last guidance methodology will had an advantage over the first technique due to experience performing the puncture.

Different medical professionals with diverse expert degrees performed three times each strategy. These tests were performed by 2 different groups: naive ($n$=56 without any or less than 2 years of medical experience) and expert ($n$=15 with more than 2 years performing minimally invasive surgeries). At the beginning of each experiment the participant was allowed to practice by reorientation the needle in the air and by performing up to 2 puncture attempts. This data is not included for the statistical analysis.

At the end of each test, the participant filled a questionnaire to score each approach according to the following questions:

- *Q0*: Score each approach from 1 (most favorite) to 10 (least favorite);
- *Q1*: Each approach based on the time needed to look to the screen from 1 (mandatory visualization throughout all procedure) and 10 (no need for visualization);
- *Q2*: The difficulty of the procedure from 1 (very difficult) to 10 (straightforward);
- *Q3*: The effort to familiarize with the technique from 1 (very difficult) to 10 (straightforward);

### 5.3.4 Animal Trials

The animal trials were performed as already described in Chapter 4.3.3-B.

## 5.4 Results

### 5.4.1 Localization Accuracy Test

The total duration of each experiment was about 10 minutes. Figure 5.11 shows the percentage of times that the target location was correctly chosen for whole participants. Figure 5.12 show the average and standard deviation errors between the marked source and target one.

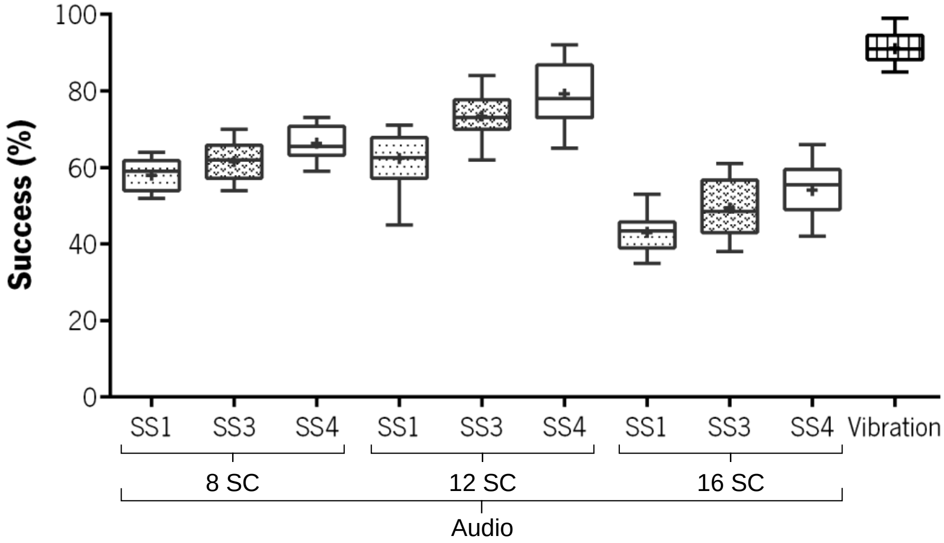

Figure 5.11. Boxplots showing the percentage of times that the user accurately mark the audio or vibration source. Average values are shown by the cross symbol.

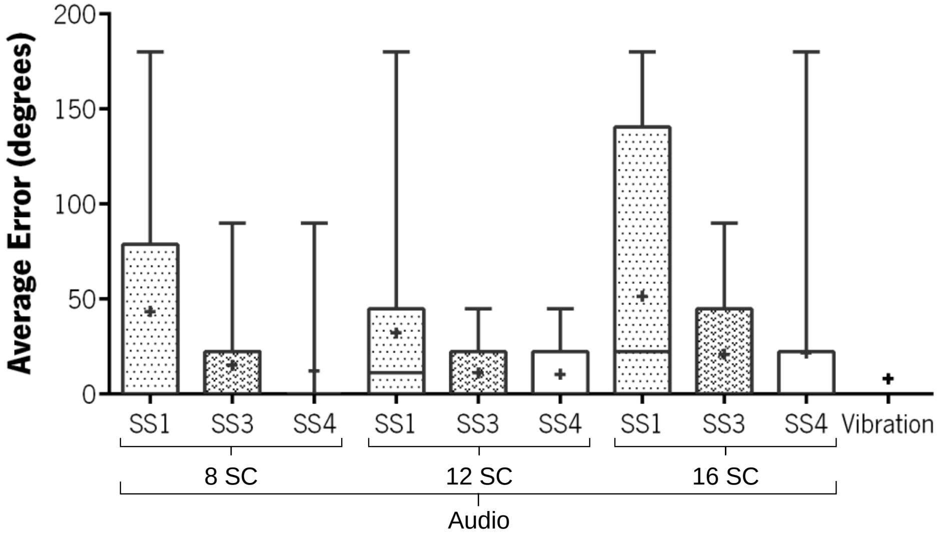

Figure 5.12. Boxplots showing the angulation error when marking the audio or vibration source. Average values are shown by the cross symbol.

When comparing the different sound strategies and audio spatial worlds, best results were achieved when using 12 audio sources together with SS4 strategy (SS4-12SC, Figure 5.4-c). Within this configuration, target sources were correctly chosen 79.2 ± 8.1% of times with an average angulation error of 10.4° degrees. The worst configuration was found with SS1 strategy when using 16 audio sources (SS1-16SC - Figure 5.4-b), showing an average angulation error of 51.5° degrees and an assertive percentage of 43 ± 6.0%.

SS4 was the best sound strategy with significant statistical differences (two-way ANOVA – see attachment 1 for more detail) when compared to SS1 ($p<0.0001$) and SS3 ($p<0.05$). SS4 was followed by SS3 that also shows significant statistical differences with SS1 ($p<0.01$). Finally, worst results were obtained with SS1. Regarding the audio world configuration, 12SC was the best one with significant statistical differences when compared to 8SC ($p<0.0001$) and 16SC ($p<0.0001$). It was followed by 8SC with also significant statistical differences with 16SC (p<0. 0001). Finally, worst results were obtained with SS1.

When listening the various sources configured with SS1, the user can easily separate left from right. However, only 62% of times he was able to identify if the sound is created at the front or back sources, creating high standard deviations between users (Figure 5.12).

From the boxplot analysis (Figure 5.12), more than 75% of participants did not show angulation errors when using the SS4-8SC and the vibration feedback.

By introducing $Sf_{front}$ and $Sf_{back}$ in SS3 and SS4 strategies, the user was able to improve its ability of detecting front or back sound to 87% of times.

By adding $S_4f$ and $S_4d$ to SS4, the user was able to accurately and promptly distinguish the sources placed at the four cardinal points (0°, 90, 180° and 270°) when compared to SS1 or SS3 (71% *vs*. 90.5%).

Finally, vibration results were the best ones. The participants can easily and accurately identify vibration sources 91.1 ± 3.6% of times with an average angulation error of 8.0° degrees. Significant statistical differences ($p<0.0001$) were found when compared to the best audio configuration (SS4-12SC).

### 5.4.2 Phantom Test

In terms of the phantom test, every subject reached the correct target in their first attempt. Figure 5.13 shows the average time for planning and puncturing in both naive and expert groups. Clearly, NeedleView alone or combined with any other modalities was the fastest strategy for planning or puncturing.

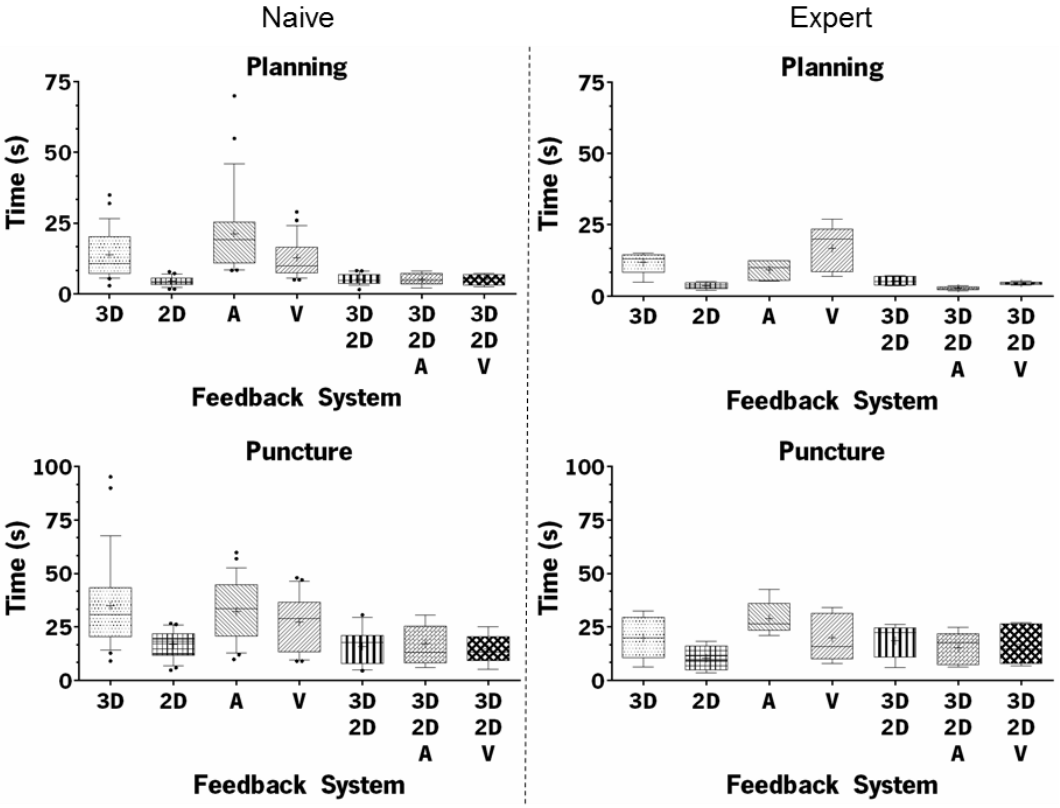

Figure 5.13. Time needed for planning and puncturing for whole elements of the naive and expert group: 3D = 3D View; 2D = NeedleView; A = Audio; V = Vibration; 3D/2D = 3D view + NeedleView; 3D/2D/A = 3D view + NeedleView + Audio; 3D/2D/V = 3D view + NeedleView + Vibration.

On the other hand, audio or vibration alone were the ones that took longer times.

Planning significant differences between naive and expert groups were only found when using audio feedback ($p<0.01$). Puncture significant differences between both groups were found when inserting the needle under 3D view ($p<0.05$). 3D, audio and vibration are the methodologies where participants show quite range of times, especially for planning.

In the naive group, planning time was minor when using the NeedleView alone (average value of 4.5 ± 1.5 s). Higher times were achieved using the Audio feedback (21.3 ± 15.1 s). In terms of the

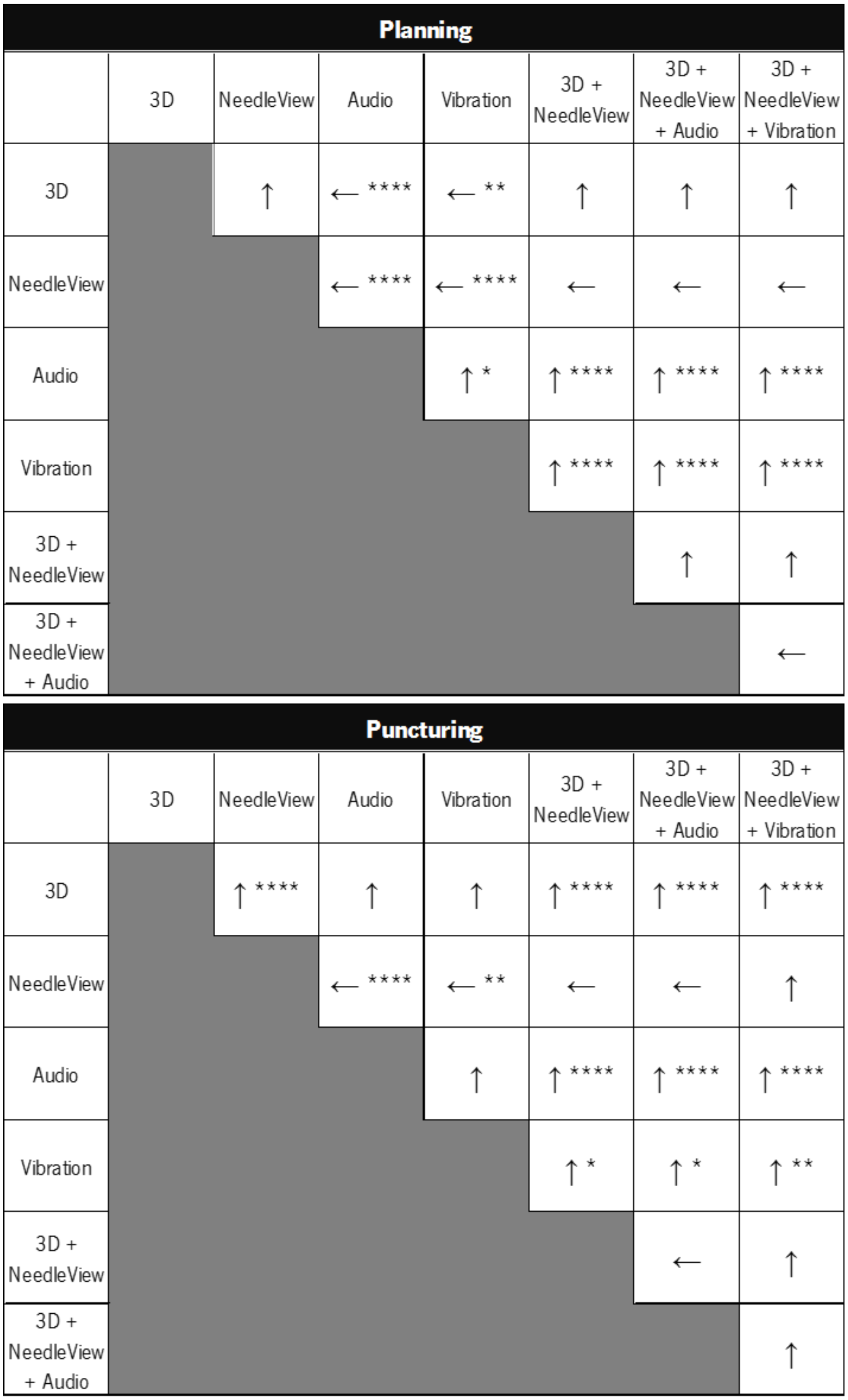

**Planning**

| | 3D | NeedleView | Audio | Vibration | 3D + NeedleView | 3D + NeedleView + Audio | 3D + NeedleView + Vibration |
|---|---|---|---|---|---|---|---|
| 3D | | ↑ | ← **** | ← ** | ↑ | ↑ | ↑ |
| NeedleView | | | ← **** | ← **** | ← | ← | ← |
| Audio | | | | ↑ * | ↑ **** | ↑ **** | ↑ **** |
| Vibration | | | | | ↑ **** | ↑ **** | ↑ **** |
| 3D + NeedleView | | | | | | ↑ | ↑ |
| 3D + NeedleView + Audio | | | | | | | ← |

**Puncturing**

| | 3D | NeedleView | Audio | Vibration | 3D + NeedleView | 3D + NeedleView + Audio | 3D + NeedleView + Vibration |
|---|---|---|---|---|---|---|---|
| 3D | | ↑ **** | ↑ | ↑ | ↑ **** | ↑ **** | ↑ **** |
| NeedleView | | | ← **** | ← ** | ← | ← | ↑ |
| Audio | | | | ↑ | ↑ **** | ↑ **** | ↑ **** |
| Vibration | | | | | ↑ * | ↑ * | ↑ ** |
| 3D + NeedleView | | | | | | ← | ↑ |
| 3D + NeedleView + Audio | | | | | | | ↑ |

Figure 5.14. Comparison between guidance strategies. The arrow points to the best method when comparing the average times for planning and puncturing. The asterisk gives the statistical significances (two-way ANOVA): without asterisk $p > 0.05$; * $p \leq 0.05$; ** $p \leq 0.01$; *** $p \leq 0.001$; **** $p \leq 0.0001$.

puncture step, best results were achieved using “3D view + NeedleView + Vibration” with an average value of 14.7 ± 8.5 s. Surprisingly, longer puncture results were achieved with the 3D view with an average time of 34.8 ± 21.0 s.

Figure 5.14. shows multiple comparisons between all guidance strategies. Statistical analysis show that all new interfaces influenced positively the procedure performance when comparing to only the 3D views presented in the previous chapter.

In the expert group, planning time was minor when using “3D view + NeedleView + Audio” with an average value of 2.7 ± 0.6 s.

Higher times were achieved using the Vibration (16.8 ± 8.1 s). With respect for the puncture step, best results were achieved when using “3D view + NeedleView + Audio” with an average value of 15.2 ± 7.7 s. Longer times were needed when using the Audio feedback with an average value of 29.1 ± 8.0 s.

The time needed for planning and puncturing is very promising, existing no statistical differences when comparing experts to naive participants in most of guidance strategies.

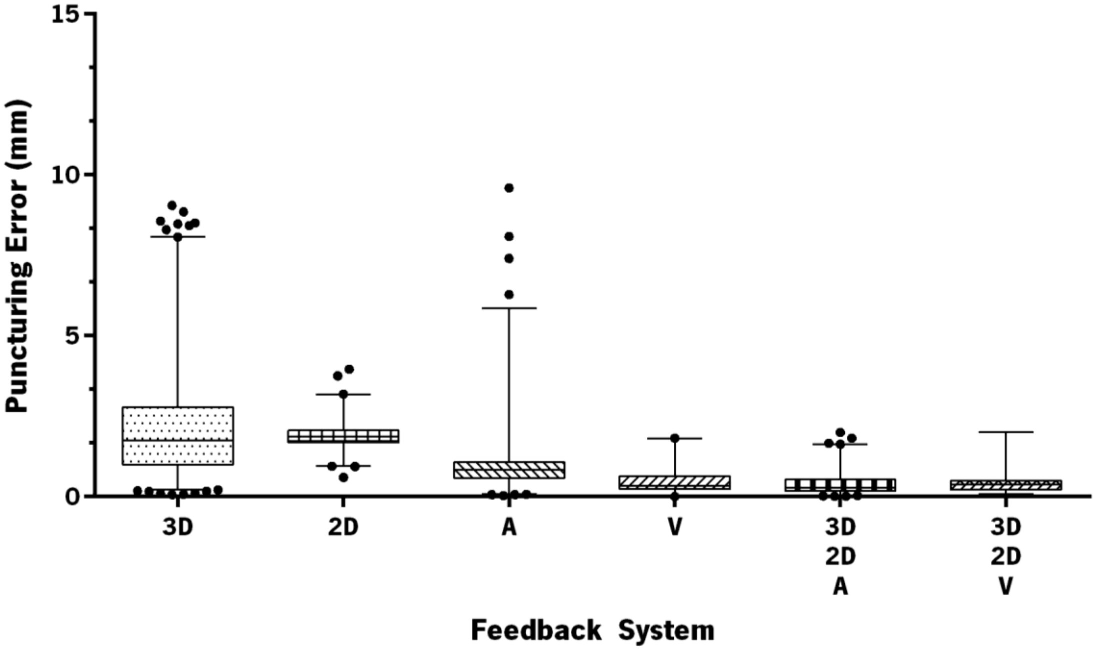

Figure 5.15. Boxplots of the errors from the ideal trajectory, according to the profiles shown in Figure 5.16: : 3D = 3D View; 2D = NeedleView; A = Audio; V = Vibration; 3D/2D/A = 3D view + NeedleView + Audio; 3D/2D/V = 3D view + NeedleView + Vibration.

Figure 5.15 and Figure 5.16 give an overview about common puncture profiles when inserting the needle with different feedbacks. As represented, using only the 3D view it was difficult to maintain the needle tip inside the 2 mm margin (white circle at the NeedleView). Errors were minimal when using "3D view + NeedleView" + "Audio" or "Vibration", because an audio or vibrotactile alert was

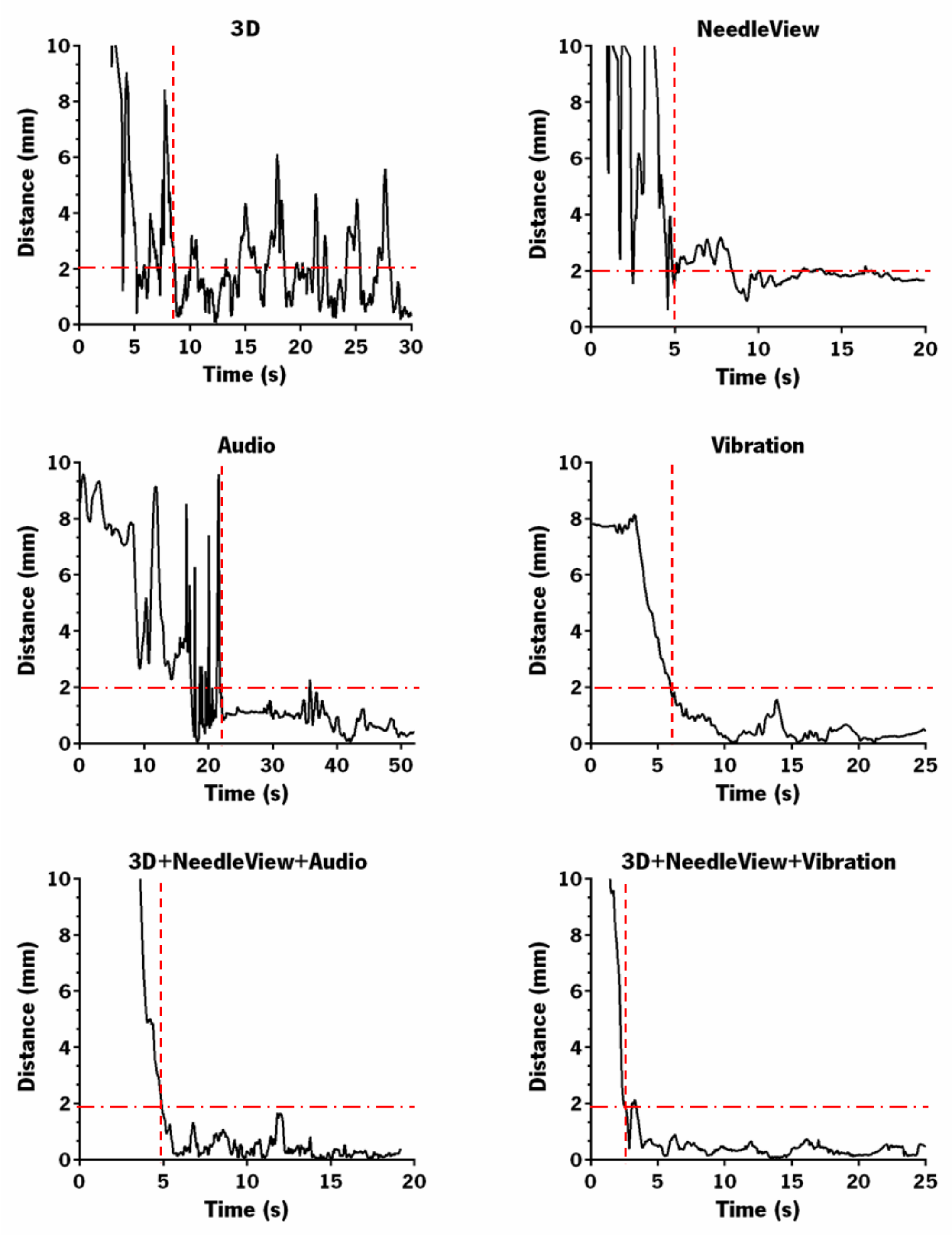

Figure 5.16. Error profile deviations from the ideal trajectory when planning or puncturing according to different guidance strategies. The vertical line indicate the end of the planning procedure.

generated each time the user increases this error. Similar errors during puncture were found when using the audio or vibration standalone, but with higher planning and puncture times.

Audio and vibration feedback seemed to precisely inform the user to keep the needle correctly aligned with the target.

All participants considered that audio or vibration feedback gives less confidence than the NeedleView, but suggested that can improve the PRA procedure. Although impractical in a real situation, results reveal that the target can be reached without spending any time looking on the screen.

The step function to control the audio loudness was easy to understand for whole users. Although one tested also an exponential function (Equation 5-5), this options was never preferred.

$$loudness = 0{,}0326e^{0{,}0799 \cdot err} \qquad \text{Equation 5-5}$$

The audio feedback combined with the NeedleView provided good directional feedback during all the procedures. This interface was the preferred and simplest one without needing any training before usage. In the presence of the NeedleView, the 3D view was frequently ignored and the audio or vibrotactile were mainly used as a warning system than a guiding one.

Table 5.2 show the questionnaire for questions Q0, Q1, Q2 and Q3 (Experiments section 5.3.3).

Table 5.2. Questionnaire results when evaluating the different guidance approaches.

| | | **3D** | **NeedleView** | **Audio** | **Vibration** | **3D + NeedleView** | **3D + NeedleView + Audio** | **3D + NeedleView + Vibration** |
|---|---|---|---|---|---|---|---|---|
| **Questions** | ***Q0*** | 6.25 ± 0.96 | 9.2 ± 0.7 | 5.3 ± 1.2 | 5.9 ± 1.1 | 8.8 ± 1.6 | 8.7 ± 0.7 | 6.3 ± 2.1 |
| | ***Q1*** | 1 | 1 | 10 | 10 | 1 | 5.4 ± 1.2 | 5.2 ± 1.5 |
| | ***Q2*** | 3.8 ± 2.3 | 10 | 2.9 ± 1.1 | 5.5 ± 0.7 | 9.5 ± 0.5 | 9.6 ± 0.5 | 9.5 ± 0.5 |
| | ***Q3*** | 4.3 ± 1.9 | 10 | 2.5 ± 0.5 | 5.7 ± 1.4 | 9.1 ± 1.1 | 8.9 ± 1.2 | 8.7 ± 1.5 |

The NeedleView followed by the "3D + NeedleView" and "3D + NeedleView + Audio" were the three most favorite methods according to Q0.

Whole users score Audio and Vibration in Q1 with 10, because they were blindfolded when performing the procedure. In contrast, visual modalities were scored with 1. Hybrid modalities that combines Visual and Audio/Vibration feedback were scored with similar values.

Regarding the question Q2, audio feedback, followed by the 3D screen, were the most difficult techniques. The easier ones were the NeedleView alone or combined with any other feedback.

Finally, Audio feedback was the most difficult technique with the highest learning curves. The NeedleView was the easiest and straightforward one, with no need for training.

Figure 5.17. Representation of the experiment setup.

### 5.4.3 Animal Trials

Eight surgeons have participated in this experiment. In order to not sacrifice many animals, surgeons start this experiment by choosing three guidance approaches. “NeedleView + 3D view”, “Audio alone” and “NeedleView + 3D view + Audio” were the selected ones. A surgical setup is represented in Figure 5.17.

Three pigs were used for this experiment. Six successful tracts to the middle of ureter were accomplished. Each ureter was punctured up to 4 times in different regions.

Due to animal’s small anatomy, it was only possible to place the ureterenoscope into a kidney calyx in two pigs. Therefore, statistical analysis was only performed for the ureter experiments.

Results are in accordance with results already presented in Chapter 4. 100% success rates were reached with only one attempt for almost all cases.

The time needed to see the needle tip in the ureter skin (Figure 5.18 –a to –d) was some seconds, but the time needle to perforate the ureter skin (Figure 5.18 –e) was more than 1 minute. The problem is that the ureter slipped and moved away when the needle was trying to perforate.

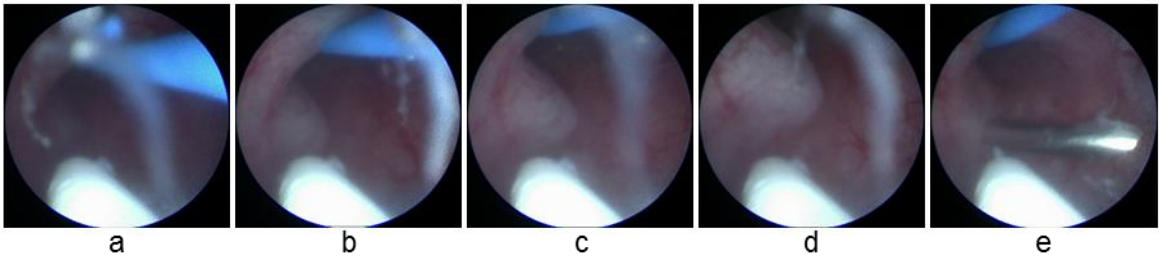

Figure 5.18. Representation of the needle trying to puncture the needle.

Figure 5.19 presents the average times for planning and puncturing until the needle tip is visualized in the ureterenoscope camera.

Results are in accordance with the ones described with the phantom test. Longer times were obtained when performing the experiment with audio alone. Statistically significant differences were found when comparing the audio with any of the other two interfaces for surgical planning ($p < 0.0001$) and puncturing ($p < 0.001$).

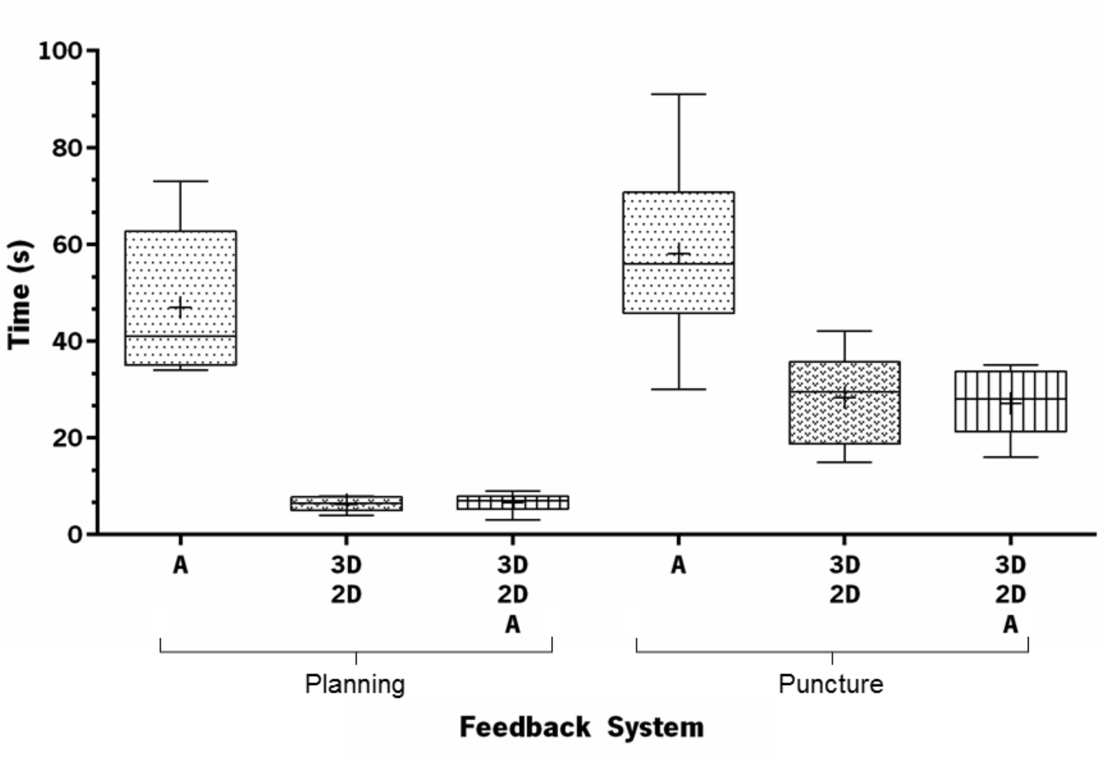

Figure 5.19. Boxplots of the average times for planning and puncturing in the animal trial.

No significant differences were found when comparing the “NeedleView + 3D view” and “NeedleView + 3D view + Audio”. But as already described in the phantom test, that audio feedback helped the surgeon keeping the correct path with minor deviations (Figure 5.16).

No major problems were found during the experiments and the most time-consuming. One attempt was needed for all surgeons.

## 5.5 Discussion

Although the KidneyNav framework already allowed surgeons to comprehend the volumetric data of the collecting system (Chapter 3) and to follow a 3D path (Chapter 4), now one explore the possibility of adding additional feedback, by recurring to the hearing and touch senses.

This chapter tested multiple interfaces where audio and vibrotactile senses were combined with visual information to provide and improve insight into complex PRA trajectories. These new ways of feedback intended not to replace visual guidance, but complement the surgeon interaction with the needle, being able to anticipate any movement even without looking to a monitor.

With this multi-sensorial interface, the surgeon must place the needle at the skin surface, align with respect to the target, and finally he should puncture the kidney according to this approved angle. When the needle is being inserted from an incorrect angle, it will miss the anatomic target which error is dependent on the angulation error. This error (originated at possible needle deflection, soft tissue displacements and human tremors) can be tracked in real-time using the 3D EMT sensors at the needle and catheter tips and used to generate a set of visual, audio or vibration signals.

The previously framework, based in a 3D view, requires some learning training. Results show that by using this view, is was not possible to precisely and easily follow a pre-computed trajectory with minimal deviations from the correct path. Regardless the user experience, he can easily misunderstood the 3D information, increasing the probability of high errors.

By using the NeedleView, the user was able to automatically and intuitively classify the error as safe and dangerous. No training was required within this interface, being a ready-to-use approach. Experimental results show that NeedleView worked reasonably well for all puncture orientations being the fastest and preferred guidance methodology.

The headphones produces different spatialized sound signals relating the position of the needle with the target. Different sound frequencies were tested to create accepted tones for all users. If the needle is corrected aligned no sound was generated, avoiding possible annoyance and distractions.

Other works have reported different angulation errors around the head using headphones: 22.3° [203], 26° [204], 34.2° [164] and 22.2° [199]. When compared to these works, results show reduced angulation errors when using the SS4 sound strategy with 12 source sounds (75% of participants show errors below 20°). The poorest scenario was shown at SS1-16SC due to the inability to clearly distinguish from front and back sounds, as well sources separated from small angles.

Although it provided limited spatial information, 3D audio feedback was enough to accurately guide the surgeons without never looking to the screen (in phantom test and animal trial). By using different audio intensities and pitches, it was possible to improve the feedback about the amount and direction of the actual deviation from the ideal trajectory.

As already reported [204], error angles are higher for headphones than for loudspeakers. Although surrounding loudspeakers will have better sound spatial accuracy, is unpractical to implement inside an operating room, due to all the medical armamentarium. Moreover, since the listener head must be centered with the sound system, 7.1 headphones presented an ideal solution to deal with these problems.

When studying the effect of vibration for guidance, results show that the source motors can be correctly identified with percentages higher than 90% for an 8-site configuration. Our results are in accordance with a recently described work [185], that tests the efficacy of providing vibration feedback using a headband holding 12 coin-type motors.

Although vibration was easily to understand and learn than audio, often users prefer the audio feedback combined with the NeedleView plus Audio (Table 5.2).

When using only audio or vibration feedback alone, the average time needed for planning or puncturing was significantly superior when compared to the NeedlleView. But when combined, these feedback helped to follow the pre-planned trajectory with minor deviations (Figure 5.16). If correctly used, the proposed methodology exhibited potential to decrease cognitive load and alert the surgeon when the needle is moving away from the accurate path without the need to continuously interpret analyze any guidance monitor. Now, the surgeon may devote more attention to the actual needle insertion and patient conditions.

# 6

# PRA Safety Assessment

In order to guarantee the safeness of PRA in terms of organ's perforation, this chapter proposes a new US probe with a needle working channel. It generates A-scanned signals along the percutaneous puncture path, to alert when some condition change [56, 57].

## Contents

## 6.1 Introduction

US technology are often used in medical imaging applications, e.g. surgical guidance and diagnosis [92, 155, 205]. An ultrasonic transducer (UT) creates an acoustic signal, which travels though the human body and reflects back when interfaces with different acoustic properties are found. UT main function is to convert electrical to mechanical energy, and contrariwise, the conversion of mechanical to electrical energy [205].

Complete ultrasonic systems, working from low (0.5-10 MHz) to high frequencies (>10 MHz), have been proposed over the years [92, 206-211]. The design of UT are currently no longer limited to simple geometries, where specialized probes have been investigated for biomedical applications, e.g. intracardiac echocardiography and intravascular US [212].

Since the overall medical diagnosis is dependent in the UT performance, it is essential to find successful and cost effective designs as well as building configurations in order to increase its sensitivity (defined as the maximum Volts amplitude of the received pulse) and resolution.

For PRA purposes, the surgeon needs high dexterity and coordination skills in both hands. One hand to hold, handle and insert the needle from the skin to a kidney calyx; another to hold, orientate and operate the UT while interpreting US images to (1) find the kidney target; (2) search for the needle tip; (3) verify that any vital organ is in the vicinity of the needle trajectory; (4) keep and maintain both the needle and UT transducer co-axial aligned. Consequently, this procedure is technically complex and difficult to accomplish by less specialized surgeons.

Current ultrasonic commercial systems are not able to easily and co-axially align the US beam and the needle orientation. Commercial needle-guide apparatuses have been proposed to overcome these alignment problems by physically attaches the needle and UT. The guide ensures that the needle tip is represented in the image for a given depth of penetration and attachment angle [213, 214]. Desal et al. [213] reported that US-guided renal access may be particularly important for the pediatric population or patients in supine position, because a dotted line can facilitate the visualization of the needle path [213, 214].

In order to reduce current imaging dependences, EMT and OMT tracking devices were already successfully tested and validated in the previous chapters. Results showed that the EMT solution was highly accurate, radiation-free, simple and fast to get percutaneous access to the kidney. Although capable of accurately guide the percutaneous puncture, due to its imageless characteristics, it is still unable to guarantee the safeness of the PRA path in terms of organs perforation, thus impeding its broader use in clinical routine practice. Moreover, despite of puncture procedures are routinely used, vital organs such as lungs, liver, spleen and colon have a quite probability of being perforated during renal access [10, 42, 44].

Considering the shortcomings of the current KidneyNav framework, this work describes a novel low-frequency transducer with a needle working channel for usage during puncture interventions. Three UTs were investigated to provide improved information by automatically comparing A-scanned signals with prior references when inserting the needle. Considering the focal length, aperture, working frequency, depth of penetration (from the skin surface to the kidney surface), this work present insight into several transducer manufacture specifications, such as piezoelectric materials selection, transducer construction, backing and matching material design.

## 6.2 Methods

### 6.2.1 System Overview

The developed UT will work together with the KidneyNav framework, alerting when unwanted anatomical structures are in between the percutaneous puncture trajectory (PPT). The proposed setup is represented in Figure 6.1 and the surgical workflow will comprise the following steps:

1. As already described (Section 4.3.2-A), the ureteral catheter with an EMT sensor at its tip must be firstly placed close to the puncture site;
2. After positioning the catheter and inserting the needle inside the UT working channel, the surgeon can reorient the needle at the skin puncture site (guided by the KidneyNav interface - Chapter 5) to create a direct trajectory towards the target (PPT).

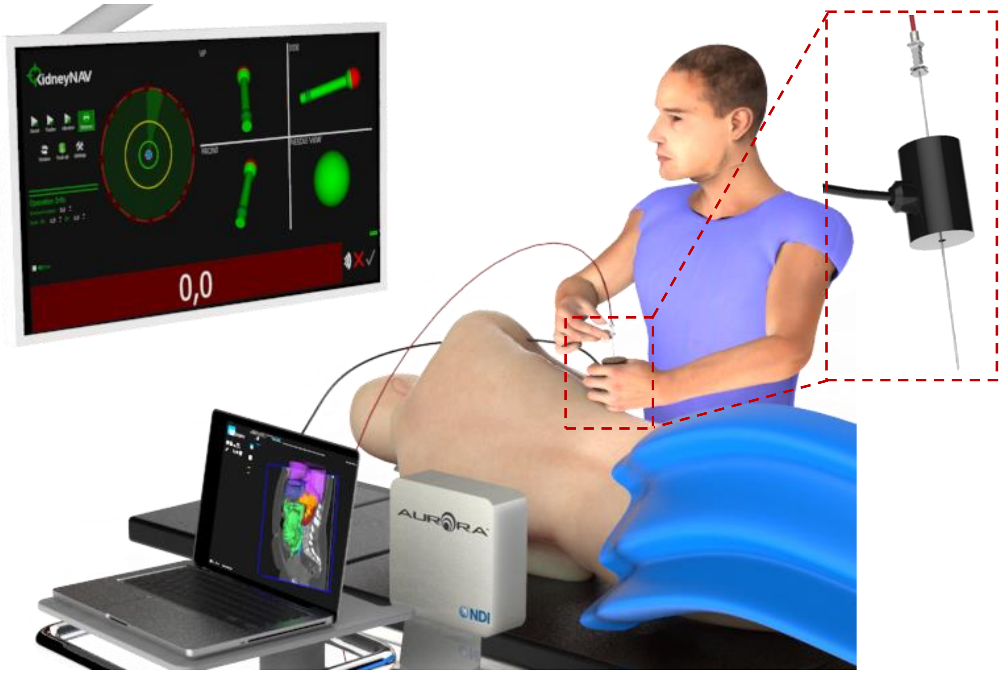

Figure 6.1. Proposed setup using the UT with a needle working channel.

3. In order to guarantee the safeness of the procedure, the surgeon should evaluate the PPT using traditional methods, e.g. US or fluoroscopy C-arm checking. One tested the possibility of using a reconstructed US volume around the PPT, from 2D US images acquired with a tracked convex probe, to automatically detect anatomical structures (See attachment 2).
4. When an organ is in between the PPT, the surgeon must redefine the catheter orientation or needle positioning at the skin puncture site;
5. Once a suitable path is found, the surgeon should continuously move the developed UT, vertically and horizontally, till the voltage value of the echoes signals becomes detectable (similar as with traditional US systems). The strength echoes will be recognized as interfaces between different objects;
6. The needle can finally be inserted and guided using the KidneyNav interface. The UT echoes will be automatically processed and compared along time, alerting the surgeon when some new echo appear or an old one disappear. Therefore, the surgeon will be notified whether the initial and safe condition was modified.

## 6.2.2 UT – Materials, Design and Fabrication

### A. Sensitivity, Resolution and Attenuation

Ideally an UT should produce echoes with high sensitivity, resolution and reliability. Axial US resolution is the ability of detecting different interfaces that are spatially close to each other along the beam's main axis. High axial resolutions can be achieved with ultrasonic pulses of short duration achieved with high frequencies.

Beside resolution, sensitivity is the capacity of detecting interfaces at a given depth with high amplitudes. It decreases as the acoustic wave travels through deeper mediums due to signal attenuation. The attenuation effect, observed in various human soft tissues, increases proportional with the frequency [215]. Therefore, high sensitivity and high resolution are often contradictory due to the increased signal loss at high frequencies.

### B. UT Design Characteristics

The development of accurate and robust US transducers requires desirable materials, ergonomic designs and a fabrication process.

A typical structure of a piezoelectric US transducer is shown in Figure 6.2. It consists in an active piezoelectric element, backing layer at the transducer back face, matching layer at the transducer front face and electrical contacts [205]. Additional lens may also be coupled to the front of the matching layer to create a focusing effect [216, 217].

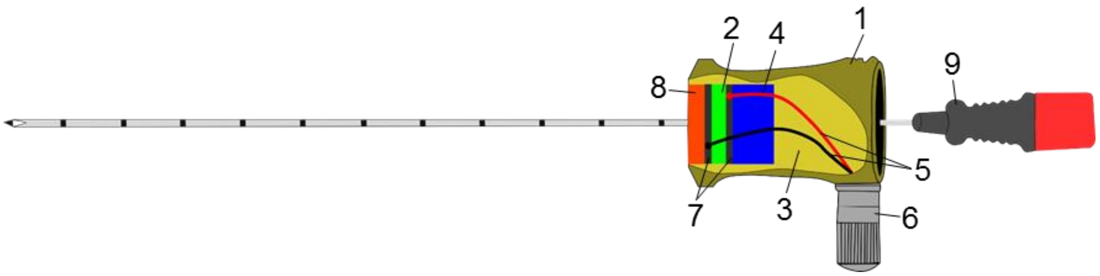

Figure 6.2. Representation of UT typical structure: 1: UT housing case; 2: piezoelectric element; 3: epoxy acoustic insulator; 4: backing material; 5: excitation and ground wires; 6: coaxial cable connector; 7: electrodes; and 8: matching layer.

Although the acoustical properties of such elements are critical for the UT performance, its sensitivity is particularly influenced by the piezoelectric element. Regarding the number of piezoelectric elements existing in the UT device, single- or multi-element transducer can be manufactured. Single-element transducer are the simplest ones, being also the base of the transducers arrays. These transducers are manufactured with a unique element which is responsible for creating all the acoustic waves. On the other hand, multi-element transducer follows the main principle of single-element transducers, but each element is often acoustically and electrically isolated. Transducers arrays are widely used for 2D or 3D image medical scans [66, 92, 152, 218, 219].

Choosing the correct thickness and acoustic impedance of the backing and matching layers are the main challenges to create UT devices.

*Backing Layer*

The backing layer is commonly created by attaching an absorbing material to the rear face of the piezoelectric ceramic. Its main function is to absorb back wall reflections, so that the length of the transmitted pulse is shortened, increasing the resolution and maintaining or enhancing the transducer bandwidth characteristics.

Because the acoustic energy is absorbed from the backward, predictably the transducer sensibility is reduced since there are less energy available for forward transmission. To this extent, another compromise should be established between sensitivity and pulse length. The pulse length can also be electrically manipulated by adding some amplification by the excitation source.

When defining a backing layer material, four main requirements should be considered. First, the backing material and piezoelectric element should have similar acoustics impedances, so that the energy will be transmitted to the backing materials with minor reflections. Second, this layer should have high attenuation coefficient in order to reduce or even eliminate possible reflections. If any backing layer exists into the transducer back, then an air-backed transducer is obtained. Third, it should be able to adhere to the piezoelectric material. Finally, it should be able to create a thick layer with high surface quality [220-223].

*Matching layer*

Another main issue for creating UT is the need of creating acoustical matching between the impedance of the piezoelectric material and the medium of propagation to increase the transducer sensitivity. For biomedical applications, this often requires matching layers with impedances ranging from 2 to 19 MRayl, similar with the human tissue [224-226].

The performance and design of matching layers have been demonstrated both theoretically and experimentally over the years [218, 220, 224, 227-229]. Ideally, the layer material should have low impedance, low attenuation and a specific thickness. Quarter-wave matching layers ($\lambda/4$) have been reported as the ideal thickness, showing high efficiency maximum energy transfer between the two media and broad bandwidth with Gaussian shaped pass-bands [230, 231]. $\lambda$ is the wavelength of the acoustic wave transmitted in a matching layer at the resonance frequency.

The main problems related to the matching layer manufacture are the unavailability of materials with correct acoustic impedance values, attenuation introduced by the matching layer itself and manufacturing considerable costs to produce layers in the nano-scale for high frequencies [220, 232].

*Crosstalk*

For multi-element UT, acoustic waves of a single element may be reduced or increased, due to destructive or constructive interference considering the acoustic output of adjacent elements. This inter-element crosstalk may degrade the overall transducer performance.

Crosstalk can be both acoustic and electrical. Electrical crosstalk is reduced by shielding the connecting transducer structure and cables. Acoustic crosstalk is associated with relatively delayed and attenuated acoustic outputs between successive array elements [233].

### C. Beam Form

An UT working zone can be divided into the near and far field. The near field is the region in front of the transducer and corresponds to its natural focus. It ends at the location of the maximum output signal. The far field distance is the area beyond the near filed distance where the output signal progressively drops to zero.

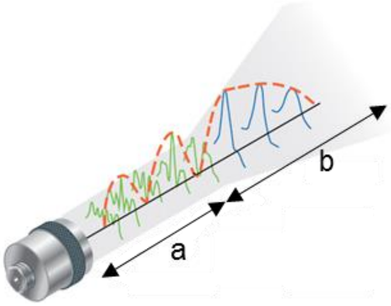

Figure 6.3. Representation of an UT near field (green waves in a) and far field (blue waves in b). The near field presents high echo amplitude variations, where the echo amplitude moves through a series of maxima and minima values. (Image adapted from [205]).

The near field distance $N$ depends on the piezo-element frequency $f$, element diameter $D$ and sound velocity of the test material according to the Equation 6-1.

$$N = \frac{D^2 f}{4v} \qquad \text{Equation 6-1}$$

The diameter and working frequency were determined in order to reach a near field which length was calculated according to the mean distance between the skin and kidney surface.

As represented in Figure 6.3, the US beam gradually narrows until the end of the near field and starts diverging at the far field. Regarding the Equation 6-1, narrow beams with big near field distances, can be obtained by high frequency UT or a larger element diameter or both.

The narrowest point at the interface between the near and far field is called the focal point, where it is possible to measure a maximum pulse/echo response. The focal point should be adjusted so that it intersects the target anatomical organ and the correspondent echo is more accurate than those from other depths. This point can be modified using acoustic lens or by constructing phased-array transducers. By definition the focal point cannot has a greater distance than its near field [205, 210].

### D. Active Element

The first step to manufacture an UT is the selection of an active element that works as the vibration source. The selection of the proper material demands careful analysis of the operational environment, bandwidth and sensitivity needs.

Due to the high variation of tissues in the abdominal area, a big challenge is to reach an adequate depth of penetration together with a sufficient spatial resolution. Since, the attenuation and resolution is reduced for lower frequencies, a good trade-off between attenuation and spatial resolution, to detect all the abdominal interfaces, has been achieved with frequencies ranging from 1.5 to 3 MHz [234, 235].

Even though there have been a considerable number of different piezoelectric materials investigated, exhibiting improved coupling coefficients and extremely high dielectric constants, the choice of commercially available materials is limited. A number of materials are currently evaluated and tested such as lead zirconate titanate (PZT), lead metaniobate, lithium sulphate, lithium niobate, quartz, barium titanate and polyvinylidene fluoride (PVDF) [216, 236-238].

PZT has been one of the most commonly used and tested material [235] for the fabrication of medical US transducers with low frequencies, because of its high-piezoelectric and dielectric constant, relative permittivity and electromechanical coupling coefficient [225, 228]. This work uses a PZT-27 as the active element, which is a standard from Ferroperm. The elements are covered by a silver electrode metal giving good electrical conductivity and chemical stability.

PZT materials work with narrowband frequencies, where its working frequency $f$ is mainly determined by the thickness $t$ and acoustic velocity $v$ of the piezoelectric element [205] (Equation 6-2).

$$f = {}^{v}/_{2t} \qquad \text{Equation 6-2}$$

All piezo ceramics are polarized along its thickness, meaning that the electric field is applied along the thickness direction.

### E. Simulation

Although an UT structure is simple in physical principal (Figure 6.2), its practical design and construction has been a trial and error process, due to many factors affecting its final performance (e.g. backing and matching layer thickness, used materials, depth of penetration, etc.).

Since experimental methodologies to test ultrasonic transducers may become very time-consuming or costly, an ideal UT configuration may be effectively evaluated under computer simulation. Several software application and theoretical calculations have been developed to estimate and design transducers with reduced ripples and pulse duration, high sensitivity and broad bandwidth operation [220, 239, 240]. Computer simulation of different transducers were carried out using a commercial software package - Wave2000 Plus (from Cyber-Logic inc., N.Y., U.S.A.).

The simulation process starts by creating a PCX file, e.g. under Photoshop CS5, of a 2D representation of the UT configuration (Figure 6.4). Transducers are made with a piezoelectric layer (1.5 mm thick x 25 mm wide; d in Figure 6.4), a matching layer (25 mm wide; f in Figure 6.4), backing layer (35 mm thick x 25 mm wide; a in Figure 6.4) and with convex or concave lens.

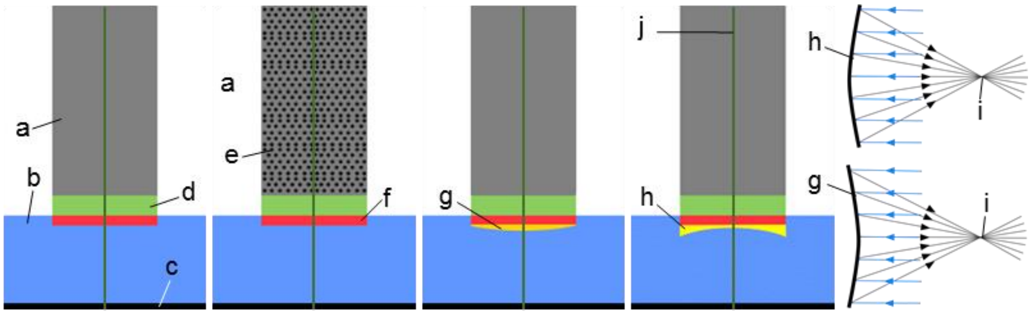

Figure 6.4. 2D representations of some UT configurations: a) backing layer; b) water; c) material with high reflexive coefficient; d) piezo electric material; e) particles inside the backing layer; f) matching layer; g) convex acoustic lens; h) concave acoustic lens; i) pulse/echo acoustic rays; j) needle.

The effect of backing and matching layers were tested with different materials and thicknesses:

- Material similar to the piezoelectric one but high damping coefficients;
- Epoxy;
- Epoxy mixed with tungsten;
- Epoxy mixed with tungsten and cork powders (particle size $\geq$ 1 mm).

The goal of using cork powders was to increase scattering losses at the same time exhibit high attenuation coefficient.

For the matching layer, three different thicknesses were tested ($\lambda/2$, $\lambda/4$, $3\lambda/4$) with epoxy and a synthetic (acoustic properties placed between water and the piezoelectric layer) material. The epoxy material was chosen because it presents low viscosity, small heat shrinkage and acoustic impedance similar of human tissue (2.4 MRayl).

Since the effect of the lens is dependent on its shape and propagation velocity, two different configurations were simulated (convex and concave, Figure 6.4). The focal length $f$ was determined according to the following equation [215, 241]:

$$\frac{1}{f} = (\frac{c_1}{c_2} - 1)(\frac{1}{R_1} + \frac{1}{R_2}) \qquad \text{Equation 6-3}$$

$c_1$ and $c_2$ are the medium and lens sound velocity, respectively, and $R_1$ and $R_2$ are the radii of curvature of the lens surface (exterior and interior ones, respectively). $R_1$ and $R_2$ are positive for a convex and negative for a concave surface. The apex of the lens was manufactured to has a thickness of $(n-1)\frac{\lambda}{4}$ (with $n$ being an even number) at the center of the transducer. The idea was to analyze the pulse/echo response at different focal lengths.

### F. Fabrication

After studying and simulate various options of UT designs, three UTs were fabricated in order to (1) generate enough acoustical power to detect tissue interfaces along the percutaneous path, (2) have a needle working channel and (4) small dimensions for easing maneuvering:

- UT1 – UT based in a single PZT-27 ceramic disc with 25.4 mm of diameter (area of 507 $mm^2$), 1.5 mm of thickness and nominal frequency of 3.3 MHz (most common frequency used in PRA procedures [66, 155, 205])
- UT2 – Identical with UT1, but with an epoxy acoustic lens;
- UT3 – UT based in an array of six PZT-27 ceramics, where each element has a trapezoid shape, 5 mm of thickness, 102 $mm^2$ of area and nominal frequency of 3.2 MHz.

Figure 6.5 and Figure 6.6 shows some fabrication steps. The manufacturing process starts with the fabrication of the mold and transducer housing. It was performed by shaping a tube (stainless steel tube for UT1 and UT2; PVC tube for UT3) using a lathe machine (0.01 mm of resolution). Such materials were chosen due to its non-ferromagnetic characteristics, easy to clean properties, waterproof capabilities and can be easily manipulated by the lathe. Each tube was drilled, cut and sanded into the desired diameter, so that it was ready to receive piezo-ceramic element, backing and matching layers.

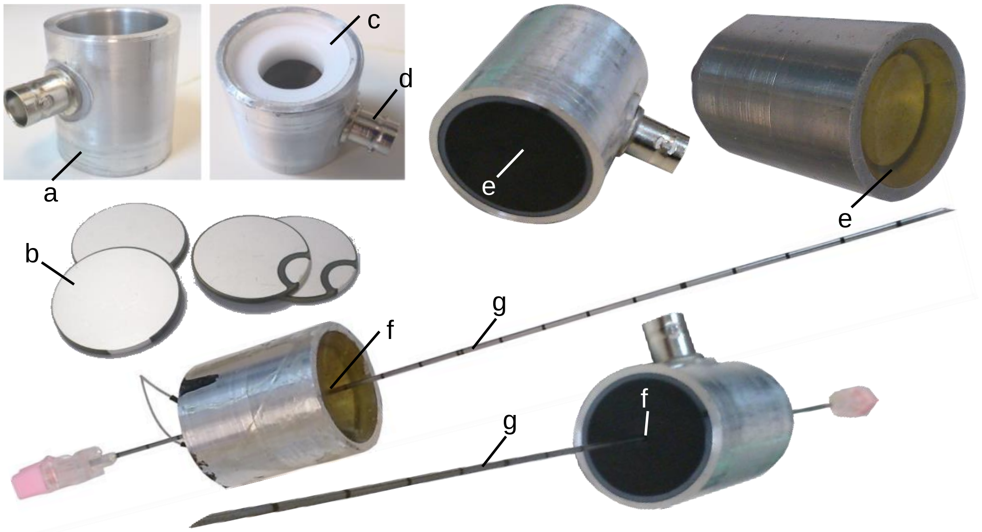

Figure 6.5. Fabrication steps for UT1 and UT2: a) stainless steel housing tube; b) piezo ceramic disc – PZT-27; c) plastic mold; d) coaxial connector; e) matching layer; f) needle working channel; g) 18G surgical needle.

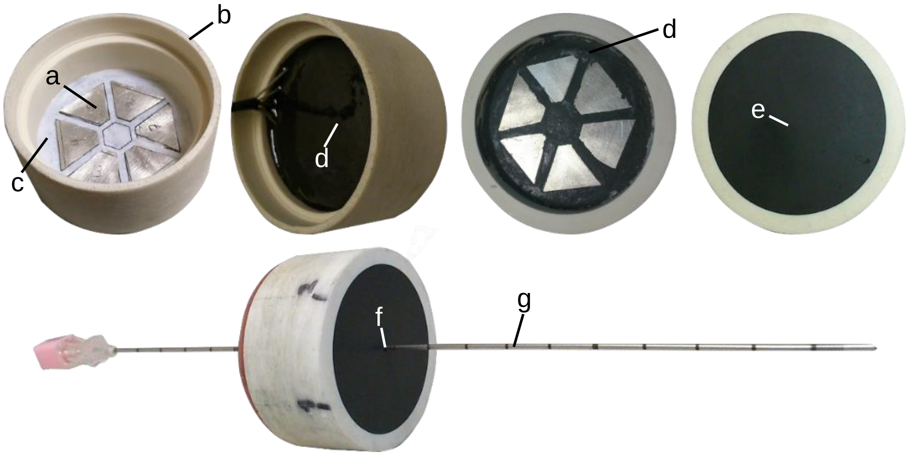

Figure 6.6. Fabrication steps for UT3: a) piezo ceramic with trapezoidal shape – PZT-27; b) PVC housing tube; c) silicon mold; d) backing layer; e) matching layer; f) needle working channel; g) 18G surgical needle.

Next, using a hot bar soldering, electrical contacts were made between the front and back ceramic faces (ground and excitation, respectively) and a BNC (Bayonet Neill–Concelman) connector. For the UT3, each trapezoidal piece was independently linked to a single connector in order to receive and process each element separately. All the electrical contacts were made with low-temperature soldering (<200 °C) in order to avoid the damage of the piezo-ceramic film. The soldered ceramics were further placed in the mold, within the housing tube, for supporting to the mold and placed in the housing tube (UT1 and UT2 with an outer diameter of 32 mm UT3 with 45 mm).

The six trapezoidal pieces in the UT3 were equally distributed, by a 60° angle, around the needle working channel (Figure 6.6). The space between each piece was minimal (~1 mm) and filled with a non-conductive silicon material in order to maximize the acoustic power.

The matching layers solution was made with epoxy resin mixed with tungsten powder (particle size of 1 micron and 99.95% purity). The tungsten powder had a volume fraction of 48% in the matching layer. Tungsten with this particle size was chosen in order to reduce the US scattering and attenuation. This solution was centrifuged during 10 minutes and then put in a vacuum chamber for 40 minutes to release trapped air bubbles. The final liquid was transferred directly on to the UT front mold designed and fabricated to have a thickness of $\lambda/4$. The matching solution was cured at room temperature during two days. After being hardened, this layer was grounded and rectified to its calculated thickness of $\lambda/4$, removing a curvature that may exist due to solution surface tension.

For the UT2, a silicon mold with a convex curvature was used to create an epoxy lens in front of the matching layer.

The backing layers were made with high-loss high-impedance tungsten-loaded epoxy mixed with cork powders (particle size $\geq$ 1 mm). These mixtures were not put in the vacuum chamber in order to obtain high acoustic attenuation and reduced back-wall reflections. This layer was also stabilized at room temperature during two days. The ceramics connected lead wires ware fixed to the backing layer with an addition amount of epoxy solution.

During the matching and backing layers fabrication, the mold guarantee that the solution does not flow to the back of it and vice versa, while applies enough pressure to ensure a good connection between components.

In the end, each transducer was drilled to create a 2 mm channel, so that 17G, 18G and 21G needles can be maneuvered within the probe.

### 6.2.3 Impedance Matching

Often, there is an impedance mismatch between the transducer and other interface devices such as the signal source or the data acquisition device. This minimize the maximum amount of power transferred from a source to a load, increase the signal reflection from the load and can even damage the source [218].

According to the maximum power-transfer theorem [225, 234], an optimum power of 50% of the total power can be achieved by making the load impedance $Z_L$ equal to the source impedance $Z_S$ (Figure 6.7).

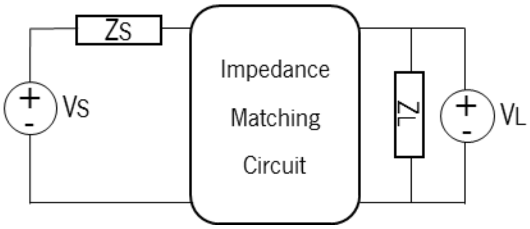

Figure 6.7. Representation of an impedance matching circuit and source and load components.

In general, impedance matching between a source and a load can be classified into three categories:

- Source and load are both resistive and unequal;
- Source is resistive and the load is complex;
- Both the source and the load are complex.

Therefore, when the load is a complex and the source is resistive, it is required a reactance cancellation. The impedance matching process starts by defining an equivalent electric circuit for each unmatched piezoelectric (UT1, UT2, and UT3). An impedance analyzer (Omicron Lab Bode 100) was used to measure the electrical impedance curves, by connecting the two ceramic polarities to independent contacts of the measuring system.

Because every transducer works within a narrower band, each ceramic piece (UT1, UT2 and each UT3 trapezoidal element) was matched with a specific circuit. Different network topologies were used to move the impedance point along the constant resistance and conductance curves.

L-Network circuits were configured with two low-pass and two high-pass versions (Figure 6.8 -a to -d). Although L-network topologies are very versatile and broadly used to attenuate signal harmonics and noise, it only can match a limited range of impedances [242]. To this extent, T-Network (Figure 6.8 -e and -f), $\pi$-Network (Figure 6.8-g and -h) and two-cascaded L-Networks (LL-Network) (Figure 6.8 -i to -l) were equally considered. Different low-pass and high-pass versions were also considered to reduce the necessity of too large or small inductance or capacitance for a given frequency range.

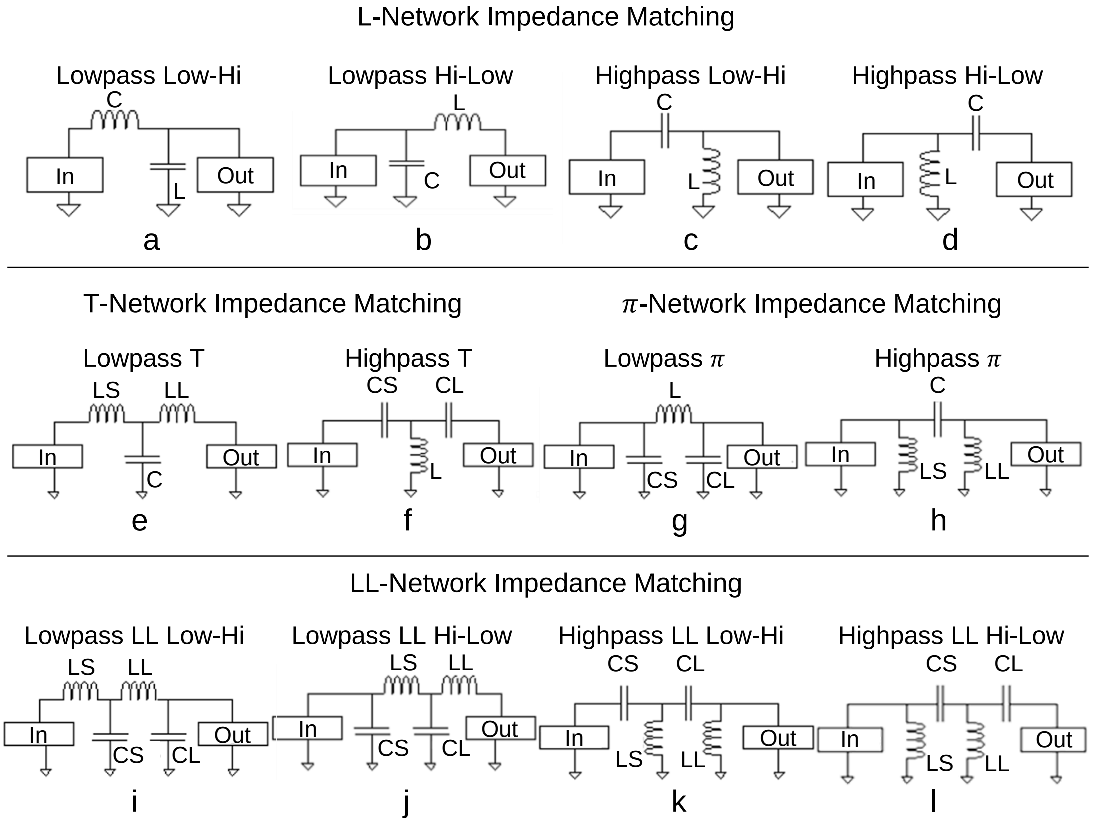

Figure 6.8. Representations of different impedance matching circuit topologies. $In = RS + jXS$ and $Out = RL + jXL$.

The inductances and capacitances values for each circuit were determined based on the resonance frequency of each transducer. These were kept under certain values so that the impedances are matched within a given quality factor $Q$ ($Q$<5). Larger bandwidths can be obtained with lower $Q$ values, which commonly requires adding more components to reach the 50 $\Omega$

impedance point. Thus, it creates a tradeoff between the desired bandwidth and the network complexity.

Each network topology was designed and simulated under Matlab R2014b using the Radio Frequency Toolbox [243]. This toolbox provide high level functions able to calculate the frequency response of the (un)matched transducer and the network gain.

By knowing the frequency operation of each transducer, $Zs$ and $ZL$, initial components values for all capacitances and inductances (C, L, CS, CL, LS and LL, Figure 6.8) were calculated based on the electric circuit analysis.

### A. Circuit Optimization

With $F_{Ti}$ being the operational frequency of $UT_i$ (i=1,2 and 3), each impedance matching transformer (IMT) must operate between $F_{Ti}$ $\pm$0.5 MHz. The initial values of the capacitances and inductances of each IMT were further optimized resulting in new output values.

Each circuit was firstly constructed under Matlab as cascaded network of radio frequency objects. The optimal component values was found by a systematic and repetitive process during which the admittances and capacitances were iteratively adjusted towards the minimization of a cost function, $f$(IMT). Although the cost function could be calculated by several ways, one have chosen to minimize the average reflection coefficient in the passband, so that the power energy transference is increased.

New capacitance and inductance values were calculated by a direct search method described by Lagarias *et al.* [244]. This method is based on the iterative update of a simplex made of $n$+1 vertices in $n$ dimensions.

Each vertex $V_i$ (for $i$=1, $n$+1) is interpreted as a possible candidate solution given the initial capacitance and inductances values and is associated with a function value $f(V_1) \leq f(V_2) \leq f(V_n) \leq f(V_{n+1})$. Because the algorithm seeks to minimize the cost function, $f(V_1)$ refers to the best function value, $f(V_2)$ as the next best function value and $f(V_n)$ as the worst function value.

At each iteration $k$, the centroid $\bar{x}(n+1)$ of the remaining $n$ vertices are computed where the worst vertex $V_{n+1}$ is excluded.

A reflected point $V_R$ is then computed with respect to the worst vertex $V_{n+1}$: $V_R = (1+\rho)\bar{V} - \rho V_{n+1}$, where $\bar{V}$ is the average value ($\bar{V} = \frac{1}{n}\sum_{i=1,n} V_i$ ), $\rho$ is a reflection coefficient and $f(V_R)$ is the function value for $V_R$. From this point, four possibilities can be computed at each iteration: reflection (when $f(V_1) \leq f(V_R) \leq f(V_n)$), expansion (when $f(V_R) \leq f(V_1)$), contraction (when $f(V_R) \geq f(V_n)$) and shrinkage (when any of the other conditions are true). These operation depend on the following coefficients: reflection $\rho = 1$, expansion $\beta = 2$, contraction $\gamma = 1/2$ and shrinkage $\sigma = 1/2$. They were chosen with standard values in order to respect the following requirements: $\rho > 0,\ \beta > 1,\ \beta > \rho,\ 0 < \gamma > 1,\ 0 < \sigma > 1$ [244].

All this steps are repeated till some stop criterion is achieved: maximum number of iterations ($nIt$) and maximum number of times that the cost function increases consecutively ($nError$).

Considering the tradeoff between speed and quality of match, $nIt$ was set to 1000 and $nError$ set to 50, increasing the probability that the cost function converge for one single minimum value.

### 6.2.4 Echo Detection

Each time $t$ that a tissue or anatomical organ move or suffer some deformation along the PPT, a new echo in the A-scan ($A_t$) signal is generated. The number of echoes, $ne_t$, are dependent on the number of interfaces between tissues with different acoustic properties.

For subsequent times $A_{t+\tau}$, ($\tau$ is a constant to get future signals) an echo amplitude can be reduced or increased. Moreover, echoes not presented at $A_t$ can now appear at $A_{t+\tau}$, and vice-versa.

An alert will be generated whenever there is a change in the number or position of echoes between $A_t$ and $A_{t+\tau}$ (Figure 6.9).

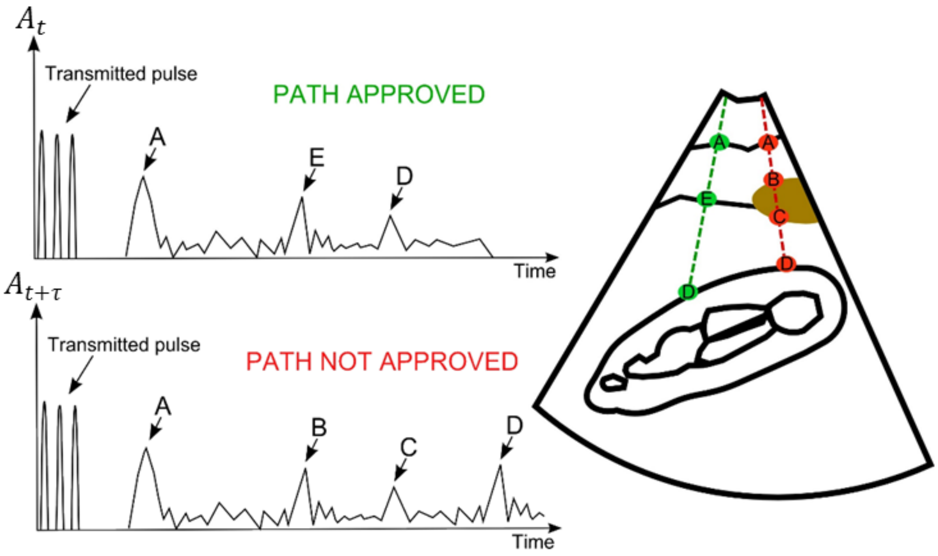

Figure 6.9. Overview of different reflected signals from tissue boundaries showing an adequate or inadequate puncture path.

Since the echo signals appear as local maxima (i.e. peaks) in the $A_t$, they can be automatic detected using peak detection algorithms. Although, this is an indispensable step to alert whether some change occurs along the PPT, it can also be a challenging task, since some $A_t$ echoes may be submerged by noise giving high false positive rate of detection.

Therefore, peak detection algorithms often combine many peak characteristics in order to differentiate interface peaks from noise peaks. To overcome these problems, various algorithms have been proposed over the literature to identify true signal peaks [245, 246]. In order to increase the sensitivity and specificity of peak detection methods, the signal was smoothed with low-pass filters to remove peaks with low intensity and random spikes [247].

The next two sub-sections describes two different approaches to deal with the peak detection problem.

### A. Peak-based method

This first approach is based on the peak detection after smoothing the input signal. Two different low-pass filters were tested and compared: Gaussian and Savitzky-Golay filter.

The Savitzky-Golay filter can be generalized as a moving average filter, performing a least-squares fitting of polynomials to segments of data. This filter is less effective for reducing noise, but more effective to keep the original signal shape, i.e. have potential to keep the echo signals without removing them. The smoothed point $y[n]$, from a signal point $x$ with $k$ points, is given by Equation 6-4, where $A_i$ controls the polynomial order [248].

$$y[n] = \frac{\sum_{i=-k}^{k} A_i x[n-i]}{\sum_{i=-k}^{k} A_i} \qquad \text{Equation 6-4}$$

On the other hand, a Gaussian filter reduces the noise corrupting the signal according a standard deviation parameter ($\sigma$). This filter gives a weighted average of a local neighborhood, where the neighborhood width and the amount of smoothness is function of the $\sigma$. For 1D signals, the Gaussian function $G(x)$ (with $\mu$ being the position of the center of the peak) is the probability density function of the normal distribution (Equation 6-5):

$$G(x) = \frac{1}{\sigma\sqrt{2\pi}} e^{\frac{-(x-\mu)^2}{2\sigma^2}} \qquad \text{Equation 6-5}$$

The smoothed signal was input to a method that detects zero-crossing in the slope differences between a point and its neighborhood. Additional constrains such as peak width $p_W$, minimum distance between peaks $min_{pD}$ and peak prominence $p_P$ were used to detect only the desired peaks and ignore the ones that present small amplitude and are too wide or too narrow. The $p_W$ were calculated by least-squares curve-fitting of a segment of original unsmoothed data in the vicinity of the zero-crossing [249].

The prominence $p_P$ measures the intrinsic height of the peak. It is calculated by extending a horizontal line from the peak top until it crosses the signal or reaches the left or right end of the peak [249]. The prominence is the vertical distance between this horizontal line and the peak top.

### B. Wavelet-based method

This second approach implements the work already described by Du *el al.* [250]. It is based on a continuous wavelet transform (CWT) methodology for peak detection. CWT is calculated as the sum over time of the signal times a scale factor, shifted by a wavelet function $\psi$. The CWT receives the input the signal without any pre-processing stage, and mathematically, can be represented in Equation 6-6.

$$c(a,b) = \int_R s(t)\psi_{a,b}(t)dt, \psi_{a,b}(t) = \frac{1}{\sqrt{a}}\psi\left(\frac{t-b}{a}\right), a \in R^{+} - \{0\}, b \in R \qquad \text{Equation 6-6}$$

where $s(t)$ is the signal, $a$ is the scale, $b$ is the translation $\psi(t)$ is the mother wavelet, $\psi_{a,b}(t)$ is the scaled and translated wavelet and $c$ is the 2D matrix of the wavelet coefficients.

The mother wavelet highly influences the peak detection, since its coefficient should reflect the similarity between the signal $s(t)$ and $\psi_{a,b}(t)$. The Mexican Hat was used for this work due to its common shape [250].

This CWT coefficients can be visualized in a color map image, where its ridges can be correlated with the spectrum peaks. The information over the 2D CWT coefficients matrix provides additional information on how the CWT coefficients change over scales. As stated in [250] the peak detection problem is now turned into finding ridges, over the 2D CWT coefficient matrix, and utilizes these coefficients to identify the echoes (Figure 6.10-b).

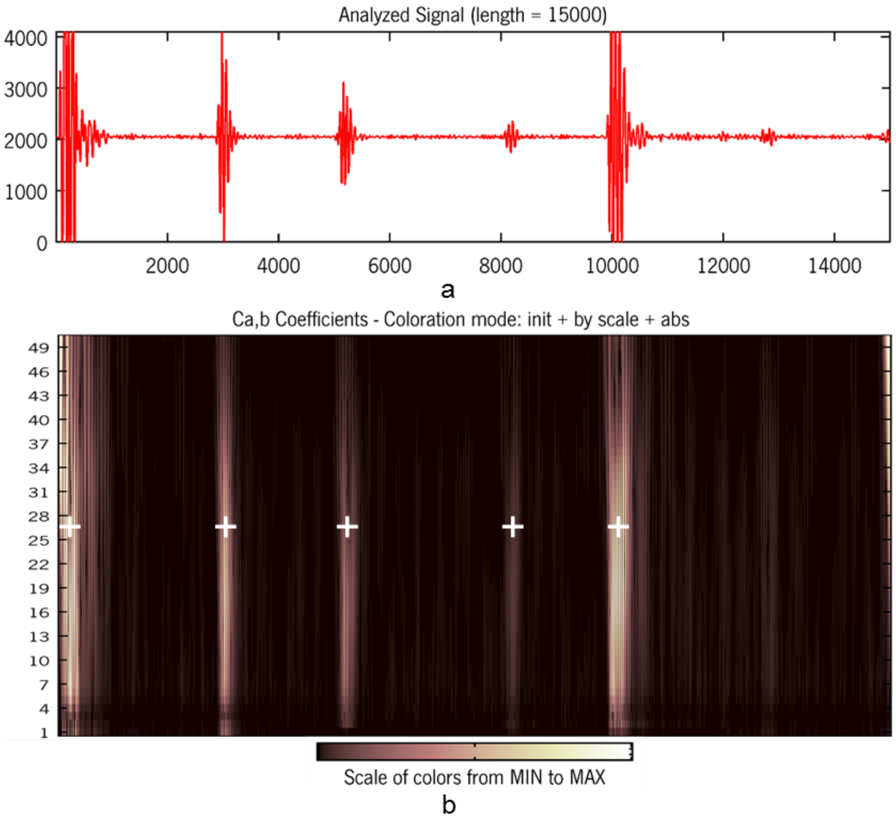

Figure 6.10. Peak identification process based on CWT: a) shows the input signal and b) shows CWT coefficient image with 50 scale levels (yellow represents high amplitude and black represents values close to zero). The crosses presents local maxima.

At each scale the corresponding CWT coefficient have a local maximum around the peak center. This local maximum gradually increases until it reaches a maximum which occurs when the scale best matches the peak width. Then, it gradually decreases again.

From Figure 6.10-b major echoes correspond to long and high ridges, while the small peaks correspond to short and low ridges. The echo center was determined by detecting the local maxima ridge of the CWT coefficients at the half scale level. First, a sliding window with size $W$ will search for continuous ridges. Its size is proportional to the wavelet support region at the scale. Then, some constraints were considered to the detected ridges:

- They must have a minimum length of $R_L$;
- Each ridge must have a gap number less than a gap threshold $G_T$ (a gap exists when a ridge line is discontinued, i.e a relative maximum is not found within a given ridge distance. The maximum allowed distance, $max_D$, between two nearest points should be less than the sliding window size at that scale level);
- The maximum amplitude, $max_A$, on the ridge line, which is proportional to the width of the peak, should be within a certain range.

Finally, the peak position is calculated based on the centroid position within a specific windows size on the ridge line.

## 6.3 Experiments

### 6.3.1 Phantom Building

In order to test the developed UTs, different acoustic phantoms were built in order to mimic some common puncture trajectories. Due to a wide range of anatomical variations, such as size, shape and composition, different phantoms setups were used to simulate acoustical tissue properties, mainly with respect to impedance and attenuation coefficients [251-253]. Different interfaces between adjacent structures were created (ST = Soft Tissue):

- ST | Muscle | Bone | ST | Liver | ST | Kidney
- ST | Muscle | ST | Muscle | Colon | ST | Kidney
- ST | Muscle | Bone | ST | Kidney

- ST | Muscle | ST | Kidney
- ST | Muscle | Colon | Muscle | ST | Kidney

The thicknesses of each phantom was defined by conducting a study with different CT datasets to quantify the following parameters:

- Distance between the skin surface and kidney surface
- Distance between the skin surface and kidney stone surface
- Number of relevant interfaces along the PPT
- Thickness of the most common organs lying at the PPT and might be injured during PRA

To this extent, points were picked along PPT with different orientations (Figure 6.11), each time a new organ was intersected (points P0 to PT in Figure 6.11).

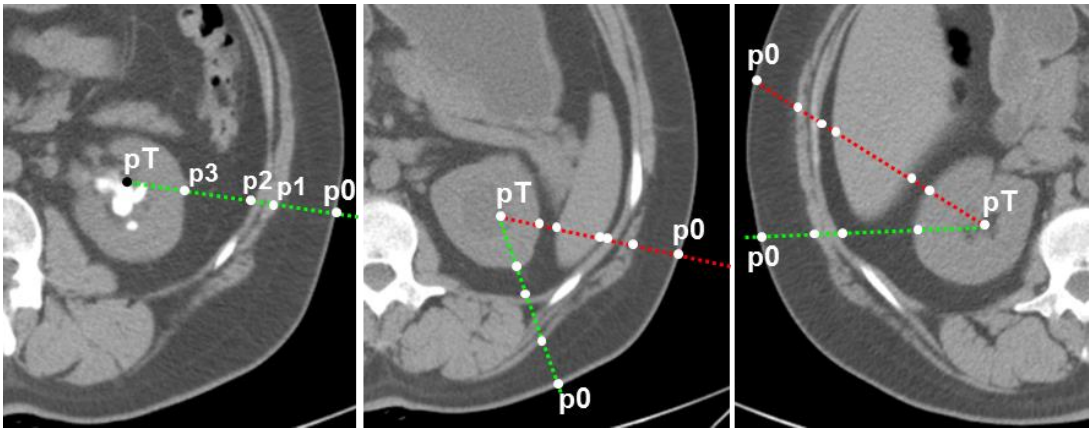

Figure 6.11 Representation of two different puncture trajectories: puncture path where some vital organ is perforated (red lines) and an ideal puncture path (green lines). All points represent picked interfaces along the PPT.

Then, acoustic properties of each phantom were determined according theoretical parameters at a measuring frequency of 1 MHz [254, 255] (Table 6.1).

Phantoms were made with a suspension of PVC (Polyvinyl chloride), called PVCP (Polyvinyl chloride - plastic) from the M-F Manufacturing Co., Fort Worth, TX, USA) [256, 257]. PVCP is a non-toxic plastic opaque solution which polymerizes and becomes translucent when heated to high temperatures.

PVCP was mixed with different concentrations of graphite powder $C_{gP}$ which controls the degree of acoustic attenuation. On the other hand, the thickness of each phantom was determined according to the average distances from the CT analysis.

Table 6.1. Typical acoustical properties of several body tissue.

| **Body Tissue** | **Density** $(Kg/m^3)$ | **Sound Velocity** $(m/s)$ | **Accoustic Impedance** $(Kg/(m^2 \cdot s) \times 10^6)$ | **Attenuation Coefficients** $(dB/cm)$ |
|---|---|---|---|---|
| Fat | 950 | 1440 | 1,37 | 1,15 |
| Blood | 1060 | 1570 | 1,61 | 0,18 |
| Kidney | 1040 | 1557 | 1,62 | 1 |
| Liver | 1060 | 1566 | 1,66 | 0,67 |
| Spleen | 1060 | 1566 | 1,66 | 0,45 |
| Muscles | 1070 | 1584 | 1,70 | 1,35 |
| Bone | 1595 | 3400 | 5,58 | 12,5 |

Each phantom solution was centrifuged during 10 minutes and then put in a vacuum chamber for about 40 minutes to release trapped air bubbles. In the end, it was heated until it reached 180° and then stabilized in room temperature in a specific glass mold.

Other inclusions were manufactured using silicone molds of irregular shapes and sizes from 5 mm to 2 mm. The inclusions were made of pure PVCP using the above methodology. A bone phantom, with high acoustic attenuation, were also fabricated using epoxy-resin materials.

The phantom attenuation and thickness are the most important parameters for this work, since they influence whether the generated signal is or not able to reach the desired distance to the kidney. This US attenuation is the decay rate of the wave as it propagates through material given by the Equation 6-7.

$$A = A_0 e^{-\alpha d} \qquad \text{Equation 6-7}$$

$A_0$ is the initial amplitude of the sound wave before entering in the medium, $A$ is the reduced amplitude after traveling the medium with an attenuation coefficient $\alpha$ and size $d$. Attenuation $\alpha$ can be determined by measuring backwall reflections in an A-scan signal according to the following Equation 6-8.

$$\alpha = \frac{0.1151}{v} dB/s \qquad \text{Equation 6-8}$$

$v$ is the velocity of sound (m/s).

### 6.3.2 Phantom Properties

The acoustic properties (attenuation coefficient and propagation velocity) were estimated individually for each phantom using two commercial UT of 1 MHz. This frequency was chosen because most of the acoustic properties are described in literature under this single frequency.

These two transducers were longitudinal aligned in a tank of distilled water at 25 °C and separated by 5 cm: one worked as the emitter of a pulse signal and the other as the receptor. Each phantom block was individually placed between the two transducers. Based on the travelling time of the sound signal and the attenuation of the signal that arrives at the receptor transducer it was possible to classified the acoustic properties of each phantom.

This consists in comparing two acoustic pulses: one propagates through the phantom and another propagates the same distance in water. Both signals are received by the receptor. Comparing the propagation time and amplitude spectra of both received pulses, it is possible to estimate the phantom propagation speed and attenuation. Nonlinear propagation effects were not considered because the amplitude pressure and propagation distance was small. Instead of literature quoted values of attenuation, this experiment gives an accurate indication of the attenuation.

Different phantom blocks were constructed in order to mimic the spleen, liver, kidney, fat and muscle, regarding to the attenuation coefficients at 1MHz [dB/cm] (Table 6.1). Such attenuation was achieved by using the following concentrations of graphite powder: $C_{gP}$=0.3%, $C_{gP}$=0.5%, $C_{gP}$=0.6% and $C_{gP}$=1%.

### 6.3.3 Impedance Matching

The UT electrical impedance curves (magnitude and phase) were accessed during all the fabrication stages, i.e, from the isolated ceramic to the complete transducer assembly, assuring that the piezo-ceramic is not damaged or losing the electrical connections.

For each circuit version (Figure 6.8) the gain and theoretical matched frequency response was computed under Matlab. The gain was calculated as the magnitude ratio obtained with the frequency response of the matched transducer and that of the unmatched transducer. The version with higher gain was considered for implementation. The real frequency response of the unmatched or matched transducer was measured using an impedance analyzer (Omicron Lab Bode 100).

In order to determine the most efficient electrical matching, each UT3 element was individually coupled to a matching circuit that centrals each element at the same resonance frequency.

### 6.3.4 Performance Mapping

UT1, UT2 and UT3 were mapped in an acoustic tank in order to evaluate their directivity pattern, focal length (distance from the transducer face to the focus) and beam cross-sectional area (area on the surface of a plane perpendicular to the beam axis consisting of all points where the pulse intensity integral is greater than 25 percent of the maximum pulse intensity integral).

Figure 6.12. Mapping setup: a) 3D robotic arm; b) UT outside the water tank; c) needle hydrophone.

The setup is composed by a:

1. Degassed (to prevent the formation of bubbles) and deionized (prevent hydrophone corrosion) water tank;
2. Transducer element (works as the emitter);
3. Needle hydrophone (from Precision Acoustics Ltd. with a diameter of 0.5 mm and 200.7 sensitivity mV/MPa) coupled to a 3D robotic table. The needle hydrophone work as the receiver and moves in different directions with a controlled temperature of 22 °C.

The mapping starts by manually aligning the emitter and receiver. Here, the needle hydrophone is aligned to the center of a piezo-element by searching the maximum peak signal. For the UT1 and UT2, this center corresponds to the center of the transducer device.

Then, the hydrophone moves inside the water tank, with a scanning volume of 50x50x150 mm and step of 0.348, 0.348 and 25 mm in the x, y and z directions, respectively.

Each transducer was excited by a signal generator AFG 3021 (from Tektronix) with 5-cycle bursts at the working frequency and amplitude of 10 Vpp. The generator operates at 50 Ω and phase 0.

Acoustic signals detected up by the hydrophone were digitalized and stored in a PC, though a Labview® program that controls an oscilloscope (TDS 3014B from Tektronix). The signals were averaged 8 times with a sampling frequency of 80 MHz and 15.000 points/signal.

UT3 was mapped six times, in order to evaluate the electrical crosstalk for each trapezoidal element. Each time, one single element was excited and the voltages of the remaining and grounded elements were measured.

### 6.3.5 Simulation

Simulation results were performed with an input signal of 10Vpp, 3-cycle bursts and 10 dB gain. The UT was configured to work with a 3 MHz as the center of frequency and a pulse/echo response into water medium. The influence of the backing materials on the UT transfer function was analysed under the assumption that all the matching layer are $\lambda/4$. Different focal lens were considered: 5 cm, 8 cm and 10 cm.

### 6.3.6 Transducer efficacy for PRA

Several experiments were performed in different phantom setups to evaluate the efficacy end effectiveness of each UT for PRA. During the tests, each transducer was excited using a US-Key pulser/receiver (from Lecoeur Electronique). Echo responses were digitized with a sampling frequency of 80 MHz and transmitted via USB interface to a Matlab software for displaying and analysis purposes [258]. Signal responses were acquired with 15 FPS. Experimental results were performed using matched UT.

#### A. Axial Resolution

The UT axial resolution was quantified by measuring the echo width in a water medium, by using a quartz-plate with a high reflection coefficient at 50 mm distance.

### B. Depth of Penetration

The depth of penetration was measured as the ability to create detectable echoes when acquiring signals with different phantom setups. To this extent, one use phantom blocks with acoustic attenuations coefficients close to soft tissues and thicknesses ranging from 2 to 12 cm. Echoes should be produced at each 2 cm.

### C. Echo Detection

Considering the described algorithms for echo detection, the optimal parameters combination were found by a systematic and repetitive process, where one parameter was individually increased/decreased while the others remained constant. To achieve a refined parameter echo estimation, each combination was tested in different signals and the average performance was

Table 6.2. Peak-based method testing parameters.

| **Parameters** | | **Values** |
|---|---|---|
| Savitzky-Golay (Equation 6-4) | $A_i$ order | 3, 5, 7 |
| | Window size | $\alpha Pe_W$, where $\alpha$ = 0.25, 0.5, 1, 1.5, 2 |
| Gaussian (Equation 6-5) | $\sigma$ | 1.5, 2 and 2.5 |
| | Window size | $\alpha Pe_W$, where $\alpha$ = 0.25, 0.5, 1, 1.5, 2 |
| $min_{pD}$ | | $\alpha Pe_W$, where $\alpha$ = 0.25, 0.5, 1, 1.5, 2 |
| $p_P$ | | $\alpha A_0$, where $\alpha$ = 2%, 2.5%, 3%, 5% and $A_0$ is the initial amplitude |
| $p_W$ | | $\alpha Pe_W$, where $\alpha$ = 0.5, 1, 1.5, 2, 4 |

Table 6.3. CWT testing parameters.

| **Parameters** | **Values** |
|---|---|
| $nScales$ (number of CWT scales) | 30, 50 and 70 |
| $G_T$ | $G_T$ between 1 and 4 with $max_D = \frac{nScales}{\alpha}$, $\alpha$ = 2, 4, 6, 8 |
| $R_L$ | $\frac{nScales}{\alpha}$, $\alpha$ = 2, 4, 6, 8 |
| Sliding window $W$ | $\alpha Pe_W$, where $\alpha$ = 0.5, 1, 1.5, 2, 4 |

accessed. Table 6.2 and Table 6.3 resumes the input parameters for both the peak-based and CWT-based algorithms, respectively.

The automatic outcome was compared with a list of ground-truth echoes. A detected echo is labeled as a false peak if its position is not within a sized window with center at the ground-truth echo and width $Pe_W \pm 0.5Pe_W$, where $Pe_W$ is pulse echo width. If multiple echoes exists within this window, they are merged and considered as one peak.

The performance of the algorithm was measured using the false discovery rate (FDR) and sensitivity. Being $FP$ the number of detectable echoes that are not present at the ground truth and $N_e$ the total number of echoes found by algorithms, FDR is defined in Equation 6-9.

$$FDR = \frac{FP}{N_e} \tag*{Equation 6-9}$$

On the other hand, being $TP$ the number of correctly identified echoes and $N_{Te}$ the total number of true echoes, sensitivity is defined in Equation 6-10:

$$Sensitivity = \frac{TP}{N_{Te}} \tag*{Equation 6-10}$$

The algorithm was finally evaluated using a performance coefficient, $PCoeff$ (Equation 6-11), which contemplates the trade-off between FDR and Sensitivity [250].

$$PCoeff = \frac{2 \times (1 - FDR) \times Sensitivity}{1 - FDR + Sensitivity} \tag*{Equation 6-11}$$

The better combination of the parameters presented in Table 6.2 and Table 6.3, the larger the $PC$. For two algorithms with the same false discovery rate, the larger the sensitivity, the better $PCoeff$. Both algorithms were evaluated in 44 phantom setups with median thickness of 80 mm (range from 70 to 120 mm).

### D. PRA Alerts

An alert is generated every time a new echo appear or disappear from a reference signal. This change must occur during a certain period of time. One estimated and tested the following times 0.5, 1.0, 1.5 and 2 seconds.

In order to test the robustness of such methodology, different setups were created (Figure 6.13):

- Setup A: phantom blocks, with acoustic properties similar to soft tissue thicknesses, stacked together to create a percutaneous path;
- Setup B: several phantom blocks, with distinct acoustic properties, stacked together to create a percutaneous path;
- Setup C: similar as B, but using phantom blocks with small inclusions which position may be changed during needle insertion;
- Setup D: dynamic test, where the phantom blocks are placed similar to Setup A or Setup B, but each block move throughout the procedure. These movements generate different alerts by creating or removing echoes.

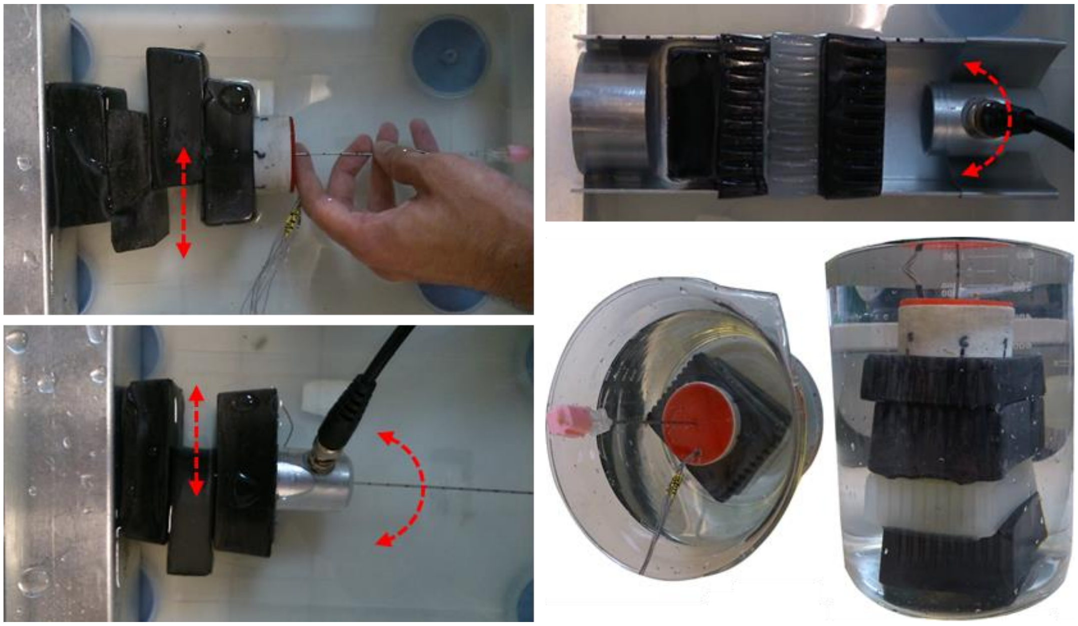

Figure 6.13. Representation of some experimental setups.

## 6.4 Results

### 6.4.1 Phantom Properties

65 CT datasets were analyzed to calculate different thicknesses between skin site and kidney target each time the path intersected a new interface (Figure 6.11). The average distance was 123.8±25.2 mm (from the skin puncture site to the kidney interface) and 154.5±26.2 mm (from the skin puncture site to the kidney calculi). The organs along the puncture path were often intersected with thicknesses ranging from 5 to 30 mm.

45 n-layer phantoms were manufactured with different properties (Figure 6.14).

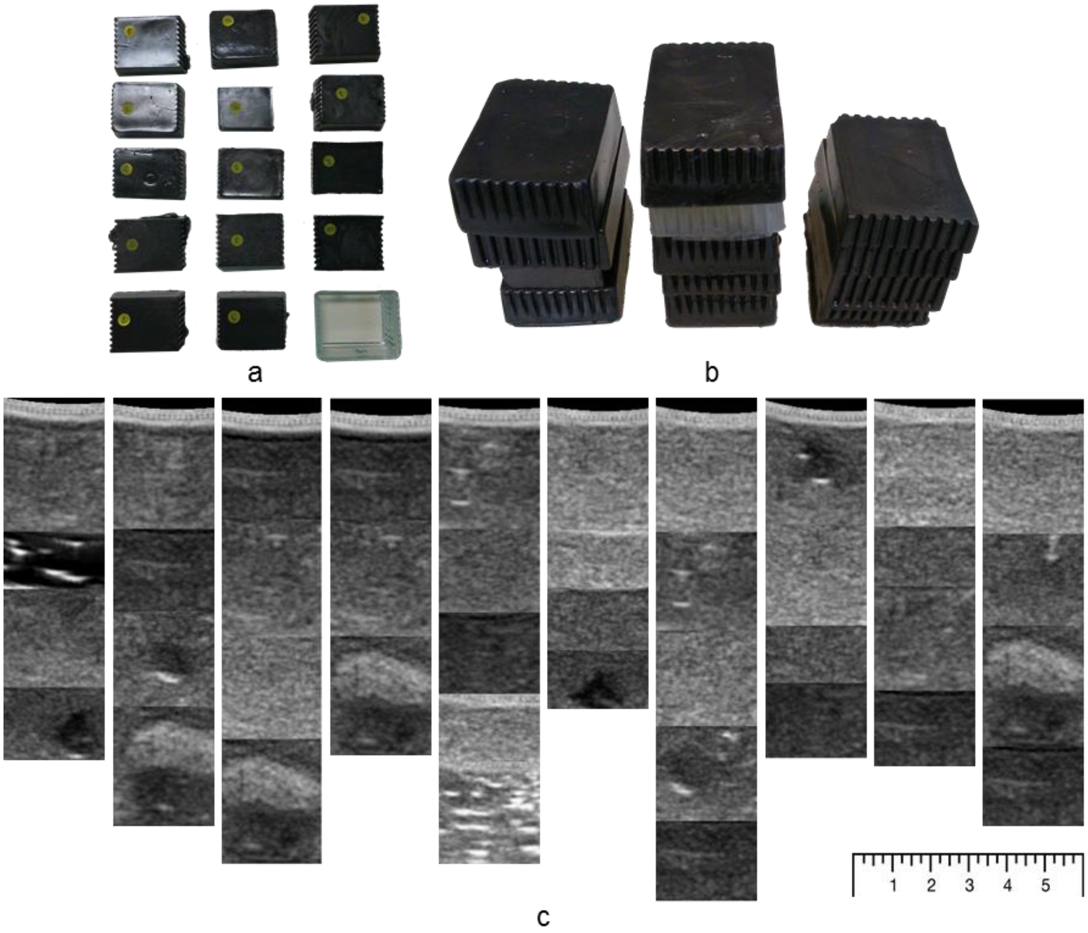

Figure 6.14. a) Phantom blocks with different acoustic properties. b) Shows phantom blocks stacked in single setups. c) Shows US images of many setups acquired using a convex probe of 3.3 MHz from the US Sonix system.

The addition of different graphite concentrations allowed different scattering levels similar to those one found in real tissues. Depending on the phantom size and by comparing the input/output amplitudes, it was possible to build individual phantom blocks with an average attenuation of 0.89±0.22 [dB/cm] (ranging from 0.62 to 1.4 [dB/cm]). The main difference with real situations was found in the propagation speed which values was approximately constant in all phantoms (~1500 m/s). In terms of US images, the visual aspect show similar intensities and textures with real situations.

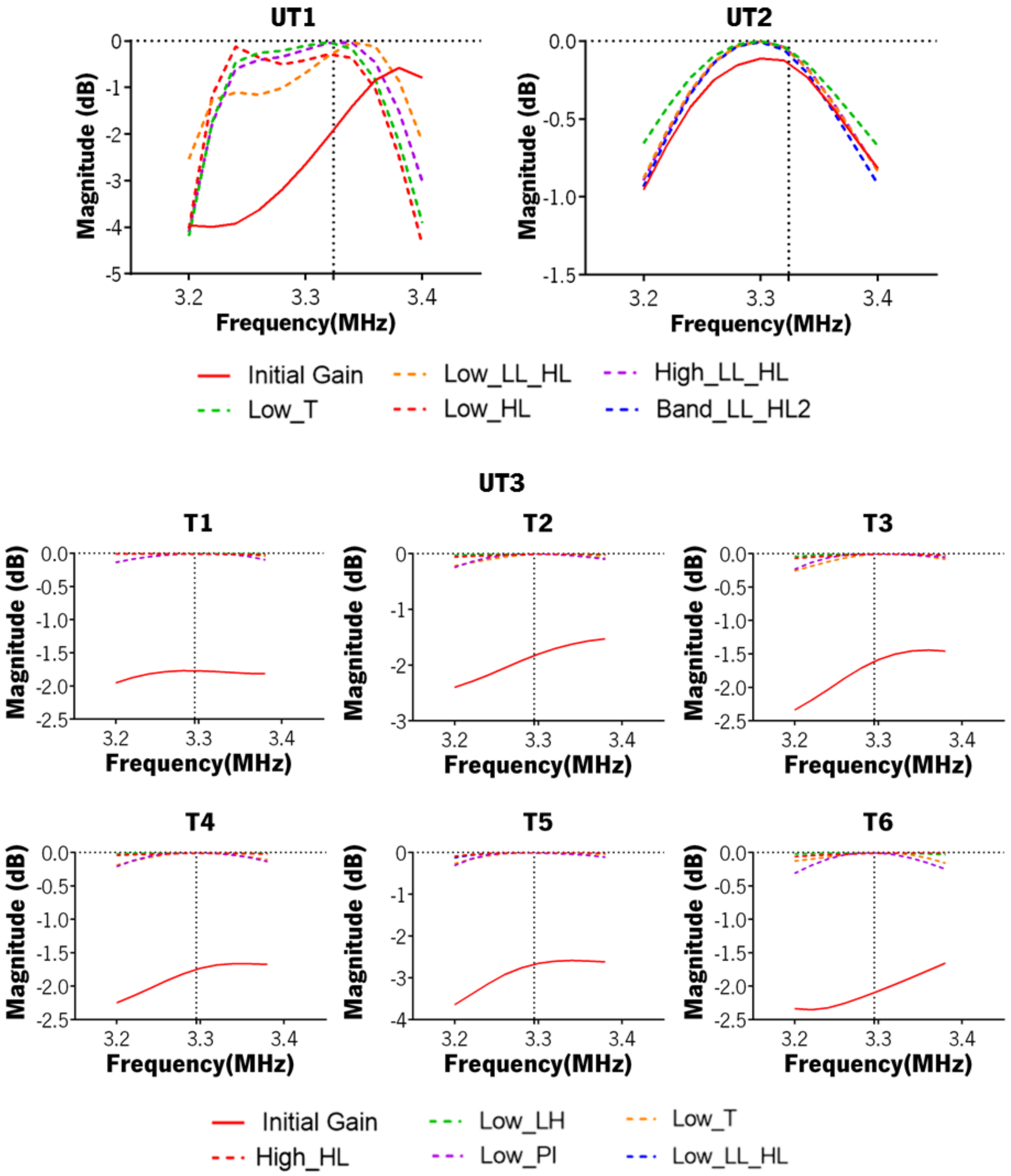

Figure 6.15. Theoretical matched gain for different impedance matching circuits topologies.

## 6.4.2 Impedance Matching

Figure 6.15 shows, for all transducers, the best 5 impedance matching circuit topologies, i.e. the ones that moves the output magnitude from negative gains (dB) to 0. Theoretical calculations show that the output power can be increased, at least, by a factor of 2 times for all UT3 trapezoidal elements and UT1.

The circuit topology was then selected according to the availability of electronic components and simplicity of the circuit. Higher gains were achieved with approximately 3.33 MHz for all the UTs. Therefore, this center frequency was chosen to maximize the benefit of the IM network.

Figure 6.16 shows the measured electrical impedance as a function of frequency for the UT1 and UT2. As calculated theoretically, it shows a working frequency around 3.3 MHz, which is the nominal frequency of the piezo-ceramic disk. After matching, the UT1 shows a matched transducers phase near 0° and a magnitude about 50 Ω. The output gain are in accordance with theoretical ones. Experimental output for UT2 was the same with or without using an impedance matching circuit.

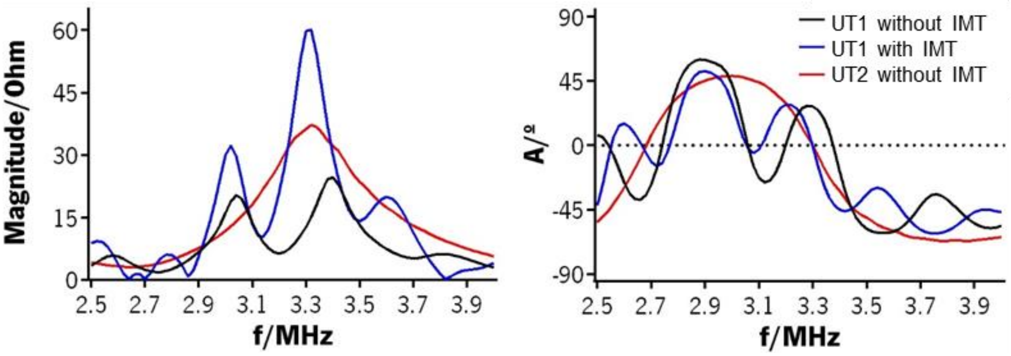

Figure 6.16. Experimental magnitude and phase for UT1 and UT2.

Figure 6.17 shows the magnitude and phase as function of frequency for each trapezoidal element of the UT3, measured with the impedance analyzer.

For the unmatched UT3, the average and standard deviation of the impedance magnitude and phase were 59.3±14.6 and -47.8±6.7°, respectively, across the elements at the resonance frequency of 3.3 MHz.

Electrical circuit elements were placed between the transducer and the function generator, to cancel the reactive or imaginary impedance at resonance, improving the electrical impedance match. For the same frequency, the average and standard deviation for the matched UT3 were 47.7 ± 4.9 and -1.0 ± 5.5°, respectively.

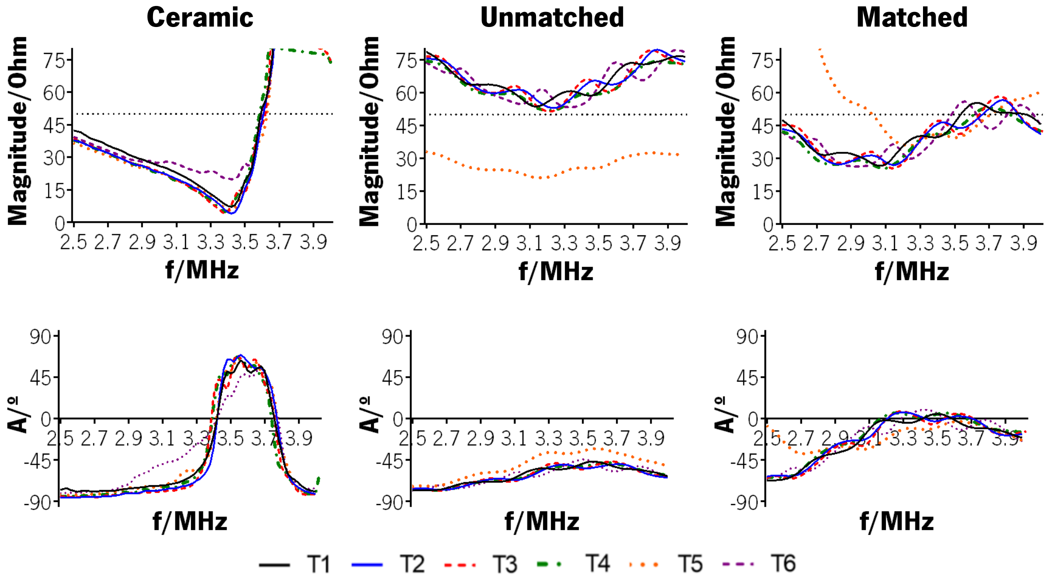

Figure 6.17. Experimental magnitude and phase for UT3.

### 6.4.3 Performance Mapping

Figure 6.18 shows the US beam for all the transducers map when the needle hydrophone was placed 100 mm away from the transducer surface.

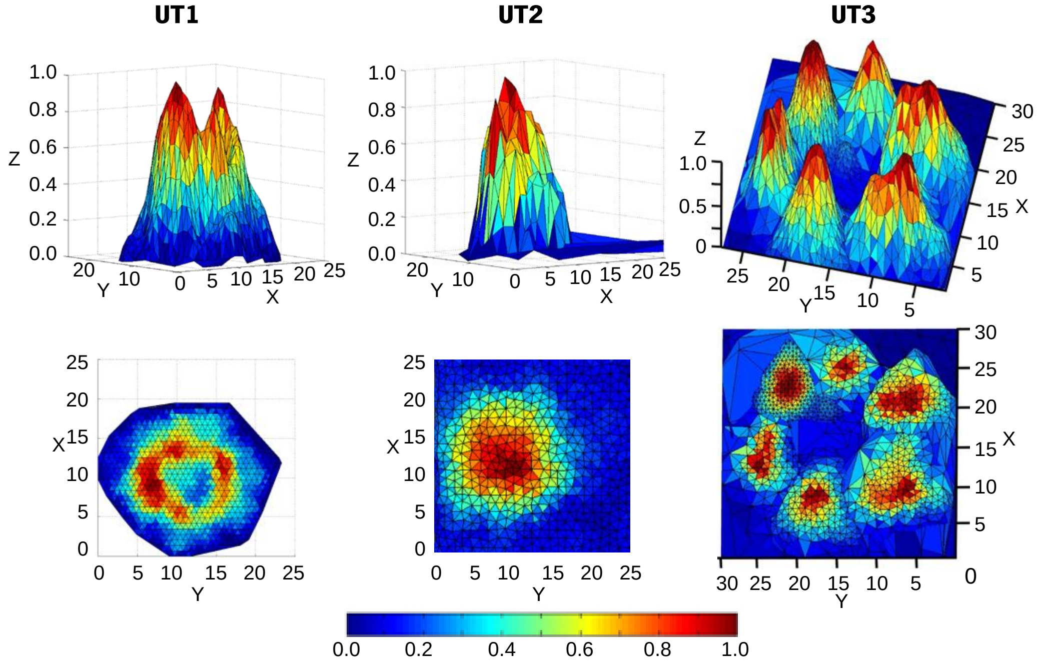

Figure 6.18. US beam mapping expressed as the ratio between the output voltages with the transmitted one.

UT mapping estimated a focal distance of 146 mm, 82 mm and 88 mm for the UT1, UT2 and UT3, respectively. The beam cross-sectional area oscillates around the ceramic area: 25 $mm^2$ for the UT1 and 102 $mm^2$ for the UT3. The UT2 beam was narrowed to 70% of the ceramic area. All transducers show symmetrical distribution of the US beam, with higher power along the central axis. Experimental tests showed that beam amplitude was reduced more than 50% when the interface angle was higher than 18° for both transducers.

Crosstalk was measured for UT3 at a single working frequency and only for the matched case. It was negligible and not affected the UT3 operation (-33 dB).

## 6.4.4 Simulation

Figure 6.19 presents simulation results for different UT configurations by transmitting and receiving pulses in water.

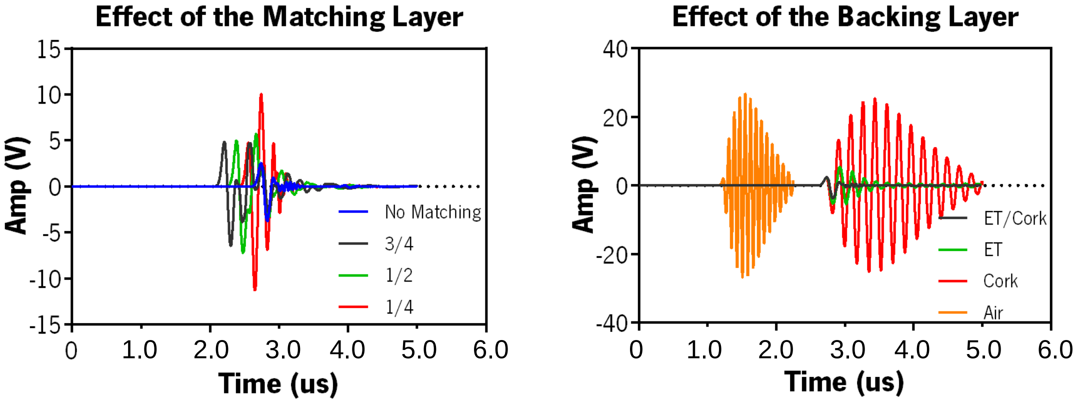

Figure 6.19. Simulation results to study the effect of the matching and backing layer materials. ET = complex epoxy/tungsten.

As illustrated, the backing layer material strongly influences how the pulse is reduced. With air-backed UT, most of the energy was transmitted into the water because the air has a negligible acoustic impedance when compared to water and piezo-ceramic impedance. This mismatch causes internal reflections, producing a long echo pulse and low axial resolution. This reflections were damped by applying a transducer backing layer.

The complex epoxy/tungsten (ET) show the high levels of damping, where the addition of cork particles improved this outcome. The cork backing layer or air backed UT by itself did not produce desirable attenuation outputs. Backing with higher impedance results in short echo pulses and better axial resolution. The main shortcoming of using a backing layer was the decrease of sensitivity due to the absorption of energy.

In terms of the matching layer, $\lambda/4$ layers of epoxy/tungsten (acoustic impedance of 4.5 MRayls) show optimal matching with high output sensitivity and low acoustic attenuation. $3\lambda/4$ and $\lambda/2$ show similar output voltages. No matching UT were the worst cases. Although the input signal excitation is the same, theoretical results show that different thicknesses influences the shape of the output signals.

The transducer front or back dictates UT operation as well its sensitivity. Similar results were obtained when using an acoustic lens. The thickness of lens together with the matching layer should have a thickness of $\alpha\lambda/4$, where $\alpha$ is an odd number.

Finally, the pulse duration was about 1 $\mu$s which corresponds spatial pulse length of 1.54 mm and axial resolution of 0.77 mm.

### 6.4.5 Transducer efficacy for PRA

The resulting $\lambda/4$ matching layer have a sound velocity of 2350 m/s and thickness of 0.63 mm for the UT1 and UT2 and 0.95 mm for the UT3. The UT2 lens have a lens curvature of 1.26 mm (Figure 6.5 and Figure 6.6).

Figure 6.20 show pulse-echo responses, of all transducers, recorded from the reflection of the quartz-plate at 70 mm distance.

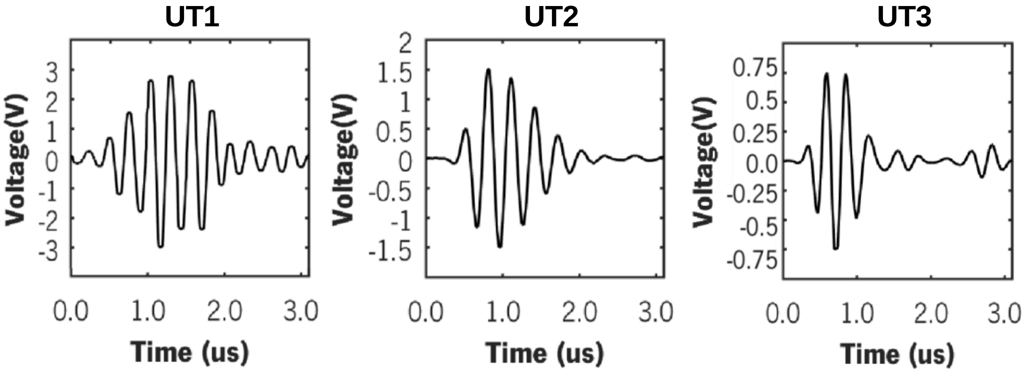

Figure 6.20. Single echo responses for the fabricated transducers.

The pulse duration for 20% of the amplitude peak was 1.33 us, 1.12 us and 0.85 us for UT1, UT2 and UT3, respectively. It is clearly seen, that UT1 is the transducer with more signal ripples in a single echo, low axial resolution and high output voltage. In contrast, each element of UT3 present the lowest amplitude voltage but highest axial resolution. The main reason for the output discrepancies between UT1 and UT2 is the acoustic lens, which slightly decreases the voltage output. The UT2 lens worked as an additional layer, improving the axial resolution due to a narrowed beam. The peak amplitude increased for $2.8 \pm 0.7$ dB, respectively, relative to the unmatched cases (values calculated at the center frequency).

With a sampling frequency of 80 MHz, $Pe_W$ = 106 points for UT1, $Pe_W$ = 90 points for UT1 and $Pe_W$ = 68 points for each element of UT3.

Regarding the depth of penetration, UT1 was able to detect interface variations up to 120 mm. UT2 and UT3 show lower sensitivity, detecting interfaces within distances less than 80 mm.

Figure 6.21 shows the performance coefficient for detecting echoes with different methodologies and parameter configurations. Figure 6.21-and Figure 6.21-b show performance coefficients when smoothing UT3 signals with the Savitzky-Golay and Gaussian filtering, respectively. Concerning Figure 6.21, Table 6.4 gives information about S0-S4 and G0-G4 configuration and Table 6.5 for w0-w4 configurations.

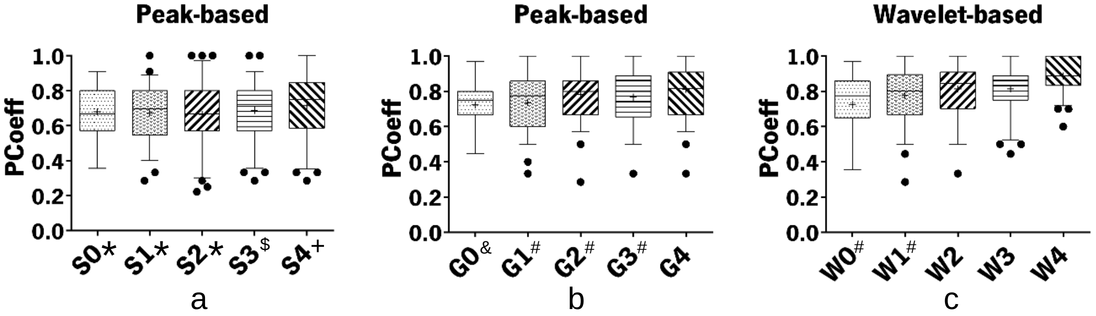

Figure 6.21. Performance coefficient for several algorithm parameter configurations: a) Savitzky-Golay smoothing; b) Gaussian smoothing; c) wavelet based detection. Two-way Anova: * statistical difference against G2 to G4 and W1 to W4; $ statistical difference against G2, G4 and W2 to W4; + statistical difference against G4 and W2 to W4; & statistical difference against W2 and W4; # statistical difference against W4.

The right parameters for smoothing were experimentally found. For both smoothing algorithms, best results were found when using a windows size of $1.5 \times Pe_W$ (Table 6.2). The polynomial order

Table 6.4. Peak-based method testing parameters.

| **Configurations (Figure 6.21)** | $min_{pD}$ | $p_P$ | $p_W$ |
|---|---|---|---|
| S0/G0 | $2 \cdot Pe_W$ | $3\% \cdot A_0$ | $4 \cdot Pe_W$ |
| S1/G1 | $2 \cdot Pe_W$ | $3\% \cdot A_0$ | $2 \cdot Pe_W$ |
| S2/G2 | $4 \cdot Pe_W$ | $2.5\% \cdot A_0$ | $2 \cdot Pe_W$ |
| S3/G3 | $2 \cdot Pe_W$ | $2.5\% \cdot A_0$ | $1.5 \cdot Pe_W$ |
| S4/G4 | $4 \cdot Pe_W$ | $2.5\% \cdot A_0$ | $1.5 \cdot Pe_W$ |

Table 6.5. Wavelet-based method testing parameters.

| **Configurations (Figure 6.21)** | $nScales$ | $G_T$ | $R_L$ | **Sliding window $W$** |
|---|---|---|---|---|
| W0 | 50 | 2 | $nScales/4$ | $6 \cdot Pe_W$ |
| W1 | 50 | 2 | $nScales/6$ | $4 \cdot Pe_W$ |
| W2 | 50 | 2 | $nScales/4$ | $2 \cdot Pe_W$ |
| W3 | 50 | 2 | $nScales/2$ | $4 \cdot Pe_W$ |
| W4 | 50 | 2 | $nScales/4$ | $4 \cdot Pe_W$ |

for Savitzky-Golay was $A_i$=5 and the Gaussian $\sigma$ was 2. After smoothing, Figure 6.21-a and Figure 6.21-b show the algorithm configuration to achieve the 5 highest $PCoeff$ (Table 6.4) (highest with the S4/G4 configuration).

Best peak-based methods configurations show average $PCoeff$ of 81%±15% (range from 33% to 100%) and 71%±18% (range from 28% to 100%), when applying the Savitzky-Golay and Gaussian filtering, respectively. Figure 6.21-c show the results for the wavelet-based detection. $PCoeff$ was higher with this second approach showing average values (W4, Figure 6.21-c) of 88%±8% (range from 59% to 100%).

Stronger peaks presents longer ridge lines. Adequately ridge lengths and the sliding windows size were the parameters that most influenced the $PCoeff$ outcome. High FDR were achieved when small ridge lines $R_L$ were used.

Results in Figure 6.21 indicate that the wavelet-based approach has much better performance (low FDRs) in detecting both strong and weak echoes.

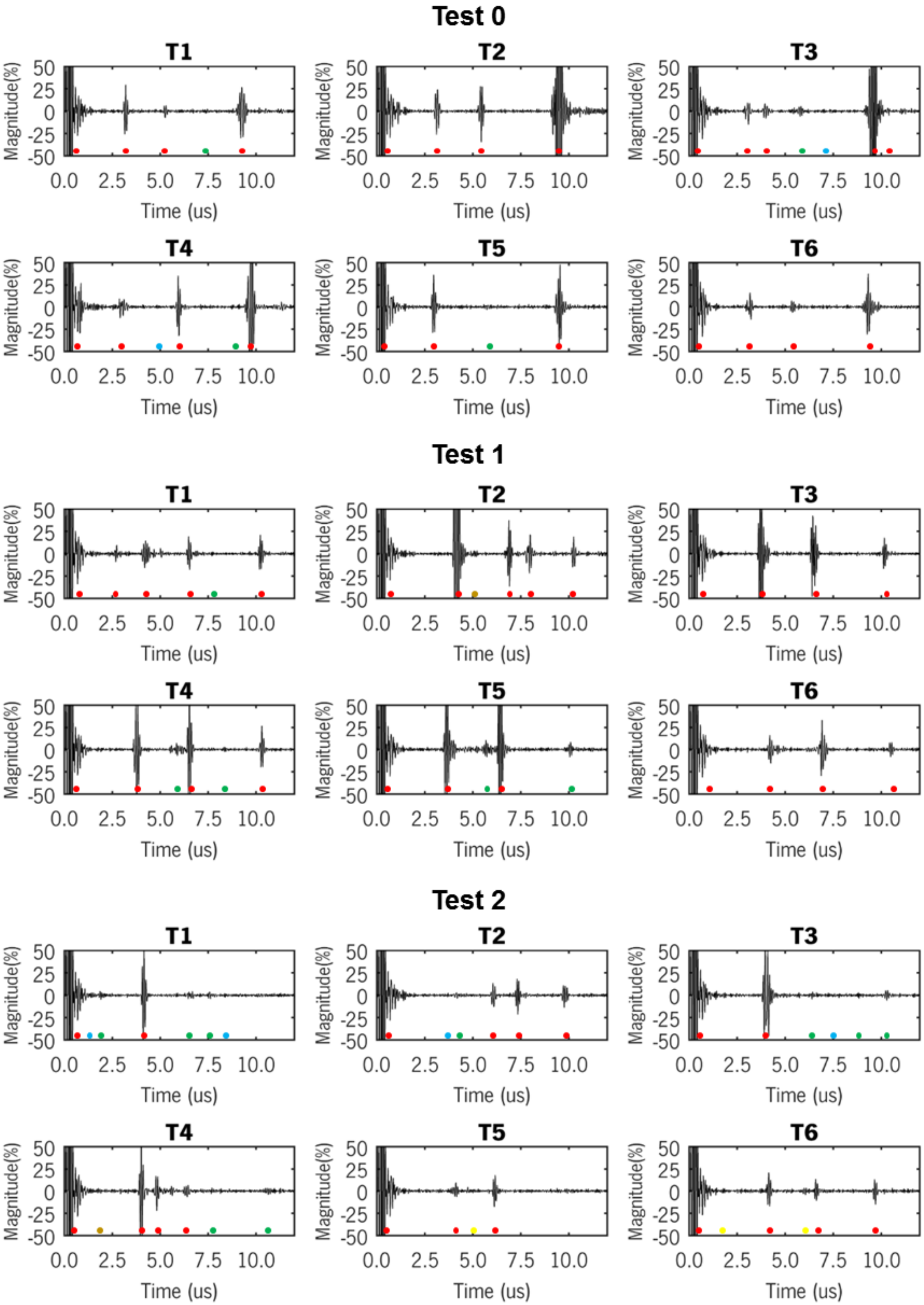

Figure 6.22. Signals generated by UT3 at different moments of time. Red circles represent peaks detected by the best configurations of the peak-based and wavelet-based methodologies. Blue circles represent echoes market in the ground truth but not detected by any algorithm. Yellow circles are the ones identified by the algorithm but not present at the ground truth.

Figure 6.22 shows examples of signals generated for each UT3 element (T1-T6) at different moments of times (Test 0, Test 1 and Test 2).

Different results were achieved when performing tests with different setups (Figure 6.13):

- Setup A: All transducers exhibited similar outputs without differences in the recorded echoes. UT3 present identical signals in all elements, increasing the output robustness and reliability due to the signal redundancy.
- Setup B and Setup C: UT1 and UT2 only produces one single signal, being not able to discriminate if the phantom properties are different around the working channel. In contrast, UT3 create six different signals, discriminating distinct situations. Figure 6.22-Test2 demonstrates a situation where element T1 and T3 have similar interfaces, but they are different from elements T4 and T6.
- Setup D: All transducers create output signals that varies according to dynamic variations. The presence of a new interface or absence of an old one, generates signals with different number and position of echoes. Differences between signals at different times were used to generate user alerts. A reduced number of false alerts were achieved when this time was at least 1 second.

When an alert is generated, the user should confirm that the experiment can continue, and the current signal is saved as the reference signal. In all tests, a safe and fast puncture was achieved when the echoes remained constant throughout the process.

## 6.5 Discussion

Inaccurate punctures can cause damage in kidneys and its surrounding tissues and organs [14, 42]. Imaging techniques have been mandatory for pre-operative planning and to guide the needle throughout PRA. US is a versatile technology, low-cost, radiation-free and allows real-time signals. Although some UT configurations and designs are well-known and commercially available, this work described UTs with a needle working channel. All developed UT guarantee that the US beam will be co-axially aligned during all the intervention, providing information about interface changes around the needle shaft.

Different tests were described and performed in order to verify the applicability of such strategy and to evaluate if the working channel does not influence the transducer operation.

The phantom study was an important step in the characterization of the UT performance, because UT often have high performance in water, but may present a low signal-to-noise ratio when used with attenuated tissues. The PVCP allowed the manufacture of stable phantoms with attenuation values close to human tissues. The main disadvantages were related to the formation of bubbles during the manufacturing process and the speed of propagation, which was approximately constant in all phantom blocks. Despite of the differences of the speed of propagation differences, it did not influence the testing results, since it mainly affects the position where the echo is represented (i.e. the echo can be represented sooner or later when compared to a real situation).

However the physical structure of the piezoelectric transducers is quite simple, due to the high number of possible combinations of layer materials and thicknesses, it is difficult to experimentally analyze whether the transducer low sensitivity is due to the manufacture process or is actually the result of the selected layers combination [216]. Therefore, physical UT were manufactured according to the simulation experiments. These were crucial to theoretically confirm that the UT is only dependent upon the backing and matching layers, regardless the diameter of the working channel.

Since matching and backing layers have been shown to affect the performance and efficiency of piezoelectric critically, many constraints were carefully considered during any manufacturer stage. By optimizing layers thicknesses, it was possible to improve the transducer sensitivity response under the compromise of bandwidth and levels of ripples [259].

Since the transmission from the transducer through the matching layers is a function of their thickness, a $\lambda/4$ layer thickness was essential to not degrade the UT performance and to match the probe to the test object. Although the mold was manufactured for $\lambda/4$ thickness, some possible error may still exist due to the small dimensions. To reach an ideal mode of operation, it was necessary to correct this differences using impedance matching circuits. By improving the power transference, it was possible to detect echoes over a greater depth of penetration.

To reduce ripples oscillations and long pulses, acoustic backing material composed by a mixture of epoxy, tungsten and cork particles were essential to absorb acoustic energy while maintaining high transducer sensitivity.

Practical echoes were wider than theoretical ones, because the possibilities of selecting materials with required acoustic impedance are limited. However, UT1, UT2 and UT3 pulses, of about 1 us, are comparable with works described in literature [210, 211, 221-223, 232, 233, 235, 259, 260].

UT3 presented two main advantages over single UT. First, the occurrence or absence of an interface normally occurs in more than one single element. Whereby, UT3 is more robust to the appearance of echoes caused by noise. Second, each echo is treated independently, being possible to evaluate and identify the orientation of such echo related to the needle shaft. Despite of all shortcomings, single transducers are easy to manufacturer and presented higher sensitivity as well as greater depth penetration. Although UT3 presents low depth of penetration, it remains the preferred device due to its advantages and since most of the puncture distance are below 90 mm. Any crosstalk was found between UT3 elements, but additional tests can also be performed at other driven high-voltages.

When comparing to needle guides apparatus, the developed UT do not require specialized equipment or complicated logistics. Although needle guides provides assistance in keeping the needle tip in the image, some disadvantages may arise since they are cumbersome to use, can lead to significant limitations when adjusting the needle, limits the US image and the anatomical overview to the current US image [155, 261].

The proposed alert system is very dependent on the performance of the echo detection algorithm, because it is created each time a true or false echo is detected. According to the achieved results, the height of the produced echoes can vary significantly in the same spectrum. Moreover, isolated echoes present similar widths, which can be altered due to the overlap of multiple echoes and background noise. As stated by Gras et al. [262], true echoes have characteristic shapes which can be described by a shape-matching function during the peak identification to create a good fit for identification methods.

The peak-based method found echoes by searching local maxima over a given peak intensity, width and prominence. This estimation was highly dependent on the peak amplitude relative to the surrounding noise level. Although these constraints decreases the FDRs of the echo detection, these algorithms were not capable of identifying both strong and weak echoes. Moreover, by smoothing the signal, real echoes may be eliminated, and can never be recovered in the subsequent analysis.

The second approach, based in CWT, makes use of additional information presented in the echoes shape, with potential to robustly detect echoes across CWT scales and with varying intensities in a single spectrum [245, 250]. It was possible to detect strong and weak echoes, keeping low FDRs and high sensitivity (higher values of $PCoeff$). In addition, the method was applied directly on the raw data, avoiding the echoes removal by a pre-processing smooth. This strategy was proven to be less vulnerable to noise, more robust and easier to use and automate.

One possible limitation using this strategy is that some echoes may result from artifacts as well known in US imaging systems, such as shadowing.

Given the achieved results, it is expected that these UT devices, when combined with the KidneyNav framework, could be capable of estimating the distance from the needle tip to a detected echo. Thus, it will be possible to generate various alerts with high, medium or low priority which are dependent on the current distance (1 cm, 3 cm and 5 cm, respectively). Such distance values can be easily changed according to the needs of the doctor and the procedure. Since the needle can still be inserted and guided according to the EMT sensors, now with these UT devices, the surgeon will be notified when the initial conditions change as result of tissue and organs movements. Thus, it has the potential to reduce the need of image acquisition or interpreting during PRA.

# 7

# Conclusions and future work

This chapter gives the final remarks and future developments for the proposed navigation system for PRA planning and guidance. It also shows different research path that may improve and complement the developed work.

**Contents**

## 7.1 Conclusion

PRA plays a key role in very common minimal invasive kidney interventions, e.g. percutaneous nephrolithotomy, kidney radiofrequency ablation, kidney biopsies, renal mass diagnosis, antegrade pyelography and pressure/perfusion studies. Therefore, the number of PRA procedures is steadily increasing, despite the fact that the number of trained urologists mastering this technique has not kept up with this growth factor.

Inaccurate and multiple needle punctures often cause complications, such as injuries in the kidney or contiguous organs, and eventually prejudice the overall surgical success and patient outcome. This thesis present a multidisciplinary framework which is able of helping and guiding the surgeon during PRA planning and puncturing. It may leverage better and easier PRA during PCNL.

KidneyNav was initially developed allowing a fast multi-organ segmentation (Chapter 3) highlighting the kidney and surrounding structures. The strategy was based on clustering several primitive volumes until a suitable number of volumes were achieved in the output image. A volume rendering technique, which implements multiple transfer functions, was used to enhance anatomical structures with similar intensity in the output volume. DSC scores showed that the method was able to detect the presence and distribution of anatomical structures inside the rib cage. Time-consumption for rendering anatomical structures of interest, user dependence and subjectivity were reduced.

Although this segmentation framework was not directly used for PRA guidance (only planning), results proved to be adequate to correctly estimate the kidney target position, to decide the calyceal fornix to be punctured, to calculate virtual trajectories for percutaneous puncture evaluating safety paths without the presence of vital structures.

Then, the KidneyNav was further modified and able to work together with an OMT system. Several experiments were used to test and validate its usability for PRA. An *in vivo* clinical trial, performed at Braga Hospital, assessed the overall KidneyNav performance in a real situation. The surgeon used an OMT system to track the needle tip inside the body and to overlap and register it with pre-operatively segmented data. Although the OMT could track the instrument without wires and mechanical parts, it required a line of view to the instruments that limited its usability needle tip tracking inside the human body. Moreover the rigid assumption to align the patient with the KidneyNav framework can also add additional limitations. Results show that the organ and needle motion and deformation were the biggest challenges to achieve robust navigation.

These results prompt us to replace the OMT solution for an EMT one. Different *in vitro* and animal experiments were performed to evaluate the efficiency of such approach. The surgeon performed the percutaneous puncture through a virtual trajectory calculated and displayed in a 3D software. This software worked as a control station by gathering and processing, in real-time, information from different equipment needed for the procedure: video from an uretero-reno-fiberscope and orientation and position of the needle and catheter tips. With a median renal and ureteral puncture times of 19 and 51 seconds respectively (range 14 to 45 and 45 to 67). Such results represent a puncture time improvements between 75% and 85% when comparing to state of the art methods.

However, one found some difficulties during the tests. The 3D interpretation of the screen during PRA guidance was a challenging task for some users. Consequently, new feedback interfaces were developed, namely 3D sound and vibrotactile feedback. Besides to the information received through our sight, these new ways of feedback were developed to provide additional information about the needle orientation. These new ways of feedback aimed to complement the surgeon interaction with the needle, allowing the anticipation of any needle correction even without looking to a monitor. It was also verified, that by using these kind of feedback, the surgeon tends to follow a virtual puncture trajectory with a reduced amount of deviations from the ideal trajectory.

Results revealed that the EMT together with these innovative ways of feedback are a promising and helpful strategy for this type of surgery. Using this system, neither Xray nor preoperative imaging is needed. Moreover, it was not influenced by physician skill or expertise and it proved to be highly accurate, simple and quick. One believes that this method has the potential to become the new PCNL puncture standard since it eliminates radiation, may broad the use of PCNL for surgeons who are less familiar with minimally invasive surgery and decreases operative cost and time.

Although *in vivo* tests showed that the proposed solution is highly accurate, radiation-free, simple and fast, due to its imageless characteristics, it is still unable to guarantee the safeness of the PRA path in terms of organs perforation, thus impeding its broader use in clinical routine practice. Therefore, one developed and tested three different transducers with a needle working channel. All transducers guarantee that the US beam will be co-axially aligned with the needle shaft giving detectable echoes in different US phantom interfaces. Such echoes were automatically detected with peak-based or CWT method alerting the user when some change occurs in between the percutaneous puncture path as a result of tissue and organs movements or deformations. The synergy of US with the EMT modality may allow guidance through the optimal path towards the precise calculus location, increasing surgeon’s confidence and reduce possible complications such as organ perforation.

Finally, due to the high number of patients suffering from kidney diseases and the predictable growth of PRA practice encouraged by the achieved results, it is expected that all this system hardware or software modules will result in an attractive commercial product. It should be emphasized that, the developed methodologies may be easily adapted to similar procedures (insertion of a catheter to reach an anatomical target followed by a needle puncture step), particularly gastrostomy, endoscopic pyelolithotomy, the treatment of upper urinary tract, urothelial tumors and caliceal diverticuli, endoscopic resection and diagnostic indications (e.g. antegrade pyelography and pressure/perfusion studies).

## 7.2 Future Work

This thesis demonstrated that it is feasible and highly accurate to guide PRA with EMT technologies, without the need of imaging modalities. In spite of the promising results, some research paths for the improvement of the developed framework may be investigated.

### 7.2.1 PRA Planning

In what concerns to PRA planning, the imaging framework, discussed in Chapter 3, may be improved and optimized, so that the kidney structure can be more accurately visualized [111-113, 119, 263]. Since PRA success is directly linked to the physician’s ability to precisely visualize and reach the anatomical target, by showing the kidney calyx and lumen with more rendering details, the surgeon will be able to evaluate the best kidney entry point. On the other hand, giving the nature of image-guided interventions, tissues/organs movements are often present. Therefore, the proposed imaging framework may also be modified in order to update, in real-time, organs displacements according to the information retrieved by the EMT sensor located at the catheter tip.

### 7.2.2 EMT for PRA access

Even though the EMT developed methodology (Chapter 4) was proven suitable, and achieved a very positive performance *in vivo*, the presented technique certainly demands further evaluation regarding its human applicability, such as presence of renal stone, patient position.

This study did not consider kidneys with renal stones, which prevents us from providing solutions to specific situations with a fair degree of certainty, such as staghorn calculi or obstructive uropathy, where a physical obstruction may hinder the positioning of the ureteral sensor inside the desired calyx. Nevertheless, this is a very relevant aspect which the authors are aware of and intend to develop further research to study ways of overcoming such situations.

Moreover, we are already carrying out the first human studies to compare the traditional PCNL procedure with the developed one, in terms of costs, security, system efficacy and practicality.

### 7.2.3 Multi-sensorial interface

Despite of PRA, the developed multi-sensorial interface (Chapter 5) can be a valuable framework for other surgical procedures, improving surgical outcomes speed of execution and quality of care. It clearly may benefit both surgeon and patient.

The guidance through audio or vibration feedback result in an increased sense of immersive environment, opening new insights for PRA or other navigated interventions. For example, when some anatomical structure moves towards the percutaneous path, the resulting action may be an alert sound clip or vibration pattern. Moreover, it can be helpful to protect risk zones, such large vessels or nerves. In this cases, the audio signal must be complemented with pre- or intra-operative image automatic analysis [200].

Other research paths may include the development of new sounds or vibration patterns aiding to understand the environment that the needle is puncturing. Such environment information can be input from imaging system or force sensors.

The vibration intensity may be synonymous of the reaction forces, guiding surgeons for better precise cutting and puncture (e.g. by rotating the needle decreases the insertion forces and needle deflections).

Finally audio effects can be also explored as a possible way to improve front-back resolution and to generate warning alerts.

### 7.2.4 US Probe with a Needle Working Channel

Although this thesis explores single matching layers to construct US probes with a needle working channel, more layers can be used with various combinations of acoustic impedances and thicknesses. These configurations have already been explored by some authors, reporting high sensitivity over a broader band of frequencies and shorter pulses. Wide frequency bandwidth may be beneficial in situations where the distance between the skin and kidney is reduced. Here, shorter pulses can be used to improve the axial resolution. However, the fabrication process is more complex, can create internal reflection and the sensitivity may be reduced since an additional absorption exists in the matching layer [220, 223, 229].

In spite of the promising results, other research paths for the improvement of the developed process should be investigated. In particular, one should explore other UT vibration sources (e.g. other piezo-ceramics, polymers and crystals [264, 265]) and multilayer matching [266, 267], in order to study their influence in the UT sensitivity. Another possible research path will be to different UT designs keeping the needle working channel. One possible way will be by using annular arrays, where the working needle channel will be centered by multiple piezo-ceramic rings with increased radius [268].

*In vivo* testing is also necessary to evaluate the overall performance, when considering real dynamic characteristics (respiratory motions, tissue and organs deformations, blood motions).

Finally, one may also developed a probe with much more elements in order to generate images around the needle shaft. In this case, the crosstalk between elements will be higher due to lack of isolation and continuous acoustic paths between piezo-ceramic elements [269].

### 7.2.5 Robotic Assisted Kidney Puncture

Finally, ongoing research focus on the programming of a robotic arm capable of supporting and drive the surgical needle, when combined with the KidneyNav framework. To this extent, the Kuka LBR iiwa has been tested to receive and updated in real time its position with respect to the EMT sensors. In this case, the surgeon will act only as a supervisor, following the whole automatic procedure through a graphical and control interface. It is expected that the development of this autonomous system will broad the use of PNL to surgeons less familiarized with minimally invasive techniques by decreasing the surgeon dependence and provide precise and stable movements, increasing the surgical performance. On the other hand, it also raises challenging robustness and safety issues that have to be tackled in future work.

# 1

# Attachment

All statistical analysis was performed under GraphPad Prism 6 software.

The Mann-Whitney test was used to compare the distributions of ranks between two groups. It assumes that both populations have distributions with the same shape but they are not normally. Since it can be viewed as a comparison of two medians, in these cases data is presented by median and range [128].

When the data follows a Gaussian distribution, the t-test Welch was used to compare the means of two matched groups. It does not assume that those distributions have the same standard deviation. The prime goal of the t-test Welch is to quantify how far apart the two means are [244].

Since t-test Welch and Mann-Whitney tests are used for normality or non-normality distributions, respectively, the D'Agostino & Pearson omnibus normality test was performed before each test to choose the correct statistical analysis [270]. Briefly it quantifies how far a distribution is from Gaussian in terms of shape and asymmetry. A single $p$ value is computed from the sum of these discrepancies, and when $p > 0.05$ the data is normal.

Finally, two-way ANOVA was used to determine whether there are any significant differences between the means of three or more unmatched groups, assuming that there are no significant outliers, exist homogeneity of variances and are approximately normally distributed [209].

For the Mann-Whitney test, t-test Welch and two-way ANOVA a $p$ value higher than 0.05 ($p > 0.05$) was used to indicate a statistically not significant difference. In contrast $p < 0.05$ is significant ($0.01 < p < 0.05$); $p < 0.01$ is very significant ($0.001 < p < 0.01$); $p < 0.001$ is extremely significant.

# 2

# Attachment

# Validation of percutaneous puncture trajectory during renal access using 4D ultrasound reconstruction

Pedro L. Rodrigues*[a,b,c], Nuno F. Rodrigues[b,c], Jaime C. Fonseca[b], João L. Vilaça[a,c]
[a]ICVS/3B's - PT Government Associate Laboratory, Braga/Guimarães, Portugal;
[b]Algoritmi Center, School of Engineering, University of Minho, Guimarães, Portugal;
[c]DIGARC – Polytechnic Institute of Cávado and Ave, Barcelos, Portugal

## ABSTRACT

Background: An accurate percutaneous puncture is essential for disintegration and removal of renal stones. Although this procedure has proven to be safe, some organs surrounding the renal target might be accidentally perforated. This work describes a new intraoperative framework where tracked surgical tools are superimposed within 4D ultrasound imaging for security assessment of the percutaneous puncture trajectory (PPT).

Methods: A PPT is first generated from the skin puncture site towards an anatomical target, using the information retrieved by electromagnetic motion tracking sensors coupled to surgical tools. Then, 2D ultrasound images acquired with a tracked probe are used to reconstruct a 4D ultrasound around the PPT under GPU processing. Volume hole-filling was performed in different processing time intervals by a tri-linear interpolation method. At spaced time intervals, the volume of the anatomical structures was segmented to ascertain if any vital structure is in between PPT and might compromise the surgical success. To enhance the volume visualization of the reconstructed structures, different render transfer functions were used.

Results: Real-time US volume reconstruction and rendering with more than 25 frames/s was only possible when rendering only three orthogonal slice views. When using the whole reconstructed volume one achieved 8-15 frames/s. 3 frames/s were reached when one introduce the segmentation and detection if some structure intersected the PPT.

Conclusions: The proposed framework creates a virtual and intuitive platform that can be used to identify and validate a PPT to safely and accurately perform the puncture in percutaneous nephrolithotomy.

**Keywords:** guided surgery, percutaneous puncture, minimal invasive surgery, electromagnetic tracking sensors, ultrasound reconstruction

## 1. INTRODUCTION

The prevalence of kidney stones has risen over the past 30 years [1-3]. Nowadays, percutaneous nephrolithotomy (PCNL) is golden standard for treating upper urinary tract stones. The stone clearance rate and treatment outcome is highly dependent on the accuracy of needle puncture in the desired calix [4, 5].

Multiple paths and technological advances have been proposed in the field of urology and minimal invasive surgery to improve this procedure. In what concerns PCNL puncture in particular, the most relevant contributions have been provided by the application of medical imaging techniques, as well as the fusion of multiple imaging procedures [6-9]. Aside from medical imaging, robotic systems [9-11], navigation systems [12-14], finite element models [15, 16] and recent developments in computer graphics and image processing [9], have been proposed in recent years to improve percutaneous puncture.

Despite all the different technological improvements, PCNL puncture step still remains the most challenging task, promoting anatomical targeting errors and damage of vital structures. Although this procedure has proven to be safe, some organs surrounding the renal target might be accidentally perforated. Injuries to the lung, liver, spleen, biliary system, colon, or small bowel have been reported [17, 18].

To this extent, in clinical routine, the PCNL needle puncture is often performed under image guidance [19]. Although medical imaging can provide further information for diagnostic and per-operative planning, it presents some drawbacks. Real-time images from computed tomography (CT) and fluoroscopy C-arm lead to a significant increase in radiation exposure both to patient and surgeon. On its turn, ultrasounds (US) and magnetic resonance (MR) have proven to be an advantageous imaging option by providing radiation-free real-time imaging. However, their targeting ability for small calculi is limited [7, 20].

In order to reduce imaging dependences, the authors have already tested and evaluated, in animal model, a new real-time electromagnetic tracking (EMT) navigation system for in vivo kidney puncture. Within this previous work, the surgeon performed the percutaneous puncture through a virtual trajectory calculated and displayed in a 3D software [14].

Although capable of directing, correctly and accurately, the puncture path, the previously developed system is unable to guarantee the safeness along the PTT in terms of organs perforation. In order to overcome this drawback, one now presents an evolution of the previous system, resorting to pre-operative US imaging to detect organs in between the PPT and alert for its presence. This system allows the surgeon to: 1) visualize a PPT between the skin puncture site and an anatomical target using an intuitive visual interface; 2) 4D ultrasound imaging around a volume of interest centered in the PPT; and 3) access the security of the PPT.

## 2. METHODS

### a. Framework

A Qt/C++ based framework – Renal Puncture (Figure 2) - was developed specially for this work. ITK (Segmentation & Registration Toolkit) libraries were used to aid 4D volume reconstruction and image segmentation. VTK (The Visualization Toolkit) libraries were used only for 3D rendering.

The volume was reconstructed using B-mode ultrasound images acquired using a 3.3 MHz convex probe from Vivid 3 Ultrasound System (GE, Medical Systems). All processing was performed using an Intel Core i7-3770K @ 3.50GHz, NVIDIA GeForce GTX 670 and 16 GB Ram.

The commercially available Aurora electromagnetic tracking system (Northern Digital Inc., Waterloo, Canada) was used to track the catheter tip, needle tip and ultrasound probe during in vitro experiments. The navigation system was composed by (1) one planar low-intensity and varying electromagnetic field generator that establishes a tracking volume; (2) three Aurora sensor interfaces that decrease the possibility of electromagnetic interferences in the testing room; and (3) one 18G/180 mm Chiba needle with 5 degrees of freedom and two ureteral catheter with 1.1 mm diameter and 2 m length with 6 degrees of freedom.

An abdominal ultrasound phantom was used to test this new methodology. It includes all abdominal organs (spleen, liver, colon and the urinary collecting system) that might be injured during renal access.

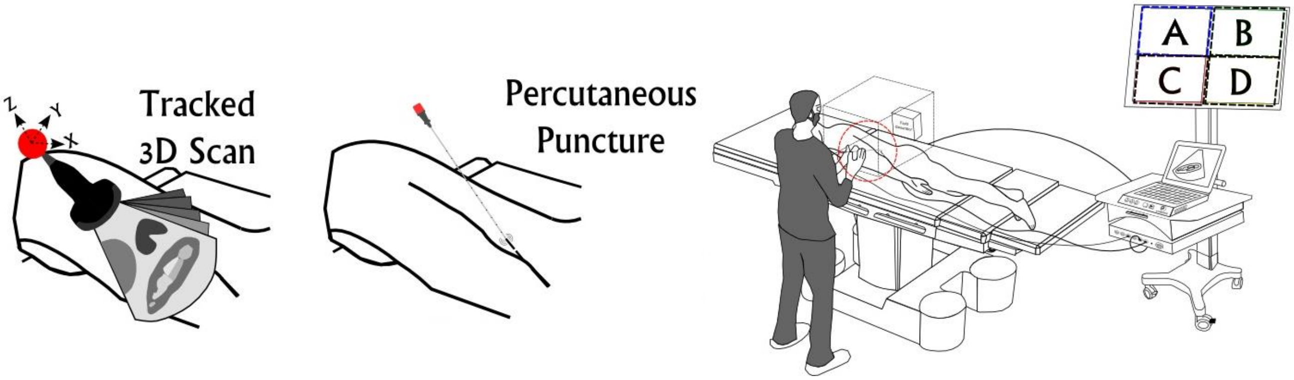

Figure 1. Overview of the 4D freehand ultrasound for PPT security validation: (left) ultrasound scan along the PPT using a tracked probe; (center) percutaneous puncture using a catheter and needle that integrate electromagnetic sensors; (right) possible surgical setup comprising the Aurora field generator, tracking volume around the patient abdominal area, ultrasound machine and interface monitor for percutaneous guidance.

### b. System overview

A system overview is shown in Figure 1.

At the first surgical step, a catheter will be inserted and guided, through an ureterorenoscope with a camera and guided tip, trans-urethrally towards the renal calix. This catheter will have a position and orientation electromagnetic sensor on its tip that will function as a real-time anatomic target locator. At the next step, the puncture one, it will be used a needle that also integrates a similar sensor. From the data provided by both sensors, it will be possible to define the PPT from where the needle will be inserted [14, 21].

This PPT will be presented to the surgeon using a graphical user interface. Here, the surgeon will be guided in order to create an ultrasound reconstructed volume using a tracked probe in order to evaluate the risk of possible perforation of vital anatomic structures. When, the PPT is checked and approved by the surgeon, the puncture procedure will be conducted without further imaging modalities. The puncture success is assured using the ureterorenoscope video camera.

### c. 4D ultrasound reconstruction

To provide PPT intraoperative imaging during percutaneous nephrolithotomy, the presented framework can reconstruct 3D and 4D ultrasound by freehand scanning using a tracked convex ultrasound probe.

2D US images, acquired with a tracked probe, were used to reconstruct a 4D ultrasound around the PPT. This volume was used to ascertain that any vital structure is in between both sensors and might compromise the surgical success.

Before testing, an Aurora catheter sensor was mounted on the ultrasound probe and calibrated using Strdx software [22]. It integrates automatic spatial and temporal calibration systems for 3D ultrasound. Firstly, a fabricated non-ferromagnetic mold rigidly attaches the sensor on the body of the ultrasound probe. Then, a 30x30x15 cm box filled with distilled water at room temperature and a flat and roughen bottom (made of cork), was used to improve the reflection of ultrasound at oblique angles. The calibration process was performed by moving the probe while imaging the bottom of the water bath by: (1) moving the probe vertically up and down without changing its orientation; (2) rotating the probe in each 3D coordinate axis (each axis individually and then all together) while keeping the scan plane and the phantom plane perpendicular; (3) translate the probe while performing motions (1) and (2). Simultaneously, Stradx track the bottom of the water bath in the image with a line detector algorithm [22]. By matching the image motion and the Aurora tracking readings, it was possible to estimate a temporal calibration the position and image streams.

After de calibration, real-time ultrasound reconstruction was achieved using different synchronized and parallel threads:

(1) Thread one buffers and receives ultrasound frames: each video frame was resampled by a factor of 2 and allocated onto an image stack along with a timestamp tv that describes when the video was acquired. The video was captured at full rate of 30 frames/s;

(2) Thread two receives and processes tracking data: the Aurora tracking information, received via serial port, was converted to a 4 by 4 matrix and pre-allocated along with a timestamp tA that describes when the tracking data was acquired;

(3) Thread three triggers a signal that specifies the starting of a new cardiac cycle for reconstruction gating. Since kidney and surround tissues may move during the reconstruction process, they must be inserted into the partially 3D volume at similar points of the cardiac cycle. To this extent, the user must specified an expected heart rate for the reconstruction procedure by averaging the heart rates recorded over a user-specified time period;

(4) Thread four updates the partially reconstructed volume, under GPU processing, by inserting the most recent US frame. Every time that Thread three triggers a signal, the period of the previous cycle is used to predict the timestamps for the upcoming cycle. The ultrasound frames and tracking matrices, with timestamps tv and tA, that are closest to these predicted values are inserted into the correct output volume using the associated tracking transforms;

(5) Thread five processes volume rendering of the output volume using color and opacity transfer functions (Figure 1-C);

(6) Thread six displays the partially reconstructed 3D ultrasound volume into the main application;

(7) Thread seven assures that there are no gaps in the reconstructed volume by triggering a function every 200 ms that searches all empty voxels and modifies its voxel intensity using a tri-linear interpolation method of the closest non-empty voxels.

### d. PPT security assessment

Thread eight assured multi-organ segmentation of volume structures and its intersection with the PPT. For segmentation, the image histogram was smoothed by solving a non-linear diffusion equation [23]. The Tukey's biweight as edge-stopping diffusivity function (1):

$$g(x,\sigma)=\begin{cases}1/2\left[1-(x/\sigma)^2\right]^2, |x|\leq\sigma \\ 0, |x|\leq\sigma\end{cases}$$

(1)

was used to create a more accurate histogram underlying different groups of objects. By estimating the histogram local maximums (specified histogram region that is concave down) it was possible to define multi-threshold levels that create 8-connected labels of different structures.

The kidney label was automatically identified by choosing the most cylindrical and largest structure in a 5 cm radius (approximately the kidney size) around the Aurora catheter sensor (real-time anatomic target locator). Then, the points along the PPT were intersected with image labelled regions. When the user starts the puncture procedure, the framework will assume that all structures that intersects the PPT are not vital and can be perforated. From there, if any anatomical structure changes along the PPT, the framework will advise the user by rendering a text and sound alert. Here, the surgeon must accept or reject this new structure as a possible vital structure and continues the puncture procedure.

## 3. RESULTS

The calibration process was performed only one time before US reconstruction and took about 6 minutes. Any further calibration was not necessary as long as the Aurora sensor does not change its position relative to ultrasound probe body. A slight latency of around 16 ms between the tracking system and ultrasound video was accurately measured with Stradx software [24] and accurately compensated during reconstruction.

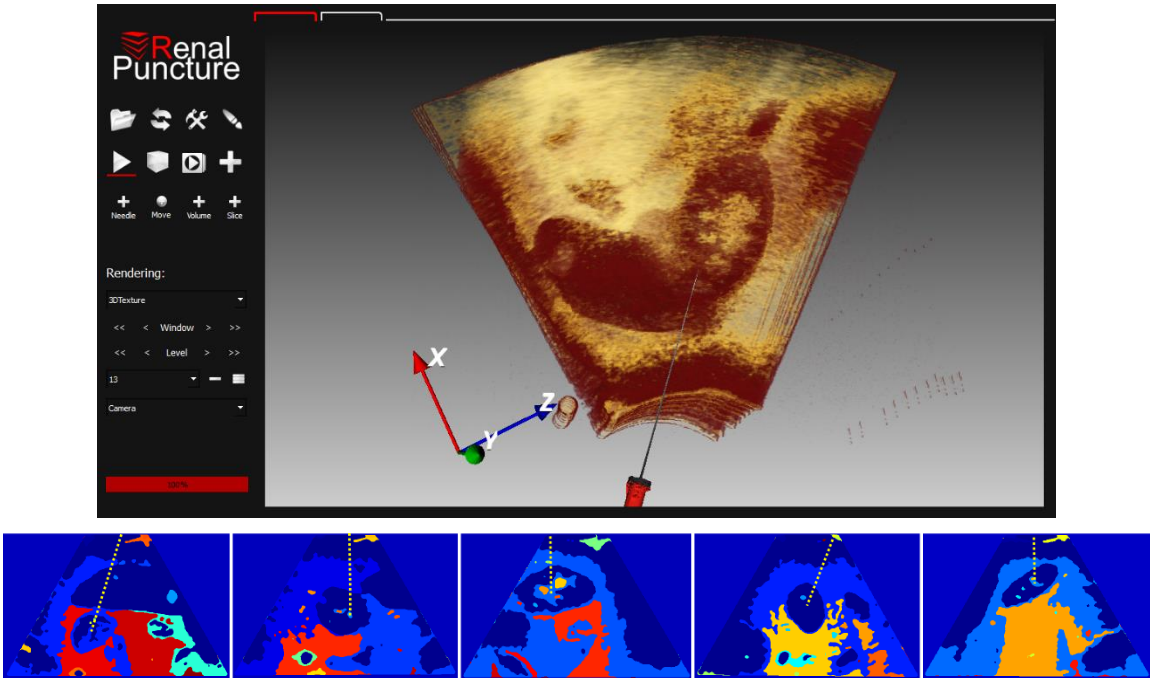

Figure 2. (up) Overview of the Renal puncture Framework; (down) Segmentation results with random PPT (yellow).

Thirty-seven US phantom volumes were reconstructed with different probe orientations. Real-time US volume reconstruction and rendering with more than 25 frames/s was only possible when only three orthogonal slice views where rendered to the user. When using the whole reconstructed volume, one achieved 15 frames/s for volume with size 7x7x15 cm3 and 8 frames/s for 10x10x15 cm3. When labelling the different image structures we obtained 3 frames/s.

The segmentation process were able to identify if any anatomical structure was in between the PPT with an efficiency of 98.89±4.28% along the PPT. The median time for ultrasound checking was 3.5 min (range 2-6 min) while the puncture step was performed in 25 seconds (range 15-54s) for doctors.

## 4. DISCUSSION

Although 4D ultrasound visualization has been integrated into commercial ultrasound systems [25], the inaccessibility of raw image data makes these system unsuitable for personalized guided surgery, advanced visualization and virtual navigation. A significant advantage of the Renal Puncture framework over literature is that both 3D and 4D ultrasound can be generated in real-time and, at the same time, different volume structures are segmented and evaluated if they intersect the PPT. The proposed framework creates a virtual and intuitive platform that can be used to identify and validate a PPT to safely and accurately perform the puncture during percutaneous nephrolithotomy.

Comparing to state of the art results, the need for image registration with pre-operative imaging was eliminated by using ultrasound checking and a miniaturized sensor that can be inserted near the anatomical target [13]. The uncertainty of possible anatomical structures in between puncture path [14, 21] was reduced by performing a 4D ultrasound before the puncture step around the puncture site. Although, compared with the work described by the authors in [14], the time for puncture planning increases with a median of 3.5 minutes, the uncertainty of some anatomical structure in between the PPT is eliminated.

Since medical imaging assistance to puncture commonly requires approximately 10 min [26-29], the puncture step itself remains faster than any literature approach, without any radiation exposure.

Although some motion artifacts where presented in the 4D ultrasound reconstruction, they did not interfere with the puncture path security assessment. Further wok needs to be conducted in particular considering in vivo testing. On the other hand, since minimally invasive surgical procedures comprising percutaneous puncture of the kidney are highly dependent on the accuracy that the needle reaches the desired target, further work may also include an automatic and real time kidney segmentation.

## 5. CONCLUSION

This paper describes a new intuitive framework for security assessment of PPT for renal access guided using EMT sensors. This new approach can guarantee the safeness of the percutaneous puncture trajectory in terms of organs perforation for the system already proposed by the authors [14].

The synergy of ultrasound checking and tracking modalities will allow puncture guidance through the optimal path towards the precise calculus location. This framework may increase surgeon’s confidence and reduce possible complications such as organ perforation. In addition, it has the potential to make percutaneous renal access free of ionizing radiation for both patient and surgeon.

## ACKNOWLEDGEMENT

The authors acknowledge to Foundation for Science and Technology (FCT) - Portugal for the fellowships with references: SFRH/BD/74276/2010. The present submission corresponds to original research work of the authors and has never been submitted elsewhere for publication.

## REFERENCES

[1] C. M. Cracco, C. M. Scoffone, and R. M. Scarpa, “New developments in percutaneous techniques for simple and complex branched renal stones,” Curr Opin Urol, (2011).

[2] A. Skolarikos, G. Alivizatos, and J. J. M. C. H. de la Rosette, “Percutaneous nephrolithotomy and its legacy,” European Urology, 47(1), 22-28 (2005).

[3] E. M. Worcester, and F. L. Coe, “Calcium Kidney Stones,” New England Journal of Medicine, 363(10), 954-963 (2010).

[4] J. W. Pugh, and B. K. Canales, “New instrumentation in percutaneous nephrolithotomy,” Indian J Urol, 26(3), 389-94 (2010).

[5] R. Viard, N. Betrouni, J. Rousseau et al., “Needle positioning in interventional MRI procedure: real time optical localisation and accordance with the roadmap,” Conf Proc IEEE Eng Med Biol Soc, 2007, 2748-51 (2007).

[6] Z. C. Li, K. Li, H. L. Zhan et al., “Augmenting intraoperative ultrasound with preoperative magnetic resonance planning models for percutaneous renal access,” Biomed Eng Online, 11, 60 (2012).

[7] C. Kalogeropoulou, P. Kallidonis, and E. N. Liatsikos, “Imaging in Percutaneous Nephrolithotomy,” Journal of Endourology, 23(10), 1571-1577 (2009).

[8] M. J. Bader, C. Gratzke, M. Seitz et al., “The "All-Seeing Needle": Initial Results of an Optical Puncture System Confirming Access in Percutaneous Nephrolithotomy,” European Urology, 59(6), 1054-1059 (2011).

[9] O. Ukimura, “Image-guided surgery in minimally invasive urology,” Current Opinion in Urology, 20(2), 136-140 10.1097/MOU.0b013e3283362610 (2010).

[10] M. M. Desai, R. Grover, M. Aron et al., “Robotic Flexible Ureteroscopy for Renal Calculi: Initial Clinical Experience,” Journal of Urology, 186(2), 563-568 (2011).

[11] P. Mozer, J. Troccaz, and D. Stoianovici, “Urologic robots and future directions,” Current Opinion in Urology, 19(1), 114-119 (2009).

[12] Z. Yaniv, E. Wilson, D. Lindisch et al., “Electromagnetic tracking in the clinical environment,” Medical Physics, 36(3), 876-892 (2009).

[13] P. L. Rodrigues, A. H. J. Moreira, N. F. Rodrigues et al., "Preliminary clinical trial in percutaneous nephrolithotomy using a real-time navigation system for percutaneous kidney access." 9036, 903606-903606-7.

[14] P. L. Rodrigues, J. L. Vilaça, C. Oliveira et al., “Collecting system percutaneous access using real-time tracking sensors: First pig model in vivo experience,” The Journal of urology, 190(5), 1932-1937 (2013).

[15] J. T. Hing, A. D. Brooks, and J. P. Desai, “A biplanar fluoroscopic approach for the measurement, modeling, and simulation of needle and soft-tissue interaction,” Medical Image Analysis, 11(1), 62-78 (2007).

[16] D. J. van Gerwen, J. Dankelman, and J. J. van den Dobbelsteen, “Needle-tissue interaction forces - A survey of experimental data,” Medical Engineering & Physics, 34(6), 665-680 (2012).

[17] J. d. l. Rosette, D. Assimos, M. Desai et al., “The clinical research office of the endourological society percutaneous nephrolithotomy global study: indications, complications, and outcomes in 5803 patients,” Journal of endourology, 25(1), 11-17 (2011).

[18] P. D. Voilette, and J. D. Denstedt, “Standardizing the reporting of percutaneous nephrolithotomy complications,” Indian journal of urology: IJU: journal of the Urological Society of India, 30(1), 84 (2014).

[19] P. L. Rodrigues, N. F. Rodrigues, J. Fonseca et al., “Kidney Targeting and Puncturing During Percutaneous Nephrolithotomy: Recent Advances and Future Perspectives,” Journal of Endourology, 27(7), 826-834 (2013).

[20] H. Karami, A. H. Arbab, A. Rezaei et al., “Percutaneous nephrolithotomy with ultrasonography-guided renal access in the lateral decubitus flank position,” Journal of Endourology, 23(1), 33-5 (2009).

[21] J. Huber, I. Wegner, H. P. Meinzer et al., “Navigated renal access using electromagnetic tracking: an initial experience,” Surgical Endoscopy and Other Interventional Techniques, 25(4), 1307-1312 (2011).

[22] L. Barber, R. Barrett, and G. Lichtwark, “Validation of a freehand 3D ultrasound system for morphological measures of the medial gastrocnemius muscle,” Journal of biomechanics, 42(9), 1313-1319 (2009).

[23] J. Weickert, and H. Scharr, “A scheme for coherence-enhancing diffusion filtering with optimized rotation invariance,” Journal of Visual Communication and Image Representation, 13(1), 103-118 (2002).

[24] R. W. Prager, A. Gee, and L. Berman, “Stradx: real-time acquisition and visualization of freehand three-dimensional ultrasound,” Medical Image Analysis, 3(2), 129-140 (1999).

[25] O. V. Solberg, F. Lindseth, H. Torp et al., “Freehand 3D ultrasound reconstruction algorithms—a review,” Ultrasound in medicine & biology, 33(7), 991-1009 (2007).

[26] X. Li, S. Liao, Y. Yu et al., “Stereotactic localisation system: a modified puncture technique for percutaneous nephrolithotomy,” Urological Research, 40(4), 395-401 (2012).

[27] H. Karami, R. Mohammadi, and B. Lotfi, “A study on comparative outcomes of percutaneous nephrolithotomy in prone, supine, and flank positions,” World Journal of Urology, 1-6 (2012).

[28] M. Ritter, M. C. Rassweiler, A. Häcker et al., “Laser-guided percutaneous kidney access with the Uro Dyna-CT: first experience of three-dimensional puncture planning with an ex vivo model,” World Journal of Urology, 1-5 (2012).

[29] O. Tanriverdi, U. Boylu, M. Kendirci et al., “The learning curve in the training of percutaneous nephrolithotomy,” European Urology, 52(1), 206-212 (2007).

# R

# References

[1] O. Ukimura, "Image-guided surgery in minimally invasive urology," *Current Opinion in Urology,* vol. 20, pp. 136-140 10.1097/MOU.0b013e3283362610, 2010.

[2] J. C. Liao and L.-M. Su, "Advances in Image-Guided Urologic Surgery," ed: Springer, 2014.

[3] S. Micali, G. Pini, D. Teber, M. C. Sighinolfi, S. De Stefani, G. Bianchi*, et al.*, "New trends in minimally invasive urological surgery. What is beyond the robot?," *World J Urol,* Sep 2 2010.

[4] D. P. Perrin, N. V. Vasilyev, P. Novotny, J. Stoll, R. D. Howe, P. E. Dupont*, et al.*, "Image Guided Surgical Interventions," *Current Problems in Surgery,* vol. 46, pp. 730-766, 2009.

[5] B. Maurin, L. Barbe, B. Bayle, P. Zanne, J. Gangloff, M. De Mathelin*, et al.*, "In vivo study of forces during needle insertions," in *Proceedings of the medical robotics, navigation and visualisation scientific workshop*, 2004, pp. 1-8.

[6] (20/11). *Thoracic Surgery*. Available: http://www.lhsc.on.ca/Patients_Families_Visitors/Thoracic_Surgery/Procedures/Percutaneous_Lung_Biopsy.htm

[7] J. Zhai, K. Karuppasamy, R. Zvavanjanja, M. Fisher, A. Fisher, D. Gould*, et al.*, "A sensor for needle puncture force measurement during interventional radiological procedures," *Medical engineering & physics,* vol. 35, pp. 350-356, 2013.

[8] D. J. van Gerwen, J. Dankelman, and J. J. van den Dobbelsteen, "Needle-tissue interaction forces - A survey of experimental data," *Medical Engineering & Physics,* vol. 34, pp. 665-680, Jul 2012.

[9] J. Lazarus and J. Williams, "The Locator: novel percutaneous nephrolithotomy apparatus to aid collecting system puncture–a preliminary report," *Journal of Endourology,* vol. 25, pp. 747-50, 2011.

[10] M. J. Bader, C. Gratzke, M. Seitz, R. Sharma, C. G. Stief, and M. Desai, "The "All-Seeing Needle": Initial Results of an Optical Puncture System Confirming Access in Percutaneous Nephrolithotomy," *European Urology,* vol. 59, pp. 1054-1059, Jun 2011.

[11] N. L. Miller, B. R. Matlaga, and J. E. Lingeman, "Techniques for fluoroscopic percutaneous renal access," *Journal of Urology,* vol. 178, pp. 15-23, Jul 2007.

[12] R. Hu, C. Montemayor-Garcia, and K. Das, "Role of Percutaneous Needle Core Biopsy in Diagnosis and Clinical Management of Renal Masses," *Human Pathology,* 2015.

[13] P. L. Rodrigues, J. L. Vilaca, C. Oliveira, A. Cicione, J. Rassweiler, J. Fonseca*, et al.*, "Collecting system percutaneous access using real-time tracking sensors: first pig model in vivo experience," *J Urol,* vol. 190, pp. 1932-7, Nov 2013.

[14] C. Kalogeropoulou, P. Kallidonis, and E. N. Liatsikos, "Imaging in Percutaneous Nephrolithotomy," *Journal of Endourology,* vol. 23, pp. 1571-1577, Oct 2009.

[15] N. Abolhassani, R. Patel, and M. Moallem, "Needle insertion into soft tissue: A survey," *Medical Engineering & Physics,* vol. 29, pp. 413-431, May 2007.

[16] J. de la Rosette, "The Time Is Now—the Ability Is Yours," *European Urology,* vol. 61, pp. 1194-1195, 2012.

[17] C. J. Colangelo, G. W. Kaplan, N. Holmes, K. Palazzi-Churas, and G. Chiang, "Ureteroscopy in Pediatric Patients with Spinal Abnormalities," *J Endourol,* Dec 23 2012.

[18] P. Mozer, J. Troccaz, and D. Stoianovici, "Urologic robots and future directions," *Current Opinion in Urology,* vol. 19, pp. 114-119, Jan 2009.

[19] E. M. Worcester and F. L. Coe, "Calcium Kidney Stones," *New England Journal of Medicine,* vol. 363, pp. 954-963, 2010.

[20] J. N. Armitage, S. O. Irving, and N. A. Burgess, "Percutaneous Nephrolithotomy in the United Kingdom: Results of a Prospective Data Registry," *European Urology,* vol. 61, pp. 1188-1193, 2012.

[21] T. Knoll, N. Buchholz, and G. Wendt-Nordahl, "Extracorporeal shockwave lithotripsy vs. percutaneous nephrolithotomy vs. flexible ureterorenoscopy for lower-pole stones," *Arab Journal of Urology,* vol. 10, pp. 336-341, 2012.

[22] O. W. Moe, "Kidney stones: pathophysiology and medical management," *The Lancet,* vol. 367, pp. 333-344, 2006.

[23] R. Lozano, M. Naghavi, K. Foreman, S. Lim, K. Shibuya, V. Aboyans*, et al.*, "Global and regional mortality from 235 causes of death for 20 age groups in 1990 and 2010: a systematic analysis for the Global Burden of Disease Study 2010," *The Lancet,* vol. 380, pp. 2095-2128, 2013.

[24] (20/11). *Functions of the Human Body Systems*. Available: https://sites.google.com/site/functionsofthehumanbodysystems/urinary-system

[25] (20/11). *Kidney Ultrasound*. Available: http://www.hopkinsmedicine.org/healthlibrary/test_procedures/urology/kidney_ultrasound_92,p07709/

[26] (February). *Ureteroscopy*. Available: http://www.kidneystoners.org/treatments/ureteroscopy/

[27] M. T. Gettman and J. W. Segura, "Management of ureteric stones: issues and controversies," *BJU international,* vol. 95, pp. 85-93, 2005.

[28] J. Rassweiler, C. Renner, and F. Eisenberger, "The management of complex renal stones," *BJU international,* vol. 86, pp. 919-928, 2000.

[29] S. D. Miller, C. S. NG, S. B. STREEM, and I. S. GILL, "Laparoscopic management of caliceal diverticular calculi," *The Journal of urology,* vol. 167, pp. 1248-1252, 2002.

[30] M. M. Osman, Y. Alfano, S. Kamp, A. Haecker, P. Alken, M. S. Michel*, et al.*, "5-year-follow-up of patients with clinically insignificant residual fragments after extracorporeal shockwave lithotripsy," *European urology,* vol. 47, pp. 860-864, 2005.

[31] H. Park, M. Park, and T. Park, "Two-year experience with ureteral stones: extracorporeal shockwave lithotripsy v ureteroscopic manipulation," *Journal of endourology,* vol. 12, pp. 501-504, 1998.

[32] J. Lingeman, J. Woods, P. D. Toth, A. Evan, and J. McAteer, "The role of lithotripsy and its side effects," *The Journal of urology,* vol. 141, pp. 793-797, 1989.

[33] M. Hruza and J. Rassweiler, "Shock Wave Lithotripsy for the Treatment of Ureteral Stones," in *Ureteral Stone Management*, ed: Springer, 2015, pp. 83-92.

[34] P. Lu, Z. Wang, R. Song, X. Wang, K. Qi, Q. Dai*, et al.*, "The clinical efficacy of extracorporeal shock wave lithotripsy in pediatric urolithiasis: a systematic review and meta-analysis," *Urolithiasis,* pp. 1-8, 2015.

[35] D. Rennie. (2016). Available: https://doctorrennie.files.wordpress.com/2012/07/shutterstock_77325922.jpg

[36] Ezyhealth. (February). Available: http://www.ezyhealth.com/magazine/kidney-pebbles/

[37] J. W. Segura, G. M. Preminger, D. G. Assimos, S. P. Dretler, R. I. Kahn, J. E. Lingeman*, et al.*, "Ureteral stones clinical guidelines panel summary report on the management of ureteral calculi," *The Journal of urology,* vol. 158, pp. 1915-1921, 1997.

[38] Khoslastonekidney. (December). Available: http://www.khoslastonekidney.com/

[39] J. S. Lam, T. D. Greene, and M. Gupta, "Treatment of proximal ureteral calculi: holmium: YAG laser ureterolithotripsy versus extracorporeal shock wave lithotripsy," *The Journal of urology,* vol. 167, pp. 1972-1976, 2002.

[40] J. P. Jessen, P. Honeck, T. Knoll, and G. Wendt-Nordahl, "Percutaneous nephrolithotomy under combined sonographic/radiologic guided puncture: results of a learning curve using the modified Clavien grading system," *World J Urol,* Jan 3 2013.

[41] O. Tanriverdi, U. Boylu, M. Kendirci, M. Kadihasanoglu, K. Horasanli, and C. Miroglu, "The learning curve in the training of percutaneous nephrolithotomy," *European Urology,* vol. 52, pp. 206-212, Jul 2007.

[42] M. S. Michel, L. Trojan, and J. J. Rassweiler, "Complications in percutaneous nephrolithotomy," *European Urology,* vol. 51, pp. 899-906, Apr 2007.

[43] G. Labate, P. Modi, A. Timoney, L. Cormio, X. Zhang, M. Louie*, et al.*, "The percutaneous nephrolithotomy global study: classification of complications," *Journal of Endourology,* vol. 25, pp. 1275-80, Aug 2011.

[44] J. J. M. C. H. de la Rosette, M. P. Laguna, J. J. Rassweiler, and P. Conort, "Training in Percutaneous Nephrolithotomy-A Critical Review," *European Urology,* vol. 54, pp. 994-1003, Nov 2008.

[45] K. R. Ghani, U. Patel, and K. Anson, "Computed tomography for percutaneous renal access," *Journal of Endourology,* vol. 23, pp. 1633-9, Oct 2009.

[46] J. R. Zuazu, M. Hruza, J. J. Rassweiler, and J. J. de la Rosette, "The Clavien classification system to optimize the documentation of PCNL morbidity," *Arch Ital Urol Androl,* vol. 82, pp. 20-2, Mar 2010.

[47] S. Mishra, J. Jagtap, R. B. Sabnis, and M. R. Desai, "Training in percutaneous nephrolithotomy," *Current Opinion in Urology,* vol. 23, pp. 147-151 10.1097/MOU.0b013e32835d4e37, 2013.

[48] N. L. Miller and J. E. Lingeman, *Management of kidney stones* vol. 334, 2007.

[49] G. M. Preminger, H.-G. Tiselius, D. G. Assimos, P. Alken, A. Colin Buck, M. Gallucci*, et al.*, "2007 Guideline for the Management of Ureteral Calculi," *European Urology,* vol. 52, pp. 1610-1631, 12// 2007.

[50] J. Rassweiler, M.-C. Rassweiler, M. Müller, E. Lima, B. Petrut, J. Huber*, et al.*, "Augmented Reality for Percutaneous Renal Interventions," in *Advances in Image-Guided Urologic Surgery*, ed: Springer, 2015, pp. 203-220.

[51] C. Bach, T. Karaolides, and N. Buchholz, "Extracorporeal shock wave lithotripsy: What is new?," *Arab Journal of Urology,* vol. 10, pp. 289-295, 9// 2012.

[52] J. J. Rassweiler, M. Muller, M. Fangerau, J. Klein, A. S. Goezen, P. Pereira*, et al.*, "iPad-Assisted Percutaneous Access to the Kidney Using Marker-Based Navigation: Initial Clinical Experience," *European Urology,* vol. 61, pp. 628-631, Mar 2012.

[53] P. L. Rodrigues, N. F. Rodrigues, J. Fonseca, E. Lima, and J. L. Vilaça, "Kidney Targeting and Puncturing During Percutaneous Nephrolithotomy: Recent Advances and Future Perspectives," *Journal of Endourology,* vol. 27, pp. 826-834, 2013.

[54] P. L. Rodrigues, J. L. Vilaça, C. Oliveira, A. Cicione, J. Rassweiler, J. Fonseca*, et al.*, "Collecting system percutaneous access using real-time tracking sensors: First pig model in vivo experience," *The Journal of urology,* vol. 190, pp. 1932-1937, 2013.

[55] P. L. Rodrigues, A. H. J. Moreira, N. F. Rodrigues, A. C. M. Pinho, J. C. Fonseca, E. Lima*, et al.*, "Preliminary clinical trial in percutaneous nephrolithotomy using a real-time navigation system for percutaneous kidney access," 2014, pp. 903606-903606-7.

[56] P. L. Rodrigues, N. F. Rodrigues, J. C. Fonseca, and J. L. Vilaça, "Validation of percutaneous puncture trajectory during renal access using 4D ultrasound reconstruction," in *SPIE Medical Imaging 2015*, Orlando, Florida, United States, 2015.

[57] P. L. Rodrigues, N. F. Rodrigues, J. C. Fonseca, M. A. von Krüger, W. A. Pereira, and J. L. Vilaça, "A-scan ultrasound system for real-time puncture safety assessment during percutaneous nephrolithotomy," in *SPIE Medical Imaging 2015*, Orlando, Florida, United States, 2015.

[58] P. L. Rodrigues, N. Rodrigues, J. C. Fonseca, J. Vilaça, and E. Lima, "Confirmação da eficácia da punção renal e ureteral em modelo experimental com a utilização de um sistema de localização eletromagnética," in *Portuguese Symposium of Urology*, 2013.

[59] P. L. Rodrigues, N. Rodrigues, J. C. Fonseca, J. Vilaça, and E. Lima, "Experiência inicial em humanos de um novo aparelho para ajuda na punção de um cálice renal na Nefrolitotomia percutânea," in *Portuguese Symposium of Urology*, 2012.

[60] S. Sivalingam, T. Al-Essawi, and D. Hosking, "Percutaneous Nephrolithotomy with Retrograde Nephrostomy Access: A Forgotten Technique Revisited," *J Urol,* Dec 3 2012.

[61] C. M. Cracco, C. M. Scoffone, and R. M. Scarpa, "New developments in percutaneous techniques for simple and complex branched renal stones," *Curr Opin Urol,* Jan 19 2011.

[62] Z. C. Li, K. Li, H. L. Zhan, K. Chen, J. Gu, and L. Wang, "Augmenting intraoperative ultrasound with preoperative magnetic resonance planning models for percutaneous renal access," *Biomed Eng Online,* vol. 11, p. 60, 2012.

[63] M. M. Desai, R. Grover, M. Aron, A. Ganpule, S. S. Joshi, M. R. Desai*, et al.*, "Robotic Flexible Ureteroscopy for Renal Calculi: Initial Clinical Experience," *Journal of Urology,* vol. 186, pp. 563-568, Aug 2011.

[64] Z. Yaniv, E. Wilson, D. Lindisch, and K. Cleary, "Electromagnetic tracking in the clinical environment," *Medical Physics,* vol. 36, pp. 876-892, Mar 2009.

[65] J. T. Hing, A. D. Brooks, and J. P. Desai, "A biplanar fluoroscopic approach for the measurement, modeling, and simulation of needle and soft-tissue interaction," *Medical Image Analysis,* vol. 11, pp. 62-78, 2007.

[66] X. Li, Q. Long, X. Chen, H. Dalin, and H. He, "Real-time ultrasound-guided PCNL using a novel SonixGPS needle tracking system," *Urolithiasis,* vol. 42, pp. 341-346, 2014.

[67] P. Mozer, P. Conort, A. Leroy, M. Baumann, Y. Payan, J. Troccaz*, et al.*, "Aid to percutaneous renal access by virtual projection of the ultrasound puncture tract onto fluoroscopic images," *Journal of Endourology,* vol. 21, pp. 460-465, May 2007.

[68] P. D. Voilette and J. D. Denstedt, "Standardizing the reporting of percutaneous nephrolithotomy complications," *Indian journal of urology: IJU: journal of the Urological Society of India,* vol. 30, p. 84, 2014.

[69] M. Graefen, "The modified Clavien system: a plea for a standardized reporting system for surgical complications," *European urology,* vol. 57, pp. 387-389, 2010.

[70] J. de la Rosette, D. Assimos, M. Desai, J. Gutierrez, J. Lingeman, R. Scarpa*, et al.*, "The Clinical Research Office of the Endourological Society Percutaneous Nephrolithotomy Global Study: indications, complications, and outcomes in 5803 patients," *Journal of Endourology,* vol. 25, pp. 11-7, Jan 2011.

[71] J. d. l. Rosette, D. Assimos, M. Desai, J. Gutierrez, J. Lingeman, R. Scarpa*, et al.*, "The clinical research office of the endourological society percutaneous nephrolithotomy global study: indications, complications, and outcomes in 5803 patients," *Journal of endourology,* vol. 25, pp. 11-17, 2011.

[72] S. Guven, O. Istanbulluoglu, U. Gul, A. Ozturk, H. Celik, C. Aygün*, et al.*, "Successful Percutaneous Nephrolithotomy in Children: Multicenter Study on Current Status of its Use, Efficacy and Complications Using Clavien Classification," *The Journal of urology,* vol. 185, pp. 1419-1424, 2011.

[73] E. Ozden, M. N. Mercimek, Y. K. Yakupoglu, O. Ozkaya, and S. Sarikaya, "Modified Clavien classification in percutaneous nephrolithotomy: assessment of complications in children," *J Urol,* vol. 185, pp. 264-8, Jan 2011.

[74] C. Coleman, W. Castaneda-Zuniga, R. Miller, P. Lange, R. Clayman, P. Reddy*, et al.*, "A logical approach to renal stone removal," *American journal of roentgenology,* vol. 143, pp. 609-615, 1984.

[75] R. Autorino and G. Giannarini, "Prone or Supine: Is This the Question?," *European Urology,* vol. 54, pp. 1216-1218, Dec 2008.

[76] J. J. M. C. H. de la Rosette, P. Tsakiris, M. N. Ferrandino, A. M. Elsakka, J. Rioja, and G. M. Preminger, "Beyond Prone Position in Percutaneous Nephrolithotomy: A Comprehensive Review," *European Urology,* vol. 54, pp. 1262-1269, Dec 2008.

[77] M. De Sio, R. Autorino, G. Quarto, F. Calabro, R. Damiano, F. Giuyliano*, et al.*, "Modified supine versus prone position in percutaneous nephrolithotomy for renal stones treatable with a single percutaneous access: A prospective randomized trial," *European Urology,* vol. 54, pp. 196-203, Jul 2008.

[78] H. Karami, R. Mohammadi, and B. Lotfi, "A study on comparative outcomes of percutaneous nephrolithotomy in prone, supine, and flank positions," *World Journal of Urology,* pp. 1-6, 2012.

[79] R. J. D. A. Honey, J. D. Wiesenthal, D. Ghiculete, S. Pace, A. A. Ray, and K. T. Pace, "Comparison of Supracostal Versus Infracostal Percutaneous Nephrolithotomy Using the Novel Prone-Flexed Patient Position," *Journal of Endourology,* vol. 25, pp. 947-954, Jun 2011.

[80] R. DasGupta and A. Patel, "Percutaneous nephrolithotomy: does position matter? – prone, supine and variations," *Current Opinion in Urology,* vol. 23, pp. 164-168 10.1097/MOU.0b013e32835d3067, 2013.

[81] J. Miller, J. C. Durack, M. D. Sorensen, J. H. Wang, and M. L. Stoller, "Renal calyceal anatomy characterization with 3-dimensional in vivo computerized tomography imaging," *J Urol,* vol. 189, pp. 562-7, Feb 2013.

[82] K. G. Yan, T. Podder, W. S. Ng, and Y. Yu, "'Smart' needle for percutaneous surgery: Influential factor investigation," *2007 Annual International Conference of the Ieee Engineering in Medicine and Biology Society, Vols 1-16,* pp. 461-464, 2007.

[83] D. J. Hernandez, V. A. Sinkov, W. W. Roberts, M. E. Allaf, A. Patriciu, T. W. Jarrett*, et al.*, "MEASUREMENT OF BIO-IMPEDANCE WITH A SMART NEEDLE TO CONFIRM PERCUTANEOUS KIDNEY ACCESS," *The Journal of urology,* vol. 166, pp. 1520-1523, 2001.

[84] N. D. Inc. (December). Available: http://www.ndigital.com/medical/products/aurora/

[85] S. P. DiMaio and S. E. Salcudean, "Needle steering and motion planning in soft tissues," *Ieee Transactions on Biomedical Engineering,* vol. 52, pp. 965-974, Jun 2005.

[86] A. M. Okamura, C. Simone, and M. D. O'Leary, "Force modeling for needle insertion into soft tissue," *Biomedical Engineering, IEEE Transactions on,* vol. 51, pp. 1707-1716, 2004.

[87] P. N. Brett, T. Parker, A. J. Harrison, T. A. Thomas, and A. Carr, "Simulation of resistance forces acting on surgical needles," *Proceedings of the Institution of Mechanical Engineers, Part H: Journal of Engineering in Medicine,* vol. 211, pp. 335-347, 1997.

[88] N. Abolhassani, R. Patel, and M. Moallem, "Experimental study of robotic needle insertion in soft tissue," in *International Congress Series*, 2004, pp. 797-802.

[89] W. G. Wein, S. Brunke, A. Khamene, M. R. Callstrom, and N. Navab, "Automatic CT-ultrasound registration for diagnostic imaging and image-guided intervention," *Medical Image Analysis,* vol. 12, pp. 577-585, Oct 2008.

[90] B. C. Meyer, O. Peter, M. Nagel, M. Hoheisel, B. B. Frericks, K. J. Wolf*, et al.*, "Electromagnetic field-based navigation for percutaneous punctures on C-arm CT: experimental evaluation and clinical application," *European Radiology,* vol. 18, pp. 2855-2864, Dec 2008.

[91] M. Ritter, M. C. Rassweiler, A. Häcker, and M. Michel, "Laser-guided percutaneous kidney access with the Uro Dyna-CT: first experience of three-dimensional puncture planning with an ex vivo model," *World Journal of Urology,* pp. 1-5, 2012.

[92] M. D. Sorensen, J. D. Harper, R. S. Hsi, A. R. Shah, M. K. Dighe, S. J. Carter*, et al.*, "B-mode Ultrasound Versus Color Doppler Twinkling Artifact in Detecting Kidney Stones," *J Endourol,* Oct 15 2012.

[93] M. R. Desai, R. Sharma, S. Mishra, R. B. Sabnis, C. Stief, and M. Bader, "Single-Step Percutaneous Nephrolithotomy (Microperc): The Initial Clinical Report," *The Journal of urology,* vol. 186, pp. 140-145, 2011.

[94] A. Leroy, P. Mozer, Y. Payan, and J. Troccaz, "Rigid registration of freehand 3D ultrasound and CT-scan kidney images," *Medical Image Computing and Computer-Assisted Intervention - Miccai 2004, Pt 1, Proceedings,* vol. 3216, pp. 837-844, 2004.

[95] P. Mozer, A. Leroy, Y. Payan, J. Troccaz, E. Chartier-Kastier, and F. Richard, "Computer-assisted access to the kidney," *International Journal of Medical Robotics and Computer Assisted Surgery,* vol. 1, pp. 58-66, Dec 2005.

[96] M. G. Linguraru, J. A. Pura, V. Pamulapati, and R. M. Summers, "Statistical 4D graphs for multi-organ abdominal segmentation from multiphase CT," *Medical image analysis,* vol. 16, pp. 904-914, 2012.

[97] X. Chen, J. K. Udupa, U. Bagci, Y. Zhuge, and J. Yao, "Medical image segmentation by combining graph cuts and oriented active appearance models," *Image Processing, IEEE Transactions on,* vol. 21, pp. 2035-2046, 2012.

[98] R. Wolz, C. Chu, K. Misawa, K. Mori, and D. Rueckert, "Multi-organ abdominal CT segmentation using hierarchically weighted subject-specific atlases," in *Medical Image Computing and Computer-Assisted Intervention–MICCAI 2012*, ed: Springer, 2012, pp. 10-17.

[99] M. Jorge Cardoso, K. Leung, M. Modat, S. Keihaninejad, D. Cash, J. Barnes*, et al.*, "STEPS: Similarity and Truth Estimation for Propagated Segmentations and its application to hippocampal segmentation and brain parcelation," *Medical image analysis,* vol. 17, pp. 671-684, 2013.

[100] P. Cinquin, "How today's robots work and perspectives for the future," *Journal of Visceral Surgery,* vol. 148, pp. E12-E18, Oct 2011.

[101] X. Li, S. Liao, Y. Yu, Q. Dai, B. Song, and L. Li, "Stereotactic localisation system: a modified puncture technique for percutaneous nephrolithotomy," *Urological Research,* vol. 40, pp. 395-401, 2012.

[102] U. Hagn, M. Nickl, S. Jorg, G. Passig, T. Bahls, A. Nothhelfer*, et al.*, "The DLR MIRO: a versatile lightweight robot for surgical applications," *Industrial Robot-an International Journal,* vol. 35, pp. 324-336, 2008.

[103] S. Nicolau, L. Soler, D. Mutter, and J. Marescaux, "Augmented reality in laparoscopic surgical oncology," *Surgical Oncology-Oxford,* vol. 20, pp. 189-201, Sep 2011.

[104] D. Teber, S. Guven, T. Simpfendörfer, M. Baumhauer, E. O. Güven, F. Yencilek*, et al.*, "Augmented Reality: A New Tool To Improve Surgical Accuracy during Laparoscopic Partial Nephrectomy? Preliminary In Vitro and In Vivo Results," *European Urology,* vol. 56, pp. 332-338, 2009.

[105] L. M. Su, B. P. Vagvolgyi, R. Agarwal, C. E. Reiley, R. H. Taylor, and G. D. Hager, "Augmented reality during robot-assisted laparoscopic partial nephrectomy: toward real-time 3D-CT to stereoscopic video registration," *Urology,* vol. 73, pp. 896-900, Apr 2009.

[106] J. Huber, I. Wegner, H. P. Meinzer, P. Hallscheidt, B. Hadaschik, S. Pahernik*, et al.*, "Navigated renal access using electromagnetic tracking: an initial experience," *Surgical Endoscopy and Other Interventional Techniques,* vol. 25, pp. 1307-1312, Apr 2011.

[107] J. G. Mancini, E. M. Raymundo, M. Lipkin, D. Zilberman, D. Yong, L. L. Banez*, et al.*, "Factors Affecting Patient Radiation Exposure During Percutaneous Nephrolithotomy," *Journal of Urology,* vol. 184, pp. 2373-2377, Dec 2010.

[108] P. Markelj, D. Tomazevic, B. Likar, and F. Pernus, "A review of 3D/2D registration methods for image-guided interventions," *Med Image Anal,* Apr 13 2010.

[109] K. Cleary and T. M. Peters, "Image-guided interventions: technology review and clinical applications," *Annu Rev Biomed Eng,* vol. 12, pp. 119-42, Aug 15 2010.

[110] J. W. Pugh and B. K. Canales, "New instrumentation in percutaneous nephrolithotomy," *Indian J Urol,* vol. 26, pp. 389-94, Jul 2010.

[111] M. Rao, J. Stough, Y.-Y. Chi, K. Muller, G. Tracton, S. M. Pizer*, et al.*, "Comparison of human and automatic segmentations of kidneys from CT images," *International Journal of Radiation Oncology* Biology* Physics,* vol. 61, pp. 954-960, 2005.

[112] D.-T. Lin, C.-C. Lei, and S.-W. Hung, "Computer-aided kidney segmentation on abdominal CT images," *Information Technology in Biomedicine, IEEE Transactions on,* vol. 10, pp. 59-65, 2006.

[113] M. Spiegel, D. A. Hahn, V. Daum, J. Wasza, and J. Hornegger, "Segmentation of kidneys using a new active shape model generation technique based on non-rigid image registration," *Computerized Medical Imaging and Graphics,* vol. 33, pp. 29-39, 2009.

[114] S.-J. Kim, S.-W. Yoo, S.-H. Kim, J.-C. Kim, and J.-W. Park, "Segmentation of kidney without using contrast medium on abdominal CT image," in *Signal Processing Proceedings, 2000. WCCC-ICSP 2000. 5th International Conference on*, 2000, pp. 1147-1152.

[115] R. Pohle and K. D. Toennies, "Segmentation of medical images using adaptive region growing," in *Medical Imaging 2001*, 2001, pp. 1337-1346.

[116] M. Kobashi and L. G. Shapiro, "Knowledge-based organ identification from CT images," *Pattern Recognition,* vol. 28, pp. 475-491, 1995.

[117] J. Krücker, A. Viswanathan, J. Borgert, N. Glossop, Y. Yang, and B. J. Wood, "An electro-magnetically tracked laparoscopic ultrasound for multi-modality minimally invasive surgery," in *International Congress Series*, 2005, pp. 746-751.

[118] J. Xie, Y. Jiang, and H.-t. Tsui, "Segmentation of kidney from ultrasound images based on texture and shape priors," *Medical Imaging, IEEE Transactions on,* vol. 24, pp. 45-57, 2005.

[119] O. Gloger, K. D. Tönnies, V. Liebscher, B. Kugelmann, R. Laqua, and H. Völzke, "Prior shape level set segmentation on multistep generated probability maps of MR datasets for fully automatic kidney parenchyma volumetry," *Medical Imaging, IEEE Transactions on,* vol. 31, pp. 312-325, 2012.

[120] C.-C. Lee, P.-C. Chung, and H.-M. Tsai, "Identifying multiple abdominal organs from CT image series using a multimodule contextual neural network and spatial fuzzy rules," *Information Technology in Biomedicine, IEEE Transactions on,* vol. 7, pp. 208-217, 2003.

[121] Y. Zhou and J. Bai, "Multiple abdominal organ segmentation: an atlas-based fuzzy connectedness approach," *Information Technology in Biomedicine, IEEE Transactions on,* vol. 11, pp. 348-352, 2007.

[122] A. Shimizu, R. Ohno, T. Ikegami, H. Kobatake, S. Nawano, and D. Smutek, "Segmentation of multiple organs in non-contrast 3D abdominal CT images," *International journal of computer assisted radiology and surgery,* vol. 2, pp. 135-142, 2007.

[123] D. Zhang, Z. Li, K. Chen, J. Xiong, X. Zhang, and L. Wang, "An optical tracker based robot registration and servoing method for ultrasound guided percutaneous renal access," *Biomed Eng Online,* vol. 12, p. 47, 2013.

[124] M. J. Black, G. Sapiro, D. H. Marimont, and D. Heeger, "Robust anisotropic diffusion," *Ieee Transactions on Image Processing,* vol. 7, pp. 421-432, Mar 1998.

[125] T. C. M. Lee, "A minimum description length-based image segmentation procedure, and its comparison with a cross-validation-based segmentation procedure," *Journal of the American Statistical Association,* vol. 95, pp. 259-270, Mar 2000.

[126] S. D. Roth, "Ray casting for modeling solids," *Computer graphics and image processing,* vol. 18, pp. 109-144, 1982.

[127] M. H. Gross, L. Lippert, A. Dreger, and R. Koch, "A New Method to Approximate the Volume-Rendering Equation Using Wavelet Bases and Piecewise Polynomials," *Computers & Graphics,* vol. 19, pp. 47-62, Jan-Feb 1995.

[128] E. R. Dougherty, R. A. Lotufo, and T. I. S. f. O. E. SPIE, *Hands-on morphological image processing* vol. 71: SPIE press Bellingham, 2003.

[129] N. Otsu, "A threshold selection method from gray-level histograms," *Automatica,* vol. 11, pp. 23-27, 1975.

[130] T. Okada, K. Yokota, M. Hori, M. Nakamoto, H. Nakamura, and Y. Sato, "Construction of hierarchical multi-organ statistical atlases and their application to multi-organ segmentation from CT images," in *Medical Image Computing and Computer-Assisted Intervention–MICCAI 2008*, ed: Springer, 2008, pp. 502-509.

[131] M. A. Nixon, B. C. McCallum, W. R. Fright, and N. B. Price, "The effects of metals and interfering fields on electromagnetic trackers," *Presence: Teleoperators and Virtual Environments,* vol. 7, pp. 204-218, 1998.

[132] G. S. Fischer and R. H. Taylor, "Electromagnetic tracker measurement error simulation and tool design," in *Medical Image Computing and Computer-Assisted Intervention–MICCAI 2005*, ed: Springer, 2005, pp. 73-80.

[133] M. Hoheisel, M. Skalej, O. Beuing, U. Bill, K. Klingenbeck-Regn, R. Petzold*, et al.*, *Kyphoplasty Interventions using a Navigation System and C-arm CT data: First Clinical Results* vol. 10. Belligham, ETATS-UNIS: Society of Photo-Optical Instrumentation Engineers, 2009.

[134] S. E. Leis and D. Ristau, "System for determining the spatial position and angular orientation of an object," ed: Google Patents, 1998.

[135] P. J. Besl and H. D. McKay, "A method for registration of 3-D shapes," *Pattern Analysis and Machine Intelligence, IEEE Transactions on,* vol. 14, pp. 239-256, 1992.

[136] A. Albert, *Regression and the Moore-Penrose pseudoinverse*: Elsevier, 1972.

[137] A. Bosnjak, G. Montilla, R. Villegas, and I. Jara, "An Electromagnetic Tracking System for Surgical Navigation with registration of fiducial markers using the iterative closest point algorithm," in *Information Technology and Applications in Biomedicine (ITAB), 2010 10th IEEE International Conference on*, 2010, pp. 1-5.

[138] N. C. Nicholas and J. R. Welsch, "Ballistic Gelatin," *Applied Research Laboratory, The Pennsylvania State University,* 2004.

[139] I. M. Germano and J. V. Queenan, "Clinical experience with intracranial brain needle biopsy using frameless surgical navigation," *Computer Aided Surgery,* vol. 3, pp. 33-39, 1998.

[140] D. Thomas, E. P. Scholz, P. A. Schweizer, H. A. Katus, and R. Becker, "Initial experience with robotic navigation for catheter ablation of paroxysmal and persistent atrial fibrillation," *Journal of Electrocardiology,* vol. 45, pp. 95-101, 2012.

[141] F. Banovac, E. Wilson, H. Zhang, and K. Cleary, "Needle biopsy of anatomically unfavorable liver lesions with an electromagnetic navigation assist device in a computed tomography environment," *Journal of vascular and interventional radiology,* vol. 17, pp. 1671-1675, 2006.

[142] E. B. Levy, H. Zhang, D. Lindisch, B. J. Wood, and K. Cleary, "Electromagnetic tracking-guided percutaneous intrahepatic portosystemic shunt creation in a swine model," *Journal of Vascular and Interventional Radiology,* vol. 18, pp. 303-307, Feb 2007.

[143] M. Nagel, M. Hoheisel, U. Bill, K. Klingenbeck-Regn, W. A. Kalender, and R. Petzold, "Electromagnetic tracking system for minimal invasive interventions using a C-arm system with CT option: First clinical results - art. no. 69180G," *Medical Imaging 2008: Visualization, Image-Guided Procedures, and Modeling, Pts 1 and 2,* vol. 6918, pp. G9180-G9180 423, 2008.

[144] M. Nagel, G. Schmidt, G. Schnuetgen, and W. A. Kalender, "Risk management for a robot-assisted needle positioning system for interventional radiology," in *International Congress Series*, 2004, pp. 549-554.

[145] C. Ozhasoglu and M. J. Murphy, "Issues in respiratory motion compensation during external-beam radiotherapy," *International Journal of Radiation Oncology*Biology*Physics,* vol. 52, pp. 1389-1399, 4/1/ 2002.

[146] A. Schweikard, G. Glosser, M. Bodduluri, M. J. Murphy, and J. R. Adler, "Robotic motion compensation for respiratory movement during radiosurgery," *Computer Aided Surgery,* vol. 5, pp. 263-277, 2000.

[147] R. Alterovitz, K. Goldberg, J. Pouliot, R. Taschereau, and I. C. Hsu, "Needle insertion and radioactive seed implantation in human tissues: simulation and sensitivity analysis," in *Robotics and Automation, 2003. Proceedings. ICRA '03. IEEE International Conference on*, 2003, pp. 1793-1799 vol.2.

[148] M. Meltsner, N. J. Ferrier, and B. Thomadsen, "Observations on rotating needle insertions using a brachytherapy robot," *Physics in medicine and biology,* vol. 52, p. 6027, 2007.

[149] Z. Yaniv, P. Cheng, E. Wilson, T. Popa, D. Lindisch, E. Campos-Nanez*, et al.*, "Needle-based interventions with the image-guided surgery toolkit (IGSTK): from phantoms to clinical trials," *Biomedical Engineering, IEEE Transactions on,* vol. 57, pp. 922-933, 2010.

[150] S. A. Müller, L. Maier-Hein, A. Tekbas, A. Seitel, S. Ramsauer, B. Radeleff*, et al.*, "Navigated Liver Biopsy Using a Novel Soft Tissue Navigation System versus CT-Guided Liver Biopsy in a Porcine Model: A Prospective Randomized Trial," *Academic radiology,* vol. 17, pp. 1282-1287, 2010.

[151] C. M. Wegner and D. B. Karron, "Surgical navigation system and method using audio feedback," ed: Google Patents, 2000.

[152] J. Banerjee, C. Klink, E. D. Peters, W. J. Niessen, A. Moelker, and T. van Walsum, "Fast and robust 3D ultrasound registration-block and game theoretic matching," *Medical image analysis,* 2014.

[153] C. Hansen, D. Black, C. Lange, F. Rieber, W. Lamadé, M. Donati*, et al.*, "Auditory support for resection guidance in navigated liver surgery," *The International Journal of Medical Robotics and Computer Assisted Surgery,* vol. 9, pp. 36-43, 2013.

[154] D. Tran, A. A. Kamani, E. Al-Attas, V. A. Lessoway, S. Massey, and R. N. Rohling, "Single-operator real-time ultrasound-guidance to aim and insert a lumbar epidural needle," *Canadian Journal of Anesthesia/Journal canadien d'anesthésie,* vol. 57, pp. 313-321, 2010.

[155] F. Lindseth, T. Langø, T. Selbekk, R. Hansen, I. Reinertsen, C. Askeland*, et al.*, "Ultrasound-based guidance and therapy," *Advancements and breakthroughs in ultrasound imaging,* pp. 28-82, 2013.

[156] A. R. Peon, C. Pacchierotti, and D. Prattichizzo, "Vibrotactile stimuli for augmented haptic feedback in robot-assisted surgery," in *World Haptics Conference (WHC), 2013*, 2013, pp. 473-478.

[157] K. Bark, P. Khanna, R. Irwin, P. Kapur, S. Jax, L. J. Buxbaum*, et al.*, "Lessons in using vibrotactile feedback to guide fast arm motions," in *World Haptics Conference (WHC), 2011 IEEE*, 2011, pp. 355-360.

[158] Ž. Obrenović, "Experimental evaluation of user performance in a pursuit tracking task with multimodal feedback," *Yugoslav Journal of Operations Research,* vol. 14, pp. 99-115, 2004.

[159] T. Hermann, A. Hunt, and J. G. Neuhoff, *The sonification handbook*: Logos Verlag Berlin, GE, 2011.

[160] R. Velãzquez, O. Bazán, and M. Magaña, "A shoe-integrated tactile display for directional navigation," in *Intelligent Robots and Systems, 2009. IROS 2009. IEEE/RSJ International Conference on*, 2009, pp. 1235-1240.

[161] G. Ng, P. Barralon, S. Schwarz, G. Dumont, and J. M. Ansermino, "Evaluation of a tactile display around the waist for physiological monitoring under different clinical workload conditions," in *Engineering in Medicine and Biology Society, 2008. EMBS 2008. 30th Annual International Conference of the IEEE*, 2008, pp. 1288-1291.

[162] F. Robineau, F. Boy, J.-P. Orliaguet, J. Demongeot, and Y. Payan, "Guiding the surgical gesture using an electro-tactile stimulus array on the tongue: A feasibility study," *Biomedical Engineering, IEEE Transactions on,* vol. 54, pp. 711-717, 2007.

[163] E. Jovanov, K. Wegner, V. Radivojević, D. Starčević, M. S. Quinn, and D. B. Karron, "Tactical audio and acoustic rendering in biomedical applications," *Information Technology in Biomedicine, IEEE Transactions on,* vol. 3, pp. 109-118, 1999.

[164] W. G. Gardner, *3-D audio using loudspeakers*: Springer Science & Business Media, 1998.

[165] A. Eldridge, "Issues in auditory display," *Artificial Life,* vol. 12, pp. 259-274, 2006.

[166] S. Pauletto and A. Hunt, "Interactive sonification of complex data," *International Journal of Human-Computer Studies,* vol. 67, pp. 923-933, 2009.

[167] A. Godbout and J. E. Boyd, "Corrective sonic feedback for speed skating: a case study," in *Proceedings of the 16th international conference on auditory display*, 2010, pp. 23-30.

[168] Z. Obrenovic, D. Starcevic, and E. Jovanov, "Experimental evaluation of multimodal human computer interface for tactical audio applications," in *Multimedia and Expo, 2002. ICME'02. Proceedings. 2002 IEEE International Conference on*, 2002, pp. 29-32.

[169] B. Cho, N. Matsumoto, S. Komune, and M. Hashizume, "A Surgical Navigation System for Guiding Exact Cochleostomy Using Auditory Feedback: A Clinical Feasibility Study," *BioMed research international,* vol. 2014, 2014.

[170] P. A. Woerdeman, P. W. Willems, H. J. Noordmans, and J. W. B. van der Sprenkel, "Auditory feedback during frameless image-guided surgery in a phantom model and initial clinical experience: Technical note," *Journal of neurosurgery,* vol. 110, pp. 257-262, 2009.

[171] D. Black, J. Al Issawi, C. Hansen, C. Rieder, and H. Hahn, "Auditory support for navigated radiofrequency ablation," *Roboter-Assistenten werden sensitiv.,* p. 30.

[172] C. Ho, H. Z. Tan, and C. Spence, "The differential effect of vibrotactile and auditory cues on visual spatial attention," *Ergonomics,* vol. 49, pp. 724-738, 2006.

[173] J. B. Van Erp, H. A. Van Veen, C. Jansen, and T. Dobbins, "Waypoint navigation with a vibrotactile waist belt," *ACM Transactions on Applied Perception (TAP),* vol. 2, pp. 106-117, 2005.

[174] S. K. Nagel, C. Carl, T. Kringe, R. Märtin, and P. König, "Beyond sensory substitution—learning the sixth sense," *Journal of neural engineering,* vol. 2, p. R13, 2005.

[175] R. Velázquez, "Wearable assistive devices for the blind," in *Wearable and Autonomous Biomedical Devices and Systems for Smart Environment*, ed: Springer, 2010, pp. 331-349.

[176] S. Cardin, D. Thalmann, and F. Vexo, "A wearable system for mobility improvement of visually impaired people," *The Visual Computer,* vol. 23, pp. 109-118, 2007.

[177] L. A. Jones and N. B. Sarter, "Tactile displays: Guidance for their design and application," *Human Factors: The Journal of the Human Factors and Ergonomics Society,* vol. 50, pp. 90-111, 2008.

[178] A. M. Okamura, M. R. Cutkosky, and J. T. Dennerlein, "Reality-based models for vibration feedback in virtual environments," *Mechatronics, IEEE/ASME Transactions on,* vol. 6, pp. 245-252, 2001.

[179] H. Regenbrecht, J. Hauber, R. Schoenfelder, and A. Maegerlein, "Virtual reality aided assembly with directional vibro-tactile feedback," in *Proceedings of the 3rd international conference on Computer graphics and interactive techniques in Australasia and South East Asia*, 2005, pp. 381-387.

[180] K. J. Kuchenbecker, J. Fiene, and G. Niemeyer, "Improving contact realism through event-based haptic feedback," *Visualization and Computer Graphics, IEEE Transactions on,* vol. 12, pp. 219-230, 2006.

[181] A. El Saddik, "Still only in its infancy, haptics promises to be a revolution in how we interact in the virtual world," *IEEE Instrumentation & Measurement Magazine,* vol. 1094, 2007.

[182] C. Cipriani, M. D. Alonzo, and M. C. Carrozza, "A miniature vibrotactile sensory substitution device for multifingered hand prosthetics," *Biomedical Engineering, IEEE Transactions on,* vol. 59, pp. 400-408, 2012.

[183] J. A. Goebel, B. C. Sinks, B. E. Parker Jr, N. T. Richardson, A. B. Olowin, and R. W. Cholewiak, "Effectiveness of head-mounted vibrotactile stimulation in subjects with bilateral vestibular loss: a phase 1 clinical trial," *Otology & Neurotology,* vol. 30, pp. 210-216, 2009.

[184] P. Bach-Y-Rita, C. C. Collins, F. A. Saunders, B. White, and L. Scadden, "Vision substitution by tactile image projection," 1969.

[185] M. K. Dobrzynski, S. Mejri, S. Wischmann, and D. Floreano, "Quantifying information transfer through a head-attached vibrotactile display: principles for design and control," *Biomedical Engineering, IEEE Transactions on,* vol. 59, pp. 2011-2018, 2012.

[186] C. Bertram, M. H. Evans, M. Javaid, T. Stafford, and T. Prescott, "Sensory augmentation with distal touch: the tactile helmet project," in *Biomimetic and Biohybrid Systems*, ed: Springer, 2013, pp. 24-35.

[187] K. Gilliland and R. E. Schlegel, "Tactile stimulation of the human head for information display," *Human Factors: The Journal of the Human Factors and Ergonomics Society,* vol. 36, pp. 700-717, 1994.

[188] F. Thullier, B. Bolmont, and F. G. Lestienne, "Vibrotactile pattern recognition: A portable compact tactile matrix," *Biomedical Engineering, IEEE Transactions on,* vol. 59, pp. 525-530, 2012.

[189] S. Peddamatham, W. Peine, and H. Z. Tan, "Assessment of vibrotactile feedback in a needle-insertion task using a surgical robot," in *Haptic interfaces for virtual environment and teleoperator systems, 2008. haptics 2008. symposium on*, 2008, pp. 93-99.

[190] B. Weber, S. Schätzle, T. Hulin, C. Preusche, and B. Deml, "Evaluation of a vibrotactile feedback device for spatial guidance," in *World Haptics Conference (WHC), 2011 IEEE*, 2011, pp. 349-354.

[191] T. Howard and J. Szewczyk, "Visuo-haptic feedback for 1-D Guidance in laparoscopic surgery," in *Biomedical Robotics and Biomechatronics (2014 5th IEEE RAS & EMBS International Conference on*, 2014, pp. 58-65.

[192] J. Bluteau, M.-D. Dubois, S. Coquillart, E. Gentaz, and Y. Payan, "Vibrotactile guidance for trajectory following in computer aided surgery," in *Engineering in Medicine and Biology Society (EMBC), 2010 Annual International Conference of the IEEE*, 2010, pp. 2085-2088.

[193] M. Brell, D. Roßkamp, and A. Hein, "Fusion of vibrotactile signals used in a tactile display in computer aided surgery," in *Haptics: Perception, Devices and Scenarios*, ed: Springer, 2008, pp. 383-388.

[194] K. Myles and J. T. Kalb, "Vibrotactile sensitivity of the head," DTIC Document2009.

[195] E. H. Weber, *EH Weber: The sense of touch*: Academic Pr, 1978.

[196] E. Jovanov, D. Starcevic, A. Marsh, Z. Obrenovic, V. Radivojevic, and A. Samardzic, "Multi modal presentation in virtual telemedical environments," in *High-Performance Computing and Networking*, 1999, pp. 964-972.

[197] R. Irwan and R. M. Aarts, "Two-to-five channel sound processing," *Journal of the Audio Engineering Society,* vol. 50, pp. 914-926, 2002.

[198] E. M. Krebs, "An audio architecture integrating sound and live voice for virtual environments," Naval Postgraduate School, 2002.

[199] M. Schreier, "Audio Server for Virtual Reality Applications," Citeseer, 2002.

[200] P. Willems, H. Noordmans, J. van Overbeeke, M. Viergever, C. Tulleken, and J. B. van der Sprenkel, "The impact of auditory feedback on neuronavigation," *Acta neurochirurgica,* vol. 147, pp. 167-173, 2005.

[201] P. Microdrives. (03/11). *Pico Vibe 8mm Vibration Motor*. Available: https://catalog.precisionmicrodrives.com/order-parts/product/308-100-8mm-vibration-motor-3mm-type

[202] Razer. (01/11). *Razer Tiamat 7.1*. Available: http://www.razerzone.com/gaming-audio/razer-tiamat-71

[203] F. L. Wightman and D. J. Kistler, "Headphone simulation of free-field listening. II: Psychophysical validation," *The Journal of the Acoustical Society of America,* vol. 85, pp. 868-878, 1989.

[204] E. M. Wenzel, M. Arruda, D. J. Kistler, and F. L. Wightman, "Localization using nonindividualized head-related transfer functions," *The Journal of the Acoustical Society of America,* vol. 94, pp. 111-123, 1993.

[205] J. Shriki, "Ultrasound physics," *Critical care clinics,* vol. 30, pp. 1-24, 2014.

[206] J. M. Cannat, J. Williams, Q. Zhou, T. Ritter, and K. K. Shung, "Development of a 35-MHz piezo-composite ultrasound array for medical imaging," *Ultrasonics, Ferroelectrics, and Frequency Control, IEEE Transactions on,* vol. 53, pp. 224-236, 2006.

[207] H.-C. Yang, J. Cannata, J. Williams, and K. Shung, "Crosstalk reduction for high-frequency linear-array ultrasound transducers using 1-3 piezocomposites with pseudo-random pillars," *Ultrasonics, Ferroelectrics, and Frequency Control, IEEE Transactions on,* vol. 59, 2012.

[208] Q. Zhou, D. Wu, C. Liu, B. Zhu, F. Djuth, and K. K. Shung, "Micro-machined high-frequency (80 MHz) PZT thick film linear arrays," *Ultrasonics, Ferroelectrics, and Frequency Control, IEEE Transactions on,* vol. 57, pp. 2213-2220, 2010.

[209] F. S. Foster, J. Mehi, M. Lukacs, D. Hirson, C. White, C. Chaggares*, et al.*, "A new 15–50 MHz array-based micro-ultrasound scanner for preclinical imaging," *Ultrasound in medicine & biology,* vol. 35, pp. 1700-1708, 2009.

[210] J. Fischer, T. Herzog, S. Walter, and H. Heuer, "Design and fabrication of a 5 MHz ultrasonic phased array probe with curved transducer," in *SPIE Microtechnologies*, 2013, pp. 87632M-87632M-6.

[211] A. Manbachi, M. Lee, F. S. Foster, H. J. Ginsberg, and R. S. Cobbold, "Design and fabrication of a low-frequency (1-3 MHz) ultrasound transducer for accurate placement of screw implants in the spine," in *SPIE Medical Imaging*, 2014, pp. 90400H-90400H-10.

[212] Z. M. Hijazi, K. Shivkumar, and D. J. Sahn, "Intracardiac echocardiography during interventional and electrophysiological cardiac catheterization," *Circulation,* vol. 119, pp. 587-596, 2009.

[213] M. Desai, "Ultrasonography-guided punctures—with and without puncture guide," *Journal of Endourology,* vol. 23, pp. 1641-1643, 2009.

[214] P. Alken, "The Early History of Percutaneous Nephrolithotomy (PNL)," in *Supine Percutaneous Nephrolithotomy and ECIRS*, ed: Springer, 2014, pp. 5-14.

[215] K. K. Shung, M. Smith, and B. M. Tsui, *Principles of medical imaging*: Academic Press, 2012.

[216] L. F. Brown, "Design considerations for piezoelectric polymer ultrasound transducers," *Ultrasonics, Ferroelectrics, and Frequency Control, IEEE Transactions on,* vol. 47, pp. 1377-1396, 2000.

[217] K. K. Shung and M. Zippuro, "Ultrasonic transducers and arrays," *Engineering in Medicine and Biology Magazine, IEEE,* vol. 15, pp. 20-30, 1996.

[218] J. An, K. Song, S. Zhang, J. Yang, and P. Cao, "Design of a Broadband Electrical Impedance Matching Network for Piezoelectric Ultrasound Transducers Based on a Genetic Algorithm," *Sensors,* vol. 14, pp. 6828-6843, 2014.

[219] L. Barber, R. Barrett, and G. Lichtwark, "Validation of a freehand 3D ultrasound system for morphological measures of the medial gastrocnemius muscle," *Journal of biomechanics,* vol. 42, pp. 1313-1319, 2009.

[220] S. Saffar, A. Abdullah, and R. Othman, "Influence of the thickness of matching layers on narrow band transmitter ultrasonic airborne transducers with frequencies< 100kHz: Application of a genetic algorithm," *Applied Acoustics,* vol. 75, pp. 72-85, 2014.

[221] T. Manh, A.-T. T. Nguyen, T. F. Johansen, and L. Hoff, "Microfabrication of stacks of acoustic matching layers for 15MHz ultrasonic transducers," *Ultrasonics,* vol. 54, pp. 614-620, 2014.

[222] T. Manh, G. U. Jensen, T. F. Johansen, and L. Hoff, "Modeling of micromachined silicon–polymer 2-2 composite matching layers for 15MHz ultrasound transducers," *Ultrasonics,* vol. 54, pp. 1088-1096, 2014.

[223] R. L. Goldberg and S. W. Smith, "Multilayer piezoelectric ceramics for two-dimensional array transducers," *Ultrasonics, Ferroelectrics, and Frequency Control, IEEE Transactions on,* vol. 41, pp. 761-771, 1994.

[224] S. Rhee, T. Ritter, K. Shung, H. Wang, and W. Cao, "Materials for acoustic matching in ultrasound transducers," in *Ultrasonics Symposium, 2001 IEEE*, 2001, pp. 1051-1055.

[225] Q. Zhou, J. H. Cha, Y. Huang, R. Zhang, W. Cao, and K. K. Shung, "Alumina/epoxy nanocomposite matching layers for high-frequency ultrasound transducer application," *Ultrasonics, Ferroelectrics, and Frequency Control, IEEE Transactions on,* vol. 56, pp. 213-219, 2009.

[226] L. C. Lynnworth, "Ultrasonic impedance matching from solids to gases," *Sonics and Ultrasonics, IEEE Transactions on,* vol. 12, pp. 37-48, 1965.

[227] G. Kossoff, "The effects of backing and matching on the performance of piezoelectric ceramic transducers," *Sonics and Ultrasonics, IEEE Transactions on,* vol. 13, pp. 20-30, 1966.

[228] F. Tiefensee, C. Becker-Willinger, G. Heppe, P. Herbeck-Engel, and A. Jakob, "Nanocomposite cerium oxide polymer matching layers with adjustable acoustic impedance between 4 MRayl and 7 MRayl," *Ultrasonics,* vol. 50, pp. 363-366, 2010.

[229] H. Persson and C. Hertz, "Acoustic impedance matching of medical ultrasound transducers," *Ultrasonics,* vol. 23, pp. 83-89, 1985.

[230] C. S. Desilets, J. D. Fraser, and G. S. Kino, "The design of efficient broad-band piezoelectric transducers," *Sonics and Ultrasonics, IEEE Transactions on,* vol. 25, pp. 115-125, 1978.

[231] A. Bybi, C. Granger, S. Grondel, A. C. Hladky-Hennion, and J. Assaad, "Electrical method for crosstalk cancellation in transducer arrays," *NDT & E International,* vol. 62, pp. 115-121, 3// 2014.

[232] T. Manh, G. U. Jensen, T. F. Johansen, and L. Hoff, "Microfabricated 1–3 composite acoustic matching layers for 15MHz transducers," *Ultrasonics,* vol. 53, pp. 1141-1149, 2013.

[233] S. Zhou, G. L. Wojcik, and J. Hossack, "An approach for reducing adjacent element crosstalk in ultrasound arrays," *Ultrasonics, Ferroelectrics, and Frequency Control, IEEE Transactions on,* vol. 50, pp. 1752-1761, 2003.

[234] J. H. Chang, D. T. Raphael, Y. P. Zhang, and K. K. Shung, "Proof of Concept: In Vitro Measurement of Correlation between Radiodensity and Ultrasound Echo Response of Ovine Vertebral Bodies," *Ultrasonics,* vol. 51, pp. 253-257, 11/03 2011.

[235] G. M. Lous, I. A. Cornejo, T. F. McNulty, A. Safari, and S. C. Danforth, "Fabrication of piezoelectric ceramic/polymer composite transducers using fused deposition of ceramics," *Journal of the American Ceramic Society,* vol. 83, pp. 124-28, 2000.

[236] M. G. Silk, "Ultrasonic transducers for nondestructive testing," 1984.

[237] Q. Chen and P. Payne, "Industrial applications of piezoelectric polymer transducers," *Measurement Science and Technology,* vol. 6, p. 249, 1995.

[238] F. S. Foster, "Transducer materials and probe construction," *Ultrasound in Medicine and Biology,* vol. 26, pp. S2-S5.

[239] H. Matthews, "Surface wave filters: Design, construction, and use," *New York, Wiley-Interscience, 1977. 521 p,* vol. 1, 1977.

[240] W. P. Mason, *Piezoelectric crystals and their application to ultrasonics*: van Nostrand, 1950.

[241] H. Kuttruff, *Ultrasonics: fundamentals and applications*: Springer Science & Business Media, 2012.

[242] L. E. Frenzel, *RF Power for Industrial Applications*: Pearson/Prentice Hall, 2004.

[243] (December). *RF Toolbox*. Available: http://www.mathworks.com/products/rftoolbox/

[244] J. C. Lagarias, J. A. Reeds, M. H. Wright, and P. E. Wright, "Convergence properties of the Nelder–Mead simplex method in low dimensions," *SIAM Journal on optimization,* vol. 9, pp. 112-147, 1998.

[245] C. Yang, Z. He, and W. Yu, "Comparison of public peak detection algorithms for MALDI mass spectrometry data analysis," *BMC bioinformatics,* vol. 10, p. 4, 2009.

[246] G. Palshikar, "Simple algorithms for peak detection in time-series," in *Proc. 1st Int. Conf. Advanced Data Analysis, Business Analytics and Intelligence*, 2009.

[247] J. Zhang, E. Gonzalez, T. Hestilow, W. Haskins, and Y. Huang, "Review of peak detection algorithms in liquid-chromatography-mass spectrometry," *Current genomics,* vol. 10, p. 388, 2009.

[248] A. Savitzky and M. J. Golay, "Smoothing and differentiation of data by simplified least squares procedures," *Analytical chemistry,* vol. 36, pp. 1627-1639, 1964.

[249] T. O'Haver, "A Pragmatic Introduction to Signal Processing," ed, 1997.

[250] P. Du, W. A. Kibbe, and S. M. Lin, "Improved peak detection in mass spectrum by incorporating continuous wavelet transform-based pattern matching," *Bioinformatics,* vol. 22, pp. 2059-2065, 2006.

[251] F. A. Duck, *Physical properties of tissues: a comprehensive reference book*: Academic Press, 1990.

[252] B. A. Angelsen, *Ultrasound imaging: waves, signals, and signal processing. 1. Basic principles wave generation, propagation, and beamforming in homogeneous tissue*: Emantec, 2000.

[253] K. Zell, J. Sperl, M. Vogel, R. Niessner, and C. Haisch, "Acoustical properties of selected tissue phantom materials for ultrasound imaging," *Physics in medicine and biology,* vol. 52, p. N475, 2007.

[254] F. A. Duck, *Physical properties of tissues: a comprehensive reference book*: Academic press, 2013.

[255] H. Azhari, "Appendix A: Typical Acoustic Properties of Tissues," *Basics of Biomedical Ultrasound for Engineers,* pp. 313-314, 2010.

[256] G. M. Spirou, A. A. Oraevsky, I. A. Vitkin, and W. M. Whelan, "Optical and acoustic properties at 1064 nm of polyvinyl chloride-plastisol for use as a tissue phantom in biomedical optoacoustics," *Physics in Medicine and Biology,* vol. 50, p. N141, 2005.

[257] G. A. Cortela, L. E. Maggi, M. A. Kruger, C. A. Negreira, and C. W. Pereira, "Ultrasonic attenuation and speed in phantoms made of polyvinyl chloride-plastisol (PVCP) and graphite powder," in *Proceedings of Meetings on Acoustics*, 2013, p. 075095.

[258] J. R. Taylor, J. J. M. Chan, and G. Thomas, "Frequency selection for compounding synthetic aperture ultrasound images," in *Imaging Systems and Techniques (IST), 2012 IEEE International Conference on*, 2012, pp. 74-77.

[259] M. Ali, "Analysis of broadband piezoelectric transducers by discrete time model," *Egypt. J. Sol,* vol. 23, pp. 287-295, 2000.

[260] T. E. G. Álvarez-Arenas and L. Diez, "Novel impedance matching materials and strategies for air-coupled piezoelectric transducers," in *SENSORS, 2013 IEEE*, 2013, pp. 1-4.

[261] B. C. Tsui, "Facilitating needle alignment in-plane to an ultrasound beam using a portable laser unit," *Regional anesthesia and pain medicine,* vol. 32, pp. 84-88, 2007.

[262] R. Gras, M. Müller, E. Gasteiger, S. Gay, P. A. Binz, W. Bienvenut*, et al.*, "Improving protein identification from peptide mass fingerprinting through a parameterized multi-level scoring algorithm and an optimized peak detection," *Electrophoresis,* vol. 20, pp. 3535-3550, 1999.

[263] S. Li, F. G. Zöllner, A. D. Merrem, Y. Peng, J. Roervik, A. Lundervold*, et al.*, "Wavelet-based segmentation of renal compartments in DCE-MRI of human kidney: initial results in patients and healthy volunteers," *Computerized Medical Imaging and Graphics,* vol. 36, pp. 108-118, 2012.

[264] M. J. Zipparo, K. K. Shung, and T. R. Shrout, "Piezoceramics for high-frequency (20 to 100 MHz) single-element imaging transducers," *Ultrasonics, Ferroelectrics, and Frequency Control, IEEE Transactions on,* vol. 44, pp. 1038-1048, 1997.

[265] K. Snook, J.-Z. Zhao, C. H. Alves, J. M. Cannata, W.-H. Chen, R. J. Meyer Jr*, et al.*, "Design, fabrication, and evaluation of high frequency, single-element transducers incorporating different materials," *Ultrasonics, Ferroelectrics, and Frequency Control, IEEE Transactions on,* vol. 49, pp. 169-176, 2002.

[266] V. Gibiat, O. Lefeuvre, T. Woignier, J. Pelous, and J. Phalippou, "Acoustic properties and potential applications of silica aerogels," *Journal of Non-Crystalline Solids,* vol. 186, pp. 244-255, 1995.

[267] T. E. G. Álvarez-Arenas, "Acoustic impedance matching of piezoelectric transducers to the air," *Ultrasonics, Ferroelectrics, and Frequency Control, IEEE Transactions on,* vol. 51, pp. 624-633, 2004.

[268] C. E. Démoré, J. Brown, and G. R. Lockwood, "Investigation of cross talk in kerfless annular arrays for high-frequency imaging," *Ultrasonics, Ferroelectrics, and Frequency Control, IEEE Transactions on,* vol. 53, pp. 1046-1056, 2006.

[269] X. Jin, Ö. Oralkan, F. L. Degertekin, and B. T. Khuri-Yakub, "Characterization of one-dimensional capacitive micromachined ultrasonic immersion transducer arrays," *Ultrasonics, Ferroelectrics, and Frequency Control, IEEE Transactions on,* vol. 48, pp. 750-760, 2001.

[270] D. Wang, E. Filoux, F. Levassort, M. Lethiecq, S. Rocks, and R. Dorey, ''Fabrication and characterization of annular-array, high-frequency, ultrasonic transducers based on PZT thick film,'' *Sensors and Actuators A: Physical,* vol. 216, pp. 207-213, 2014.